The hard physics of soft muons: novel measurement of the top-quark mass and differential cross-sections of top-quark pair production using the ATLAS detector at the LHC

Lewis Joseph Wilkins

Department of Physics
Royal Holloway, University of London

A thesis submitted to the University of London
for the degree of Doctor of Philosophy

Declaration

I declare that the work presented in this thesis is my own. The work presented in this thesis was performed as part of the ATLAS experiment and therefore was carried out in collaboration with many people. Chapters 1 to 4 contain background information related to the underlying physics theory and experimental setup. The top-quark mass measurement outlined in Chapters 5 to 9 was performed as part of a team and was presented in Ref. [1]. The studies presented in Sections 6.1.3, 6.2.2, 6.3, 8.5, and 8.6 were performed by myself. In addition to these studies, I also contributed significantly to the development of the software used for the analysis chain. The differential cross-section measurement presented in Chapter 10 is entirely my own work.

Lewis Wilkins
March 2020

Abstract

The mass of the top quark is measured in lepton+jets top-quark pair events with an experimental technique exploits the semileptonic decay of b hadrons. An invariant mass is constructed between the lepton from the W-boson decay and a soft muon originating from a b-hadron decay. A binned-template likelihood fit is performed to the invariant mass distribution yielding the most precise ATLAS measured value of the top-quark mass of $m_t = 174.44 \pm 0.76\,(\text{stat+syst})\,\text{GeV}$. Measurements of differential cross-sections of top-quark pair production are performed as a function of several observables related to the decay of the W boson and b hadron. These measured cross-sections are compared to various predictions.

Acknowledgements

First, and foremost, I would like the thank my supervisor Véronique Boisvert for her guidance and support over the past few years. I could not have had a more suitable supervisor to support my studies throughout my PhD. I would also like the thank the whole ATLAS group at Royal Holloway for many interesting discussions and guidance over my time there. Thanks must go to Francesco Spanò for imparting his knowledge on all things top quark and statistics.

Special thanks must go to Jay Howarth. While we never worked in the same department or even analysis team, he has put up with many hours of my incessant questioning and continued to help me until the bitter end.

From my time spent at CERN, I would like to thank the numerous people with whom I spent many hours drinking beer in R1 with. Wednesdays do not feel complete with kebab and beer. Eddie and Deshan were the best house mates I could have asked for and I cannot thank them enough for the hours of endless nonsense and mischief we had in Geneva. A special mention must go to Deshan. Over our time at CERN we managed to live in the same flat, work in the same office and socialise with the same people for over a year and not go too insane. Fair play Desh.

To the Treehouse, I owe you my sanity. Thankyou for the Saturday morning video calls and the endless stubbies which kept me going over the last few years. Greek, I owe you a seafood dinner.

I would also like to thank a few people who have helped me over the year. My Masters supervisor Jaap Velthuis, thankyou for taking a punt on me as a project student, without that I would not be writing this. Back to my school years, special thanks must go to Mr Roberts and Mr Downes. Both of your lessons inspired me over many years to go on and study physics.

I would like to thank my family for their support. Dad, Nicky, Jordan, Jake and Beth, Anna, Mike and to a certain extent Evie, Grandma and Grandad, this would not have been possible without you.

Finally, I suppose I have to thank Caitlin. Thank you for putting up with my hours of complaints, for your hours travelling to visit me and your frequent care packages. Love you really.

Contents

1 Introduction **21**

2 Theoretical foundations **23**

2.1 The Standard Model 23

2.2 Top quark physics 33

3 The Large Hadron Collider and the ATLAS Experiment **43**

3.1 The Large Hadron Collider 43

3.2 The ATLAS experiment 46

4 Data simulation and object reconstruction **61**

4.1 Monte Carlo simulation 61

4.2 Object definitions 64

5 Object and event selection **77**

5.1 Data 77

5.2 Simulation samples 77

5.3 Electrons 83

5.4 Muons 83

5.5 Jets 84

5.6 *b*-tagging 84

5.7 Particle level objects 84

5.8 Event selection 85

6 Simulation modelling **88**

6.1 Signal modelling . . . 88

6.2 Background modelling . . . 96

6.3 Particle level reweighting . . . 114

7 Sample composition and event yields **120**

7.1 Sample composition . . . 120

8 Sources of uncertainty **127**

8.1 Luminosity . . . 127

8.2 Data and MC statistics . . . 127

8.3 Leptons . . . 129

8.4 Jets and missing transverse energy . . . 130

8.5 Jet flavour composition uncertainty . . . 130

8.6 Pileup ρ topology uncertainty . . . 136

8.7 Flavour tagging . . . 143

8.8 Pileup . . . 144

8.9 Signal modelling . . . 145

8.10 Background modelling . . . 154

9 Mass extraction **156**

9.1 Binned template profile-likelihood fit . . . 156

9.2 Fit setup . . . 160

9.3 Fit to Asimov dataset . . . 161

9.4 Fit to data . . . 164

9.5 Result . . . 164

9.6 Conclusions . . . 172

10 Measurement of top-quark pair differential cross-sections **173**

10.1 Analysis outline . . . 173

10.2 Unfolding . . . 175

10.3 Binning optimisation . . . 194

10.4 Systematic uncertainties 200
10.5 Results 209
10.6 Discussion 215

11 Conclusions **217**

References **220**

A ρ topology control plots **236**

Figures

2.1 Visualisation of the Higgs potential. The expectation value of the Higgs field, v, occurs at any point on the plane of the minimum. 32

2.2 Examples of production channels for top quark pair-production. 34

2.3 The MSTW group 2008 NLO PDF for the proton as a function of the momentum fraction x and at resolution scale $Q^2 = 10\text{GeV}^2$ (left) and $Q^2 = 10^4\text{GeV}^2$ (right) 35

2.4 The leading order channels for single top quark production. 35

2.5 The Higgs potential as a function of top quark and Higgs masses with regions of absolute stability, meta-stability and instability highlighted 39

2.6 A summary of direct top-quark mass measurements from the ATLAS and CMS Collaborations 40

2.7 A summary of recent indirect top-quark mass measurements from the ATLAS and CMS Collaborations 41

2.8 Feynman diagram of the decay channel used in the analysis. 42

3.1 A diagram of the CERN accelerator and experiment complex 45

3.2 A cut-away diagram of the ATLAS detector, with the various subsystems labeled 46

3.3 The layout of the Inner Detector, with the key components labelled 48

3.4 Diagram of the barrel region of the EM calorimeter 51

3.5 Drawing of a tile calorimeter section 52

3.6 A computer generated image of the muon system 56

3.7 A computer generated image of the magnet system 57

3.8 A diagram of the ATLAS trigger and data acquisition system 58

4.1 A computer generated diagram of the event generation process 63
4.2 Example of *anti-k_T* (a) and k_T (b) jet clustering algorithm with $R = 1$ 71
4.3 A summary of the calibration steps for jets in the ATLAS experiment 71
4.4 The results of the in-situ calibration. The ratio of the data and MC response, R, from the three event topologies is shown with different markers as a function of jet-p_{T}. 74
4.5 The output `MV2c10` discriminant for b jets (blue), c jets (green) and light flavour jets (red) 75

6.1 Comparison between data and MC for SMT-jet p_{T} (a) and leading jet p_{T} (b) with the nominal event selection applied. The uncertainty bands include the statistical and systematic uncertainties. 93
6.2 Pre and post-fit plots for the SMT jet calibration derivation. 94
6.3 The real and fake efficiencies for electrons. 102
6.4 The real and fake efficiencies for muons. 103
6.5 Comparison of data and prediction for electrons in the $N_{\mathrm{Jet}} \geq 2$ control region. 106
6.6 Comparison of data and prediction for electrons in the $N_{\mathrm{Jet}} \geq 3$ control region. 107
6.7 Comparison of data and prediction for electrons in the $N_{\mathrm{Jet}} \geq 4$ control region. 107
6.8 Comparison of data and prediction for electrons in the $N_{\mathrm{Jet}} \geq 2$ and at least one b-tagged jet control region. 108
6.9 Comparison of data and prediction for electrons in the $N_{\mathrm{Jet}} \geq 3$ and at least one b-tagged jet control region. 108
6.10 Comparison of data and prediction for electrons in the $N_{\mathrm{Jet}} \geq 4$ and at least one b-tagged jet control region. 109
6.11 Comparison of data and prediction for muons in the $N_{\mathrm{Jet}} \geq 2$ control region. . 109
6.12 Comparison of data and prediction for muons in the $N_{\mathrm{Jet}} \geq 3$ control region. . 110
6.13 Comparison of data and prediction for muons in the $N_{\mathrm{Jet}} \geq 4$ control region. . 110
6.14 Comparison of data and prediction for muons in the $N_{\mathrm{Jet}} \geq 2$ and at least one b-tagged jet control region. 111

6.15 Comparison of data and prediction for muons in the $N_{\text{Jet}} \geq 3$ and at least one b-tagged jet control region. . . . 111
6.16 Comparison of data and prediction for muons in the $N_{\text{Jet}} \geq 4$ and at least one b-tagged jet control region. . . . 112
6.18 Plot of the response matrix derived fromPowheg+Pythia8 A14-r_b $t\bar{t}$ sample. 117
6.19 Comparison of $m_t = 174.5$ $t\bar{t}$ sample at reconstructed level with particle level sample, reweighted to reconstructed level with transfer function. . . . 118
6.20 Comparison of the Powheg+Pythia8 A14 $t\bar{t}$ sample at reconstructed level with particle level sample reweighted to reconstructed level with transfer function derived from the Powheg+Pythia8 A14-r_b sample. . . . 119

7.1 Comparison of data and prediction for $p_{\text{T}}(\ell^{\text{primary}})$. . . . 123
7.2 Comparison of data and prediction for $\eta(\ell^{\text{primary}})$. . . . 124
7.3 Comparison of data and prediction for $p_{\text{T}}(\mu^{\text{SMT}})$. . . . 124
7.4 Comparison of data and prediction for $m_{\text{T}}(W)$. . . . 125
7.5 Comparison of data and prediction for $E_{\text{T}}^{\text{miss}}$. . . . 125
7.6 Comparison of data and prediction for p_{T}(leading jet). . . . 126
7.7 Comparison of data and MC prediction for p_{T}(SMT jet). . . . 126

8.1 Distribution of the track multiplicity, n_{track}, for jets initiated from quark and gluons using the Pythia8 generator . . . 131
8.2 Plots of the gluon fraction as a function of jet-p_{T} and jet-η with its associated uncertainty in each of the four channels. . . . 134
8.3 Plots of gluon fraction as a function of jet p_{T} in five η regions. Each colour represents a different channel and run year as described in the legend. Uncertainty bands include the statistical error on the gluon fraction. . . . 135
8.4 A comparison of the data and two MC predictions for (a) lepton-p_{T}, (b) lepton-η, (c) leading jet-p_{T} and (d) subleading jet-p_{T} for the Z+jets topology. . . . 140
8.5 A comparison of the data and two MC predictions for (a) jet multiplicity, (b) leading jet-η, (c) reference object p_{T} and (d) ρ for the Z+jets topology. . . . 141
8.6 Linear fit of ρ vs $\langle\mu\rangle$ profile for the Z+jets topology. . . . 142

8.7 Linear fit of ρ vs $\langle\mu\rangle$ profile for the γ+jets topology. . . . 143
8.8 Linear fit of ρ vs $\langle\mu\rangle$ profile for the dijet topology. . . . 144
8.9 Fractional uncertainty map for ρ binned in jet-p_{T} and jet-η. . . . 145
8.10 Comparison between $B^0 \to D^- \mu\nu$ (black) and $B^0 \to D^*(2010)^- \mu\nu$ (red) for (a) $p_{\mathrm{T}}^{\text{smt-jet}}$, (b) $p_{\mathrm{T}}^{\text{smt-}\mu}$ and (c) $m_{\ell\mu}$. . . . 148
8.11 These plots show the comparison between $B^+ \to \overline{D^0}\mu\nu$ (black) and $B^0 \to D^*(2010)^- \mu\nu$ (red) for (a) $p_{\mathrm{T}}^{\text{smt-jet}}$, (b) $p_{\mathrm{T}}^{\text{smt-}\mu}$ and (c) $m_{\ell\mu}$. . . . 149
8.12 (a) Comparison of the effect of the systematic uncertainty for $B^0 \to \overline{D^0}(2010)\mu\nu$ and (b) $B^+ \to \overline{D^*}(2007)^0 \mu\nu$ exclusive decays. . . . 150
8.13 A comparison of the A14-r_b and A14 tunings of POWHEG+PYTHIA8 as a function of x_B. The uncertainty associated with r_b is shown in light blue and both r_b and FSR uncertainty is shown in pink. . . . 153

9.1 Sensitivity of the $m_{\ell\mu}$ distribution to the input top-quark mass, estimated using simulated events for (a) OS and (b) SS samples. . . . 157
9.2 Visualisation of the morphing technique. . . . 159
9.3 Distribution of the nuisance parameter pulls and constraints from the fit to the Asimov dataset. . . . 162
9.4 Ranking plot from the combined fit to the Asimov dataset. . . . 163
9.5 Distribution of the nuisance parameter pulls and constraints from data. . . . 165
9.6 Comparison of data and prediction for $p_{\mathrm{T}}(\ell^{\text{primary}})$. . . . 166
9.7 Comparison of data and prediction for $\eta(\ell^{\text{primary}})$. . . . 166
9.8 Comparison of data and prediction for $p_{\mathrm{T}}(\mu^{\text{SMT}})$. . . . 167
9.9 Comparison of data and prediction for $m_{\mathrm{T}}(W)$. . . . 167
9.10 Comparison of data and prediction for $E_{\mathrm{T}}^{\text{miss}}$. . . . 168
9.11 Comparison of data and prediction for p_{T}(leading jet). . . . 168
9.12 Comparison of data and prediction for p_{T}(SMT jet). . . . 169
9.13 Ranking plot from the combined fit to data. . . . 170

10.1 Correction factors for $m_{\ell\mu}$. . . . 182
10.2 Correction factors for $p_{\mathrm{T}}(W$-lepton). . . . 183

10.3 Correction factors for $p_{\mathrm{T}}(\mu\text{-soft})$. 184
10.4 Correction factors for $p_{\mathrm{T}}^{\mathrm{rel}}(\mu\text{-soft})$. 185
10.5 Correction factors for $p_{\mathrm{T}}(\mu\text{-soft})/p_{\mathrm{T}}(\text{SMT jet})$. 186
10.6 Correction factors for $p_{\mathrm{T}}^{\mathrm{z}}(\mu\text{-soft})$. 187
10.7 Correction factors for $p_{\mathrm{T}}(\text{SMT jet})$. 188
10.8 The χ^2/NDF as a function of the number of iterations used for the D'Agostini unfolding method for the $m_{\ell\mu}$ observable. 189
10.9 The split closure tests for a selection of observables. The unfolded pseudodata is compared to the MC prediction from the training sample and the uncertainty bands include the statistical uncertainty on the unfolding. 191
10.10 The split closure tests for a selection of observables. The unfolded pseudodata is compared to the MC prediction from the training sample and the uncertainty bands include the statistical uncertainty on the unfolding. 192
10.11 The data/MC (left) and linear (right) stress tests for $m_{\ell\mu}$ and $p_{\mathrm{T}}(W\text{-lepton})$. The stressed pseudodata is compared with the stressed test particle level sample and the uncertainty band includes the statistical uncertainty on the unfolding. 195
10.12 The data/MC (left) and linear (right) stress tests for $p_{\mathrm{T}}(\mu\text{-soft})$ and $p_{\mathrm{T}}^{\mathrm{rel}}(\mu\text{-soft})$. The stressed pseudodata is compared with the stressed test particle level sample and the uncertainty band includes the statistical uncertainty on the unfolding. 196
10.13 The data/MC (left) and linear (right) stress tests for $p_{\mathrm{T}}(\mu\text{-soft})/p_{\mathrm{T}}(\text{SMT jet})$ and $p_{\mathrm{T}}(\text{SMT jet})$. The stressed pseudodata is compared with the stressed test particle level sample and the uncertainty band includes the statistical uncertainty on the unfolding. 197
10.14 The data/MC (left) and linear (right) stress tests for $p_{\mathrm{T}}^{\mathrm{z}}(\mu\text{-soft})$. The stressed pseudodata is compared with the stressed test particle level sample and the uncertainty band includes the statistical uncertainty on the unfolding. 198
10.15 The bump injection stress tests for $m_{\ell\mu}$. The stressed pseudodata is compared with the stressed test particle level sample and the uncertainty band includes the statistical uncertainty on the unfolding. 198

10.16Comparison between data and MC predictions at reconstructed level for several observables. The uncertainty bands include both the systematic and statistical uncertainties. 201
10.17Comparison between data and MC predictions at reconstructed level for several observables. The uncertainty bands include both the systematic and statistical uncertainties. 202
10.18Comparison between the measured normalised differential cross-section and various signal predictions for $m_{\ell\mu}$. (a) shows several standard signal predictions and (b) compares signal predictions with various hadronisation parameters. . . 209
10.19Comparison between the measured normalised differential cross-section and various signal predictions for $p_{\mathrm{T}}(W\text{-lepton})$. (a) shows several standard signal predictions and (b) compares signal predictions with various hadronisation parameters. 210
10.20Comparison between the measured normalised differential cross-section and various signal predictions for $p_{\mathrm{T}}(\mu\text{-soft})$. (a) shows several standard signal predictions and (b) compares signal predictions with various hadronisation parameters. 210
10.21Comparison between the measured normalised differential cross-section and various signal predictions for $p_{\mathrm{T}}^{\mathrm{rel}}(\mu\text{-soft})$. (a) shows several standard signal predictions and (b) compares signal predictions with various hadronisation parameters. 211
10.22Comparison between the measured normalised differential cross-section and various signal predictions for $p_{\mathrm{T}}(\mu\text{-soft})/p_{\mathrm{T}}(\text{SMT jet})$. (a) shows several standard signal predictions and (b) compares signal predictions with various hadronisation parameters. 211
10.23Comparison between the measured normalised differential cross-section and various signal predictions for $p_{\mathrm{T}}(\text{SMT jet})$. (a) shows several standard signal predictions and (b) compares signal predictions with various hadronisation parameters. 212

10.24Comparison between the measured normalised differential cross-section and various signal predictions for $p_{\mathrm{T}}^{\mathrm{z}}(\mu\text{-soft})$. (a) shows several standard signal predictions and (b) compares signal predictions with various hadronisation parameters. 212

Tables

2.1 List of the SM fermions and their properties 26

2.2 List of the SM gauge bosons and their properties 27

5.1 Generator and settings used to produce the signal and alternative $t\bar{t}$ samples. . 80

5.2 Generator and settings used to produce the alternative $t\bar{t}$ mass samples and background samples. 81

5.3 Generator and settings used to produce the alternative $t\bar{t}$ signal samples used in the differential analysis. 82

6.1 The production fraction values for b hadrons and c hadrons in the PDG and Powheg+Pythia8 91

6.2 Hadron to μ branching ratios in the PDG and Powheg+Pythia8 92

6.3 Breakdown of the systematic uncertainties of the $k_{\text{SMT-jet}}$ scale factor fit. . . . 95

6.4 Parameterisation 1 of the real and fake efficiencies. This parameterisation is the default recommended by the Top Fakes group. 104

6.5 Parameterisation 2 of the real and fake efficiencies. In this case, both the real and fake efficiencies use the same parameterisation. This parameterisation is used by another analysis with a similar event selection. 105

6.6 Parameterisation 3 of the real and fake efficiencies. In this case, both the real and fake efficiencies use the same parameterisation. This parameterisation is used by another analysis where a full parameterisation optimisation has been carried out. 105

6.7 Parameterisation 4 of the real and fake efficiencies. In this case, both the real and fake efficiencies use the same parameterisation. This parameterisation is used as the alternative parameterisation for parametrisation 3. 105

7.1 Fraction of MC $t\bar{t}$ events split into components of direct and sequential decays, and decays not belonging to the b from the $t \to Wb$ decay chain. 121

7.2 Events yields with $m_{\ell\mu}$ between 15 and 80 GeV, seperately for OS and SS regions. Uncertainties shown include statistical and systematic contributions. 122

8.1 Summary of all the sources of uncertainty currently included in the analysis. Where appropriate, the number of independent components considered is indicated. 128

8.2 Comparison of the BR ratios between the PDG values and from MC. 147

8.3 The shifts on the mean of the $m_{\ell\mu}$ distributions, arising from applying the individual decay uncertainties. 148

9.1 Breakdown of the impact of the various sources of uncertainty on m_t, as obtained from the combined OS+SS binned template profile-likelihood fit to the real data. 171

10.1 A breakdown of the systematics uncertainties in each bin for $m_{\ell\mu}$. The uncertainties are given in %. 203

10.2 A breakdown of the systematics uncertainties in each bin for $p_{\mathrm{T}}(W\text{-lepton})$. The uncertainties are given in %. 204

10.3 A breakdown of the systematics uncertainties in each bin for $p_{\mathrm{T}}(\mu\text{-soft})$. The uncertainties are given in %. 204

10.4 A breakdown of the systematics uncertainties in each bin for $p_{\mathrm{T}}^{\mathrm{rel}}(\mu\text{-soft})$. The uncertainties are given in %. 205

10.5 A breakdown of the systematics uncertainties in each bin for $p_{\mathrm{T}}(\mu\text{-soft})/p_{\mathrm{T}}(\text{SMT jet})$. The uncertainties are given in %. 206

10.6 A breakdown of the systematics uncertainties in each bin for $p_{\mathrm{T}}(\text{SMT jet})$. The uncertainties are given in %. 207

10.7 A breakdown of the systematics uncertainties in each bin for $p_{\mathrm{T}}^{\mathrm{z}}(\mu\text{-soft})$. The uncertainties are given in %. 208

10.8 Comparison of the relative differential cross-sections and several different predictions. For each prediction he χ^2 test statistic and p-value is calculated. p-values highlighted in red indicate the prediction hypothesis is rejected for the given observable. 214

For Grandma and Grandad.

"In a way, aren't all so-called qualifications meaningless?"

— Jeremy Usborne

Chapter 1

Introduction

The Standard Model of Particle Physics provides an wonderful description of the universe, providing extremely accurate predictions of many phenomena. Quantum Electrodynamics, which is part of the Standard Model, is frequently referred to as "the most precisely tested theory in the history of science" due to the, almost impossibly, precise measurement of the anomalous magnetic coupling of the electron, g [2]. In this measurement, g is measured to 11 decimal places, all of which match exactly with the prediction from Quantum Electrodynamics.

Although the Standard Model offers impressive predictions, it is clear that it is not the full picture. For example, the Standard Model only describes three of the four fundamental forces of the universe and there is no explanation for why the universe is dominated by matter instead of anti-matter.

In order to find the cracks in the Standard Model, broadly two approaches can be taken. One is to search for signs of new particles not predicted by the Standard Model by finding unexpected bumps in invariant mass spectra. Finding such a bump would be considered a smoking gun that something new had been found. The other, and slightly more subtle, method, is to measure the parameters of the Standard Model to such precision that it becomes over-constrained and therefore, the self-consistency of the theory potentially becomes questionable.

One such parameter is the mass of the top quark, which is not predicted by the Standard Model. In this thesis a measurement of the top-quark mass is presented using a novel technique that

utilises a partial reconstruction of the top-quark decay products using an observable constructed from the kinematics of associated leptons.

Precision measurement of Standard Model parameters requires a sound modelling of the physics processes involved. In order to improve simulation of Standard Model physics processes, measurements of well-understood differential cross-sections are used to inform the optimisation of simulation parameters. A differential cross-section measurement is also presented in this thesis using the same event selection and objects that are used for the top-quark mass extraction. The differential cross-sections presented in this thesis show observables sensitive to the b-quark fragmentation that have been measured in LHC data for the first time.

The layout of this thesis is as follows. Chapter 2 presents a brief overview of the Standard Model and discusses in more detail the top quark and the motivation for top-quark mass measurements. Chapter 3 gives an overview of the LHC accelerator complex and ATLAS experiment; the simulation of physics processes and how they manifest in the ATLAS detector are outlined in Chapter 4. Chapters 5 to 8 describe the event selection, data and simulation samples and systematic uncertainties that are common to both the top-quark mass measurement and the differential cross-section measurement. The extraction of the top-quark mass is detailed in Chapter 9 and the results are discussed. Then in Chapter 10, the motivation for measuring differential cross-sections, which stems from the top-quark mass measurement, is introduced and the measurements of the differential cross-sections are presented. Finally, in Chapter 11, the conclusions of both analyses are presented and a brief discussion of future work is outlined.

Chapter 2

Theoretical foundations

In the following chapter, the theoretical foundations of particle physics are outlined. The top quark is introduced and the motivation for studying its mass is discussed. Finally, an outline of the top-quark mass measurement presented in this thesis is detailed.

2.1 The Standard Model

The Standard Model of particle physics (SM) is a theory that offers a description of the observable Universe at the smallest scales. It encapsulates how the elementary particles (quarks and leptons) interact with each other via the fundamental forces (electromagnetic, weak and strong)[1] and allows for precise calculations of properties of the Universe. These precise calculations can then be tested with experimental data from a plethora of different experiments.

The SM is a quantum field theory (QFT) [3] and can be described by a *Lagrangian density*[2]. Furthermore, the SM is what is known as a *gauge theory*, whereby the Lagrangian is invariant under local transformations for certain symmetry groups. To demonstrate this, consider a Lagrangian for free spin one-half particle particles,

$$\mathcal{L} = \bar{\Psi}(i\partial\!\!\!/ - m)\Psi, \tag{2.1}$$

[1] Gravity is not included in the SM however, it is described by the general theory of relativity.
[2] Shortened to Lagrangian in this thesis.

where Ψ is the spinor field, $\not{\partial}$ is the derivative and m is the mass. For the one-dimensional unitary symmetry group, $U(1)$, the following local transformation can be defined,

$$\Psi(x) \rightarrow e^{-\alpha(x)}\Psi(x), \tag{2.2}$$

where $\alpha(x)$ is a real function of x. In this case, Equation 2.1 is not invariant. In order to force the Lagrangian to be invariant under the $U(1)$ symmetry group, additional terms must be included. By making the following substitution,

$$\partial_\mu \rightarrow D_\mu \equiv \partial_\mu + iqA_\mu, \tag{2.3}$$

where a new vector field, A, has been introduced that couples to the field Ψ with a coupling strength q. This additional field is known as a *gauge field*. The Lagrangian obtained by imposing invariance to $U(1)$ transformations is in fact that of Quantum Electrodynamics, which is discussed further in Section 2.1.2.

Another important property of gauge theories is that they are *renormalisable*. This means that when infinities arise in calculations, normally from *loop diagrams*, there exists a method to remove the divergences above some renormalisation scale, μ_R. This is an important property which is discussed further in Section 2.1.2.

The full SM Lagrangian can be summarised as,

$$\mathcal{L}_{\text{SM}} = \mathcal{L}_{\text{Gauge}} + \mathcal{L}_{\text{Fermion}} + \mathcal{L}_{\text{Higgs}} + \mathcal{L}_{\text{Yukawa}}. \tag{2.4}$$

Each of the four parts will be discussed in more detail in the following sections. These sections are based on Refs. [4–6].

2.1.1 Fermion fields

All matter in the observable Universe is made up of fermions. Fermions are spin-$\frac{1}{2}$ particles and are split into quarks and leptons. Protons and neutrons are made up of two types of quark, *up* and *down*. With the addition of a lepton, the *electron*, nuclei can be formed which make up most of the everyday world. The field responsible for fermions, is expressed in the fermion term of the SM Lagrangian,

$$\mathcal{L}_{\text{Fermion}} = i\bar{\Psi}\not{D}\Psi, \tag{2.5}$$

as Ψ. The symbol $\not{D}$ represents the covariant derivative, which arises as a consequence of imposing a gauge symmetry. The covariant derivative dictates the interaction of the fermion field with the gauge fields. In the case of the SM, the gauge fields propagate the strong, weak and electromagnetic forces, which are discussed in Section 2.1.2.

In total there are 12 fermions (plus another 12 *anti-particle* counterparts) in the SM, six quarks and six leptons. Both the quarks and leptons are arranged in three *generations*. In the quarks, each generation has an *up*- and a *down*- type quark. They are differentiated by whether they have a positive or negative charge. Each fermion also has a "handedness". This is known as chirality and can be either "left-handed" or "right-handed". The quarks carry electric, weak and coloured charges, which allow them to interact with all of the gauge fields. Within an quark type, all generations of quarks are identical in electric, weak and colour charges; the only thing that differs is their mass.

The leptons are arranged similarly into three generations. Again, there are two types per generation and they differ by charge. Each electrically charged lepton has an electrically neutral counterpart known as a *neutrino*.

In the SM, neutrinos are generally treated as massless. This is because, unlike the other fermions, right-handed neutrinos have not been experimentally observed. However, it has been shown experimentally that they have mass through the observation of *neutrino oscillations*. Neutrino oscillations are the process by which a neutrino is produced as a given flavour and is

Name	Mass	Charge	Coloured?
u	$2.16^{+0.49}_{-0.26}$ MeV	$+\frac{2}{3}$	Yes
d	$4.67^{+0.48}_{-0.17}$ MeV	$-\frac{1}{3}$	Yes
c	1.27 ± 0.02 GeV	$+\frac{2}{3}$	Yes
s	93^{+11}_{-5} MeV	$-\frac{1}{3}$	Yes
t	173.34 ± 0.76 GeV	$+\frac{2}{3}$	Yes
b	$4.18^{+0.03}_{-0.02}$ GeV	$-\frac{1}{3}$	Yes
e^-	$0.511 \pm 3.1 \times 10^{-9}$ MeV	-1	No
ν_e	< 2 eV	0	No
μ^-	$105.66 \pm 2.4 \times 10^{-6}$ MeV	-1	No
ν_μ	< 0.19 MeV	0	No
τ	$1.77 \pm 1.2 \times 10^{-4}$ GeV	-1	No
ν_τ	< 18.2 MeV	0	No

Table 2.1 List of the SM fermions and their properties [7].

later detected as another. This requires an extension to the SM whereby the neutrinos' mass eigenstate is different to the flavour eigenstate. The neutrinos interact with weak processes in their flavour eigenstates but propagate through space in the mass eigenstates. The flavour eigenstates are linear combinations of the mass eigensates and because each neutrino has a different mass, the quantum mechanical phase of the mass eigensates will oscillate at different rates as the neutrinos propagate through space. Once the neutrino is then absorbed by some other weak process, the mass eignstates will be different to when it was emitted and therefore the linear comnbination that makes up the flavour eigenstate will also be different.

As in the quarks, each lepton generation is identical to the others except for mass although, currently, the mass hierarchy of the neutrinos is unknown. The leptons are colourless objects so do not interact via the strong force. A list of the fermions in the SM is shown in Table 2.1.

.

Name	Mass [GeV]	Charge	Spin
$W^{\pm}$	80.4	± 1	1
Z^0	91.2	0	1
γ	0	0	1
g	0	0	1

Table 2.2 List of the SM gauge bosons and their properties [7].

2.1.2 Gauge fields

The SM is constructed as a quantum field theory that is invariant under the symmetry group,

$$\mathrm{SU}(3)_C \otimes \mathrm{SU}(2)_L \otimes \mathrm{U}(1)_Y. \tag{2.6}$$

Here, $U(n)$ is the unitary group and $SU(n)$ is the special unitary group of dimension n. These symmetries are related to some conserved currents by Noether's theorem [8]. The conserved currents for the SM symmetry group are the *colour* C, the weak *isospin* L and the weak *hypercharge* Y. As previously mentioned, in order to to satisfy the gauge invariance, each symmetry in the symmetry group introduces additional gauge fields. The kinetic and self interaction terms of the gauge fields is described by

$$\mathcal{L}_{\mathrm{Gauge}} = \frac{1}{4} F_{\mu\nu} F^{\mu\nu}. \tag{2.7}$$

Here, $F_{\mu\nu}F^{\mu\nu}$ is the scalar product of the gauge fields and the bosons which these fields give rise to are summarised in Table 2.2.

Electroweak interaction Originally, electromagnetic and weak interactions were developed independently. The electromagnetic interaction is described by a theory know as *Quantum Electrodynamics* (QED) and is responsible for governing the interactions between electrically charged particles via the photon. In QED, the photon is massless and the electromagnetic interaction can propagate over an infinite range. The electromagnetic interaction has a coupling

constant, g_e, which is often expressed as $\alpha_e = g_e^2/4\pi = 1/137$. The fact that α_e is less than one means that QED calculations can be computed *perturbatively* by expanding in powers of α_e. Often calculations will be described as leading order (LO) or next-to-leading order (NLO). At LO the calculation has been expanded to first order of the coupling constant and at NLO the second order. The weak interaction acts on left-handed fermions which carry the weak isospin quantum number via the weak bosons. The weak bosons are massive and therefore the range of the weak interaction is short.

Due to the difference in the ranges of the two interactions, it seems that the electromagnetic and weak interactions are completely separate processes. However, Glashow, Salam and Weinberg [9–11] were able to show that a gauge invariant theory, which combined both the electromagnetic and weak interactions, could be constructed. This is what is referred to as *electroweak unification* and the resulting electroweak interaction is described by the $\mathrm{SU}(2)_L \otimes \mathrm{U}(1)_Y$ symmetry group.

Imposing the electroweak gauge symmetry requires the introduction of four gauge fields, W_μ^k where, $k \in 1, 2, 3$ and B_μ. These fields do not have a physical state, however; there instead exists linear combinations of these fields that represent the physical fields associated with bosons that can be observed. These are

$$A_\mu = +B_\mu \cos\theta_\mathrm{W} + W_\mu^3 \sin\theta_\mathrm{W}, \tag{2.8}$$

$$Z_\mu = -B_\mu \sin\theta_\mathrm{W} + W_\mu^3 \cos\theta_\mathrm{W}, \tag{2.9}$$

$$W_\mu^\pm = \frac{1}{\sqrt{2}}(W_\mu^1 \mp i W_\mu^2), \tag{2.10}$$

where A_μ is the field of the photon, Z_μ is the filed of the Z boson and $W_\mu^\pm$ are the fields of the charged $\mathrm{W}^\pm$ bosons. Here, the W bosons carry the weak charge and the Z boson and photon carry the electric charge. The gauge symmetry requires the $W^\pm$ and Z bosons to be massless, although experimentally these bosons are observed to be massive. In order to explain this theoretically, another field must be introduced, the Higgs field, which will be discussed further in Section 2.1.3. The quantity, θ_W, is known as the weak mixing angle. This relates the masses of the W and Z bosons, as $\cos\theta_\mathrm{W} = \frac{m_W}{m_Z}$.

In the weak sector, the weak eigenstates are not the same as the mass eigenstates for quarks, as is the case for neutrinos. The mixing is parameterised by the Cabbibo-Kobayashi-Maskawa (CKM) matrix [12, 13]

$$V = \begin{pmatrix} V_{ud} & V_{us} & V_{ub} \\ V_{cd} & V_{cs} & V_{cb} \\ V_{td} & V_{ts} & V_{tb} \end{pmatrix}. \tag{2.11}$$

Each element in the CKM matrix, V_{ij} represents the coupling between the quark i and j. The magnitudes of the CKM matrix are [7]

$$|V_{ij}| = \begin{pmatrix} 0.9738 & 0.2272 & 0.0040 \\ 0.2271 & 0.9730 & 0.0422 \\ 0.0081 & 0.0416 & 0.9991 \end{pmatrix}. \tag{2.12}$$

The W bosons that are generated by the linear combinations of the B and W^3 fields mediate the weak charge. This means interactions involving fermions and W bosons will have different flavours for the incoming and outgoing fermions.

Quantum Chromodynamics The $\mathrm{SU}(3)_C$ symmetry describes *Quantum Chromodynamics* (QCD), which governs the strong interaction. In QCD, colour charge is the conserved quantity. The strong force is mediated by the *gluon* which is the boson associated with the gauge field. Due to the $\mathrm{SU}(3)_C$ having eight generators, this means there are also eight associated gauge bosons, in this case the gluons. The gluons can carry one unit each of colour and anticolour charge and are electrically neutral. Unlike the weak bosons, they are also massless.

The strength of the strong interaction is determined by the strong coupling constant, α_s. Contrary to the name, α_s is not actually constant but instead is dependent on energy [14] (referred to as the *running* of the coupling constant). In QCD, due to the gluons being colour charged they have a self-interaction unlike photons in QED. The strong coupling constant can

be expressed as

$$\alpha_s(Q^2, \mu_R^2) = \frac{\alpha_s(\mu_R^2)}{1 + \frac{\alpha_s(\mu_R^2)}{12\pi}(11n_c - 2n_f)\ln(Q^2/\mu_R^2)}, \tag{2.13}$$

where Q^2 is the energy scale of the interaction, the renormalisation scale, μ_R, n_c is number of colours and n_f is the number of flavours of quark involved. At low energies, where $Q^2 \to 0$, the coupling constant increases. A consequence of this is that at low enough energies, the coupling constant has a value greater than one and therefore a perturbative expansion in α_s will no longer converge. Equation 2.13 can be rearranged into

$$\alpha_s(Q^2, \mu_R^2) = \frac{12\pi}{(11n_c - 2n_f)\ln(Q^2/\Lambda^2_{\mathrm{QCD}}(\mu_R^2))}, \tag{2.14}$$

where $\Lambda^2_{\mathrm{QCD}}(\mu_R^2)$ is the scale at which the perturbation series no longer converges. Below this scale, QCD is said to be *non-perturbative*. Conversely, at high energies, the coupling constant tends to zero. This process is known as *asymptotic freedom*.

A further result of the running of the strong coupling constant is that due to the larger coupling constant at low energies, quarks must be bound in a colour neutral state. This phenomenon is known as quark *confinement* and prevents quarks being found in isolation.

2.1.3 Higgs mechanism

As discussed in Section 2.1.2, the $W^{\pm}$ and Z^0 bosons do not nominally have mass when imposing the SM symmetry group on the Lagrangian. To allow these bosons to be massive, as they have been confirmed to be experimentally, an additional scalar field must be introduced. This idea, now known as the Brout-Englert-Higgs mechanism was proposed by three groups independently in 1964 [15–18]. Each of the papers detailed the idea known as *spontaneous symmetry breaking*.

The proposed mechanism was to introduce a new scalar field ϕ and a potential of the form

$$V(\phi) = \mu^2\phi^\dagger\phi + \lambda(\phi^\dagger\phi)^2, \tag{2.15}$$

where μ and λ are free parameters. Taking the case where $\lambda > 0$ and $\mu^2 < 0$, non-zero minima occur at $V(\phi) = -\mu^2/2\lambda \equiv v$. This value, v, is known as the *vacuum expectation value* which is shown in in Figure 2.1. It can be seen that there is a plane in ϕ when the field is at a minimum. When the field takes a value of ϕ that is located at the minimum, the field has a non-zero value, which leads to the symmetry being spontaneously broken. Due to this symmetry breaking, the $W^{\pm}$ and Z^0 bosons gain mass terms in the Lagrangian, while maintaining gauge invariance. There is also now an additional degree of freedom, which is the mass of the excitation of this Higgs field, known as the Higgs boson (H). The mass of the H boson is defined as $m_H = \sqrt{(\lambda/2)v}$ where λ corresponds to the self-coupling of the H boson and $v \approx 246$ GeV. The gauge bosons will interact with the Higgs field through the following term, which is added to the SM Lagrangian density:

$$\mathcal{L}_{\text{Higgs}} = (|D_\mu \phi|^2 - V(\phi)). \tag{2.16}$$

The H boson was the final piece of the SM to be discovered when, in 2012, the ATLAS [19] and CMS [20] Collaborations announced they had seen a particle whose properties were consistent with those of a H boson. Although a mechanism for giving mass to bosons has been introduced, the fermions also require a mechanism to allow them to be massive, while retaining gauge invariance.

2.1.4 Yukawa coupling

In a SM without the Higgs field, the fermions must be massless to ensure gauge invariance. To generate a mass for a field Ψ, quadratic terms of the form

$$m_f \bar{\Psi} \Psi \tag{2.17}$$

are required. Under the $\mathrm{SU}(2)_L \otimes \mathrm{U}(1)_Y$ electroweak symmetry, these terms are not invariant and therefore the mass must be set to zero. The addition of the Higgs field results in the

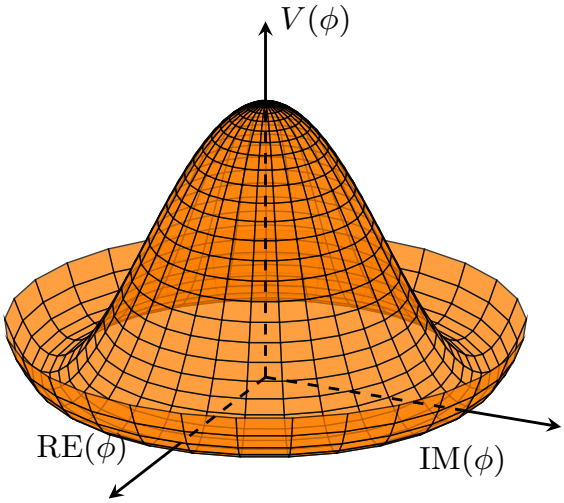

Figure 2.1 Visualisation of the Higgs potential. The expectation value of the Higgs field, v, occurs at any point on the plane of the minimum.

addition of terms of the form

$$\mathcal{L}_{\text{Yukawa}} = \Psi_i y_{ij} \Psi_j \phi + \text{h.c.}. \tag{2.18}$$

These describe the interaction between the fermions and the Higgs field. Here, Ψ are the fermion fields, ϕ is the Higgs field and y_{ij} is the given element of the Yukawa matrix, which represents the strength of each interaction. The fermion mass, m_f, is found to be proportional to the vacuum expectation value of the Higgs field through the following relation

$$m_f = y_f \frac{v}{\sqrt{2}}. \tag{2.19}$$

For the Yukawa coupling to work for neutrinos, a fine tuning down to extremely small values would be required. Additional mechanisms have been proposed in order to generate the neutrino masses such as the seesaw mechanism [21].

2.2 Top quark physics

The top quark was first hypothesised by Kobayashi and Maskawa [12] in 1973 in order to explain the observation of CP-violation in neutral Kaons. At the time there were only two generation of fermions and their solution was to add a third. After the discovery of third generation fermions, the τ lepton [22], and the bottom quark [23] in 1975 and 1977m respectively, the discovery of the top quark seemed likely. However, it was not discovered until 1995, 22 years after it was first proposed, by the CDF [24] and D0 [25] experiments at the Tevatron collider.

The top quark is the heaviest of the SM particles with a mass of around 173 GeV [26], around that of a gold atom. The next largest particle is the Higgs, which has a mass of around 125 GeV [19] and the down-type counterpart of the top quark, the bottom quark, has a mass of only 4.18 GeV [27]. Its large mass, both in absolute terms and relative to the other quark masses, make the top quark interesting to investigate. Firstly, the large mass means that the Yukawa coupling for the top quark is $y_t \sim 1$, suggesting that the top quark may play some role in the Higgs mechanism. Secondly, the large mass means that the top quark has a very short lifetime before it decays. The lifetime is $\tau_t \approx 10^{-25}$ s [28], which is an order of magnitude shorter than the average time taken for a quark to hadronise (10^{-24} s). This means that the top quark decays before it has a chance to form a bound state and therefore allowing for the study of a "bare" quark. By studying the decay products of the top quark, information about its original state, such as spin correlations, can be inferred because the process of hadronisation cannot have altered the top quark's state.

2.2.1 Top quark production

2.2.1.1 Top quark pair-production

Generally at the LHC, top quarks are produced in pairs via the strong interaction. At LO, top quarks can be produced via gluon-gluon fusion or quark-antiquark annihilation as shown in Figure 2.2. At the LHC at a centre-of-mass energy of 14 TeV, around 90% of top-quark pairs are produced via gluon-gluon fusion and 10% from quark-antiquark annihilation. This fraction

(a) $gg \to t\bar{t}$ **(b)** $q\bar{q} \to t\bar{t}$

Figure 2.2 Examples of production channels for top quark pair-production.

depends on the particles being collided and the centre-of-mass energy of the collisions, $\sqrt{s}$. The LHC collides protons (pp) whereas the Tevatron collided protons with anti-protons ($p\bar{p}$). In $p\bar{p}$ collisions, the annihilation process is more likely to happen because the anti-quarks can be from the valence quarks of the anti-proton whereas in pp collisions the anti-quarks must come from the quark sea. The other difference is that the higher $\sqrt{s}$ the smaller the fraction of the protons energy, x, is needed to reach the $t\bar{t}$ production threshold. These two effects can be summarised in Figure 2.3, which shows the parton distribution function (PDF) of the proton. The PDF describes the probability density for finding a particle of momentum fraction x and at a resolution scale Q^2. At low x, the gluon carries has a much larger probability density than the quarks, as can be seen in Figure 2.3. This effect becomes more pronounced as $\sqrt{s}$ increases.

2.2.1.2 Single top quark production

Top quarks can also be produced singly at the LHC, although this happens much less often than $t\bar{t}$ production. Single top production is a weakly initiated process and therefore has a lower cross-section than $t\bar{t}$ production. At the LHC, at LO, there are three single top production channels; s-channel, t-channel and Wt-channel. The Feynman diagrams for each of these can be seen in Figure 2.4.

2.2.2 Top quark decay

The top quark decays into a b quark and a W boson over 95% of the time [28]. The W boson can decay either hadronically into two quarks or leptonically into a lepton and its corresponding

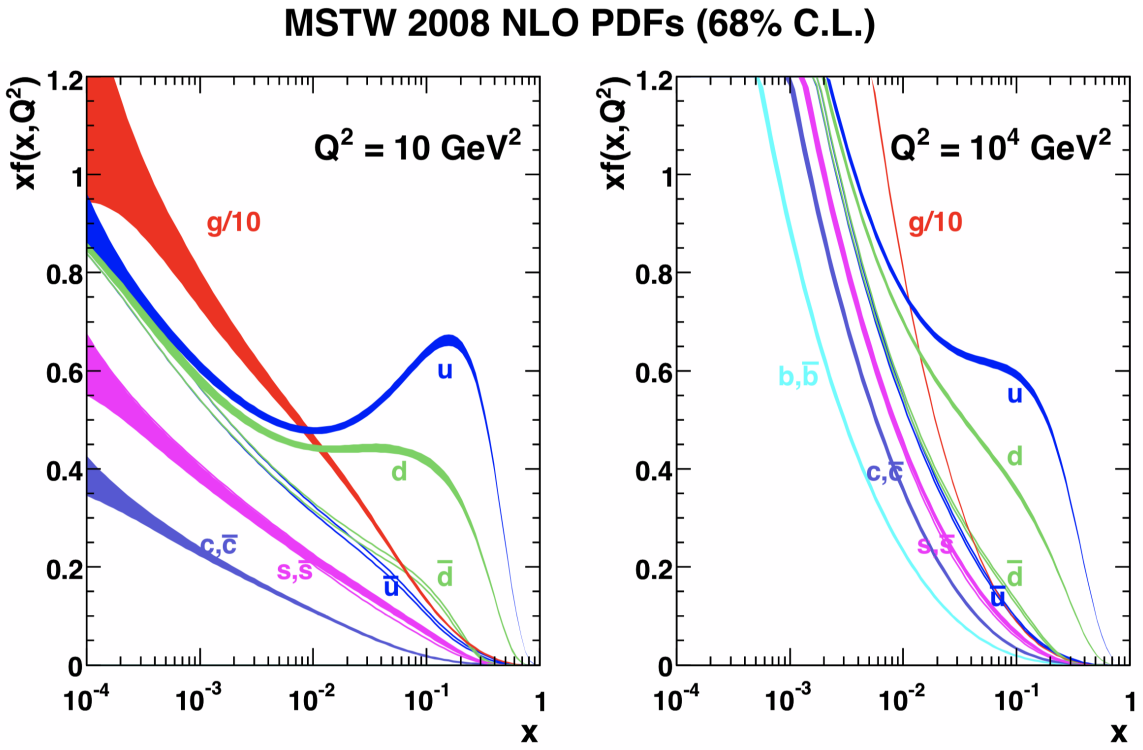

Figure 2.3 The MSTW group 2008 NLO PDF for the proton as a function of the momentum fraction x and at resolution scale $Q^2 = 10\text{GeV}^2$ (left) and $Q^2 = 10^4\text{GeV}^2$ (right) [29].

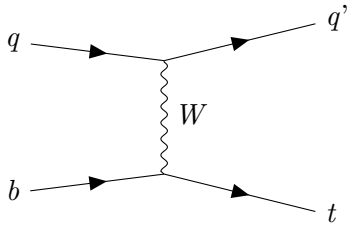

(a) The t-channel.

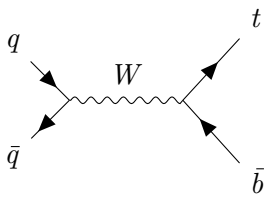

(b) The s-channel.

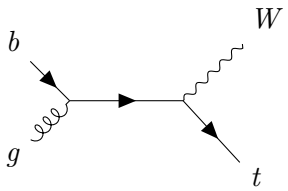

(c) The Wt-channel.

Figure 2.4 The leading order channels for single top quark production.

neutrino. The hadronic decay occurs 67.4% of the time [7]. The remaining 32.6% of the time the leptonic decay occurs, with decays to each generation occurring roughly equally.

Due to the two possible decay modes of the W boson, there are three possible final states in a $t\bar{t}$ event. These are:

- **All hadronic**: this channel occurs when both of the W bosons decay hadronically. This gives a final state of $t\bar{t} \rightarrow W^+ b W^- \bar{b} \rightarrow b\bar{b}q'\bar{q}''q'''\bar{q}''''$. This channel has the largest branching ratio (46% [28]) due to the W mainly decaying to hadrons. While this large branching ratio means the number of events produced will be large, the nature of the final state means it is challenging to distinguish between $t\bar{t}$ events of this type and those in which multiple jets are produced.

- **Dilepton**: this channel occurs when both of the W bosons decay into a charged lepton and the corresponding neutrino, resulting in a final state of $t\bar{t} \rightarrow W^+ b W^- \bar{b} \rightarrow b\bar{b}\ell\bar{\nu}_\ell\bar{\ell}\nu_\ell$. The channel contains two charged leptons in the final state, which can be measured more precisely than hadrons, making it desireable for a precision measurement. The drawback is that this channel has the lowest branching fraction (11% [28]) and therefore results in the smallest event sample. Additionally, the presence of two undetectable neutrinos makes reconstructing the $t\bar{t}$ system more difficult.

- **Lepton+jets**: this channel was seen as the *golden channel* at the Tevatron because it has the best parts of the dilepton and all-hadronic channels. In the lepton+jets channel, one of the W bosons decays hadronically and the other leptonically, resulting in a final state of $t\bar{t} \rightarrow W^+ b W^- \bar{b} \rightarrow b\bar{b}\ell\bar{\nu}_\ell q'\bar{q}''$. One W boson decaying hadronically increases the size (the branching ratio in this case is approximately 44% [28]) of the event sample, while the presence of a charged lepton helps more precisely reconstruct the system. For the studies presented in this thesis, the lepton+jets channel is used.

2.2.3 Top quark mass

The top-quark mass, m_t, is an important SM parameter to measure. It plays an important role in the stability of the Higgs vacuum. Current values for m_t and the Higgs mass point towards a *metastable* Higgs vacuum as shown in Figure 2.5. A metastable vacuum would imply that the Higgs vacuum expectation value is a *false vacuum* and that the Universe appears to favour a vacuum expectation value in local minimum and rather than a global one. If the vacuum was found to be unstable, new physics at the TeV scale would be required. However, if it is only metastable, there could still be new physics found but it is not required for the universe to be in a metastable state.

The masses of the top quark, the Higgs and the W boson are correlated due to the presence of higher-order quantum corrections to the top-quark mass in the electroweak sector. Therefore, precisely measuring all three can lead to strong test of the internal consistency of the SM. Inferring the top-quark mass from a combined electroweak fit involving direct mass measurements of the W and Higgs bosons currently favours a higher value [30] than those from independent direct measurements. This further motivates the desire for ever more precise measurements of the top-quark mass.

The interpretation of the top-quark mass and its uncertainties has been discussed at length by many theorists in recent times [31–33]. The main issue lies with how to interpret what is measured in a collider experiment. The top mass is generally determined in two ways: *direct* measurements or *indirect* measurements. In direct measurements, the top-quark mass is determined by reconstructing, partially or fully, the decay products of the $t\bar{t}$ system. The parameter measured in this case is often referred to as m_t^{MC}, a parameter of the Monte Carlo simulation rather than the SM m_t. In these measurements, some observable related to the reconstructed $t\bar{t}$ system is compared to a prediction from Monte Carlo simulation known as a *template*. Unfortunately this parameter is not easily relatable to a parameter in the SM due to the non-perturbative calculations of Monte Carlo simulations.

A more theoretically sound, while not perfect, parameter is what is known as the *pole* mass, m_t^{pole}. The m_t^{pole} can be thought of a similar to the electron mass in QED which is the pole of

the QED propagator. The advantage of this parameter is that it is gauge invariant at all orders of perturbation theory and calculations can be evaluated at a given order. The issue is that in a full QCD calculation, due to quark confinement, the quarks do not generate poles and this ambiguity leads to large, irreducible corrections of the order of the QCD scale. The pole mass is often determined from indirect measurements by looking at the total or differential cross sections and comparing them to fixed order predictions.

The top-quark mass can also be defined in what is known as the modified minimal subtraction scheme, $\overline{\text{MS}}$, $m_t^{\overline{\text{MS}}}$. In this scheme the mass is scale dependent or *runs* in a similar way to the coupling constants. The $m_t^{\overline{\text{MS}}}$ must be defined at a given *scale*, μ and can be related to m_t^{pole} by

$$m_t^{\text{pole}} = m_t^{\bar{\text{MS}}}(R, \mu) + \delta m_t(R, \mu) \tag{2.20}$$

where R is a scale parameter. The corrections $\delta m_t(R, \mu)$ have recently been calculated to four loops [34]. The current ambiguity between the top-quark pole mass and $\overline{\text{MS}}$ mass is estimated to be below 250 MeV [32]. There are other schemes in which the top-quark mass can be defined however, these three definitions are the most commonly measured at collider experiments in recent years.

2.2.3.1 Previous top-quark mass measurements

There have been many measurements of the top-quark mass since its discovery in 1995. Furthermore, many different techniques have been attempted. Figure 2.6 summarises the direct top quark mass measurements from the ATLAS and CMS Collaborations. The current most precise single measurement of the top-quark mass from direct measurements (corresponding to m_t^{MC}) is from the CMS Collaboration using the lepton+jets channel [36] with an observed top-quark mass of $m_t = 172.25 \pm 0.08\,(\text{stat+JSF}) \pm 0.62\,(\text{syst})$ GeV. The measurement uses the ideogram method where the top-quark mass is fitted simultaneously with a jet energy scale (JES) factor that is constrained using the W-boson mass. The simultaneous fitting of the jet

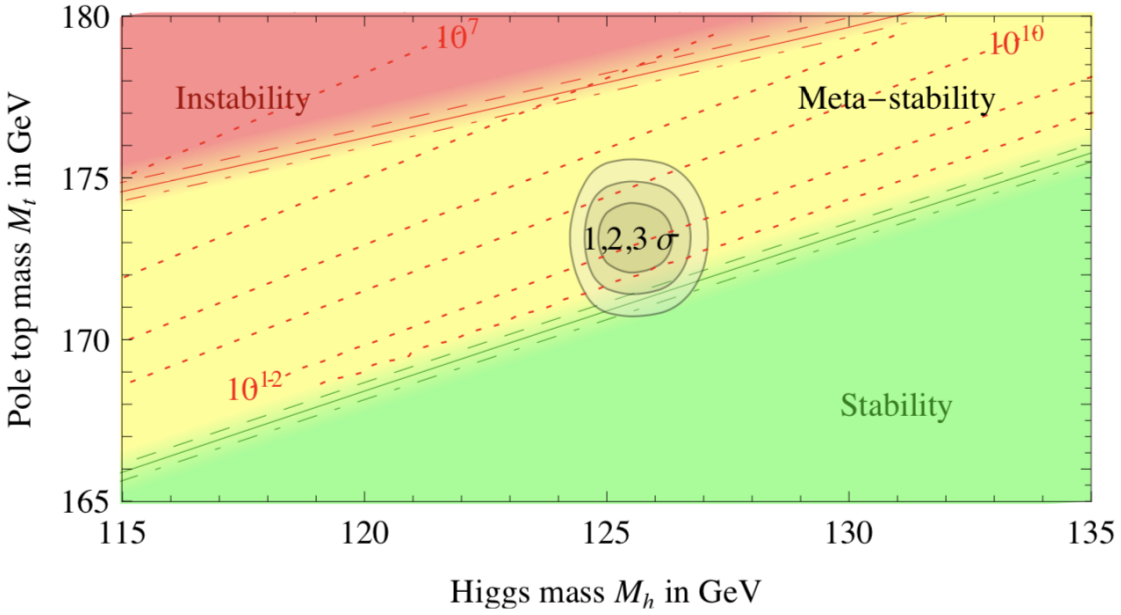

Figure 2.5 The Higgs potential as a function of top quark and Higgs masses with regions of absolute stability, meta-stability and instability highlighted [35].

energy scale factor helps reduced the associated uncertainty, which often dominates top-quark mass measurements.

A summary of some recent indirect measurements of the top-quark mass are shown in Figure 2.7. The summary plot shows mass measurements using the inclusive $t\bar{t}$ cross-section and differential cross-sections of $t\bar{t}$ production and $t\bar{t}$ production in association with a single jet. The current most precise measurement is from the CMS Collaboration using triple differential cross-sections [38]. In this case the measurements are used together with a fixed-order NLO QCD calculation to extract values for both the strong coupling strength, α_s, and the top quark pole mass.

2.2.3.2 Top-quark mass measurement motivation and outline

The current best measurements of m_t by the ATLAS Collaboration use direct reconstruction techniques where the decay products of the $t\bar{t}$ system are reconstructed and compared to

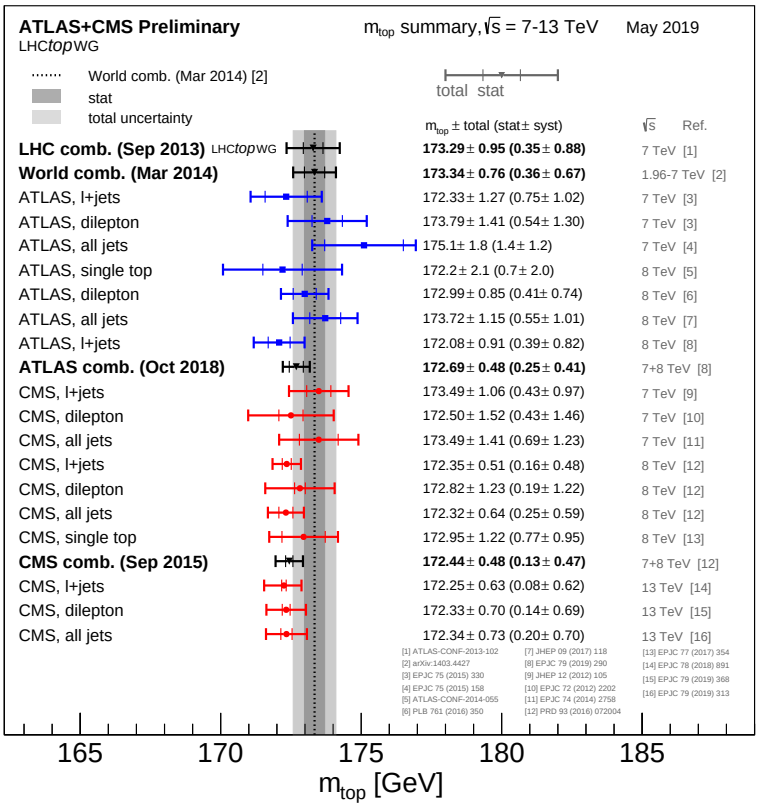

Figure 2.6 A summary of direct top-quark mass measurements from the ATLAS and CMS Collaborations [37].

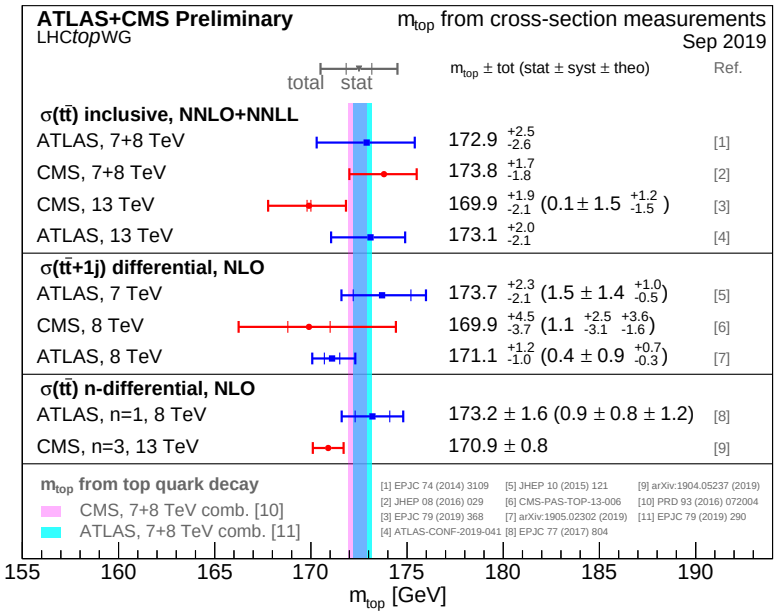

Figure 2.7 A summary of recent indirect top-quark mass measurements from the ATLAS and CMS Collaborations [37].

simulated templates. The measurement in the lepton+jets channel achieved a precision of $\pm 0.39(\text{stat}) \pm 0.82(\text{syst})$ GeV [39] and from the dilepton channel $\pm 0.41(\text{stat}) \pm 0.74(\text{syst})$ GeV [40]. Common to both of these analyses is the dominant systematic uncertainty arising from the measurement and modelling on the JES. In this thesis, an alternative direct reconstruction method is presented that greatly reduces the dependence on the JES and its uncertainties.

In this method, instead of reconstructing the full decay products of the $t\bar{t}$ system, a partial reconstruction based solely on final state leptons is used. An invariant mass, $m_{\ell\mu}$, is constructed from the charged lepton, ℓ ($\ell = e, \mu$) from the W boson decay and a muon, μ, from the semi-leptonic decay of a b hadron. A Feynman diagram of the specific decay used and the invariant mass can be seen in Figure 2.8. This invariant mass is sensitive to m_t and is a purely leptonic observable that is consequently relatively insensitive to JES uncertainties. Furthermore, the boost-invariance of the observable will reduce sensitivity on the top-quark production modelling compared to methods based on the decay of the W-boson alone [41] where modelling systematics are often substantial. In order to reduce any bias in the measurement, the analysis

is performed *blinded*. This means that the final fit result is not looked at until the analysis optimisation is complete.

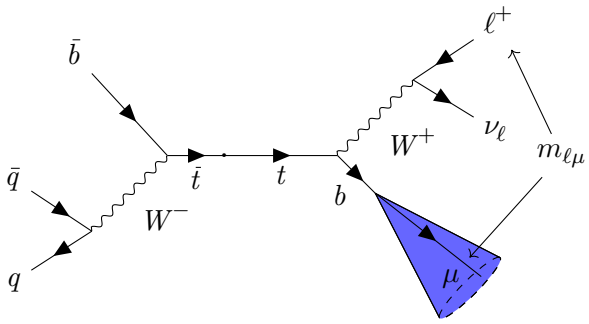

Figure 2.8 Feynman diagram of the decay channel used in the analysis.

This method was attempted at CDF as a "proof of principle" study [42]. Similar method using the decay of $J/\psi \to \mu\mu$ from the b-quark was also performed by CMS [43] however, due to the small branching fraction $b \to J/\psi$ decay, the measurement had large statistical uncertainties.

Chapter 3

The Large Hadron Collider and the ATLAS Experiment

The following chapter describes the Large Hadron Collider and the ATLAS Experiment, which was used to collect the data for the analyses presented in this thesis.

3.1 The Large Hadron Collider

The Large Hadron Collider (LHC) [44] is the world's largest particle accelerator, located at the European Centre for Nuclear Research (CERN) in Geneva, Switzerland. The LHC comprises a 27 km circumference ring of superconducting magnets and radiofrequency cavities currently capable of accelerating protons to 6.5 TeV. Two beams circulate the ring in opposite directions, colliding at four interaction points at a centre-of-mass energy of 13 TeV. Before entering the LHC, protons are accelerated through a complex of smaller accelerators, depicted in Figure 3.1.

Hydrogen gas is fed from a bottle into the complex where it is ionised and accelerated to 50 MeV using a linear accelerator called LINAC2. The beam of protons is then injected into the Proton Synchrotron Booster (PSB), a synchrotron made up of four superimposed, 25 m synchrotron rings that accelerate the protons up to 1.4 GeV. From the PSB, the protons are then directed to the Proton Synchrotron (PS), which accelerates the proton beam to 25 GeV.

This 628 m circumference synchrotron not only accelerates protons from the PSB, but it can also accelerate heavy ions from the Low Energy Ion Ring (LEIR). After the protons leave the PS, they are passed to the Super Proton Synchrotron (SPS), the final stage before entering the LHC. The SPS is a 7 km circumference synchrotron which, prior to the LHC era, was used to accelerate proton and anti-protons and provided collisions to the UA1 and UA2 experiments. The UA1 and UA2 experiments discovered the $W^{\pm}$ [45, 46] and Z [47, 48] bosons in 1983. Currently, the SPS accelerates protons from 25 GeV up to 450 GeV[1] and can deliver them to either the LHC or one of the various fixed target experiments, such as NA62 [49]. Finally, the protons are injected into two beam pipes, each accelerating protons in opposite directions around the main ring. The LHC uses 1232 superconducting dipole magnets, each weighing 35 tonnes, to bend the proton beam around the accelerator. Two independent linear accelerating radiofrequency cavities accelerate the protons in each beam up to 6.5 TeV.

Generally, protons are injected into the LHC in bunches of $\sim 10^{11}$ protons once every 25 ns. The LHC uses 392 quadrupole magnets to focus the proton beams. A focussed beam is important to providing a high *instantaneous luminosity*. Instantaneous luminosity is a measure of the particle flux at a given point. Assuming two identically shaped beams, each with a Gaussian profile independent of position along the bunch, the instantaneous luminosity $\mathcal{L}$ is given by

$$\mathcal{L} = \frac{f n_b N^2 \gamma}{4\pi\varepsilon\beta^*} F, \tag{3.1}$$

where f is the collision frequency, n_b is the number of bunches per beam, N is the average number of protons per bunch, γ is the relativistic γ-factor of the beam and F is a geometric factor that takes into account the bunch length and crossing angle. The emittance ε is a measure of the beam quality and the amplitude β^* is a measure of the beam size at the interaction point. This amplitude function is controlled by squeezing the beam size using quadrupole magnets. By reducing the size of the beam, the instantaneous luminosity can be increased.The values for ε and β^* vary between runs but are generally around $\varepsilon = 3$ µm and $\beta^* = 30$ cm [50]. The total

[1] The protons delivered to the fixed target experiments are accelerated only to 400 GeVbefore delivery.

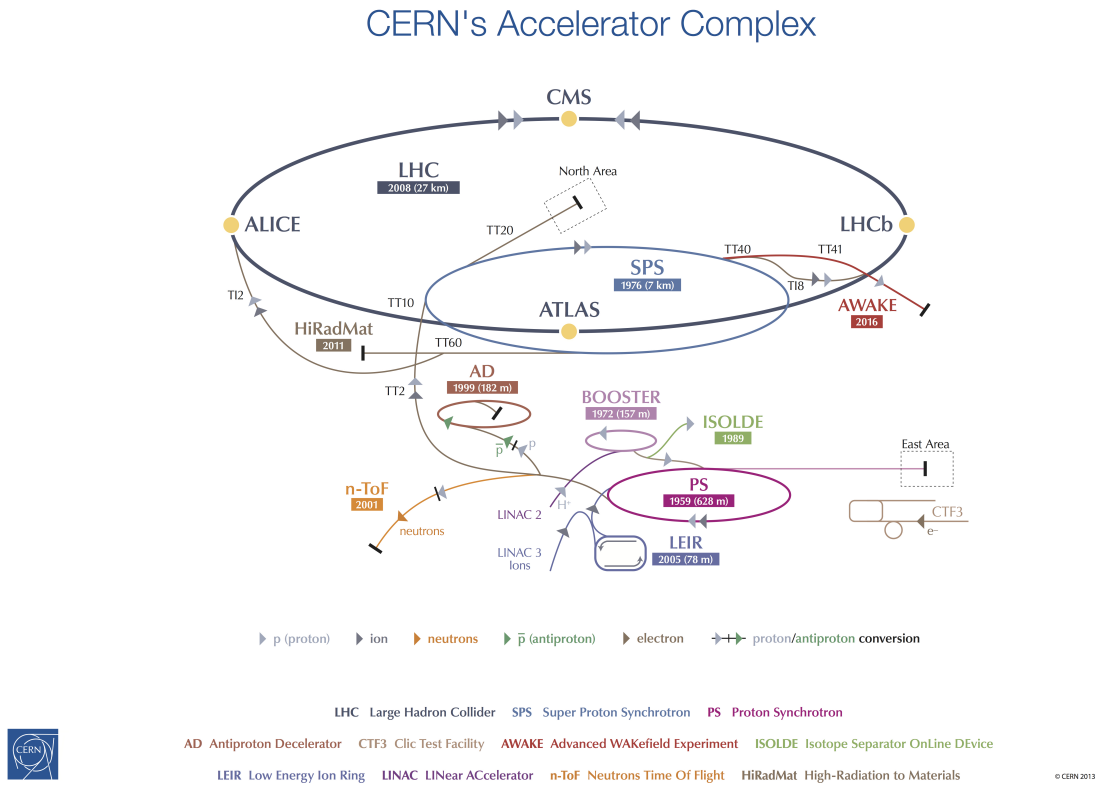

Figure 3.1 A diagram of the CERN accelerator and experiment complex [52].

dataset size is expressed in terms of the integrated luminosity, which is given by

$$\mathcal{L}_{\text{nt}} = \int \mathcal{L} dt, \tag{3.2}$$

with the units normally given in inverse femtobarns (fb^{-1}) for LHC experiments. For Run 2 of the LHC (2015-2016), the integrated luminosity was 36.1 fb^{-1}. The typical instantaneous luminosity is around 2×10^{34} cm^2 s^{-1} [51].

The LHC collides protons at four interactions points, each with a detector located at it. At the interaction points the two beams are brought together and collided. Two of the detectors, ATLAS and CMS experiments, are general purpose detectors. The other two are specialised detectors for b-physics (LHCb), and heavy ion physics (ALICE).

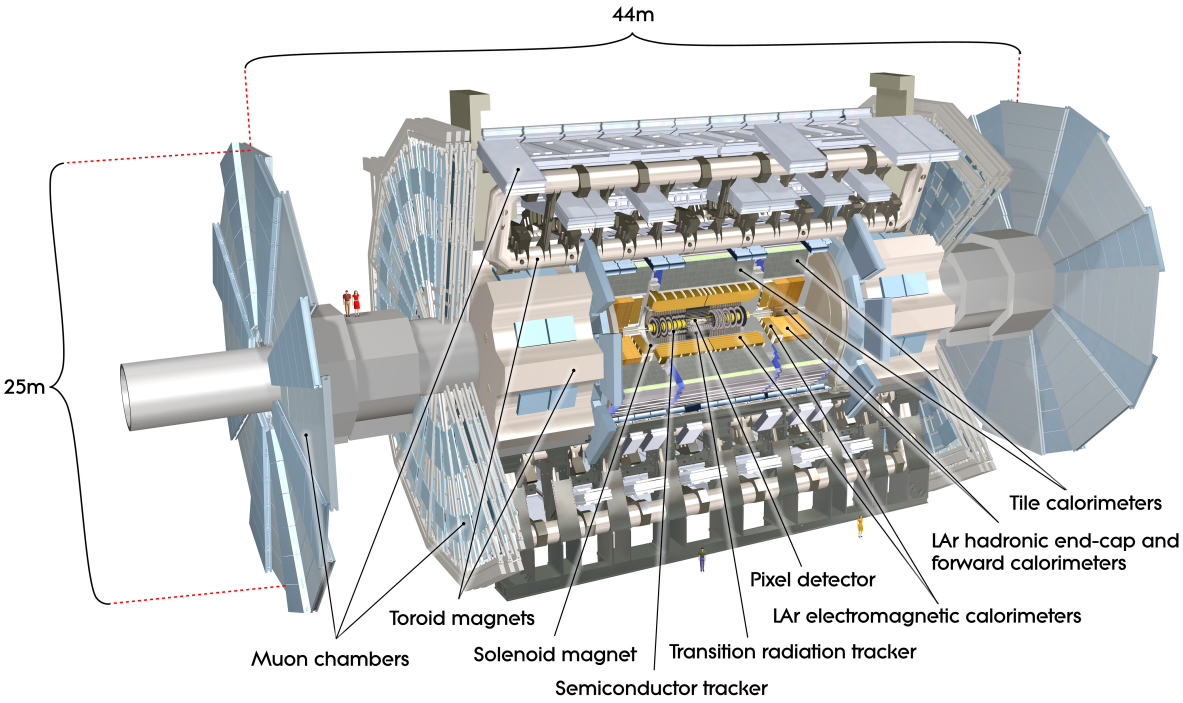

Figure 3.2 A cut-away diagram of the ATLAS detector, with the various subsystems labeled [53].

3.2 The ATLAS experiment

The ATLAS experiment (acronym for A Toroidal LHC ApparatuS) is the largest experiment on the LHC ring by both volume and mass. The detector is a barrel shape with a length of 44 m and a diameter of 25 m, weighing approximately 7000 tonnes. An illustration of the ATLAS detector is shown in Figure 3.2. The ATLAS detector is a general purpose detector, combining many different technologies. The detector is built radially outwards in layers, with different technologies at each layer in order to detect a wide range of particles.

The ATLAS experiment comprises the detector itself as well as magnets, triggers and data acquisition systems. There are four electromagnet systems that provide a strong magnetic field across the detector to aid in identifying particles and measuring their momentum. Closest to the interaction point is the *inner detector*, which precisely tracks the trajectories and momenta of charged particles. Further out from the interaction point are the *electromagnetic* and *hadronic*

calorimeter systems, which measure the energy and direction of particles. The outermost layer of the detector is dedicated to the *muon spectrometer* used to identify muons and measure their kinematics. Each of these sub-systems will be described in the following sections.

ATLAS uses a right-handed coordinate system with the interaction point as the origin. The x axis points points towards the centre of the LHC ring, the y axis towards the surface and the z axis along the beamline. A cylindrical coordinate system is also used where r is the radial distance to the point of interest, θ is the polar angle in the $z-y$ plane and ϕ is the azimuthal angle in the $x-y$ plane. Generally θ is not used in LHC experiments. Instead *pseudorapidity*, defined as $\eta = -\ln\tan\frac{\theta}{2}$, is used becauase differences in η are Lorentz invariant under boosts along the z axis.

3.2.1 Inner Detector

The Inner Detector (ID) [54], shown in Figure 3.3, is the detector sub-system that sits closest to the interaction point and its purpose is to reconstruct charged particle tracks. The ID is surrounded by a 2 T solenoid magnet (discussed further in Section 3.2.4). The magnetic field bends the path of charged particle tracks, enabling the ID to measure their momentum. The ID is composed of three subdetectors, each using a different and complementary technology. These are the *pixel detector*, the *semiconductor tracker* and the *transition radiation tracker*. Both the pixel detector and semiconductor tracker use doped silicon sensors to track charged particles. As charged particles transverse the silicon, electron-hole pairs are produced. A potential difference is applied across the silicon, which causes the electron-hole pairs to drift in opposite directions. The charge from the electron-hole pairs is then collected at diodes.

The pixel detector is composed of the Insertable B-Layer (IBL) [56] and three more layers in the barrel region. The IBL was installed in 2014 between Run 1 and Run 2. The IBL pixels are closest to the centre of the beampipe at a radius of $R = 33.25$ mm with each pixel only 50×250 µm^2 in $R \times \theta z$. The spatial resolution in $R\phi$ for the IBL pixels is 8 µm and 75 µm in z. The pixels in the other layers have an area of 50×400 µm^2 and extend out to a radius of 122.5

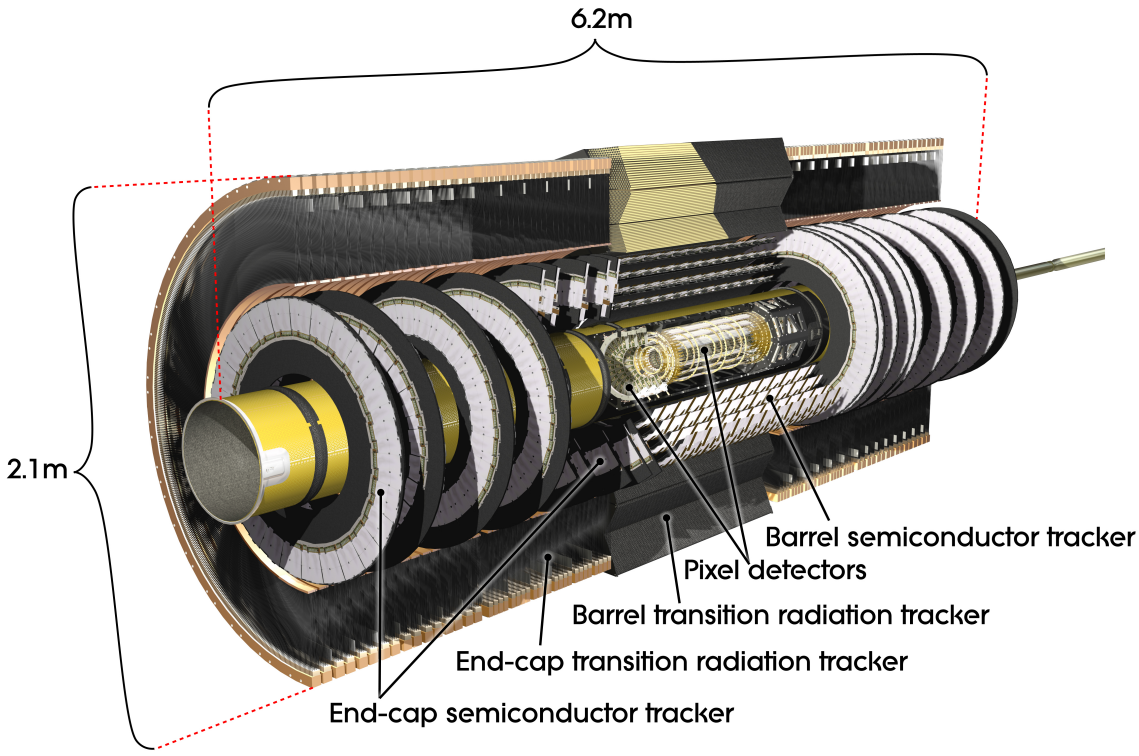

Figure 3.3 The layout of the Inner Detector, with the key components labelled [55].

mm. Their spatial resolutions are 10 µm in $R\phi$ and 115 µm in z. There are 1968 silicon sensors making up the pixel detector, covering $|\eta| < 2.5$, with a total of 86.4 million readout channels.

The semiconductor tracker (SCT) surrounds the pixel detector and uses similar silicon technology. However, instead of pixels it comprises strips arranged in four layers in the barrel and nine disks in the forward region. The strips are arranged in pairs at a stereo angle of 40 mrad and have a resolution of 17 µm in $R\phi$ and 580 µm in z. The SCT in the barrel region covers the radius from 300 mm to 520 mm.

The transition radiation tracker (TRT) is the outermost part of the ID. It comprises around 137000 straw tubes filled with a mixture of Xe(70%), CO_2(27%) and O_2(3%). Inside each tube is a gold-plated tungsten wire that acts as an anode, while the outer tube is the cathode. As a charged particle passes through the straw, the gas is ionised and an electron avalanche is detected as an electrical current in the wire. In the barrel region, the TRT comprises 50000 1.5 m long straw tubes arranged in parallel to the beam axis, at a radius of between $560 - 1070$ mm. In each end-cap there are 12000 0.4 m long straw tubes arranged perpendicular to the beampipe. The spatial resolution of each straw is 170 µm, however, combining measurements from many straws this reduces to 50 µm. The TRT aids in particle identification using transition radiation. When a ultra-relativistic charged particle passes through the boundary of two materials with different dielectric constants, the probability of the charged particle emitting radiation is proportional to the γ factor. Therefore, the radiation produced will vary depending on the rest mass of the charged particle.

For tracks with $1 < p_{\mathrm{T}} < 2$ GeV and $0 < \eta < 0.2$, the vertex resolution is around 60 µm for the transverse impact parameter, d_0, and 120 µm for the longitudinal impact parameter, z_0 [57].

3.2.2 Calorimeters

Located outside the solenoid magnet is the calorimeter system. The purpose of the calorimeter system is to measure the energy of charged and neutral particles. To do so, ATLAS uses *sampling calorimeters*, which make use of alternating layers of dense absorption material and

detecting scintillator material. As particles pass through the dense material, showers are produced and the secondary particles are then detected in the scintillator material.

The ATLAS calorimeter system is divided into an *electromagnetic calorimeter* (EM) and a *hadronic calorimeter* HCAL). The EM calorimeter measures the energy of electrons and photons, whereas the hadronic calorimeter measures hadron energies. The combination of the ID and calorimeter systems can measure most particles of the Standard Model, excluding minimum ionising muons and neutrinos.

3.2.2.1 Electromagnetic calorimeter

The EM calorimeter system (ECAL) [58] uses liquid argon as the active scintillating material and lead for the absorber. The system is divided into a barrel region covering $|\eta| < 1.475$ and two end-cap regions covering $1.375 < |\eta| < 3.2$. The ECAL is divided up into cells of different dimensions. In the barrel region, it consists of three different granularities of cells that vary as a function of the radius, as shown in Figure 3.4. The innermost layer of the EM calorimeter has a very fine cell granularity in η, with dimensions of 0.0031×0.98 in $\Delta\eta \times \Delta\phi$. The second layer, constituting the majority of the system, has a cell granularity of 0.025×0.025. Finally, the outermost layer has the largest cell granularity at 0.05×0.1 and is mainly used to discriminate between electromagnetic and hadronic showers. In the region $|\eta| < 1.8$ there is a presampler that measures the energy lost by electrons and photons before entering the calorimeter. This has a cell granularity of 0.025×0.1.

Additionally, there are two two-stage end-cap EM calorimeters in the forward regions covering $1.375 < |\eta| < 2.5$ with three layers and $2.5 < |\eta| < 3.2$ with two lower cell granularity layers. Both wheels are constructed similarly to the barrel region.

3.2.2.2 Hadronic calorimeter

Beyond the EM calorimeter sits the HCAL, which measures the energy of hadrons which do not interact in the the EM calorimeter. As with the EM calorimeter, the HCAL is composed

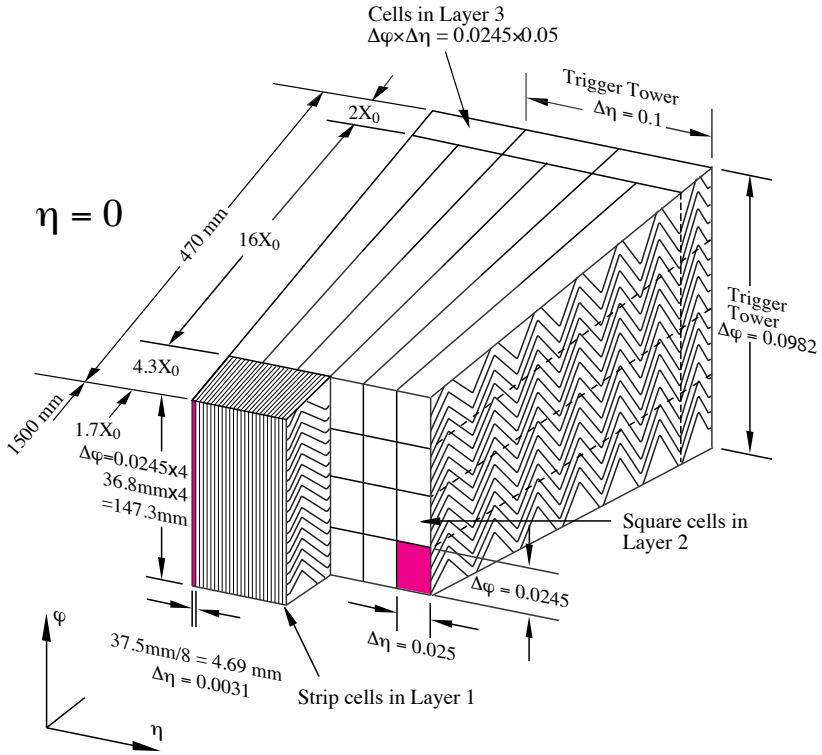

Figure 3.4 Diagram of the barrel region of the EM calorimeter [59].

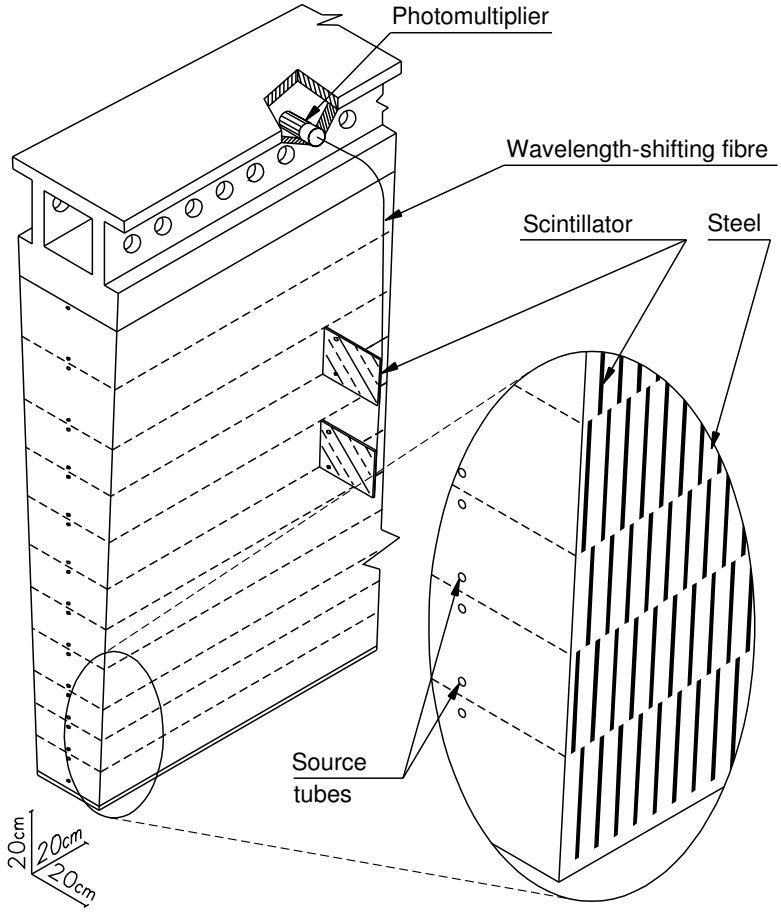

Figure 3.5 Drawing of a tile calorimeter section [59].

of different subsystems in different regions. Located in the barrel region $|\eta| < 1.7$ is the *tile calorimeter*[60]. The tile calorimeter uses steel absorber plates and plastic scintillator tile elements with three segmented layers. In the first two layers the cell granularity is 0.1×0.1 in $\eta \times \phi$ and 0.2×0.1 in the final layer. A drawing of a tile module can be found in Figure 3.5.

In the forward region at $1.5 < |\eta| < 3.2$ are the *hadronic end-cap calorimeters*, which are also liquid argon sampling calorimeters. These end-cap calorimeters use copper as the absorber material with a width of 25 mm in the inner wheels and 50 mm in the outer. The hadronic end-cap calorimeters sit behind the EM end-cap calorimeters.

3.2.2.3 Forward calorimeters

Further sampling calorimeters [58] are used in the extreme forward region at $3.1 < |\eta| < 4.9$, which act as both electromagnetic and hadronic calorimeters. These calorimeters again use liquid argon as the active material; however, for the absorber layer both copper (for EM) and tungsten (for hadronic) are used. The granularity at $|\eta| = 3$ is around 0.15×0.15 in $\eta \times \phi$ and 0.3×0.3 at $|\eta| = 4.5$.

3.2.2.4 Calorimeter performance

The energy resolution of calorimeters can, in general, be parameterised as,

$$\frac{\sigma_E}{E} = \frac{a}{\sqrt{E}} \oplus b \oplus \frac{c}{E}, \tag{3.3}$$

where $\oplus$ is the sum in quadrature, a is the constant in the stochastic term, b is a constant term, c is the constant in a term related to electronic noise and E is the energy in GeV. The stochastic term, is due to statistical fluctuations in the shower, dead material in the calorimeter or sampling fluctuations. The constant term is due to calibration uncertainties and detector non-uniformity and the final term in Equation 3.3 parametrises effects from electrical noise.

The performance of the calorimeter systems has been determined using test beam experiments and using electron and pion test beams. The resulting resolution for the barrel EM calorimeter is [61],

$$\frac{\sigma_E}{E} = \frac{(10.1 \pm 0.4)\% \times \sqrt{\text{GeV}}}{\sqrt{E}} \oplus (0.4 \pm 0.1)\%. \tag{3.4}$$

For the hadronic calorimeters, pion test beams were directed at a combined module of liquid argon electromagnetic and hadronic tile calorimeters. In this case, the energy resolution was observed to be [62],

$$\frac{\sigma_E}{E} = \frac{1.6\,\text{GeV}}{E} \oplus \frac{(52.0 \pm 1.0)\% \times \sqrt{\text{GeV}}}{\sqrt{E}} \oplus (3.0 \pm 0.1)\%. \tag{3.5}$$

3.2.3 Muon system

The outermost layer of the ATLAS detector is the muon spectrometer (MS) [63]. Its role is to detect and measure the energy and momenta of particle that have passed through the calorimeters. The majority of these particles will be muons, which do not deposit much of their energy in the calorimeters. The muon spectrometer consists of four different technologies: Monitored Drift Tubes (MDT), Cathode Strip Chambers (CSC), Resistive Plate Chambers (RPC) and Thin Gap Chambers (TGC). The layout of the muon spectrometer is shown in Figure 3.6. The MDT and CSC are primarily used for precise tracking, while the RPC and TGC for fast triggering. The MS is immersed in a magnetic field provided by ATLAS's toroidal magnet system (discussed further in Section 3.2.4). This magnetic field bends the path of the charged particles to aid in determining their momenta.

3.2.3.1 Monitored drift tubes

The monitored drift tube chambers [64] the region $0 < |\eta| < 2.7$ with between three and eight layers of 30 mm diameter tubes that work in a similar way to the TRT. Each tube contains a Tungsten-Rhenium wire and is filled with a mixture of Ar and CO_2 held at a pressure of 3 bar. The spatial resolution of a single MDT is 80 mm; however, this is enhanced by having multiple layers of tubes per module to an average of 35 mm in the z direction. These MDTs cover around 99.5% of the active detector area.

3.2.3.2 Cathode strip chambers

The remainder of the active detector area not covered by the MDTs, is instead covered by cathode strip chambers [65]. These CSCs are present in the high-flux region of the detector at $2.0 < |\eta| < 2.7$ to help provide finer granularity and to cope with higher rate. Again, the CSCs use a similar principle as the TRT and MDTs to operate. The difference is that instead of using tubes, there are cathodes strips above and below the anode wires. One set of wires runs perpendicular to the wires and the other in parallel to provide radial and transverse

measurements. The CSCs have a combined resolution of 40 µm in η and 4 mm in ϕ. The combination of the CSCs and MDTs provide a p_{T} resolution of $\sigma_{p_{\mathrm{T}}}/p_{\mathrm{T}} \approx 10\%$ for muons with a $p_{\mathrm{T}} = 1$ TeV [63].

3.2.3.3 Resistive plate chambers

The resistive plate chambers are used to quickly identify muons for triggering. They are made of two parallel resistive plates with a gas filling the volume between them. The plates are kept at a potential difference of 9.8 kV. As a muon passes through the chamber, the gas is ionised, causing an avalanche of electrons which are collected on aluminum strips on the back of the plates. The RPCs have a short response time of less than 25 ns, which allows quick identification of muons and therefore fast triggering.

3.2.3.4 Thin gap chambers

As with the measurement of muon kinematics, the identification of muons is achieved with a second system in the forward region. In the end-cap between $1.05 < |\eta| < 2.4$, thin gap chambers are used because of their ability to withstand much higher flux while still maintaining < 25 ns response time. The TGCs are multi-wire proportional chambers that function in a similar manner to the CSCs. The main difference is the distance between the cathode cases and the anode wires. The wires are arranged such that the resolution in r is $2 - 6$ mm and 7 mm in ϕ. The combination of the RPCs and TGCs provide fast identification for triggering.

3.2.4 Magnets

The ATLAS detector uses 4 superconducting magnet systems to aid the measurement of charged particle momentum. These magnets produce large magnetic fields that bend the path of charged particles. The curvature of the particle path is proportional to the momentum and therefore by measuring the curvature, the momentum can be calculated. An illustration of the magnet system can be seen in Figure 3.7.

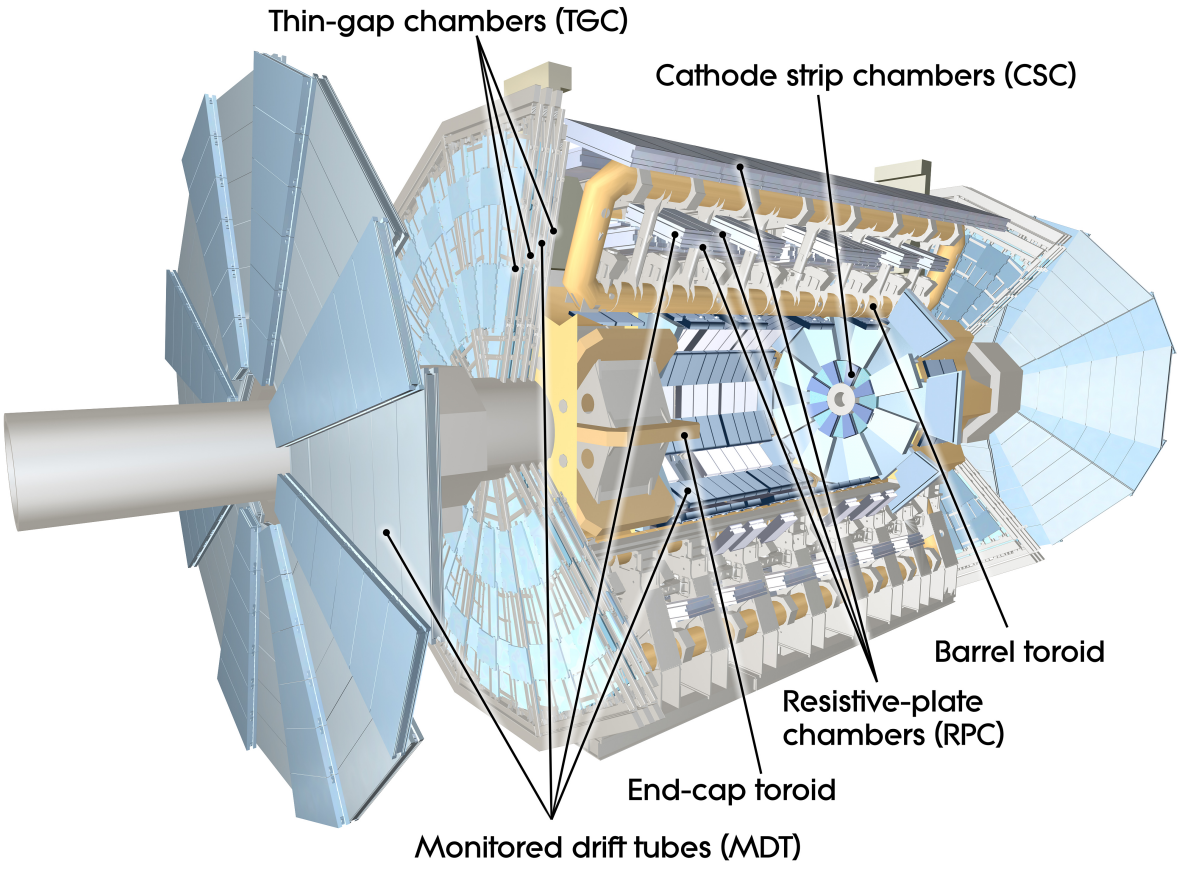

Figure 3.6 A computer generated image of the muon system [66].

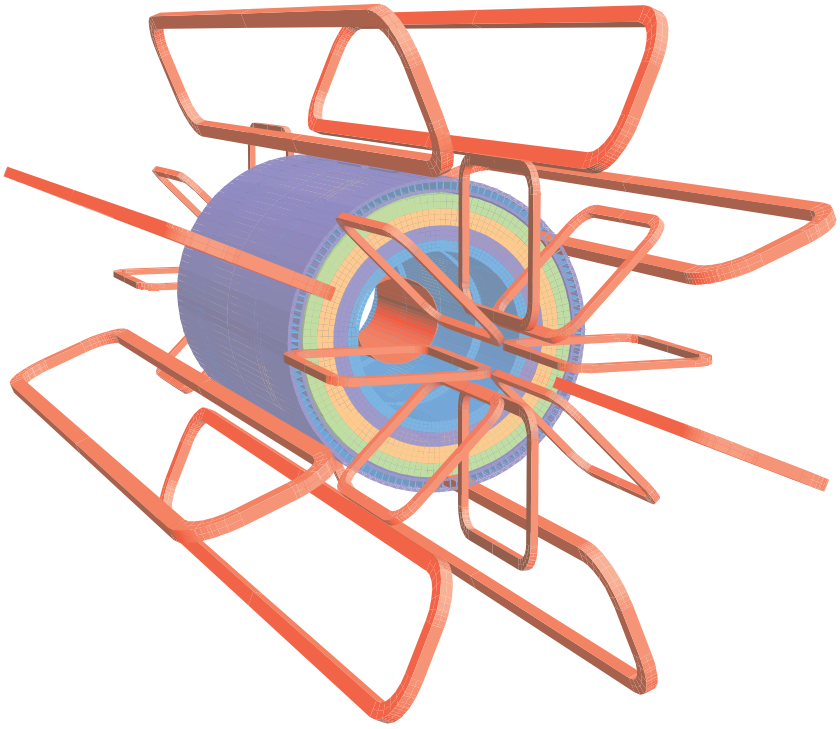

Figure 3.7 A computer generated image of the magnet system [59].

As mentioned in Section 3.2.1, the ID is surrounded by a 2 T solenoid magnet [67]. The solenoid sits between the ID and the ECAL. It has been designed to be thin and light so as to minimise the probability of particles interacting with it as they pass through.

There are several toroidal magnets in the outer regions of the ATLAS detector. In the barrel region ($|\eta| < 1.35$) there are eight magnets [68], producing on average, a 0.6 T magnetic field. In the forward region, from $1.55 < |\eta| < 2.7$, are the end-cap toroids [69]. Each end-cap contains eight toroids, which produce on average, a 1 T magnetic field. The combination of the solenoid magnet bending particles in one direction and the different toroidal magnets bending particles in another direction aids in the precise measurement of muon kinematics.

3.2.5 Trigger and data acquisition

Currently, the LHC collides protons with a bunch spacing of 25 ns, which equates to an event rate of 40 MHz. Reading out every part of the detector (around 100 million channels) at this

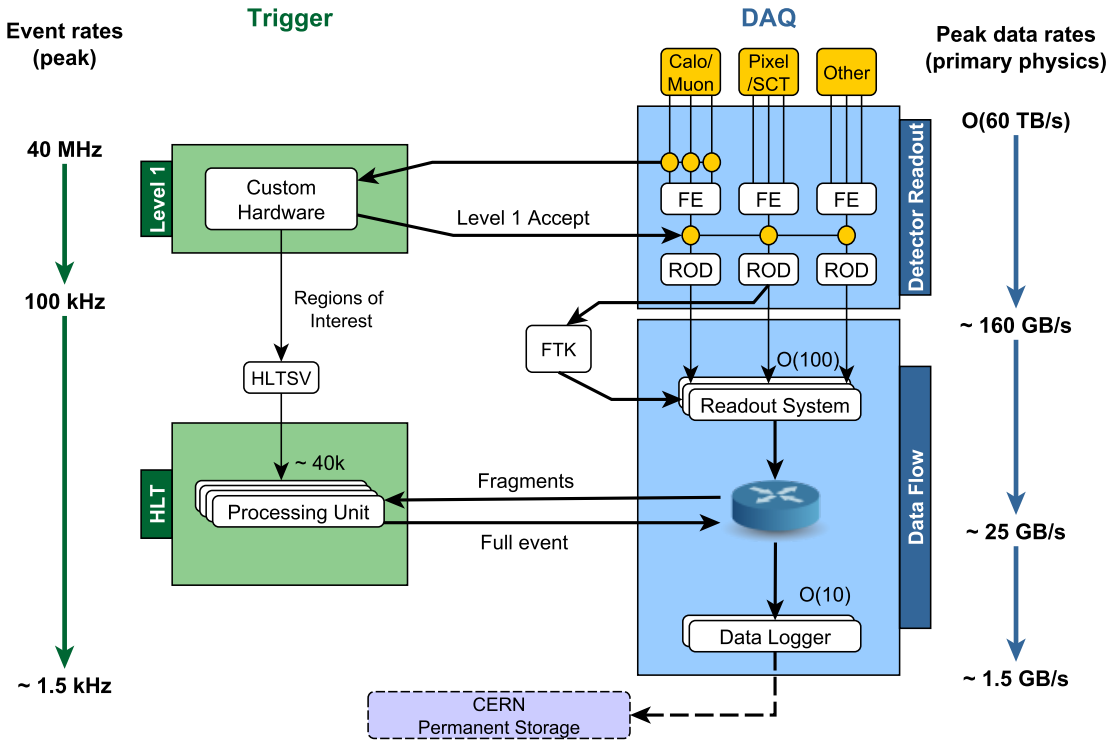

Figure 3.8 A diagram of the ATLAS trigger and data acquisition system [72].

rate would be unfeasible, requiring huge bandwidth. In addition, many of the events are not particularly interesting or useful for analysis. To select only interesting events and reduce the rate, ATLAS employs a two-stage trigger system. The fist stage, known as the Level 1 (L1) trigger [70], utilises extremely fast, custom hardware. The second stage is known as the High Level Trigger (HLT) [71], which uses commercial PCs and software-based algorithms. While the trigger system makes a decision on a given event, the data acquisition system buffers the data from the various subdetectors and controls whether the data is saved. A diagram of the ATLAS trigger and data acquisition system can be seen in Figure 3.8.

3.2.5.1 Level 1 trigger

The L1 trigger reduces the rate from 40 MHz down to around 100 kHz using ASIC/FPGA-based hardware. The custom hardware has the trigger algorithms built in, allowing for a decision to be made in less than 2.5 µs. To make the decision, the L1 trigger uses reduced-granularity input from the calorimeters and muon spectrometer. Using this information it can identify high p_{T} objects such as electrons, muons, jets and hadronically decaying taus. If an event contains an object that passes the L1 trigger requirement, the Region-of-interest (ROI) is passed onto the HLT.

3.2.5.2 High level trigger

The HLT system is implemented in software and is run on a 40000 core commercial computing cluster. Once a L1 accept signal is received, the HLT can make use of the full granularity information from the detector ROI to make a decision. Due to the reduced input rate, the HLT is able to make use of parallel processing. Algorithms are combined into *chains* that can be executed in parallel. Early algorithms will build more simple objects which can then be used to make a trigger decision. This saves time by not running the more complex and time consuming algorithms later on.

If an event passes all of the HLT requirements, the event is read out and saved in permanent storage. The final output rate from the HLT is around 1 kHz, which is far more manageable than the original input rate of 40 MHz.

3.2.5.3 Read out system

The ATLAS readout system (ROS) [73] acts as a buffer for the data while the HLT is making a decision and then handles requests for data fragments. If the event is accepted by the HLT, the data is then written to disk, otherwise it is deleted. The ROS is implemented on around 100 commercial PCs, each with four custom *RobinNP* cards. The data is input into the PCs using 1850 optical links at a rate of 100 kHz. At the output rate of 1 kHz, the data transfer rate is

around 1 GB/s, which is sent via a network to the CERN Worldwide LHC Computing Grid (WLCG) [74]. The WLCG is a global network of compute and storage clusters that is shared by all LHC experiments.

3.2.6 Luminosity measurements

In order to measure the luminosity delivered to the ATLAS detector, three subdetectors are used. The one located closest to the interaction point is the LUminosity measurement using a Cherenkov Integrating Detector (LUCID) [75]. LUCID uses Cherenkov detectors located 17m either side of the interaction point. Next, the Zero Degree Calorimeters (ZDC) [76] are located 140m from the interaction point on either side of the ATLAS detector. Both of these subdetectors measure neutral particles from meson decays in the forward regions. Finally, at 240m from the interaction point, the Absolute Luminosity For ATLAS (ALFA) [77] detector is located. This subdetector measures elastic proton-proton collisions at very low angles.

Chapter 4

Data simulation and object reconstruction

In order to test the SM using the ATLAS detector, an understanding of how the physics will manifest in the detector must be established. In this chapter, the idea of *Monte Carlo* simulation is introduced as a method of producing predictions that experimental data can be compared to. A description of the various physics objects that can be reconstructed in the ATLAS detector is then provided.

4.1 Monte Carlo simulation

To understand what the final state of any given physics process will look like would look like, *Monte Carlo* simulation (MC) is used to model both the initial and final state of the process of interest, as well as the propagation of particles through the detector. The same reconstruction algorithms used to reconstruct data (discussed in Section 4.2) are also applied to all MC samples.

4.1.1 Event simulation

The simulation of each event is broken up into several stages as can be visualised in Figure 4.1. The simulation starts with the incoming protons (shown as two dark green ovals). From these, the initial-state partons are extracted and their momenta determined using the proton PDFs.

The cross section for the hard scatter (shown as a red dot) is determined from the fixed order matrix element (ME) and integrated over the phase space of the final state particles, which are shown in the figure as the red lines/dots leaving the hard scatter. The ME calculation also predicts their momenta.

The particles produced by the hard scatter then undergo a process of *parton showering*, where the quarks and gluons produce a "shower" of further coloured particles (gluons, plus quark-antiquark pairs produced via gluon splitting). These are shown in blue in the figure, along with the coloured particles that make up the proton remnants. The parton showering process is modelled by the DGLAP equations [78] until the energy scale is below 1 GeV. At the end of this process, all coloured particles that remain will recombine to form colourless hadrons (shown in dark green) in a process known as *hadronisation* (depicted by the light green disks in the figure). Additional QED radiation may also be emitted from the final state particles (shown in yellow). As well as the original hard scatter, additional interactions between other partons within the proton must be included (known as the *underlying event*). These may include additional hard interactions. Finally, *pile-up* collisions also overlaid, which originate from collisions of other protons in the beam.

Simulating the particle interactions is extremely complex, due to the number of particles involved in any individual interaction. For the non-perturbative parts of the calculation, such as the hadronisation, models are used to approximate these processes. There exist models to approximate the fraction of the parent quark momentum which is carried into the meson which forms from it, known as *fragmentation functions*. Depending on the MC simulator, different paramaterisations of the fragmentation function are used.

For hadronisation, two main models exist, the *string model* [79] and the *cluster model* [80]. In the Pythia event generator [81] the string model is used whereas the Herwig event generator [82] uses the cluster model. The differences in performance of these models can be used to assess the uncertainty due to the model chosen. This will be discussed further in the coming chapters.

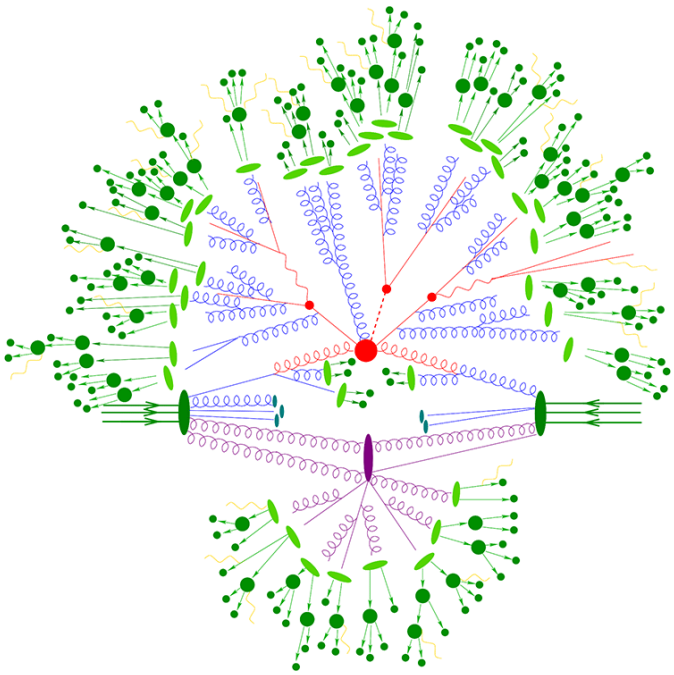

Figure 4.1 A computer generated diagram of the event generation process [83].

Each MC generator comes with many tunable parameters. In order to give the best possible description of nature, these parameters must be optimised, or *tuned*, using experimental datasets of events produced via well-understood physical processes.

4.1.2 Detector simulation

The output of the MC event generation process is used as an input to a simulation of the ATLAS detector. This simulation describes all of the detector material and geometry, as well as any defects in the material or electrical problems. The simulation is built using the GEANT4 [84–86] simulation software, which, like the event generation models, is tuned and calibrated to ensure the accuracy of the model. Problems such as radiation damage to detectors must be calibrated for over time. The output of the detector simulation is reconstructed in the exact same way as data to allow the two to be compared directly.

The simulation of the passage of particles through the detector is very computationally expensive. This is mainly due to simulation of the calorimeters because it is extremely time consuming to simulate the particle showers. To speed this up, an approximate simulation, `ATLASFAST-II` (AFII) [87], is often used. This approximate model simulates the particle showers in the calorimeters using parameterised functions applied to particle energy, rather than carrying out the full shower simulation.

4.2 Object definitions

Using the data that has been collected or the MC simulation produced, the electrical signals from the detector (or simulation of detector) need to be translated into physics objects that can be used for physics analysis. To do so, *reconstruction* algorithms are applied to the data and MC. This next section details the physics objects used in the analyses presented in this thesis.

4.2.1 Tracks and vertices

Starting from the centre of the detector, the ID is used to reconstruct *tracks*. Tracks are a key physics object used to reconstruct many other physics objects and to identify *vertices*. A track is reconstructed using hits in the ID to map the path of a charged particle traversing through the IDt. As discussed in Section 3.2.4, the solenoid magnet bends the path of the charged particle and it is the curvature of the track which is used in the determination of the particles momentum.

In order to reconstruct a track, the pixels and strips in the ID are grouped together if they have significant energy deposits. From this a collection of *space-points* are defined using connected component analysis and those from the inner most layer of the SCT are used as *track seeds*. Expanding to the outer layers from the track seeds produces *track candidates*. These track candidates are then fitted using a Kalman filter [88]. Any scattering of the track by the detector material is taken into account by the Kalman filter. Using the χ^2 of the fit and the number missing hits, poor quality tracks are rejected. The tracks are then extended to the TRT and

the final reconstructed tracks are built by fitting using all parts of the ID. Each track can then be described with five parameters: the transverse impact parameter d_0, the longitudinal impact parameter z_0, azimuthal angle ϕ, polar angle θ and the charge momentum ratio q/p.

Once tracks are identified, they are used to find primary and secondary vertices by looking for the points from which the tracks emerge. These vertices are found using an adaptive fitting algorithm [89]. The primary vertex is then defined as the pp interaction vertex which has the highest sum of transverse momentum. This vertex is most likely to be from where the hard-scatter originates. All other vertices are then labelled as secondary vertices. The primary vertex is used to identify the hard-scatter interaction in the event, whereas the secondary vertices are from further decays from long lived particles or from other interactions. Tracks may also come from from pile-up. Pile-up tracks originate from other pp interactions in the beam which do not contain the hard-scatter interaction. There are two types of pile-up, in- and out-of-time. In-time pile-up comes from tracks that originate from the same event whereas out of time pile-up originates from a different event. Secondary vertices are used to identify b-hadrons and will be discussed further in Section 4.2.5.

4.2.2 Electron reconstruction

Electrons (and positrons) are reconstructed by matching tracks with deposits in the ECAL. The ECAL is divided into towers of approximately the granularity of the second calorimeter layer. The energy deposited in the first, second and third calorimeter layers in each tower is summed. Electron cluster candidates are seeded from a sliding-window algorithm using 3×5 towers in $\eta \times \phi$ space [90] by identifying clusters with a total energy above 2.5 GeV, where the cluster energy is the sum of the corresponding tower energies. Tracks are then matched to the electron clusters using the cluster seed position. If more than one track matches with a given cluster, the match that is closest is chosen. If there are no matches, the cluster is considered to be a photon candidate instead. The single electron reconstruction efficiency is above 99% for electrons with $E_{\mathrm{T}} > 20$ GeV [90]. Here, E_{T} is the energy of the object in the plane transverse to the beam axis.

In order to ensure that only genuine electron candidates are used for physics analysis, a multivariate likelihood (LH) based identification is used. The LH is built from inputs from each layer of the calorimeter, the track parameters and the track-cluster matching. A likelihood for both signal and background is used to calculate a discriminant on which the identification is based. There are three working points used: *Loose*, *Medium* and *Tight* which vary how strict the identification requirements are. The efficiency of identifying an electron at $E_{\mathrm{T}} = 40$ GeV for the three working points are 93%, 88% and 80% respectively [90].

The electrons must also be isolated. This is quantified through the electron isolation *isolation* that quantifies how much other activity surrounds an electron in the detector. There two methods to require isolation; calorimeter and track-based isolation. In calorimeter isolation, a cone of some ΔR size around the electron candidate is formed and the sum of the energy deposits within the cone is calculated. The ΔR criteria will vary depending on the working point chosen. After subtracting the electron energy deposits, selection requirements can be made to require there be little extra energy deposited in the calorimeter near the electron. Track-based isolation works in a similar way by defining a cone, but in this case, the number of tracks within the cone are counted. Various combinations of these two requirements make up the different working points, which can be found in [90].

4.2.3 Muon reconstruction

Muons are built using information from both the ID and the MS. First, the tracks in each subsystem are reconstructed independently. In the ID, muon tracks are reconstructed as discussed in Section 4.2.1, as are any charged particle tracks. In the MS, hit patterns are sought in each of the muon chambers using a Hough transform [91]. Seed track segments are formed and then track candidates are selected using a combinatorial search [92]. For each track candidate, the hits are fitted with a global χ^2 fit and the candidate is accepted if the χ^2 meets a given criterion.

To build the combined ID-MS muons, algorithms are used based on the information from the ID, MS and calorimeters. The different combinations of input information leads to four different *types* of reconstructed muons:

- **Combined muons (CB)**: tracks are reconstructed independently in the ID and MS then a combined track is formed using a global refit. Tracks are generally first reconstructed in the MS and then extrapolated into the ID and matched to a track. The inverse approach is sometimes used.
- **Segment-tagged muons (ST)**: tracks from the ID are extrapolated to the MS and if one local track segment in the MS is associated with it, the track is classified as a muon. These are usually low p_{T} muons or those that fall in reduced acceptance regions of the MS.
- **Calorimeter-tagged muons (CT)**: ID tracks that are matched to an energy deposit in the calorimeter that is compatible to a minimum ionising particle is classified as a CT muon. These muons have low purity but are useful for identifying muons which fall in the region of the MS where cabling and infrastructure run.
- **Extrapolated muons (ME)**: the reconstructed trajectory of ME muons uses only the MS track and some loose requirement that its origin is the interaction point. The ME muons are used to extend reconstruction acceptance to areas not covered by the ID.

If two muon types share ID tracks CB tracks are favoured. For ME muons, any overlapping tracks are removed by selecting the best quality fit with the highest number of hits.

For muon identification, muons from W decays are considered *prompt* muons whereas those coming from pion or kaon decays are *non-prompt* muons. Requirements are placed on muon candidates in order to suppress the contribution from non-prompt muons. In CB tracks, the variables commonly used to distinguish between prompt and non-prompt muons are:

- $\boldsymbol{q/p}$ **significance**: the absolute difference of the ratio of charge and momentum of muons from the ID and MS divided by the sum in quadrature of the uncertainties.

- $\boldsymbol{\rho'}$: the absolute difference between the p_{T} from the ID and MS, divided by the p_{T} of the combined track.
- $\boldsymbol{\chi^2}$: the normalised χ^2 of the combined track fit.

There are four muon identification working points; *Medium*, *Loose*, *Tight* and *High-p_T* [92].

- **Medium muons**: This is the default working point used by the ATLAS collaboration. Only CB and ME tracks are used. The CB tracks are required to have ≥ 3 hits in at least two MDT layers. The ME are required to have hits associated with them in ≥ 3 MDT/CSC layers. However, this is only used in the $2.5 < |\eta| < 2.7$ region where the ID has no coverage. In order to suppress hadrons misidentified as muons, the q/p significance is required to be less than seven. The reconstruction efficiency for this working point in the range $20 < p_{\mathrm{T}} < 100$ GeV is 96.1%.
- **Loose muons**: all CB and ME muons that satisfy the Medium requirement are also included in the Loose selection. The Loose selection is optimised to maximise the reconstruction efficiency, while still retaining only good quality muon tracks. Loose muons are around 97.5% CB muons in the $|\eta| < 2.5$ region [92]. The reconstruction efficiency for Loose muons in the range $20 < p_{\mathrm{T}} < 100$ GeV is 98.1%.
- **Tight muons**: The Tight muon selection is optimised for high purity even if the reconstruction efficiency is reduced. CB muons are required to have at hits in at least two stations of the MS and to have passed the Medium selection requirements. The Tight muon selection requires $\chi^2 < 8$ and a two-dimensional cut on ρ' and q/p significance as a function of muon p_{T}. This two-dimensional cut rejects lower p_{T} muons where the misidentification is normally higher. The reconstruction efficiency for Tight muons in the range $20 < p_{\mathrm{T}} < 100$ GeV is 91.8%.
- **High-$\boldsymbol{p_{\mathrm{T}}}$ muons**: The High-p_{T} muon selection is optimised for analyses searching for high-mass resonances using muons. CB muons are required to pass the Medium selection and have at least three hits in three MS stations. This selection maximises the momentum resolution for muons with $p_{\mathrm{T}} > 100$ GeV.

As with electrons, a further measure of a muon candidate is the isolation. Prompt muons will normally be produced in isolation from other particles, whereas non-prompt from a decay-in-flight may be surrounded by other particles. For muons there are two methods to assess isolation: calorimeter and track-based isolation. For track-based isolation, a variable , $p_{\mathrm{T}}^{\mathrm{varcone30}}$, is defined as the scalar sum of the p_{T} of tracks with $p_{\mathrm{T}} > 1$ GeV in a cone of $\Delta R = \min(10\mathrm{GeV}/p_{\mathrm{T}}^{\mu}, 0.3)$ around the muon, excluding the p_{T} of the track associated with the muon itself. The calorimeter-based isolation builds a similar variable, $E_{\mathrm{T}}^{\mathrm{topocone20}}$, which is defined as the sum of the E_{T} values of the topological clusters in a cone of size $\Delta R = 0.2$, after subtracting the the contribution from the muon and pile-up effects. There are seven isolation working points defined and a full breakdown of their definitions can be found in [92].

4.2.4 Jet reconstruction

When quarks and gluons are produced in an interaction they undergo hadronisation. A consequence of this is that collimated "jets" of particles are formed and as they traverse the detector many tracks and calorimeter deposits are left. These clusters of tracks and calorimeter deposits are known as *jets*. The total energy deposited by the jet can be equated to the energy of the quark or gluon from which the jet originated.

4.2.4.1 Reconstruction

In order to reconstruct a jet, a method of grouping tracks and calorimeter deposits must be defined. To do so, many *clustering* algorithms exist and are now required to follow "The Snowmass Conditions" [93]. These conditions stipulate that a clustering algorithm must be simple to implement both experimentally and theoretically, independent of hadronisation model and also produce reasonable theoretical predictions in perturbation theory. Importantly, it is required that the clustering algorithm is both *collinear* and *infrared* safe. This requires that the algorithm is invariant to infinitesimally soft or small angle radiation. The most commonly used algorithm in the ATLAS Collaboration is the *anti-k_T* algorithm [94].

The clustering algorithms make use of the calorimeter information in the form of *topological cell clusters* [95]. The topological cell clusters are used to mitigate the noise from the calorimeters. In the *anti-k_T* algorithm topological cell clusters are used as input by treating them as massless pseudo-particles with a four momentum defined from the energy and direction of energy weighted by the barycentre of the cell cluster. The algorithm then calculates the distance between each pair of inputs, i and j, using,

$$d_{ij} = \min(k_{T,i}^{2p}, k_{T,j}^{2p}) \frac{\Delta_{ij}^2}{R^2}, \tag{4.1}$$

where,

$$\Delta_{ij}^2 = (y_i - y_j)^2 - (\phi_i - \phi_j)^2, \tag{4.2}$$

and the distance from each input i to the beam axis is defined as,

$$d_{iB} = k_{T,i}^{2p}. \tag{4.3}$$

Here k_T is the transverse momentum and y and ϕ are the rapidity and azimuthal angle of the input particle. p is a parameter which determines the order of the clustering. In the case of the *anti-k_T* algorithm, $p = -1$. R determines the size of the final jets that are output by the algorithm.

The algorithm first calculates the smallest distance d. If the smallest is d_{ij}, then clusters i and j are combined. If d_{iB} is the smallest, then i is called a jet and is removed from the list of clusters. These distances continue to be calculated until there are no clusters left in the list. When the parameter p is positive, the algorithm will cluster constituents from softest to hardest, whereas when it is negative it behaves in the opposite manner. When $p = -1$ the algorithm will cluster jets in an approximately conical shaped way. A visual example of the *anti-k_T* and k_T algorithms can be seen in Figure 4.2.

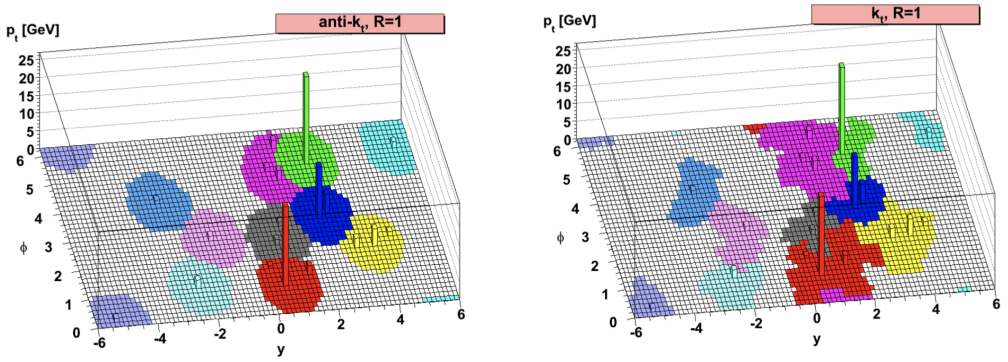

(a) **(b)**

Figure 4.2 Example of *anti-k_T* (a) and k_T (b) jet clustering algorithm with $R = 1$ [94].

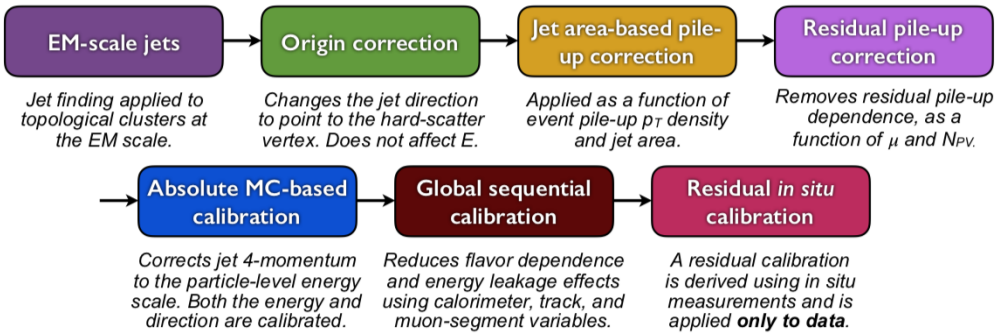

Figure 4.3 A summary of the calibration steps for jets in the ATLAS experiment [96].

4.2.4.2 Calibration

Generally in the ATLAS Collaboration, jets are reconstructed with a radius parameter $R = 0.4$. These are referred to as "small jets" and are required to have $p_{\mathrm{T}} > 25$ GeV and $|\eta| < 2.5$. Additionally, a requirement on the *jet vertex tagger* (JVT) multivariate discriminant is made for jets with $p_{\mathrm{T}} > 50$ GeV and $|\eta| < 2.4$. The JVT uses two track based variables and a two dimensional profile likelihood fit to determine the probability a jet originates from pile-up.

Once the jet objects are reconstructed, several stages of calibration are performed [97]. Figure 4.3 shows a summary of the various stages to the process.

Firstly, the jet axis is corrected so the origin points to the primary vertex rather than the centre of the detector, which helps improve the resolution in η. Next, corrections are applied to mitigate against for pile-up effects. The p_{T} of the jet is corrected as follows,

$$p_{\mathrm{T}}^{\mathrm{corrected}} = p_{\mathrm{T}} - \rho A - \alpha(p_{\mathrm{T}}, \eta)(N_{PV} - \beta(p_{\mathrm{T}}, \eta)\mu. \tag{4.4}$$

The ρA term removes the effect of the pile-up by estimating the median energy density ρ. This term is discussed further in Section 8.6. After this correction, the p_{T} is still found to have a dependence on the amount of pile-up so an additional correction is needed. There is found to be a dependence on the number of primary vertices N_{PV} and the mean number of additional pp collisions per bunch crossing μ. The dependence on N_{PV} is sensitive to "in-time" pile-up and μ to "out-of-time" pile-up. This correction is determined with two functions α and β that are fit to MC [96].

After pile-up corrections a MC-based calibration is applied. The *absolute* jet energy scale (JES) corrects the reconstructed jet four-momentum to the true energy scale (according to simulation). The mean energy response is calculated by looking at the ratio of reconstructed E_{T} and true E_{T} from MC simulation and is applied to the jets in regions of E_{T} and η. The η calibration corrects for any biases in the jet η reconstruction. The η biases are generally a consequence of the layout of the calorimeters.

The next stage is known as the *global sequential calibration*. Even after the MC corrections there are still some dependencies of the JES on the longitudinal and transverse jet features remaining. Differences in the calorimeter response to the constituent jet particles is found, often due to the differing compositions of quark- and gluon-initiated jets. In total there are five variables for which biases are corrected:

- The fraction of jet energy measured in the first layer of the Tile calorimeter;
- The fraction of jet energy measured in the third layer of the electromagnetic LAr calorimeter;
- The number of tracks with $p_{\mathrm{T}} > 1$ GeV;
- The average p_{T} weighted jet radius;
- The number of muon track segments.

Finally, a *residual in-situ* calibration is applied, which corrects for biases in the MC using well measured event topologies. The η-calibration uses jets from the well calibrated central region to correct the p_{T} of jets in the forward region by balancing the p_{T} of dijet events. The jet p_{T} is then corrected with three further calibrations derived by measuring the p_{T} response, R. Using Z+jets and γ+jets events, the p_{T} of central jets is balanced against a well calibrated photon or Z-boson in order to determine the response in the central region. These two measurements are performed in parallel and then combined. Then to correct high-p_{T} jets, several well calibrated low-p_{T} jets are balanced against one high-p_{T} using multijet events. The measured response for each event topology can be seen in Figure 4.4, with all three showing good agreement.

4.2.5 *b*-tagging

The identification of jets originating from b quarks is important for the analyses involving the top quark due to the top quark predominantly decaying to b quarks. Identifying jets originating from b quarks is made easier by the presence of b-hadrons. b-hadrons have a much longer lifetime than light hadrons and therefore leave displaced tracks within the jet. These displaced

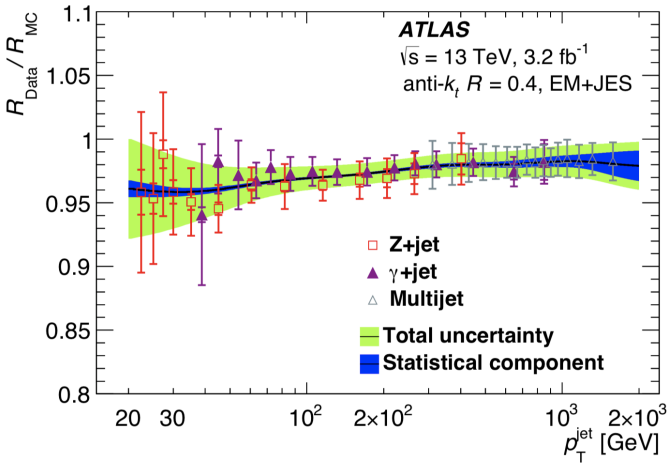

Figure 4.4 The results of the in-situ calibration. The ratio of the data and MC response, R, from the three event topologies is shown with different markers as a function of jet-p_{T}. The black line shows the combination of the three topologies [96].

tracks will originate from secondary vertices, which can be identified from the transverse d_0 and longitudinal $z_0 \sin\theta$ impact parameters.

A common tagging algorithm used in the ATLAS Collaboration is the `MV2c10` algorithm [98]. The `MV2c10` is a multivariate discriminant that takes as input three complementary b-tagging algorithms to discriminate between jets originating from b, c or light quarks[1]. The three algorithms used as input are:

- **IP2D and IP3D impact parameter algorithms**: The two impact parameter algorithms use the transverse (IP2D and IP3D) and longitudinal (IP3D) impact parameters of the tracks associated with the jet. The IP3D algorithm contains more information than the IP2D algorithm; however, IP3D is more sensitive to pile-up due to the longitudinal impact parameters' dependence on pile-up. The output is a log-likelihood ratio for each combination of outcomes (u, d or light quark), which is used as input to the `MV2c10` [99].

- **Secondary vertex (SV)**: The reconstructed secondary vertex information of the tracks associated with the jet can be used to discriminate between heavy and light quark initiated jets. There are eight outputs from the SV algorithms used in `MV2c10`: invariant mass of

[1] Light quarks refer to u, d and s quarks.

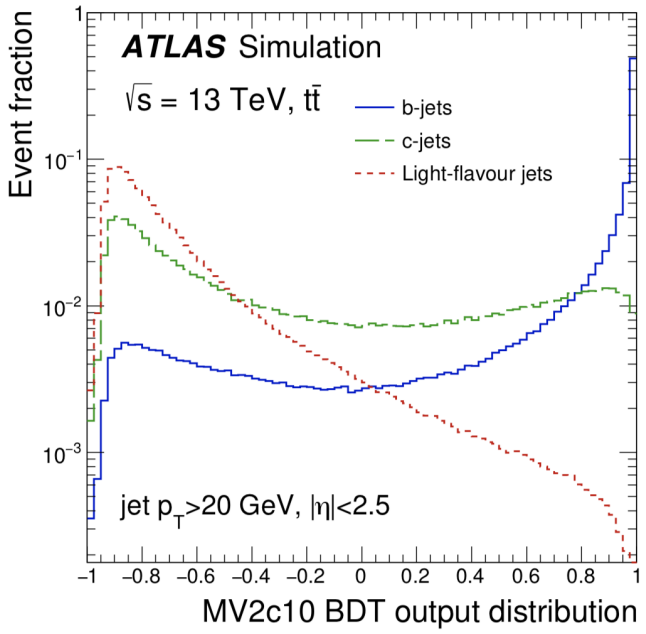

Figure 4.5 The output `MV2c10` discriminant for b jets (blue), c jets (green) and light flavour jets (red) [99].

tracks matched to the SV, $\Delta R(\text{jet}, \text{SV})$, jet energy fraction, number of tracks used in the SV, number of two track vertex candidates and the three distance measures [99].

- **JetFitter**: The JetFitter uses similar information to the SV algorithm but instead reconstructs the full decay using a Kalman Filter [88]. The JetFitter also outputs similar variables to the SV algorithm [99].

In addition to the outputs from the three b-tagging algorithms, the p_{T} and η of the jets are also used as input to the discriminant. The model is then trained on simulated $t\bar{t}$ events. The signal events are those containing jets originating from a b quark and the background events contain jets initiated by c or light quarks. In the case of `MV2c10`, the background is 7% c quarks and 93% light flavour quarks. Other variations of the algorithm exist with different c-to-light flavour fractions. Four working points are defined for the algorithm with differing b-jet selection efficiencies. The working points are 60%, 70%, 77% and 80%. The working point used in the following analyses is 77%, which corresponds to a rejection factor of around 12 for c-jets and 380 for light jets. The distribution of the `MV2c10` discriminant can be seen in Figure 4.5.

Other techniques exist to tag heavy flavour quarks, one of which is a soft muon tagger (SMT) that makes use of semileptonic decays of B hadrons into muons. This tagger is used in the analyses presented in this thesis and is discussed in more detail in Section 5.4.1.

4.2.6 Missing energy

In pp or $p\bar{p}$ colliders where composite particles are collided, it is not possible to know the momentum fraction carried by a given parton. Assuming a head on collision, it is therefore not possible to know the momentum in the z-direction. However, using this assumption, it can be assumed that the total p_{T} of the event should be zero. Events where this is appears not the case can be attributed to the presence of one or more particles that have not in interacted with the detector. In $t\bar{t}$ events in the lepton+jets or dilepton channels, this *missing transverse momentum*, $\mathbf{p}_{\mathrm{T}}^{\mathrm{miss}}$, can be attributed to the neutrino(s) from the leptonic W boson decay. In other analyses it could also be interpreted as the presence of a new particle. The $\mathbf{p}_{\mathrm{T}}^{\mathrm{miss}}$ is calculated by summing the p_{T} from all physics objects present in the event plus an additional soft radiation term [100]. A more often used variable is the *missing transverse energy*, $E_{\mathrm{T}}^{\mathrm{miss}}$, which is the magnitude of $\mathbf{p}_{\mathrm{T}}^{\mathrm{miss}}$, with a direction of ϕ^{miss}.

Chapter 5

Object and event selection

The physics objects used for the event selection in the top-quark mass measurement and differential cross-section measurements are: electrons, muons, jets and b-jets. The objects are reconstructed with the process described in Section 4.2. The dataset and simulation samples used in these analyses are detailed in this chapter along with the selection for each object.

5.1 Data

This analysis is performed using 2015 and 2016 $\sqrt{s} = 13$ TeV pp collision data collected by the ATLAS detector at the LHC corresponding to an integrated luminosity of 36.1 fb^{-1}. The average number of pp interactions per bunch crossing, μ, is between 14 and 25. Data are only used if beam conditions are stable and all ATLAS subdetector systems are operational. All data are processed as described in Section 4.2.

5.2 Simulation samples

MC simulations are used to model the expected signal and background distributions using the methods described in Section 4.1. For all samples, the Pythia-8.186 event generator [81] with the MSTW2008 LO PDF set [101, 102] and the AUET2 tune [103] is used to generate additional

pp collisions that are overlaid to model the effects of in- and out-of-time pileup. The additional collisions are superimposed on the signal and background events with the same luminosity profile as in the data. To improve the heavy flavour decay modelling, the EVTGEN-1.2.0 generator [104] is used for all samples except those simulated with the SHERPA generator [105].

5.2.1 $t\bar{t}$ simulation

The nominal $t\bar{t}$ sample is generated using *hvq* generator [106] in the POWHEG-BOX V2 generator [107–109] and the NNPDF3.0 parton distribution function (PDF) set [110] and $m_t = 172.5$ GeV. The *hvq* program uses on-shell matrix elements for next-to-leading order (NLO) production of $t\bar{t}$ pairs. The off-shell effects and top-quark decays are modelled using MADSPIN [111]. For the parton shower and hadronisation, PYTHIA8.2 [112] is used with a custom A14-r_b version of the ATLAS A14 tune [113]. The motivation and derivation of this custom tuning is detailed in Section 6.1.1. The radiation in top-quark decays is handled by the parton-shower generator, which implements matrix-element corrections at an effective NLO level. The parameter h_{damp}, which controls the high-p_{T} radiation emission, is set to twice the top quark mass of each sample. The $t\bar{t}$ sample is normalised to the TOP++2.0 [114] theoretical cross-section of 823^{+46}_{-51} pb. This cross-section is calculated at NNLO in QCD and including resummation of next-to-next-to-leading logarithmic (NNLL) soft gluon terms [115–119].

5.2.2 Background simulation

The main background processes in the analysis are from single-top quark production and from W or Z boson production in association with jets (W/Z +jets). A small contribution arises from diboson (WW, WZ or ZZ) production. Events not containing a real prompt lepton can be included in the sample through the misidentification of a jet or photon as an electron or from non-prompt electrons or muons passing the prompt lepton isolation requirements. This is referred to as "multijet" background.

The W/Z +jets and diboson samples are simulated using the SHERPA generator. In the W/Z +jets samples the matrix element is calculated for up to two loops at NLO and up to four

loops at LO using the COMIX [120] and OpenLoops generators [121]. The ME+PS@NLO prescription [122] is used to merge with the Sherpa parton shower. The CT10 PDF set is used in conjunction with dedicated parton shower tuning developed by the Sherpa authors. The normalisation for the W+jets sample along with the relative fractions of W boson production in association with heavy flavour quarks is estimated from data by exploiting the intrinsic W charge-asymmetry of W boson production [123]. The normalisation for the Z+jets is extracted from the MC only however it is cross checked in data with a control region. The diboson samples are generated in the same manner but with up to one (for ZZ) or zero (WW and WZ) additional partons at NLO and up to three additional partons at LO. They are normalised to their respective NLO cross-section calculated by the generator used to simulate the diboson events.

Samples of the Wt and s-channel single top quark events are generated with the Powheg-Box V1 and V2 respectively, using the CT10 PDF set. The diagram removal prescription [124] is used to remove the overlap between the $t\bar{t}$ and Wt final states. Electroweak t-channel single top quark events are generated using the Powheg-Box V1 generator, which uses the four-flavour scheme for the NLO matrix elements calculations together with the fixed four-flavour PDF set CT10f4. For this process, the top quarks are decayed using MADSPIN [125], preserving all spin correlations. All single-top quark samples are interfaced to Pythia 6.428 [126] with the Perugia 2012 [127] underlying-event tune. The EvtGen v1.2.0 program is used to model properties of the bottom and charm hadron decays. The single-top quark t- and s-channel samples are normalised to the approximate NNLO theoretical cross sections [128–130].

Finally the multijet background is estimated from data using the matrix method [131]. This is discussed in further detail in Section 6.2.2.

A full list of the signal and alternative samples can be found in Table 5.1,the alternative mass and background samples in Table 5.2 and the various signal samples for the differential cross-section analysis in Table 5.3.

Table 5.1 Generator and settings used to produce the signal and alternative $t\bar{t}$ samples.

Process	Generator, parton shower and settings	Reco/truth level
Nominal $t\bar{t}$		
POWHEG+PYTHIA8 with A14-r_b tune	POWHEG+PYTHIA8, $h_{\text{damp}} = 1.5m_t$, $r_b = 1.05$	AFII
POWHEG+PYTHIA8 with standard A14 tune	POWHEG+PYTHIA8, $h_{\text{damp}} = 1.5m_t$	FullSim, AFII
$t\bar{t}$ variations		
POWHEG+HERWIG7.1.3 angular-ordered showering	POWHEG+HERWIG7.1.3, $h_{\text{damp}} = 1.5m_t$	AFII
aMC@NLO+PYTHIA8 with r_b retuned	aMC@NLO+PYTHIA8, $r_b = 1.05$	AFII
POWHEG+PYTHIA8 with aMC@NLO-like Pythia settings	POWHEG+PYTHIA8, $h_{\text{damp}} = 1.5m_t$, $r_b = 1.05$	AFII
POWHEG+PYTHIA8 ISR up variation with retuned r_b	POWHEG+PYTHIA8, $h_{\text{damp}} = 3m_t$, $\mu_R^{ME} = \mu_F^{ME} = 0.5$, $r_b = 1.05$, A14V3CUP	AFII
POWHEG+PYTHIA8 ISR down variation with retuned r_b	POWHEG+PYTHIA8, $h_{\text{damp}} = 1.5m_t$, $\mu_R^{ME} = \mu_F^{ME} = 2.0$, $r_b = 1.05$, A14V3CDO	AFII
POWHEG+PYTHIA8 colour reconnection max variation	POWHEG+PYTHIA8, $h_{\text{damp}} = 1.5m_t$, $r_b = 1.05$, CR range = 10	Truth-level
POWHEG+PYTHIA8 colour reconnection off variation	POWHEG+PYTHIA8, $h_{\text{damp}} = 1.5m_t$, $r_b = 1.05$, CR off	Truth-level
POWHEG+PYTHIA8 early resonance decay variation	POWHEG+PYTHIA8, $h_{\text{damp}} = 1.5m_t$, $r_b = 1.05$, EarlyResonanceDecays	Truth-level
POWHEG+PYTHIA8 underlying event up variation	POWHEG+PYTHIA8, A14V1UP, $h_{\text{damp}} = 1.5m_t$, $r_b = 1.05$	Truth-level
POWHEG+PYTHIA8 underlying event down variation	POWHEG+PYTHIA8, A14V1DO, $h_{\text{damp}} = 1.5m_t$, $r_b = 1.05$	Truth-level
POWHEG+PYTHIA8 r_b up variation	POWHEG+PYTHIA8, $h_{\text{damp}} = 1.5m_t$, $r_b = 1.071$	Truth-level
POWHEG+PYTHIA8 r_b down variation	POWHEG+PYTHIA8, $h_{\text{damp}} = 1.5m_t$, $r_b = 1.029$	Truth-level
POWHEG+PYTHIA8 FSR scale up variation with retuned r_b	POWHEG+PYTHIA8, $h_{\text{damp}} = 1.5m_t$, $\mu_R^{PS} = \mu_F^{PS} = \sqrt{2}$, $r_b = 1.0356$	AFII
POWHEG+PYTHIA8 FSR Scale down variation with retuned r_b	POWHEG+PYTHIA8, $h_{\text{damp}} = 1.5m_t$, $\mu_R^{PS} = \mu_F^{PS} = 1/\sqrt{2}$, $r_b = 1.0802$	AFII

Table 5.2 Generator and settings used to produce the alternative $t\bar{t}$ mass samples and background samples.

Process	Generator, parton shower and settings	Reco/truth level
$t\bar{t}$ mass variations		
POWHEG+PYTHIA8($m_t = 165.0$ GeV) with A14-r_b tune	POWHEG+PYTHIA8, $h_{\text{damp}} = 1.5m_t$, $r_b = 1.05$	Truth-level
POWHEG+PYTHIA8($m_t = 169.0$ GeV) with A14-r_b tune	POWHEG+PYTHIA8, $h_{\text{damp}} = 1.5m_t$, $r_b = 1.05$	Truth-level
POWHEG+PYTHIA8($m_t = 170.5$ GeV) with A14-r_b tune	POWHEG+PYTHIA8, $h_{\text{damp}} = 1.5m_t$, $r_b = 1.05$	Truth-level
POWHEG+PYTHIA8($m_t = 171.0$ GeV) with A14-r_b tune	POWHEG+PYTHIA8, $h_{\text{damp}} = 1.5m_t$, $r_b = 1.05$	Truth-level
POWHEG+PYTHIA8($m_t = 171.5$ GeV) with A14-r_b tune	POWHEG+PYTHIA8, $h_{\text{damp}} = 1.5m_t$, $r_b = 1.05$	Truth-level
POWHEG+PYTHIA8($m_t = 172.0$ GeV) with A14-r_b tune	POWHEG+PYTHIA8, $h_{\text{damp}} = 1.5m_t$, $r_b = 1.05$	Truth-level
POWHEG+PYTHIA8($m_t = 173.0$ GeV) with A14-r_b tune	POWHEG+PYTHIA8, $h_{\text{damp}} = 1.5m_t$, $r_b = 1.05$	Truth-level
POWHEG+PYTHIA8($m_t = 173.5$ GeV) with A14-r_b tune	POWHEG+PYTHIA8, $h_{\text{damp}} = 1.5m_t$, $r_b = 1.05$	Truth-level
POWHEG+PYTHIA8($m_t = 174.0$ GeV) with A14-r_b tune	POWHEG+PYTHIA8, $h_{\text{damp}} = 1.5m_t$, $r_b = 1.05$	Truth-level
POWHEG+PYTHIA8($m_t = 174.5$ GeV) with A14-r_b tune	POWHEG+PYTHIA8, $h_{\text{damp}} = 1.5m_t$, $r_b = 1.05$	AFII
POWHEG+PYTHIA8($m_t = 176.0$ GeV) with A14-r_b tune	POWHEG+PYTHIA8, $h_{\text{damp}} = 1.5m_t$, $r_b = 1.05$	Truth-level
POWHEG+PYTHIA8($m_t = 180.0$ GeV) with A14-r_b tune	POWHEG+PYTHIA8, $h_{\text{damp}} = 1.5m_t$, $r_b = 1.05$	Truth-level
$t\bar{t}$ dilepton		
POWHEG+PYTHIA8 with standard A14 tune	POWHEG+PYTHIA8, $h_{\text{damp}} = 1.5m_t$	FullSim, AFII dilepton
POWHEG+HERWIG7.0.4	POWHEG+HERWIG7.0.4, $h_{\text{damp}} = 1.5m_t$	AFII dilepton
aMC@NLO+PYTHIA8	aMC@NLO+PYTHIA8	AFII dilepton
Background samples		
single top t-channel	POWHEG+PYTHIA6	FullSim
single top s-channel	POWHEG+PYTHIA6	FullSim
single top Wt channel	POWHEG+PYTHIA6	FullSim
W+jets	SHERPA 2.2.1	FullSim
Z+jets	SHERPA 2.2.1	FullSim
Diboson WW, WZ, ZZ	SHERPA	FullSim

Table 5.3 Generator and settings used to produce the alternative $t\bar{t}$ signal samples used in the differential analysis.

Process	Generator, parton shower and settings	Reco/truth level
$t\bar{t}$ mass variations		
POWHEG+HERWIG7.1.3 dipole shower	POWHEG+HERWIG7.1.3, $h_{\text{damp}} = 1.5m_t$	Truth-level
POWHEG+PYTHIA8 with $r_b = 1.000$	POWHEG+PYTHIA8, $h_{\text{damp}} = 1.5m_t$, $r_b = 1.000$	Truth-level
POWHEG+PYTHIA8 with$r_b = 1.100$	POWHEG+PYTHIA8, $h_{\text{damp}} = 1.5m_t$, $r_b = 1.100$	Truth-level
POWHEG+PYTHIA8 FSR scale up variation	POWHEG+PYTHIA8, $h_{\text{damp}} = 1.5m_t$, $\mu_R^{PS} = \mu_F^{PS} = \sqrt{2}$	Truth-level
POWHEG+PYTHIA8 FSR scale down variation	POWHEG+PYTHIA8, $h_{\text{damp}} = 1.5m_t$, $\mu_R^{PS} = \mu_F^{PS} = 1/\sqrt{2}$	Truth-level
POWHEG+PYTHIA8 ISR up variation	POWHEG+PYTHIA8, $h_{\text{damp}} = 3m_t$, $\mu_R^{ME} = \mu_F^{ME} = 0.5$, A14V3CUP	AFII
POWHEG+PYTHIA8 ISR down variation	POWHEG+PYTHIA8, $h_{\text{damp}} = 1.5m_t$, $\mu_R^{ME} = \mu_F^{ME} = 2.0$, A14V3CDO	AFII
POWHEG+PYTHIA8 with Monash tuning	POWHEG+PYTHIA8, $h_{\text{damp}} = 1.5m_t$	AFII
POWHEG+PYTHIA8 with Monash tuning and Peterson fragmentation	POWHEG+PYTHIA8, $h_{\text{damp}} = 1.5m_t$	AFII

5.3 Electrons

Electrons are reconstructed as described in Section 4.2.2. Candidates in the calorimetry transition regions $1.37 < |\eta_{\text{cluster}}| < 1.52$ are excluded and only electrons with $|\eta_{\text{cluster}}| < 2.47$ are used. Electron candidates are required to pass the *tight* likelihood identification requirement. The following criteria are applied to the transverse and longitudinal impact parameters: $|z_0 \sin\theta| < 0.5$ mm and $|\frac{d_0}{\sigma d_0}| < 5$. All electrons must have $p_{\text{T}} > 25$ GeV. To reduce the background from non-prompt electrons, candidates must pass the *gradient* isolation working point.

5.4 Muons

Muons are reconstructed as described in Section 4.2.3 and are required to have $p_{\text{T}} > 4$ GeV and $|\eta| < 2.5$. Different requirements are applied in order to distinguish between muons from the leptonic decay of the W-boson (referred to as 'prompt' muons) and those from the semileptonic decay of b-hadrons (referred to as 'soft' or SMT-muons).

Prompt muon candidates are required to have $p_{\text{T}} > 25$ GeV and to satisfy the *medium* quality requirement. The transverse and longitudinal impact parameters are required to meet $|z_0 \sin\theta| < 0.5$ mm and $|\frac{d_0}{\sigma d_0}| < 3$. The muon candidates must also be isolated from jet activity by requiring the *gradient* isolation working point and to be within $\Delta R > 0.4$ of the nearest selected jet. However, if this jet has fewer than three associated tracks, the muon is kept and the jet is removed to avoid losing high energy muons that undergo significant energy loss in the calorimeters.

5.4.1 Soft muon tagger (SMT)

Muons with $p_{\text{T}} > 4$ GeV that do not pass the prompt muon selection are selected as soft muon candidates. In order to be tagged as soft muons, the muons are required to pass the *tight* quality requirement and to be $\Delta R < 0.4$ within a selected jet. Very loose requirements are

applied to the impact parameters, $d_0 < 3$ mm and $|z_0 \sin\theta| < 3$ mm in order to reject edge cases. If more than one muon passes the criteria for a given selected jet, the soft muon with the highest p_{T} is chosen. The closest jet to a soft muon is defined as "SMT-tagged" and therefore there can only be one "SMT-tagged" jet per event.

5.5 Jets

After the reconstruction and calibration detailed in Section 4.2.4, jet candidates are required to have $p_{\mathrm{T}} > 25$ GeV and $|\eta| < 2.5$. Quality criteria are imposed to identify jets arising from non-collision sources or detector noise and any event containing at least one such jet is removed. To avoid selecting jets from secondary pp interactions, an additional requirement on the JVT is made for low p_{T} ($p_{\mathrm{T}} < 60$ GeV) jets in the central ($|\eta| < 2.4$) region of the detector. During jet reconstruction, no distinction is made between electron candidates and energy deposits therefore, if any jets lie within $\Delta R < 0.2$ of a selected electron, the single closest jet is removed in order to avoid double counting. Following this, any electrons within $\Delta R < 0.4$ of a jet are removed.

5.6 *b*-tagging

Jets are identified as originating from a b-quark using the multivariate algorithm described in Section 4.2.5. The mv2c10 tagger with a 77% efficiency working point is used for the analysis. In addition to the multivariate b-tagger, the soft muon tagger is also used to tag jets originating from b-quarks. Events are required to have jets tagged by both the multivariate tagger and the soft muon tagger.

5.7 Particle level objects

For some cross check studies and crucially for the alternative top-quark mass samples, particle level samples are used. Particle level is defined as the collection of stable particles (mean

lifetime $> 3 \times 10^{-11}$s) from the matrix element and parton shower generators without any simulation of the particle interactions with the detector. Due to the time required to simulate samples with detector reconstruction, particle samples are used for the alternative $t\bar{t}$ mass samples. In order to make the same selection at particle level as at reconstructed level, the analogous particle objects are required. In Section 6.3, a method to reweight particle level samples to reconstructed level is discussed for use with $t\bar{t}$ mass variation samples.

5.8 Event selection

The event selection is seeded by the lowest un-prescaled (where prescaled trigger means only a given fraction of the events passing the trigger are saved) single electron and single-muon triggers. The single lepton triggers identify events where there is at least one single lepton present. For the simulated samples, a pseudo run-number is randomly assigned to each event. The pseudo run-numbers are sampled from the run numbers of the 65 runs in the 2015 and 150 runs of the 2016 data sets. The pseudo-run numbers will ensure the simulated samples have the same integrated luminosity as the corresponding real data run. Simulated events with a pseudo run-number corresponding to the 2015 (2016) data set are required to satisfy the same trigger requirements as the real data events of the 2015 (2016) data set. In addition, events are required to contain at least one reconstructed vertex with at least two tracks of $p_{\mathrm{T}} > 0.4$ GeV and to be consistent with the beam-collision region in the $x - y$ plane. If multiple vertices are reconstructed, the vertex with the largest $\sum p_{\mathrm{T}}^2$ of its associated tracks is taken as the primary vertex.

Events are selected based on the following requirements:

- Pass the lowest un-prescaled single-lepton, where a lepton is either an electron or muon, trigger;
- Has exactly one *prompt* isolated lepton with $p_{\mathrm{T}} > 27$ GeV that is matched to the corresponding trigger;

- No additional prompt leptons with $p_{\mathrm{T}} > 25$ GeV in order to reject events that are from the dilepton decay channel of the $t\bar{t}$ system;
- $E_{\mathrm{T}}^{\mathrm{miss}} > 30$ GeV and $E_{\mathrm{T}}^{\mathrm{miss}} + m_{\mathrm{T}}(W) > 60$ GeV. $m_{\mathrm{T}}(W) = \sqrt{2p_{\mathrm{T}}^{\ell}E_{\mathrm{T}}^{\mathrm{miss}}(1-\cos\Delta\phi)}$, where p_{T}^{ℓ} is the transverse momentum of the lepton and $\Delta\phi$ is the azimuthal angle between the lepton and the direction of the missing transverse momentum. These criteria help reduce the multijet and W+jets backgrounds (discussed in Section 5.2.2);
- At least one soft muon is required to have $p_{\mathrm{T}} > 8$ GeV and $|\eta| < 2.5$ in order to suppress fake soft muons. The highest p_{T} soft muon is chosen and matched to a jet that is referred to as the SMT-jet;
- The SMT-jet is required to have $p_{\mathrm{T}} > 25$ GeV and $|\eta| < 2.5$. A further jet energy calibration is applied to SMT-jets and is discussed in Section 6.1.3;
- The four leading jets in the event (excluding the SMT jet if this is one of the four) are required to have $p_{\mathrm{T}} > 30$ GeV and $|\eta| < 2.5$. The higher p_{T} cut on the non-SMT tagged jet reduces the non-$t\bar{t}$ background and uncertainty from the JES;
- At least one jet b-tagged by the MV2C10 algorithm and one by the SMT (could be the same jet);
- Finally, the invariant mass of the soft muon and the prompt lepton, $m_{\ell\mu}$, is required to be between 15 and 80 GeV.

  The soft muon and the prompt lepton are required to be separated by $\Delta R < 2$ to help increase the fraction of events in which the soft muon and prompt lepton originate from the decay of the same top quark;
- Two orthogonal signal regions are defined based on the charge of the soft muon and prompt lepton. The opposite sign (OS) region requires the soft muon and prompt lepton to have opposite electric charge while the same sign region (SS) requires them to have the same electric charge. The OS region is enriched in muons originating from $b \to \mu$

whereas the SS is enriched with muons from $b \to c \to \mu$. Although the SS region is less sensitive to m_t, using the combination of both regions improves the result.

Chapter 6

Simulation modelling

The following chapter details the modelling of the signal and background processes used in both the top-quark mass measurement and differential cross-section measurement.

6.1 Signal modelling

Due to the intended precision of the measurement, using the MC simulation with the default settings is not good enough. Several aspects of the $t\bar{t}$ signal samples are optimised for the analysis and are detailed in this section.

6.1.1 Modelling of *b*-quark fragmentation

Correct modelling of the momentum transfer between the b-quark and the b-hadron is imperative to this analysis. The MC event generators, such as Pythia, Herwig and Sherpa generators, describe the transition from quark to hadron using phenomenological models. As discussed in Section 4.1.1, the two models used are the string and cluster models, with each containing a number of parameters that are tuned to data. Pythia8 allows for the use of several different parameterisations for the b-quark fragmentation function, whereas Herwig and Sherpa use non-parametric models, which handle the complete parton shower evolution. The free parameters in these models are normally fit to measurements from e^+e^- collider experiments. For this

analysis it is assumed that b-quark fragmentation properties at a given energy scale are the same in e^+e^- and hadron collisions.

In Pythia8 the Lund-Bowler parameterisation [132, 133] for b-quark fragmentation is used and is given by

$$f(z) = \frac{1}{z^{(1+br_b m_b^2)}}(1-z)^a \exp(-bm_{\mathrm{T}}^2/z), \tag{6.1}$$

where a, b and r_b are the function parameters, m_b is the b-quark mass, m_{T} is the b-hadron transverse mass and z is the fraction of the longitudinal energy of the b-hadron with respect to the b-quark, in the light cone reference frame

$$z = \frac{(E+p_{||})_B}{(E+p)_b}. \tag{6.2}$$

Here, $p_{||}$ is the hadron momentum in the direction of the b-quark and $(E+p)_b$ is the sum of the energy and momentum of the b-quark before hadronisation takes place. The fragmentation function is defined at the hadronisation scale and is evolved by the parton shower to the process scale through the DGLAP evolution equations.

In the Monash [134] Pythia8 tune, the a and b parameters have been fitted to data that is sensitive to light quark fragmentation and are assumed to be universal between light and heavy quarks. The parameter r_b, however, is specific to b-quark fragmentation and controls the position of the peak of the distribution represented by Equation 6.1. In the Monash tune, the b-quark fragmentation is tuned to SLD measurements, which fit a value of $r_b = 0.855$.

The default tuning for ATLAS is the A14 tune, which is based on the Monash tune and inherits the fragmentation and hadronisation parameters. To improve the modelling of the b-quark fragmentation in the A14 tune, a fit of the r_b parameter is performed using e^+e^- collision data from ALEPH, DELPHI and OPAL at the LEP collider and from the SLD experiment at the SLC collider [135–138]. The x_B distribution is defined at LEP as

$$x_B = \frac{2p_B \cdot p_Z}{m_Z^2}, \tag{6.3}$$

where p_B and p_Z are the four-momenta of the b hadron and Z boson, respectively. Using $Z \to b\bar{b}$ events, the x_B distribution is fitted to extract the value of r_b. Here, x_B is used instead of z because it is built from experimentally measurable quantities. At the LHC, x_B takes a different form

$$x_B = \frac{1}{1 - m_W^2/m_t^2 + m_b^2/m_t^2} \cdot \frac{2p_B \cdot p_t}{m_t^2}. \tag{6.4}$$

The tuning is performed using Professor v2.2 [139] for the minimisation and Rivet v2.5.4 [140] for the implementation of the measurements. The resulting fitted value is $r_b = 1.05 \pm 0.021$. This setting is referred to as A14-r_b and is applied to all MC samples produced with Pythia8 for the simulation of the parton shower.

6.1.2 Modelling of *b*- and *c*-hadron production and decay

In addition to understanding the momentum transfer from the b quark to the b and c hadrons, the production and decay rates of these hadrons must be accurately modelled. In Pythia, the decay rates of the b and c hadrons is modelled by EvtGen. While EvtGen offers an improved modelling over the default Pythia settings, the production fractions and decay rates may not be up-to-date. In order to ensure the correct production fraction and decay rates are used, both are rescaled to the values as reported by the PDG [7].

6.1.2.1 *b* and *c*-hadron production fractions

The production fractions of the weakly decaying b and c hadrons are rescaled to the values shown in Table 6.1. These values are produced by the Heavy Flavour Averaging Group (HFLAV) [141] based on measurements from DELPHI [138], CDF [142–145], LHCb [146–148] and ATLAS [149] experiments. The direct rate measurements from the aforementioned experiments are combined with the world average of the time-integrated mixing probability averaged over an unbiased sample of semileptonic b-hadron decays. The combination assumes the production fractions are independent of the centre-of-mass energy of the events. A scale factor is applied to each b

Table 6.1 The production fraction values for b hadrons and c hadrons in the PDG and POWHEG+PYTHIA8. The relative scale factors applied to POWHEG+PYTHIA8 are also shown. The values under the PDG column are derived from Ref. [7] and [150]. The same scale factors are applied to the charge-conjugate hadrons.

Hadron	PDG (%)	POWHEG+PYTHIA8	Scale Factor
B^0	0.404±0.006	0.429	0.941±0.014
B^+	0.404±0.006	0.429	0.942±0.014
B_s^0	0.103±0.005	0.095	1.088±0.052
b-baryon	0.088±0.012	0.047	1.874±0.255
D^+	0.226±0.008	0.290	0.780±0.027
D^0	0.564±0.015	0.553	1.020±0.027
D_s^0	0.080±0.005	0.093	0.857±0.054
c-baryon	0.109±0.009	0.038	2.898±0.237

hadron in a simulated event, with the overall weight given by the product of all b-hadron scale factors in the event. The production fractions in all POWHEG+PYTHIA8 samples are measured to be the same allowing the same scale factors to be applied in all samples.

6.1.2.2 b and c-hadron to μ branching ratios

The branching ratios of b and c hadron decays that contain a μ are rescaled to values from the PDG [7], shown in Table 6.2. The $b \to \mu$ branching ratio was determined from DELPHI [151], L3 [152, 153] and OPAL [154] data, with the final predicted values calculated by the Electroweak Heavy Flavour Working Group [155]. The scale factors for the branching fractions of the semileptonic decays of c-hadrons are only applied to semileptonic c-hadron decays when the c-hadron does not come from the cascade decay of a b-hadron.

Table 6.2 Hadron to μ branching ratios in the PDG and POWHEG+PYTHIA8. The relative scale factors applied to POWHEG+PYTHIA8 are also shown. The values under the PDG column are derived from Ref. [7] and [150].

Hadron	PDG	POWHEG+PYTHIA8	Scale Factor
$b \to \mu$	$0.1095^{+0.0029}_{-0.0025}$	0.106	$1.032^{+0.0027}_{-0.0023}$
$b \to \tau$	0.0042 ± 0.0004	0.0064	0.661±0.062
$b \to c \to \mu$	0.0802 ± 0.0019	0.085	0.946±0.022
$b \to \bar{c} \to \mu$	0.016 ± 0.003	0.018	0.888±0.167
$c \to \mu$	0.082 ± 0.005	0.084	0.976±0.059

6.1.3 SMT-jet calibration

The p_{T} spectrum of SMT-jets shows a slight miscalibration as can be seen in Figure 6.1a. This miscalibration is likely due to a missing correction factor in the overall JES calibration sequence for jets containing semileptonic decays. Jets that contain semileptonic decays will contain undetectable neutrinos and muons that are not included in the clustering and are therefore likely to have a different response. To improve the modelling of the SMT-jets, a dedicated SMT jet calibration factor is derived.

The observable used is the ratio between the p_{T} of SMT-jet and the average p_{T} of the non-SMT tagged jets (referred to as the p_{T}-ratio in this section) in the event. Figure 6.1b shows the p_{T} of the leading jet and a clear trend in the data/MC ratio can be seen. This is due to mismodelling of the top-quark p_{T}, discussed further in Section 9.5, rather than the SMT-jet miscalibration. The ratio of the SMT-jet p_{T} and the average p_{T} of the non-SMT tagged jets is used to remove the effect of the top quark p_{T} mismodelling from the calibration factor. A similar selection to the OS region of the main analysis is used; however, instead of at least four jets in the event, exactly four jets are required. This requirement removes any dependence on mismodelling of jet multiplicity in the event.

To derive the correction factor, a binned-template likelihood fit is performed on the p_{T}-ratio distribution. The technique used is similar to that used in the mass extraction in Chapter 9,

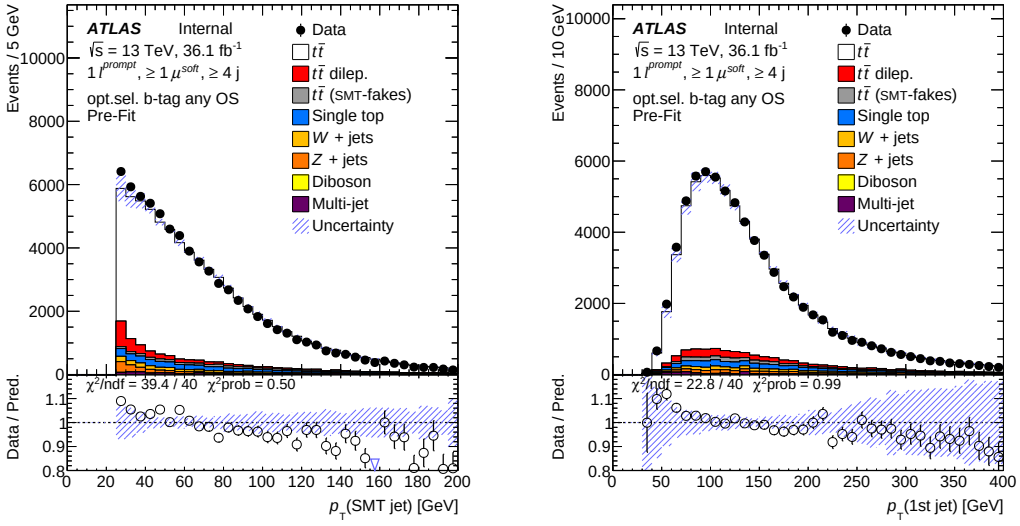

(a) SMT-jet p_{T}. **(b)** Leading jet p_{T}.

Figure 6.1 Comparison between data and MC for SMT-jet p_{T} (a) and leading jet p_{T} (b) with the nominal event selection applied. The uncertainty bands include the statistical and systematic uncertainties.

where more details can be found. First, templates of the p_{T}-ratio distribution are generated with different SMT-jet calibration values and a morphing technique is used to interpolate between the templates with a piece-wise function built bin-by-bin. Then these templates are used as input to the binned likelihood fit where the parameter $k_{\text{SMT-jet}}$,the SMT jet scaling factor, is free in the fit.

The systematic uncertainties are evaluated by repeating the fit on the histograms produced with each systematic variation applied to simulated events and comparing with the result obtained on a fit to the nominal histogram. The result of the fit gives a value of $k_{\text{SMT-jet}} = 0.967 \pm 0.005 \pm 0.021$, where the first uncertainty is statistical and the second is the systematic uncertainty. The pre and post-fit plots can be seen in Figure 6.2 and an explanation of these uncertainties can be found in Chapter 8. A breakdown of the systematic uncertainties can be seen in Table 6.3. The scale factor derived is close to unity. The calibration factor is applied to all $t\bar{t}$ signal samples.

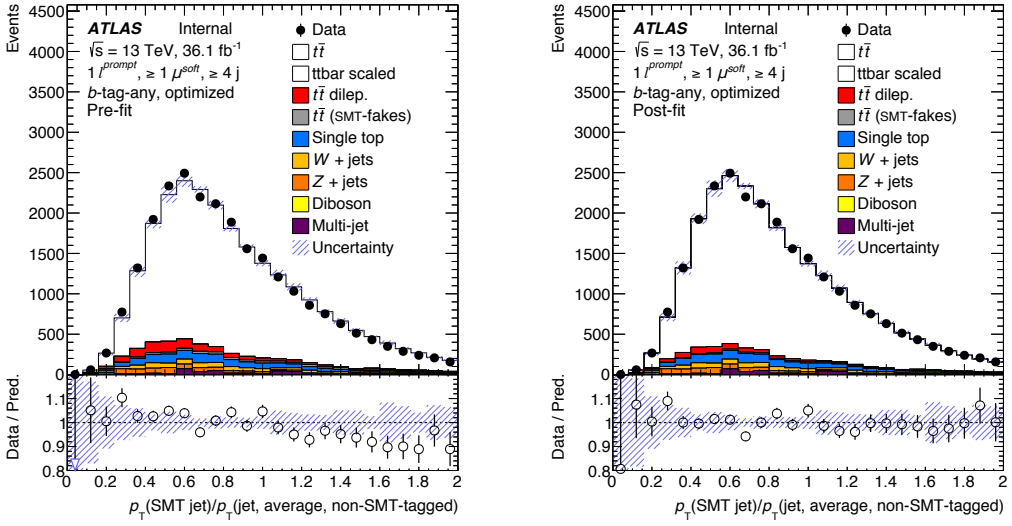

(a) Pre-fit plot. **(b)** Post-fit plot.

Figure 6.2 Pre and post-fit plots for the SMT jet calibration derivation.

6.1.3.1 $k_{\text{SMT-jet}}$ dependence on m_t

To verify $k_{\text{SMT-jet}}$ is not dependent on m_t, the nominal signal sample is replaced by a sample with $m_t = 174.5$ GeV and the fit is repeated. The result of the fit is $k^{174.5}_{\text{SMT-jet}} = 0.963 \pm 0.005$, where the quoted uncertainty is statistical only. The result is compatible with the nominal fit and therefore it is assumed there is no dependence on m_t.

6.1.3.2 Fit stability in SS region

The nominal fit setup for the mass extraction uses a combined binned profile likelihood fit performed on the $m_{\ell\mu}$ distribution in two orthogonal regions, OS and SS. The OS region is used to derive the nominal $k_{\text{SMT-jet}}$ scale. To check the fit is also behaving correctly in the SS region, the fit is also performed on the p_{T}-ratio distribution in the SS region. The result of the fit is $k^{\text{SS}}_{\text{SMT-jet}} = 0.974 \pm 0.008$, where the quoted uncertainty is statistical only. The result is compatible with that performed in the OS region.

Table 6.3 Breakdown of the systematic uncertainties of the $k_{\text{SMT-jet}}$ scale factor fit.

Source	Shift (±)
Statistical error on fit	0.0053
MC statistical error	0.0013
Statistical error on fakes	0.0016
b-tag component b 0	0.0052
JER	0.0018
JES (BJES response)	0.0038
JES (pileup ρ topology)	0.0010
Pileup	0.0020
$t\bar{t}$ BR $b \to c$ WS	0.0033
$t\bar{t}$ FSR	0.0010
$t\bar{t}$ Parton shower and hadronisation	0.0024
$t\bar{t}$ MC event generator	0.0209
$t\bar{t}$ Colour reconnection	0.0023
$t\bar{t}$ Underlying event	0.0025
Total Systematic	0.0231
Total Stat+Syst	0.0237

6.2 Background modelling

For most background samples in this analysis, the MC simulation is satisfactory. However, for W+jets and multijet backgrounds this is not the case and a data-driven method is therefore required. W+jets events will pass the $t\bar{t}$ selection when the W-boson decays leptonically in association with at least one b-quark initiated jet, as well as several other light flavour jets. The W+jets background is estimated using MC samples with a data-driven scale factor for the normalisation using the charge asymmetry method [123]. For the multijet background, the $t\bar{t}$ selection can be passed if a fake or non-prompt lepton is produced in a association with at least one b-quark initiated jet and several other light flavour jets. The multijet background is estimated using a fully data-driven approach.

6.2.1 W+jets background measurement

The data-driven approach for the W+jets measurement consists of a measurement of the overall W+jets normalisation and a measurement of the relative contributions of $W+cc$, $W+bb$, $W+c$ and W+light subcomponents. There are three steps to the measurement:

1. Estimation of the W+jets normalisation using the charge asymmetry method in a $N_{\text{jet}} = 2$ (pre-tag) sample of data. A scale factor C_A is calculated.

2. The scale factor, C_A, is applied to the W+jets MC sample and the flavour composition is measured in a $N_{\text{jet}} = 2$, $N_{\text{b-jet}} >= 1$ (tagged) sample of data. A correction factor $K_{i \in F}$ is calculated per flavour fraction (F).

3. The correction factors, K_i, are applied to pre-tag data and (2) and (3) are repeated until C_A and K_i are stable.

The measurement of the W+jets normalisation uses the charge asymmetry method. which exploits the charge-asymmetric nature of W+jets production at the LHC. This charge asymmetry is due to the the PDF of the proton and the pp initial state. In protons the mean of the $u(x)$ distribution is larger than that of the $d(x)$ therefore the production of W^+ is favoured over

W^- at the LHC. This asymmetry leads to an excess of positively charged leptons in W+jets events. The ratio $r = \frac{\sigma(pp\to W^+)}{\sigma(pp\to W^-)}$ is theoretically well understood and can be estimated in MC accurately. In contrast to W+jets, most other backgrounds in this analysis will symmetrically produce positively and negatively charged leptons[1]. There is a small asymmetry in diboson events; however, this has a negligible impact on the normalisation estimation. Using these assumptions the following equation can be defined

$$N_{W^+} + N_{W^-} = \frac{\left(N^{\mathrm{MC}}_{W^+} + N^{\mathrm{MC}}_{W^-}\right)}{\left(N^{\mathrm{MC}}_{W^+} - N^{\mathrm{MC}}_{W^-}\right)}(D^+ - D^-) = \left(\frac{r_{\mathrm{MC}}+1}{r_{\mathrm{MC}}+-1}\right)(D^+ - D^-), \tag{6.5}$$

where D^+ and D^- are the number of events in the data sample with a positive or negative high-p_{T} lepton and $N^{\mathrm{MC}}_{W^\pm}$ are the number of events in the MC sample with a $W^\pm$. The single-top contribution is estimated in MC and subtracted from the data. The normalisation scale, C_A, can then be expressed as

$$C_A = \frac{\left(\frac{r_{\mathrm{MC}}+1}{r_{\mathrm{MC}}+-1}\right)(D^+ - D^-)}{\left(N^{\mathrm{MC}}_{W^+} + N^{\mathrm{MC}}_{W^-}\right)}. \tag{6.6}$$

The flavour composition of W+jets events is broken down into four categories: W+cc, W+bb, W+c and W+light. A set of scaling factors, $K_{i\in F}$, are determined for the flavour fractions using a $N_{\text{jet}} = 2$, $N_{\text{b-jet}} \geq 1$ region. The flavour fractions, $f_{i\in F}$, are determined from MC simulation and are fixed at those values. Using the constraint that the flavour fractions sum to unity along with the total number of positively and negatively charged data events, a system of three equations can be used to fit the data for the correction factors K_i

$$\begin{bmatrix} C_A \cdot \left(N^{bb}_{MC,W^-} + N^{cc}_{MC,W^-}\right) & C_A \cdot N^{c}_{MC,W^-} & C_A \cdot N^{lf}_{MC,W^-} \\ (f_{bb} + f_{cc}) & f_c & f_{\mathrm{lf}} \\ C_A \cdot \left(N^{bb}_{MC,W^+} + N^{cc}_{MC,W^+}\right) & C_A \cdot N^{c}_{MC,W^+} & C_A \cdot N^{lf}_{MC,W^+} \end{bmatrix} \cdot \begin{bmatrix} K_{bb,cc} \\ K_c \\ K_{\mathrm{lf}} \end{bmatrix} = \begin{bmatrix} D_{W^-} \\ 1.0 \\ D_{W^+} \end{bmatrix} \tag{6.7}$$

[1] Single-top production via s or t channel is an exception.

where $D_{W^{\pm}}$ is the total number of positively or negatively charged data events with all events not coming from MC simulation of W+jets and multijet background events subtracted. In order to solve the equation for the four correction factors K_i using only three equations, the scaling factors for K_{bb} and K_{cc} are set equal to each other. The scale factors can be extracted by inverting the matrix.

The derived normalisation factor for the W+jets background sample is $C_A = 1.119 \pm 0.158$. The corresponding flavour fraction correction factors are $K_{bbcc} = 0.982 \pm 0.349$, $K_c = 1.041 \pm 0.349$ and $K_{\mathrm{lf}} = 0.992 \pm 0.085$, where the quoted uncertainty includes both statistical and systematic effects. The systematic uncertainties evaluated are the same as those detailed in Chapter 8. The three correction factors are all close to unity.

6.2.2 Multijet background estimation

The multijet background comprises events containing a non-prompt or "fake" lepton, which mimics the signal from a real prompt isolated lepton. Generally fake leptons arise from a QCD jet or photon being reconstructed as an isolated lepton. To fake an electron, a track in the ID is required in addition to an energy deposit in the ECAL. A QCD jet may contain a charged meson which leaves a track in addition to a π_0, which will decay to photons and therefore produce an energy deposit in the ECAL. Producing a fake muon is more difficult because a larger energy jet is required to deposit energy in the MS and therefore fake leptons are more likely to be electrons. Non-prompt leptons occur from the semileptonic decay of heavy-quark hadrons or from the decay in flight of a pion or kaon. Simulation of the multijet background is not accurate enough. Simulating fake leptons requires a precise knowledge of the detector geometry and is dependent on the materials present in the detector. Therefore, it is much more difficult to simulate than, for example, the W+jets background, which is only dependent on the physics process. A data-driven method known as the matrix method [131] is therefore used to estimate the multijet background.

6.2.2.1 The matrix method

The method makes use of a data region enriched in fake[2] leptons by relaxing the lepton isolation requirement. Events passing this requirement are defined as *loose*. Conversely, events passing the standard requirement are defined as *tight*.

The total selection, S, can be constructed from events exclusively passing the tight selection, T, and those passing only the loose selection, L. The sample could also be split into events with a real lepton, R, or a fake lepton F. Using these definitions the following equation must hold

$$S = L + T = F + R. \tag{6.8}$$

Using Equation 6.8, the following equation for the number of tight and loose events can be found

$$\begin{bmatrix} D_T \\ D_L \end{bmatrix} = \begin{bmatrix} \varepsilon_r & \varepsilon_f \\ \overline{\varepsilon_r} & \overline{\varepsilon_f} \end{bmatrix} \cdot \begin{bmatrix} n_R \\ n_F \end{bmatrix}. \tag{6.9}$$

The observed number of tight and loose events in data, D_T and D_L, can be related to the unknown number of events with a fake or real lepton, n_F and n_R, through two coefficients, ε_F and ε_R, known as the fake and real efficiencies. These efficiencies describe the probability that a fake (real) loose lepton passes the tight requirement. The coefficients $\overline{\varepsilon_i}$ are defined as $\overline{\varepsilon_i} = 1 - \varepsilon_i$.

To estimate the multijet background, given by the estimated number of fake events passing the tight selection $\varepsilon_f n_F$, Equation 6.9 can be inverted assuming $\varepsilon_f \neq \varepsilon_r$

$$\begin{bmatrix} n_R \\ n_F \end{bmatrix} = \frac{1}{\varepsilon_r - \varepsilon_f} \begin{bmatrix} \overline{\varepsilon_f} & -\varepsilon_f \\ -\overline{\varepsilon_r} & \varepsilon_r \end{bmatrix} \cdot \begin{bmatrix} n_T \\ n_L \end{bmatrix}. \tag{6.10}$$

[2] Fake will refer to both fake and non-prompt leptons in this section.

An estimate for the number of fake events is then given by

$$\varepsilon_f n_F = \frac{\varepsilon_f}{\varepsilon_r - \varepsilon_f}(\varepsilon_r(n_T + n_L) - n_T), \tag{6.11}$$

using the observed number of tight and loose events. The estimation of the background in a given bin is estimated with a weight per event, given by

$$w_i = \frac{\varepsilon_f}{\varepsilon_r - \varepsilon_f}(\varepsilon_r - \delta_{i\in T}), \tag{6.12}$$

where $\delta_{i\in T} = 1$ for tight events and 0 otherwise.

6.2.2.2 Estimation of real and fake efficiencies

The fake and real efficiencies are measured in data control samples that are enriched in fake or real leptons. For the fake enriched region the following selection is applied:

- exactly one lepton and one jet;
- $E_T^{\text{miss}} < 20$ GeV (e+jets channel);
- $|d_0^{\text{sig}}| > 5$ (μ+jets channel).

The efficiency is taken as the number of tight lepton events divided by the number of total events. The selection requirements in the e+jets channel will cut prompt electrons because these events will have a larger amount of E_T^{miss} than fake electrons from QCD jets. The $|d_0^{\text{sig}}| > 5$ requirement in the μ+jets channel selects events where the muon is offset from the primary vertex and is therefore more likely to be non-prompt. These will likely be muons from semileptonic decay of c or b quarks where the muon will not come from the primary vertex.

The real efficiency is measured using events that contain $Z \to \ell\ell$ and the tag and probe method. Events are selected providing they contain a pair of leptons with opposite electric charge and an invariant mass that satisfies $60 < M_{\ell\ell} < 120$ GeV. If one of the leptons passes the tight requirement, it is considered the tag and the other is the probe. The efficiency is then the number of probes that pass the tight requirement divided by the total number of probes.

6.2.2.3 Triggers

The triggers used for the tight selection are the same as used in the main analysis. The loose selection differs slightly for 2016 runs. The lowest p_{T} triggers for both electron and muons in 2016 runs (`HLT_e26_lhtight_nod0_ivarloose` and `HLT_mu26_ivarmedium`) apply an isolation and tightened ID requirements. These triggers are not suitable for the loose requirement due to the isolation requirements that would bias the sample with prompt leptons. Instead `HLT_e24_lhmedium_nod0_L1EM18VH` and `HLT_mu24` are used. These triggers are prescaled so the appropriate prescale must be applied to the weight, w_i, for events in the low-p_{T} region.

6.2.2.4 Efficiency parameterisations

The fake and real efficiencies are parameterised as a function of different observables to better model the multijet background. A set of efficiency files parameterised with the following observables are provided by the central physics group

- $p_{\mathrm{T}}(\ell)$ - prompt lepton transverse momentum;
- $\eta(\ell)$ - prompt lepton pseudorapidity;
- $p_{\mathrm{T}}(j_0)$ - leading jet transverse momentum;
- $N_{b-\mathrm{jet}}$ - number of b-tagged jets;
- $m_{\mathrm{T}}(W)$ - transverse mass of the W-boson;
- $\Delta\phi(\ell, E_{\mathrm{T}}^{\mathrm{miss}})$ - azimuthal separation of the lepton and missing transverse energy;
- $\Delta R(\ell, j)$ - distance between the lepton and the closest jet.

The real and fake efficiencies for electrons and muons as a function of the aforementioned observables are shown in Figures 6.3 and 6.4.

These observables are chosen for their discriminating power between prompt leptons and fake or non-prompt leptons. To estimate the multijet background in a given analysis, a combination of different parameterisations is used. The individual efficiencies from each parameterisation

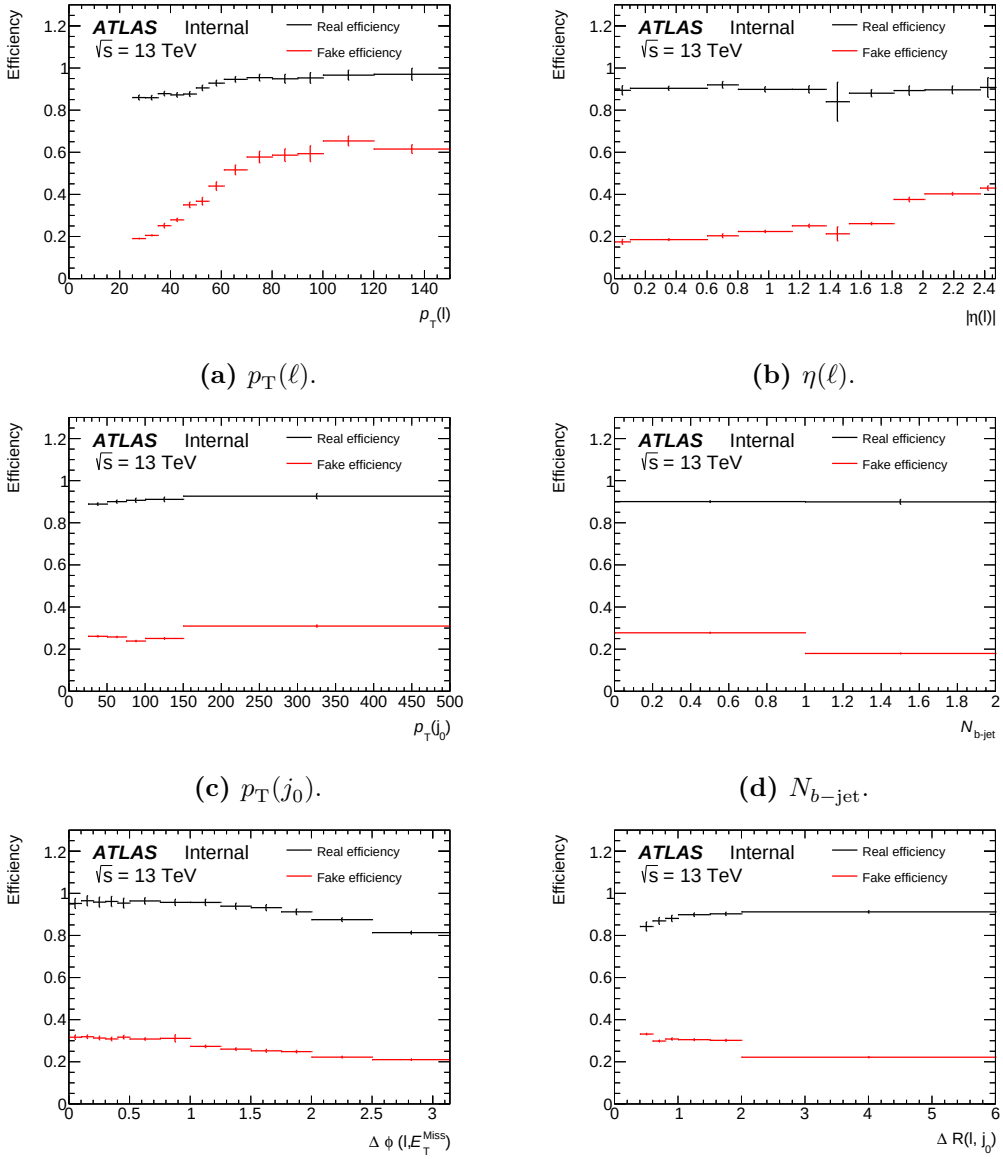

(a) $p_{\mathrm{T}}(\ell)$. **(b)** $\eta(\ell)$.

(c) $p_{\mathrm{T}}(j_0)$. **(d)** $N_{b-\mathrm{jet}}$.

(e) $\Delta\phi(\ell, E_{\mathrm{T}}^{\mathrm{miss}})$. **(f)** $\Delta R(\ell, j)$.

Figure 6.3 The real and fake efficiencies for electrons.

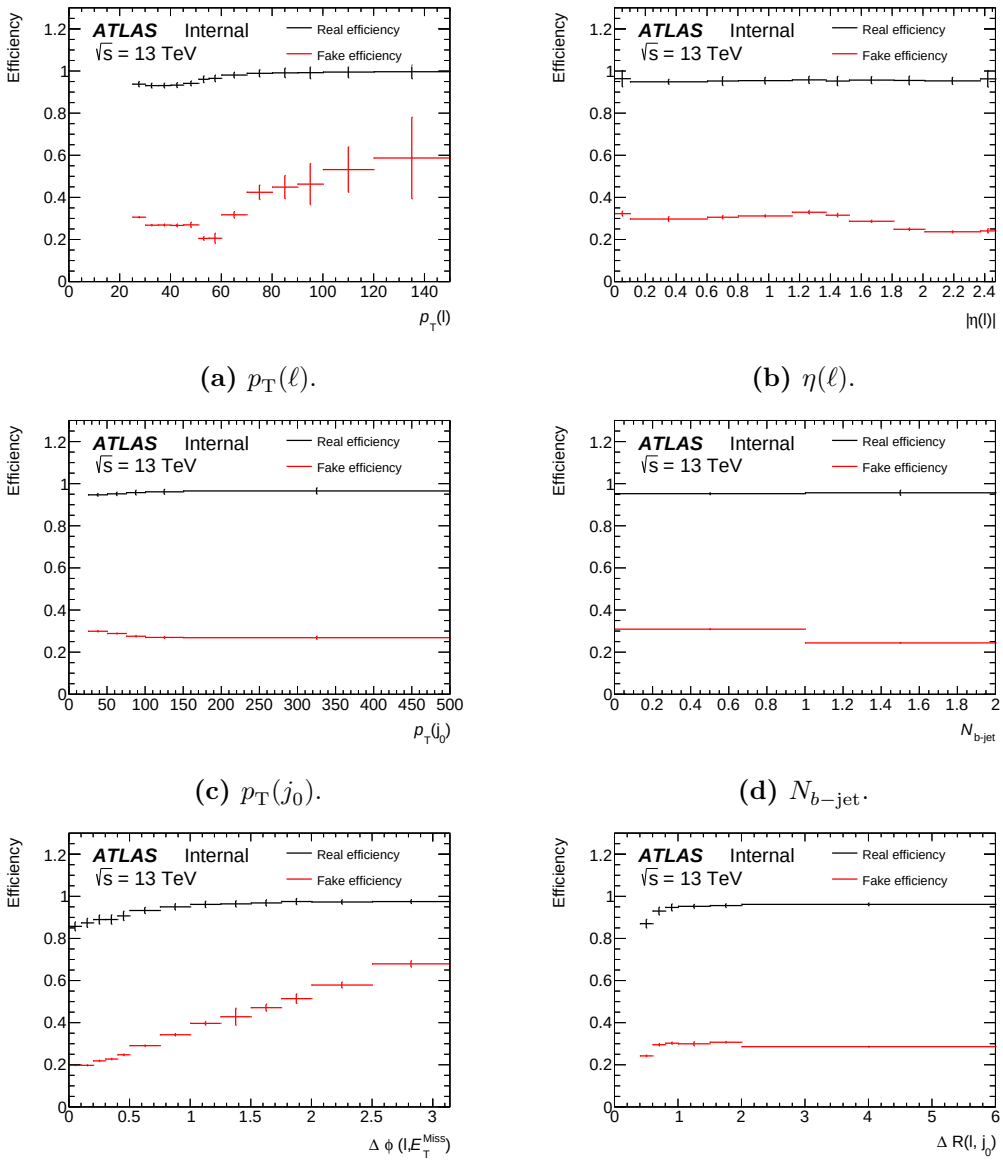

(a) $p_{\mathrm{T}}(\ell)$. **(b)** $\eta(\ell)$.

(c) $p_{\mathrm{T}}(j_0)$. **(d)** $N_{b-\mathrm{jet}}$.

(e) $\Delta\phi(\ell, E_{\mathrm{T}}^{\mathrm{miss}})$. **(f)** $\Delta R(\ell, j)$.

Figure 6.4 The real and fake efficiencies for muons.

Table 6.4 Parameterisation 1 of the real and fake efficiencies. This parameterisation is the default recommended by the Top Fakes group.

Year	Channel	Parameterisation
2015	e+jets	Real:$\eta^{\text{lep}} \oplus p_T^{\text{lep}} \oplus \Delta R$, Fake: $\eta^{\text{lep}} \oplus p_T^{\text{lep}} \oplus \Delta\phi(\ell, E_T^{\text{miss}})$
2015	μ+jets	Real:$\eta^{\text{lep}} \oplus p_T^{\text{lep}} \oplus \Delta R$, Fake: $\eta^{\text{lep}} \oplus p_T^{\text{lep}} \oplus \Delta\phi(\ell, E_T^{\text{miss}})$
2016	e+jets	Real:$\eta^{\text{lep}} \oplus p_T^{\text{lep}} \oplus \Delta R$, Fake: $\eta^{\text{lep}} \oplus p_T^{\text{lep}} \oplus \Delta\phi(\ell, E_T^{\text{miss}})$
2016	μ+jets	Real:$\eta^{\text{lep}} \oplus p_T^{\text{lep}} \oplus \Delta R$, Fake: $\eta^{\text{lep}} \oplus p_T^{\text{lep}} \oplus \Delta\phi(\ell, E_T^{\text{miss}})$

are combined according to

$$\varepsilon_{\text{combined}} = \varepsilon_{k=0} \cdot \prod_{k \in 1,\cdots,n-1} \frac{\varepsilon_k}{\bar{\varepsilon}}, \tag{6.13}$$

where $k \in \{0, \cdots, n-1\}$ are the parameterisations and $\bar{\varepsilon}$ is the average efficiency extracted from a linear fit to the parameterisation distribution.

Several different parameterisation combinations are investigated to find the best multijet background estimation. To find the optimal parameterisation combination, the data are compared to the MC and multijet samples in control regions with low N_{jet}. Control plots in low N_{jet} regions for $p_{\text{T}}(\ell)$, $E_{\text{T}}^{\text{miss}}$ and $m_{\text{T}}(W)$. These three observables will have distinctly different shapes in $t\bar{t}$ signal events and multijet background events. In $p_{\text{T}}(\ell)$, multijet events will dominate at the low p_{T} end of the spectrum. $E_{\text{T}}^{\text{miss}}$ will generally be higher in $t\bar{t}$ signal events for electrons and $m_{\text{T}}(W)$ will peak at the W-boson mass. The control regions investigated are $N_{\text{jet}} \geq 2, 3, 4$ with no b-tagging and $N_{b-\text{jet}} \geq 1$. The agreement between the data and prediction for each parameterisation is compared for each observable in each control region and the goodness of agreement is quantified using a χ^2 test statistic. The χ^2 calculation takes into account the systematic uncertainties and their correlations. In the control plots, only the systematic uncertainty for the multijet estimation is present. The systematic uncertainty for the multijet estimation is composed of two parts; a 50% normalisation uncertainty and a shape variation. The shape variation is derived from an alternative parameterisation combination. The parameterisation combinations investigated are shown in Tables 6.4 to 6.7.

Table 6.5 Parameterisation 2 of the real and fake efficiencies. In this case, both the real and fake efficiencies use the same parameterisation. This parameterisation is used by another analysis with a similar event selection.

Year	Channel	Parameterisation
2015	e+jets	$\eta^{\text{lep}} \oplus p_T^{j_0} \oplus \Delta R$
2015	μ+jets	$\eta^{\text{lep}} \oplus p_T^{\text{lep}} \oplus \Delta R$
2016	e+jets	$\eta^{\text{lep}} \oplus p_T^{j_0} \oplus \Delta R$
2016	μ+jets	$\eta^{\text{lep}} \oplus p_T^{\text{lep}} \oplus \Delta R$

Table 6.6 Parameterisation 3 of the real and fake efficiencies. In this case, both the real and fake efficiencies use the same parameterisation. This parameterisation is used by another analysis where a full parameterisation optimisation has been carried out.

Year	Channel	Parameterisation
2015	e+jets	$\eta^{\text{lep}} \oplus N_{b\text{-jet}} \oplus p_T^{j_0}$
2015	μ+jets	$\eta^{\text{lep}} \oplus N_{b\text{-jet}}$
2016	e+jets	$\eta^{\text{lep}} \oplus p_T^{j_0}$
2016	μ+jets	$\Delta\phi(\ell, E_T^{\text{miss}})$

6.2.2.5 Efficiency parameterisation combination optimisation

The comparison of the first three parameterisation combinations suggested parameterisation 1 has the best agreement between data and prediction in the observables most applicable to

Table 6.7 Parameterisation 4 of the real and fake efficiencies. In this case, both the real and fake efficiencies use the same parameterisation. This parameterisation is used as the alternative parameterisation for parametrisation 3.

Year	Channel	Parameterisation
2015	e+jets	$\eta^{\text{lep}} \oplus \Delta R \oplus p_T^{j_0}$
2015	μ+jets	$p_T^{\text{lep}} \oplus \Delta\phi(\ell, E_T^{\text{miss}})$
2016	e+jets	$p_T^{\text{lep}} \oplus \Delta\phi(\ell, E_T^{\text{miss}}) \oplus p_T^{j_0}$
2016	μ+jets	$\eta^{\text{lep}} \oplus \Delta R \oplus p_T^{j_0}$

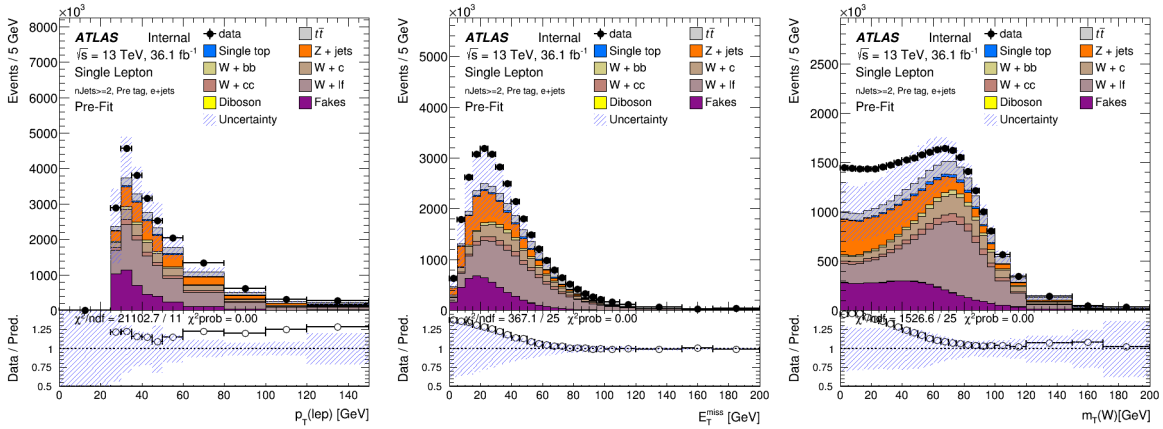

(a) $p_{\mathrm{T}}(\ell)$ **(b)** $E_{\mathrm{T}}^{\mathrm{miss}}$ **(c)** $m_{\mathrm{T}}(W)$

Figure 6.5 Comparison of data and prediction for electron+jets events with $N_{\mathrm{Jet}} \geq 2$ before any selection has been applied on the number of b-tagged or SMT-tagged jets.

the analysis, in this case p_{T}^{ℓ}. The other two configurations show a large shape mismodelling in the low p_{T} region for electron channels, likely due to the parameterisation combinations not using p_{T}^{ℓ}. As p_{T}^{ℓ} is closely related to the final observable $m_{\ell\mu}$, the modelling in this variable is prioritised. The control plots associated with using parameterisation 1 for the e+jets channel can be seen in Figures 6.5 to 6.10 and the μ+jets channel in Figures 6.11 to 6.16. Each plot shows the comparison between data and MC prediction and the shaded bands show the uncertainty from the limited statistics in the MC predictions and the uncertainty associated with the multijet background estimation.

The yields for the multijet background are shown in Table 7.2. The multijet background is one of the smaller backgrounds in the final selection.

6.2.3 SMT mistag rate

The rate at which light jets are misidentified by the SMT is known as the SMT mistag rate or SMT fake rate. The SMT mistag rate is measured in data using the technique outlined in [156]. The principle is to use a sample of W+1 jet events to measure the rate at which the SMT tags light jet events in order to derive a data-to-MC scale factor, $S_{\text{SMT-mistag}}$. The

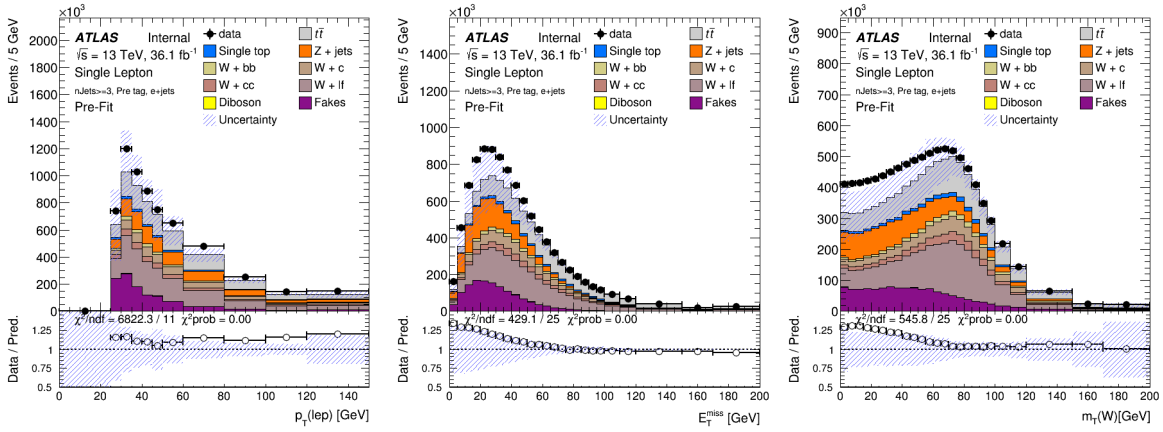

(a) $p_{\mathrm{T}}(\ell)$ **(b)** $E_{\mathrm{T}}^{\mathrm{miss}}$ **(c)** $m_{\mathrm{T}}(W)$

Figure 6.6 Comparison of data and prediction for electron+jets events with $N_{\mathrm{Jet}} \geq 3$ before any selection has been applied on the number of b-tagged or SMT-tagged jets.

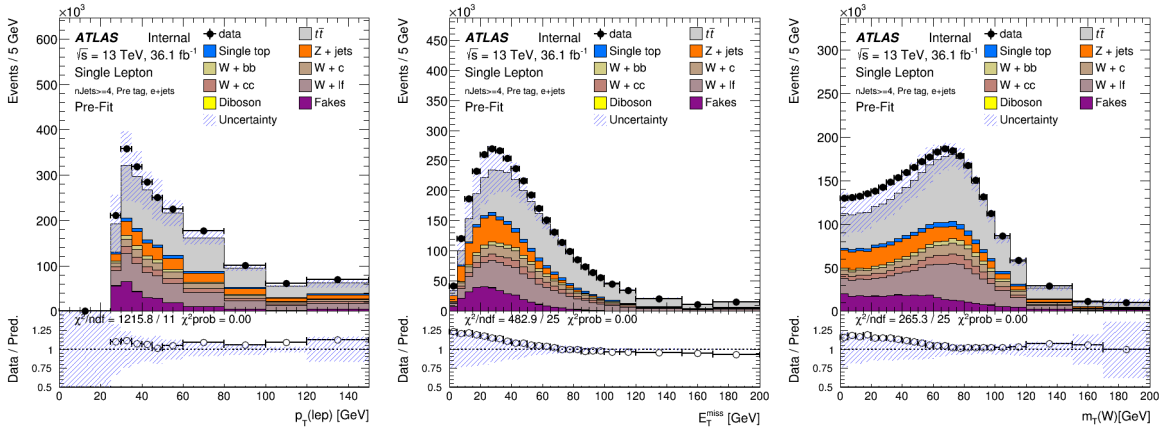

(a) $p_{\mathrm{T}}(\ell)$ **(b)** $E_{\mathrm{T}}^{\mathrm{miss}}$ **(c)** $m_{\mathrm{T}}(W)$

Figure 6.7 Comparison of data and prediction for electron+jets events with $N_{\mathrm{Jet}} \geq 4$ before any selection has been applied on the number of b-tagged or SMT-tagged jets.

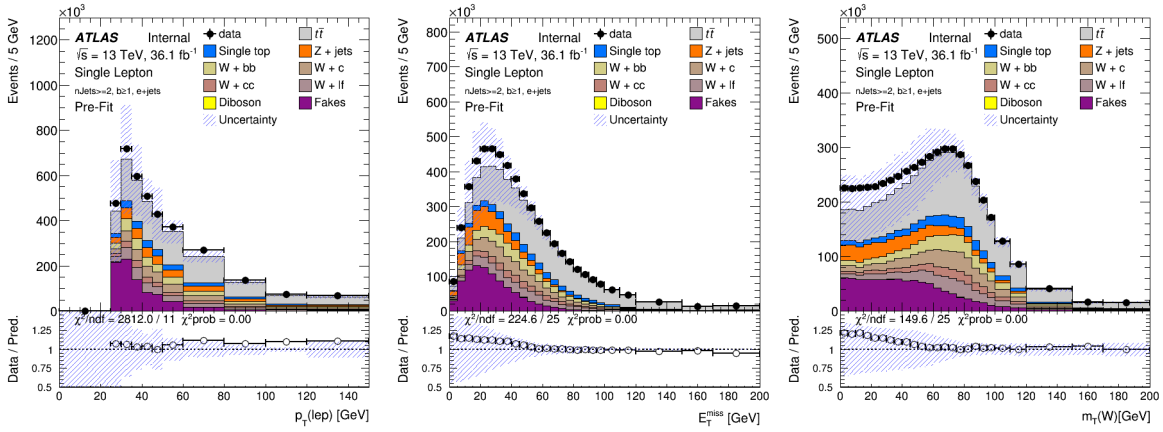

(a) $p_{\mathrm{T}}(\ell)$ **(b)** $E_{\mathrm{T}}^{\mathrm{miss}}$ **(c)** $m_{\mathrm{T}}(W)$

Figure 6.8 Comparison of data and prediction for electron+jets events with $N_{\mathrm{Jet}} \geq 2$, requiring at least one b-tagged jet.

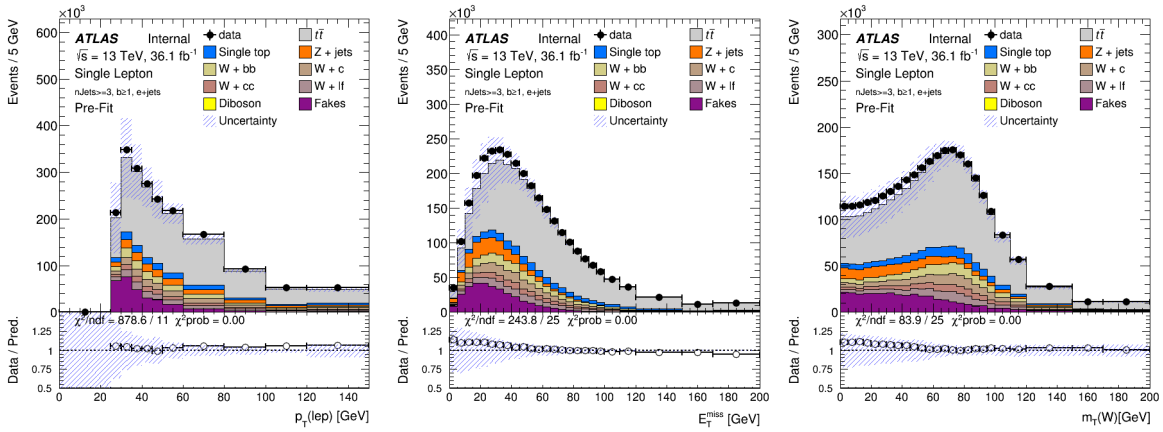

(a) $p_{\mathrm{T}}(\ell)$ **(b)** $E_{\mathrm{T}}^{\mathrm{miss}}$ **(c)** $m_{\mathrm{T}}(W)$

Figure 6.9 Comparison of data and prediction for electron+jets events with $N_{\mathrm{Jet}} \geq 3$, requiring at least one b-tagged jet.

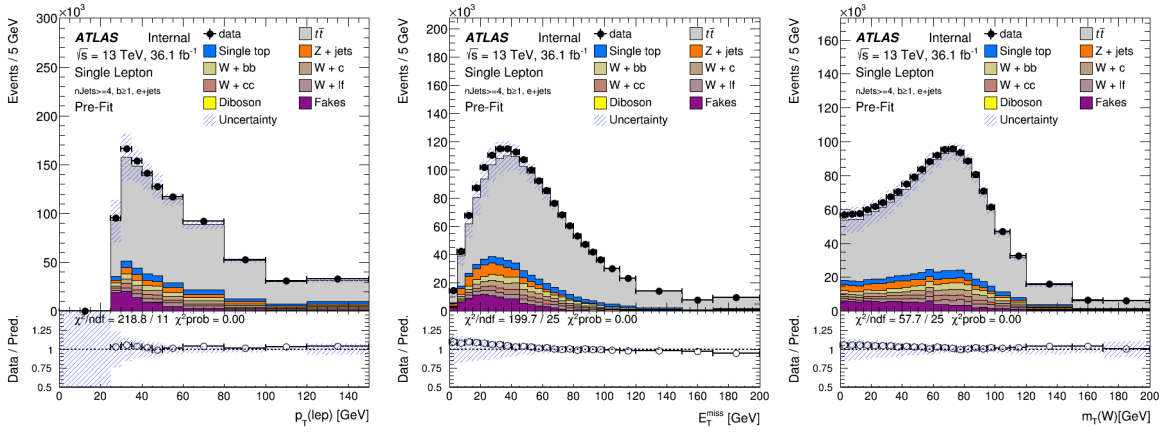

(a) $p_{\mathrm{T}}(\ell)$ **(b)** $E_{\mathrm{T}}^{\mathrm{miss}}$ **(c)** $m_{\mathrm{T}}(W)$

Figure 6.10 Comparison of data and prediction for electron+jets events with $N_{\mathrm{Jet}} \geq 4$, requiring at least one b-tagged jet.

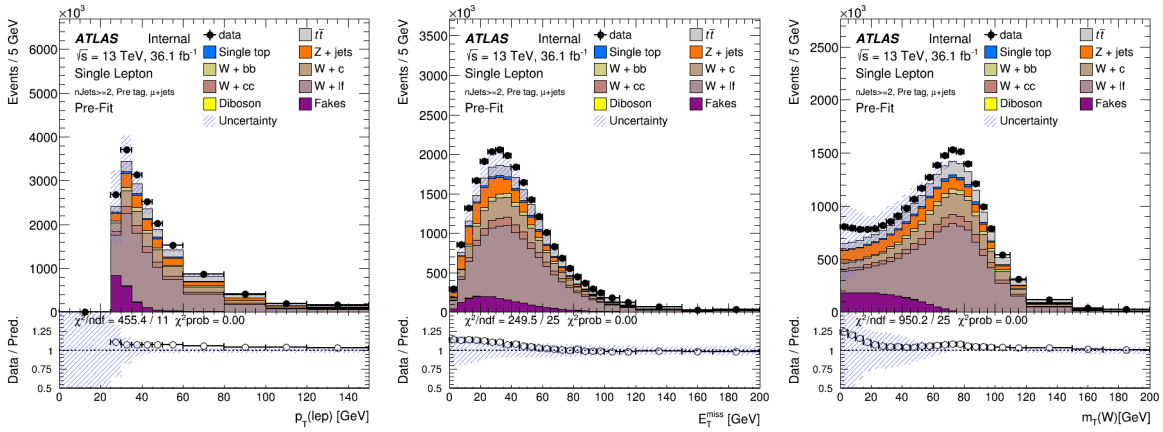

(a) $p_{\mathrm{T}}(\ell)$ **(b)** $E_{\mathrm{T}}^{\mathrm{miss}}$ **(c)** $m_{\mathrm{T}}(W)$

Figure 6.11 Comparison of data and prediction for muon+jets events with $N_{\mathrm{Jet}} \geq 2$ before any selection has been applied on the number of b-tagged or SMT-tagged jets.

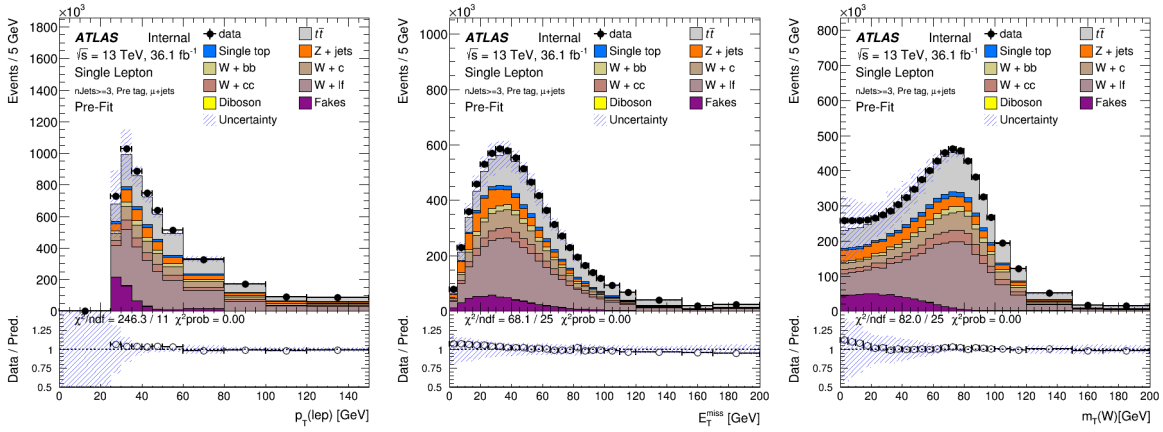

(a) $p_{\mathrm{T}}(\ell)$ **(b)** $E_{\mathrm{T}}^{\mathrm{miss}}$ **(c)** $m_{\mathrm{T}}(W)$

Figure 6.12 Comparison of data and prediction for muon+jets events with $N_{\mathrm{Jet}} \geq 3$ before any selection has been applied on the number of b-tagged or SMT-tagged jets.

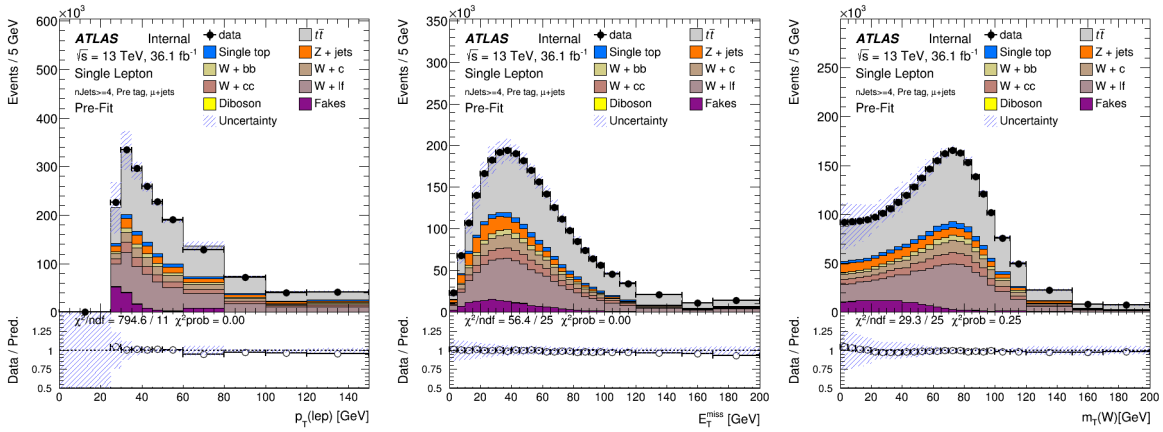

(a) $p_{\mathrm{T}}(\ell)$ **(b)** $E_{\mathrm{T}}^{\mathrm{miss}}$ **(c)** $m_{\mathrm{T}}(W)$

Figure 6.13 Comparison of data and prediction for muon+jets events with $N_{\mathrm{Jet}} \geq 4$ before any selection has been applied on the number of b-tagged or SMT-tagged jets.

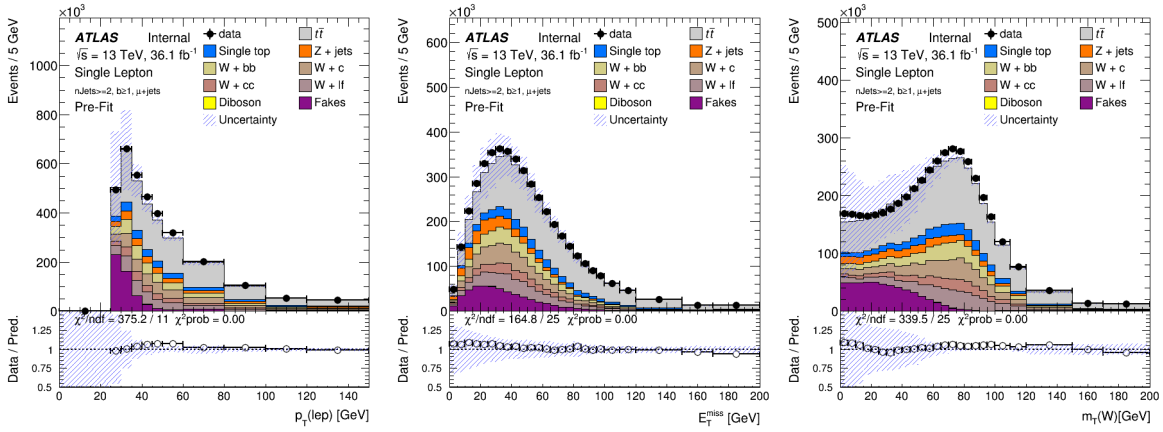

(a) $p_{\mathrm{T}}(\ell)$ **(b)** $E_{\mathrm{T}}^{\mathrm{miss}}$ **(c)** $m_{\mathrm{T}}(W)$

Figure 6.14 Comparison of data and prediction for muon+jets events with $N_{\mathrm{Jet}} \geq 2$, requiring at least one b-tagged jet.

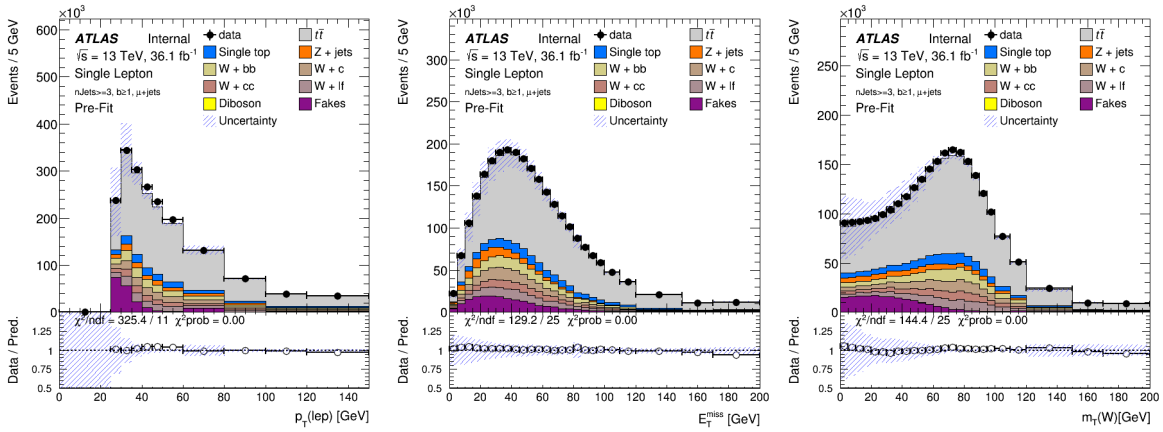

(a) $p_{\mathrm{T}}(\ell)$ **(b)** $E_{\mathrm{T}}^{\mathrm{miss}}$ **(c)** $m_{\mathrm{T}}(W)$

Figure 6.15 Comparison of data and prediction for muon+jets events with $N_{\mathrm{Jet}} \geq 3$, requiring at least one b-tagged jet.

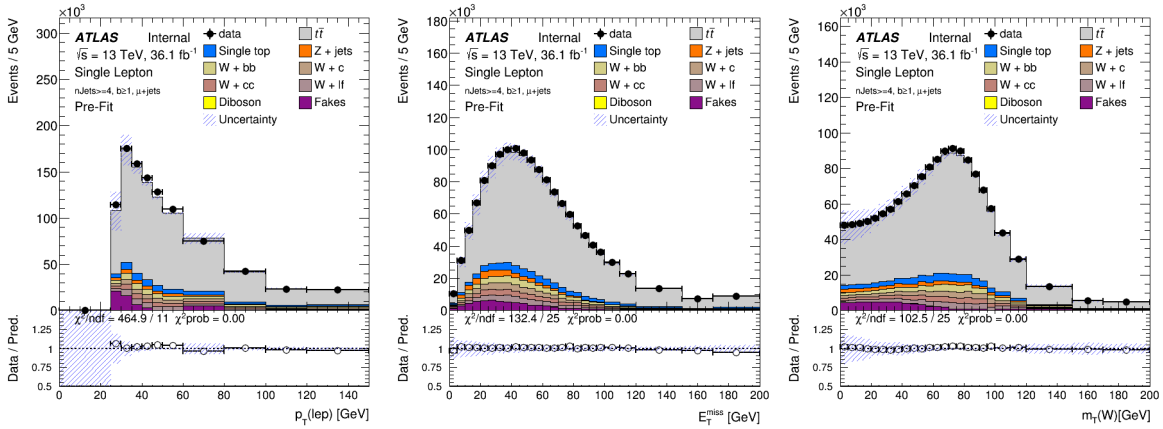

(a) $p_{\mathrm{T}}(\ell)$ **(b)** $E_{\mathrm{T}}^{\mathrm{miss}}$ **(c)** $m_{\mathrm{T}}(W)$

Figure 6.16 Comparison of data and prediction for muon+jets events with $N_{\mathrm{Jet}} \geq 4$, requiring at least one b-tagged jet.

$W \to \mu\nu$ channel is used because of the higher contamination from multijet background in the $W \to e\nu$ channel [157]. The W+jets normalisation and flavour fraction scale factors, as well as the multijet background estimation derived in the previous sections are used for the mistag rate measurement. The result is $S_{\text{SMT-mistag}} = 1.10 \pm 0.14$.

6.2.4 SMT reconstruction efficiency

As discussed in Section 5.4.1, the soft muon candidates must pass the tight quality requirement and therefore reconstruction efficiency scale factors are available from the central muon group. However, these scale factors are derived for isolated muons, whereas the soft muons will, by definition, be inside a jet. In order to verify that the scale factors provided were sufficient for the soft muons, additional studies were performed to check the reconstruction efficiencies for muons inside jets and non-prompt muons.

The reconstruction efficiencies were checked in MC samples, by finding true, particle level muons that originate from a b- or c-hadron and then trying to geometrically match them to reconstructed muons. The reconstruction efficiency is then defined the fraction of true muons that are matched to reconstructed muons.

In addition to checking MC sample, a study using the tag-and-probe method is also used. Pure samples of $J/\psi \to \mu\mu$ and $Z \to \mu\mu$ are used selected by applying cuts to the invariant mass of the dimuon candidates. The efficiency scale factors derived are very close to those provided by the central muon group and therefore no additional corrections are required.

6.3 Particle level reweighting

Due to the time taken to simulate the passage of particles through the detector and the limited resources available, MC samples with detector reconstruction are not available for all scenarios. The following samples, used in this analsyis, consist of particle level information only:

- Alternative m_t samples;
- Colour reconnection variation samples;
- Underlying event variation samples;
- r_b variation samples.

In order to use these samples in the analysis a method to "smear" the particle level samples to reconstructed level is developed. The following section details this method and its validation.

6.3.1 Particle level selection

The particle level selection is defined to be as close to the reconstructed level selection as possible. The pre-selection, based on particle level objects, is as follows:

- The prompt lepton is defined as the highest p_{T} lepton coming from the $t \to W \to \ell$ or $t \to \tau \to \ell$ (ℓ is e or μ) with a $p_{\mathrm{T}} > 27$ GeV and $|\eta| < 2.5$;
- If there is a second lepton coming from $t \to W \to \ell$ or $t \to \tau \to \ell$ also passing the selection, the event is vetoed;
- $E_T^{miss} > 30$ GeV and $E_T^{miss} + M_{\mathrm{T}}(W) > 60$ GeV;
- At least four true jets with $p_{\mathrm{T}} > 25$ GeV, $|\eta| < 2.5$;
- At least one true jet must be labelled as a b-jet;
- A muon is tagged as the soft muon if $p_{\mathrm{T}} > 8$ GeV and $|\eta| < 2.5$ and the closest jet is within $\Delta R(\mu\text{-soft}, \text{jet}) < 0.4$;

- At least one of the selected true jets must be labelled as a b-jet. This can be the SMT-jet or another;
- $\Delta R(\mu\text{-soft}, \ell) < 2$;
- The soft muon and lepton must have opposite electric charge;
- All jets not SMT-tagged must have $p_{\mathrm{T}} > 30$ GeV;
- Veto events where the soft muon originates from a $t \to W \to \mu$ or $t \to \tau \to \mu$ decay. These events are considered a background.

6.3.2 Transfer function

In order to use particle level events at the reconstructed level, only the information from the $m_{\ell\mu}$ distribution is required. Therefore, a *transfer function* is defined with a bin-by-bin weight as follows

$$w_i = \frac{N_i^{\mathrm{reco}}}{N_i^{\mathrm{truth}}} \tag{6.14}$$

where i denotes the ith bin of the $m_{\ell\mu}$ distribution and N_i are the number of events in the ith bin of the particle and reconstructed level $m_{\ell\mu}$ distributions. The transfer function is defined using the nominal $t\bar{t}$ signal sample (PP8 A14-r_b). A comparison of the transfer functions derived from the Powheg+Pythia8 A14-r_b and Powheg+Pythia8 A14 samples can be seen in Figure 6.17.

The general strategy is to use the transfer function derived from the nominal $t\bar{t}$ signal sample to reweight particle level distributions for the alternative mass and signal variation samples. The use of the transfer function is based on the assumption that because $m_{\ell\mu}$ is a leptonic observable there will be limited smearing of the observable by the detector. The response matrix is defined as

$$R_{ij} = P(\text{observed in bin } i | \text{true value in bin } j). \tag{6.15}$$

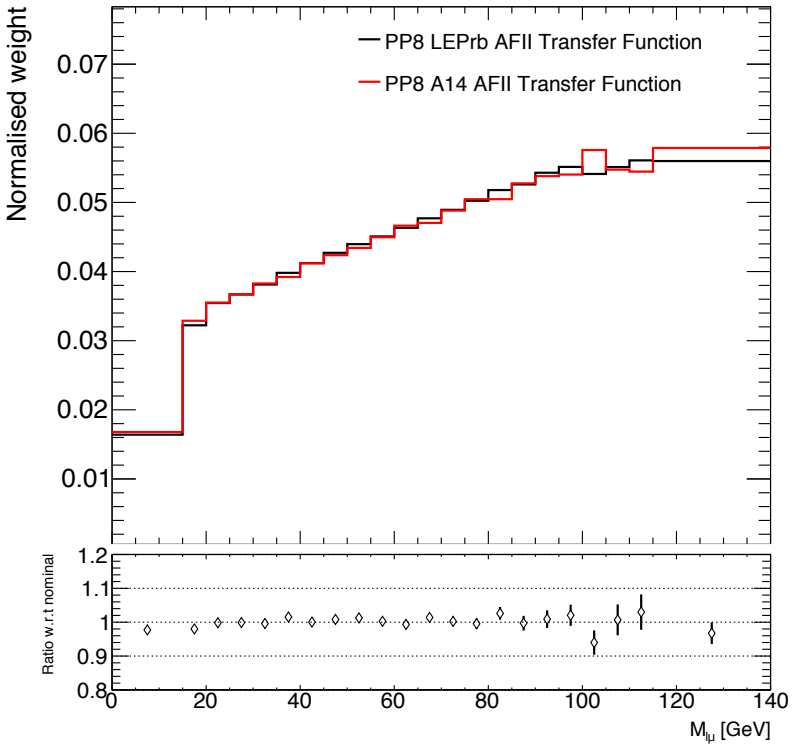

Figure 6.17 A comparison of the transfer functions derived from POWHEG+PYTHIA8 A14-r_b and POWHEG+PYTHIA8 A14 $t\bar{t}$ samples.

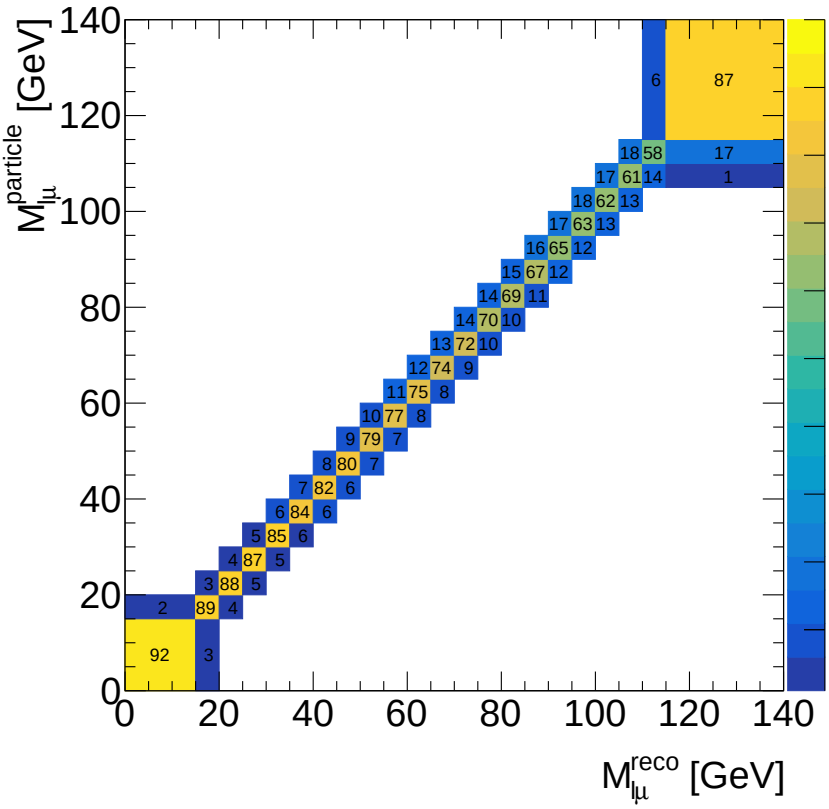

Figure 6.18 Plot of the response matrix derived from POWHEG+PYTHIA8 A14-r_b $t\bar{t}$ sample. Note the final selection limits $15 < m_{\ell\mu} < 80$ GeV

.

As can be seen in Figure 6.18, which shows the response matrix, there is very little migration between bins and therefore, the assumption is valid. A further assumption is that the transfer function should have limited dependency on the kinematics of $m_{\ell\mu}$ due to the different $t\bar{t}$ samples being reweighted. The following sections test these assumptions.

6.3.3 Transfer function dependency on m_t

The main use for the transfer function is to reweight particle level samples of alternative m_t predictions for use in the mass extraction process detailed in Chapter 9. In order to verify the transfer function is suitable for use on samples with different m_t, a single sample with $m_t = 174.5$ GeV is simulated at reconstructed level (AFII) and compared with the particle level sample with the transfer function reweighting applied. Figure 6.19 shows the comparison

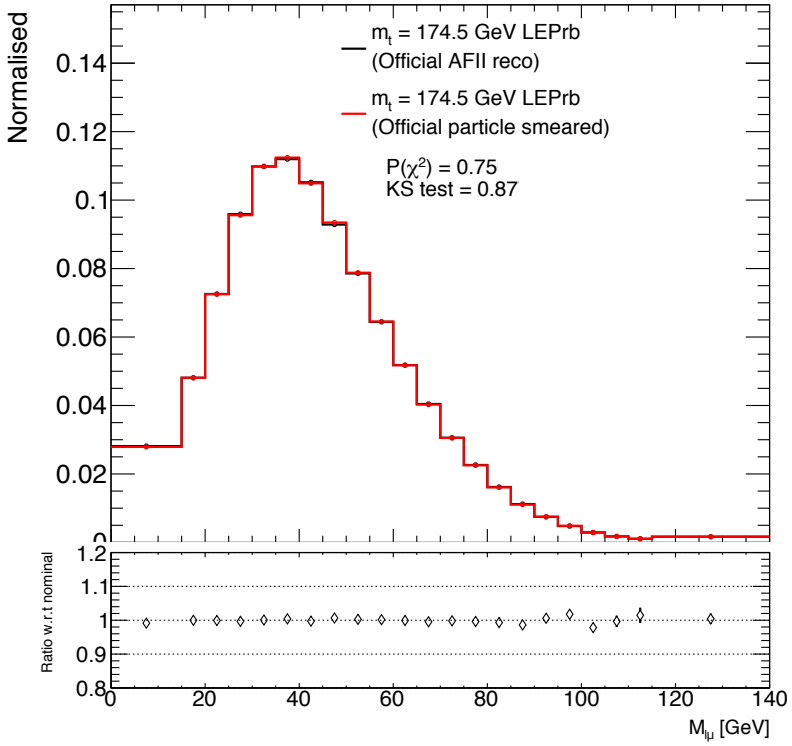

Figure 6.19 Comparison of $m_t = 174.5$ $t\bar{t}$ sample at reconstructed level with particle level sample, reweighted to reconstructed level with transfer function for $m_{\ell\mu}$.

between the two samples. The comparison of the two distributions gives a $P(\chi^2) = 0.75$, a Kolmogorov compatibility test results in a compatibility of 0.87, and the difference in the average of the $m_{\ell\mu}$ distribution is $\langle m_{\ell\mu}^{AFII} \rangle - \langle m_{\ell\mu}^{truth,TF} \rangle = 0.000 \pm 0.013$ GeV. These results indicate the samples are fully compatible and therefore the transfer function is safe to use with the alternative m_t $t\bar{t}$ samples.

6.3.4 Transfer function dependency on modelling variations

In addition to the alternative m_t samples, the colour reconnection, r_b and underlying event variation samples are also only at particle level. For the r_b variations, Figure 6.17 shows a comparison of the transfer function defined with a sample using $r_b = 1.05$ (A14-r_b nominal and a sample using $r_b = 0.855$ (original A14 sample). This range of r_b is larger than the range used

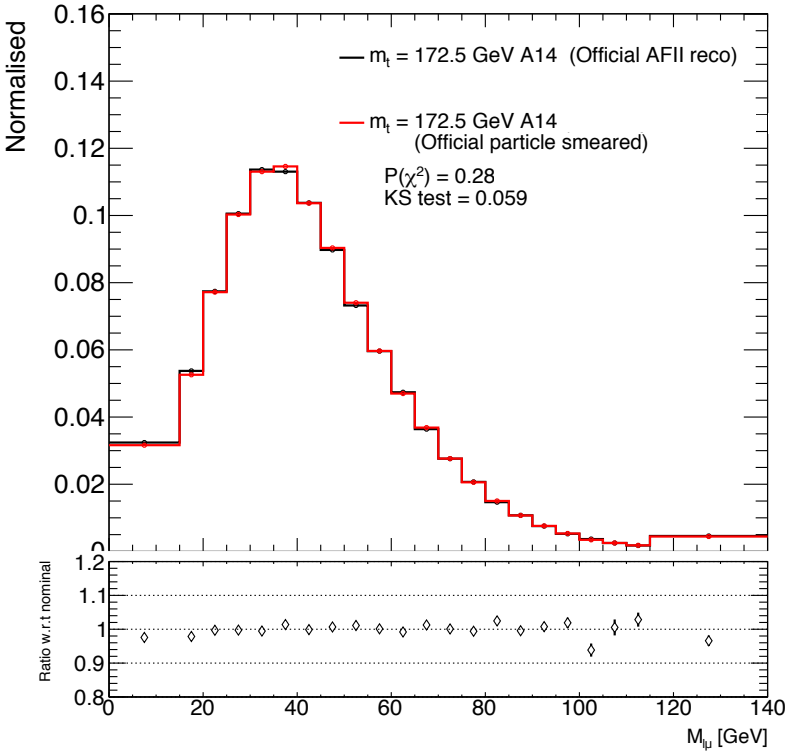

Figure 6.20 Comparison of the POWHEG+PYTHIA8 A14 $t\bar{t}$ sample at reconstructed level with particle level sample reweighted to reconstructed level with transfer function derived from the POWHEG+PYTHIA8 A14-r_b sample for $m_{\ell\mu}$.

in the variation samples ($r_b = 1.071$ and $r_b = 1.029$). Figure 6.20 shows a comparison of the reconstructed level POWHEG+PYTHIA8 A14 sample with the particle level POWHEG+PYTHIA8 A14 sample reweighted with a transfer function defined from the POWHEG+PYTHIA8 A14-r_b sample. Both Figure 6.17 and Figure 6.20 show good agreement; therefore, the transfer function is safe to use with these samples.

Both the colour reconnection and underlying event uncertainties are small for the analysis (see Chapter 8) and therefore contribute a negligible impact to the total uncertainty. For these reasons, the transfer function defined from the nominal signal sample is considered to be sufficient.

Chapter 7

Sample composition and event yields

After the object and event selection requirements are applied, the composition of the sample and event yields are checked. This chapter details the categorisation of events according to the origin of the soft muon and then the comparison of event yields from the signal and background MC samples with the measured data.

7.1 Sample composition

The soft muons in $t\bar{t}$ events can come from various sources. In the MC samples, particle level information is used to identify the origin of the soft muons by checking back through the event record to see what the muon's ancestry was. Using this, four categories are identified:

- Muons originating from the decay chain of a b quark produced in a $t \to Wb$. This includes events that contain $B \to \mu$, $B \to D \to \mu$, $B \to \tau \to \mu$ and $B \to D \to \tau \to \mu$. This category is referred to as the $t\bar{t}$ SMT-signal.
- Muons originating from the decay chain of a b quark that did not originate from a top decay. These b quarks come from initial or final state gluon splitting ($g \to b\bar{b}$). It also includes muons originating from c quarks not produced by a top decay, but rather which are produced by gluon splitting or from the $W \to sc$ decay. This category is referred to as $t\bar{t}$ SMT-background events.

- Muons that are prompt leptons from the leptonically decaying W, but which have not passed the prompt lepton requirements and are close to a jet. These muons are mainly from $t\bar{t}$ dileptonic decays and are referred to as $t\bar{t}$ dilepton events.
- Muons that are reconstructed without an associated muon in the particle level information for the event. These are muons originating from the decay of light hadrons and which are added to the particle-level information only during the detector simulation stage. These are referred to as SMT-fake events.

The $t\bar{t}$ SMT-signal category will have the highest sensitivity to m_t; however, for the remainder of this chapter, SMT-signal and SMT-background are combined and referred to as $t\bar{t}$ (SMT from b- or c-hadron). Table 7.1 shows the fraction of events falling in each sub-category involving direct and sequential decays and those not belonging to the top decay chain. The other two categories are treated as backgrounds to the analysis.

Table 7.1 Fraction of MC $t\bar{t}$ events split into components of direct and sequential decays, and decays not belonging to the b from the $t \to Wb$ decay chain.

	OS [%]	SS [%]
Processes involving a μ from a t or $\bar{t}$		
$t \to B \to \mu$	73.6	51.2
$t \to B \to D \to \mu$	16.7	44.2
$t \to B \to \tau \to \mu$	2.0	1.3
$t \to B \to D \to \tau \to \mu$	0.8	0.8
Processes involving a μ not from a t or $\bar{t}$		
$B \to \mu$	0.6	0.9
$D \to \mu$	5.8	1.4
Other ($\tau \to \mu$)	0.5	0.1

7.1.1 Event yields

The expected event yields for the signal and background components in addition to the number of observed data events can be seen in Table 7.2 for both the OS and SS regions. The selection

contains over 90% $t\bar{t}$ events when including the cases from the signal, dilepton events and fake SMT events. The contribution from the backgrounds is minimal, with the single top Wt channel contributing the largest single contribution. The Z+jets background makes a small contribution at the peak of the $m_{\ell\mu}$ distribution, but is more important around the peak of the Z-boson mass.

Table 7.2 Events yields with $m_{\ell\mu}$ between 15 and 80 GeV, seperately for OS and SS regions. Uncertainties shown include statistical and systematic contributions.

Process	Yield (OS)	Yield (SS)
$t\bar{t}$ (SMT from b- or c-hadron)	56000 ± 4000	34800 ± 2800
$t\bar{t}$ (SMT from $W \to \mu\nu$)	2190 ± 320	4.9 ± 3.6
$t\bar{t}$ (SMT fake)	1490 ± 210	1240 ± 170
Single top t-channel	770 ± 70	490 ± 40
Single top s-channel	63 ± 6	49 ± 4
Single top Wt channel	1840 ± 140	1260 ± 100
W+jets	1600 ± 400	1080 ± 240
Z+light jets	210 ± 80	15 ± 6
Z+HF jets	550 ± 170	310 ± 100
Diboson	17.2 ± 2.9	6.3 ± 1.4
Multijet	530 ± 140	480 ± 130
Total Expected	65000 ± 5000	39800 ± 3000
Data	66891	42087

In 83% of selected $t\bar{t}$ events in the OS region the soft muon and the prompt lepton originate from the same top quark (same-top decay). There are a further 10% of events in which the soft muon and prompt lepton originate from different top quarks. This purity stems from the $\Delta R(\ell, \mu\text{-soft}) < 2$ cut, which preferentially selects events containing same-top decays. In the remaining 7% of decays the soft muon does not originate from either of the b-quarks from top decays. In the SS region the corresponding fractions are 57%, 41% and 2%, respectively.

The data are compared to the sum of the signal and background predictions and visualised as a function of several observables in order to verify the predictions. Figures 7.1 to 7.7 show the

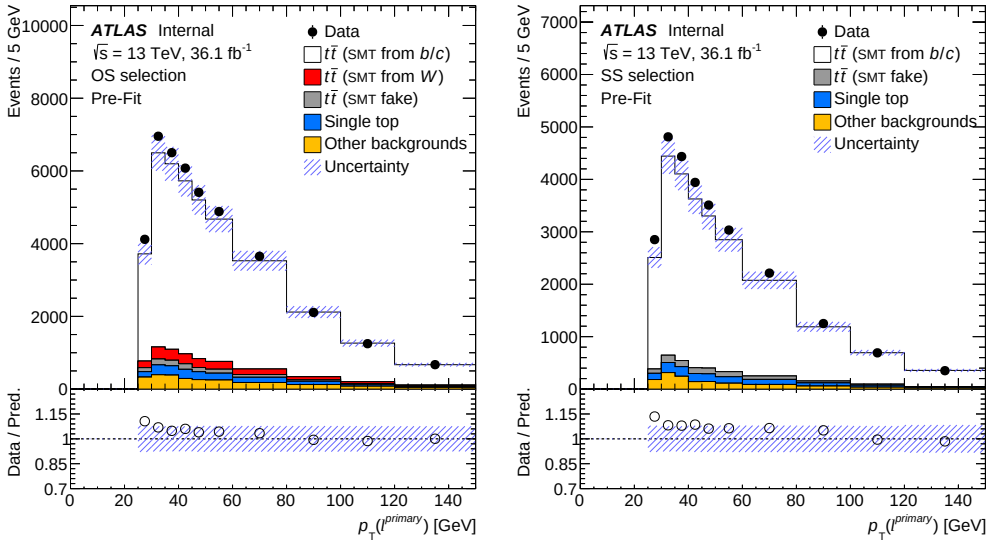

(a) $p_{\mathrm{T}}(\ell^{\mathrm{primary}})$ in the OS region. **(b)** $p_{\mathrm{T}}(\ell^{\mathrm{primary}})$ in the SS region.

Figure 7.1 Comparison of data and prediction for $p_{\mathrm{T}}(\ell^{\mathrm{primary}})$ for the OS (a) and SS (b). The prediction is the sum of the expected signal and background events. The shaded band includes both the statistical and systematic uncertainties.

comparison for several physical quantities related to the event selection and the kinematics of the constituent parts of $m_{\ell\mu}$. The agreement between the data and prediction is assessed with a χ^2 test, which takes into account the full bin-by-bin correlation matrix. All distributions agree at a level of better than two standard deviations.

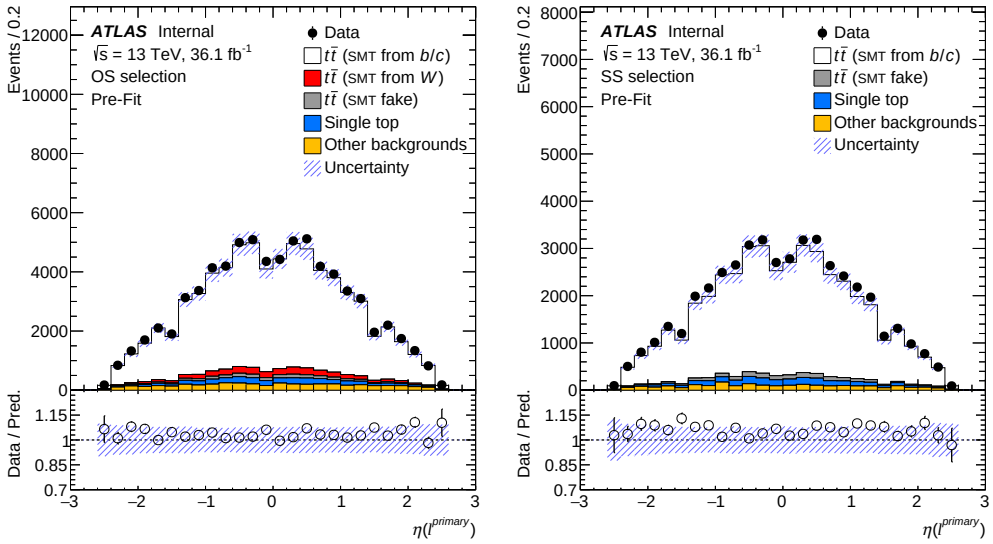

(a) $\eta(\ell^{\text{primary}})$ in the OS region. **(b)** $\eta(\ell^{\text{primary}})$ in the SS region.

Figure 7.2 Comparison of data and prediction for $\eta(\ell^{\text{primary}})$ for the OS (a) and SS (b). The prediction is the sum of the expected signal and background events. The shaded band includes both the statistical and systematic uncertainties.

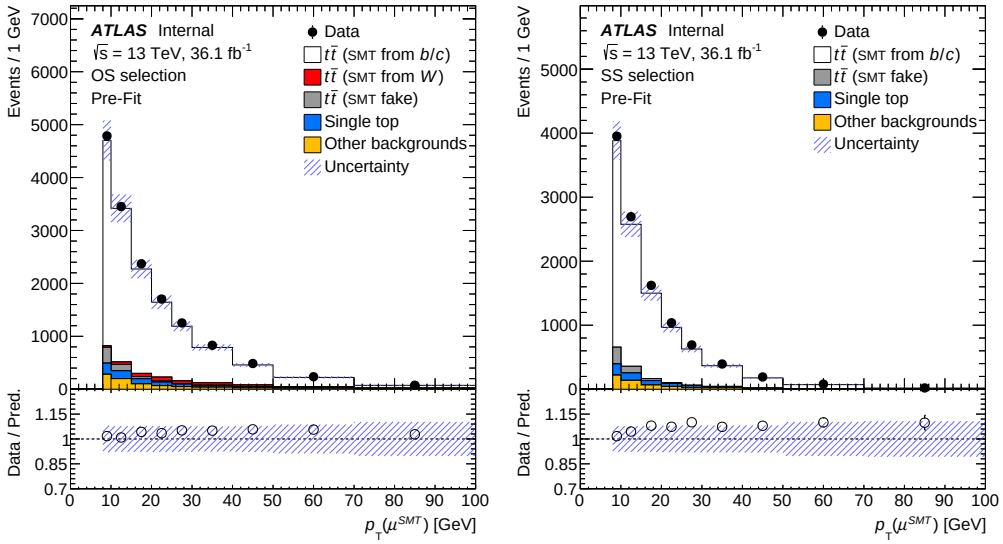

(a) $p_{\text{T}}(\mu^{\text{SMT}})$ in the OS region. **(b)** $p_{\text{T}}(\mu^{\text{SMT}})$ in the SS region.

Figure 7.3 Comparison of data and prediction for $p_{\text{T}}(\mu^{\text{SMT}})$ for the OS (a) and SS (b). The prediction is the sum of the expected signal and background events. The shaded band includes both the statistical and systematic uncertainties.

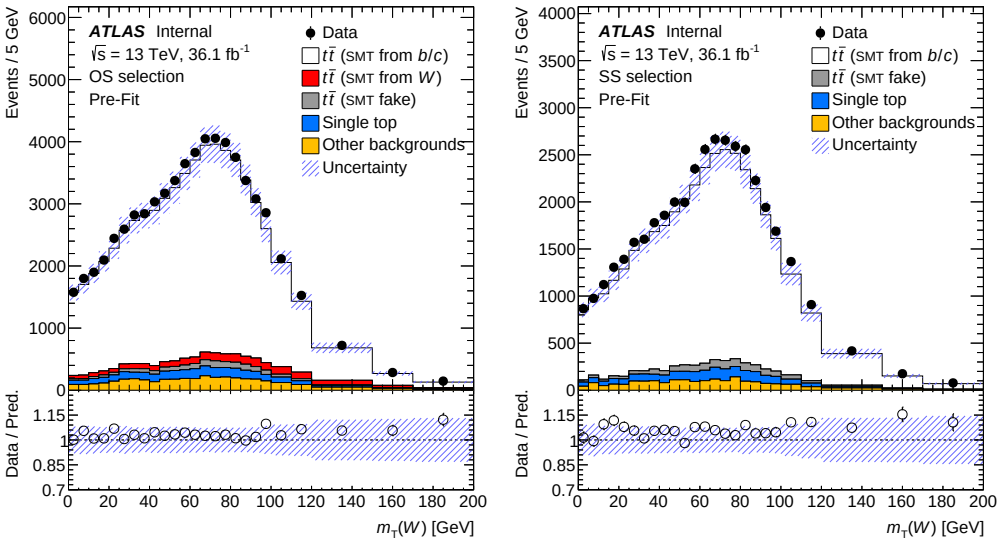

(a) $m_{\mathrm{T}}(W)$ in the OS region. **(b)** $m_{\mathrm{T}}(W)$ in the SS region.

Figure 7.4 Comparison of data and prediction for $m_{\mathrm{T}}(W)$ for the OS (a) and SS (b). The prediction is the sum of the expected signal and background events. The shaded band includes both the statistical and systematic uncertainties.

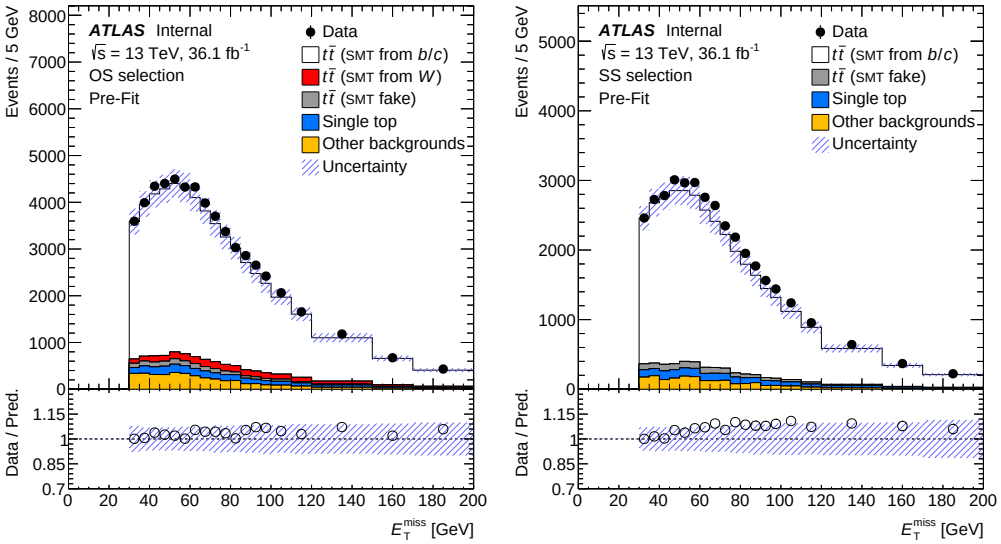

(a) $E_{\mathrm{T}}^{\mathrm{miss}}$ in the OS region. **(b)** $E_{\mathrm{T}}^{\mathrm{miss}}$ in the SS region.

Figure 7.5 Comparison of data and prediction for $E_{\mathrm{T}}^{\mathrm{miss}}$ for the OS (a) and SS (b). The prediction is the sum of the expected signal and background events. The shaded band includes both the statistical and systematic uncertainties.

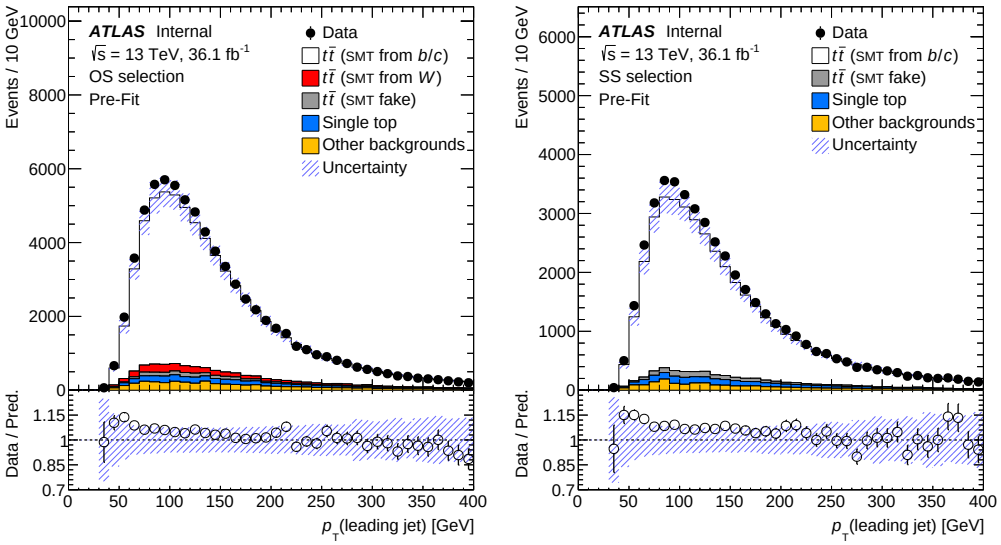

(a) p_{T}(leading jet) in the OS region. **(b)** p_{T}(leading jet) in the SS region.

Figure 7.6 Comparison of data and prediction for p_{T}(leading jet) for the OS (a) and SS (b). The prediction is the sum of the expected signal and background events. The shaded band includes both the statistical and systematic uncertainties.

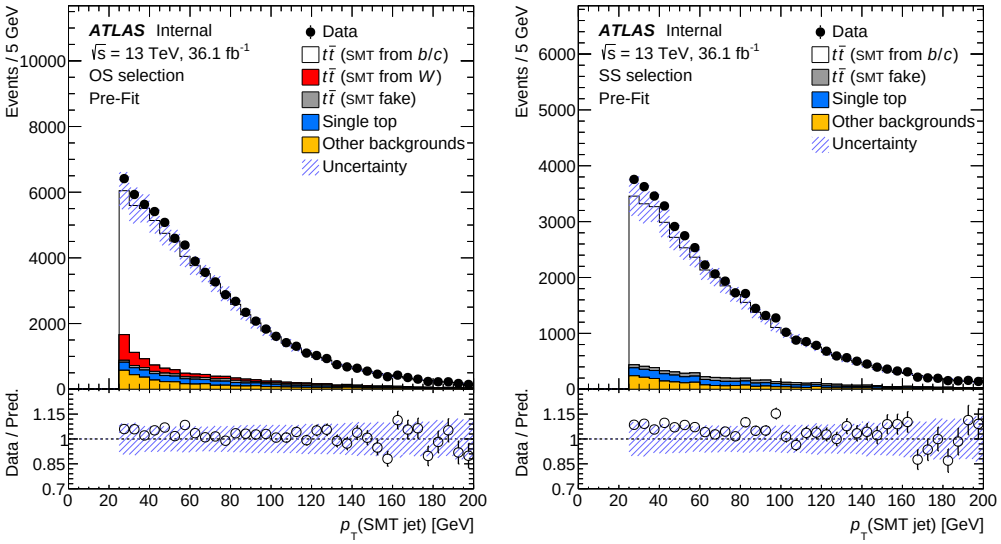

(a) p_{T}(SMT jet) in the OS region. **(b)** p_{T}(SMT jet) in the SS region.

Figure 7.7 Comparison of data and prediction for p_{T}(SMT jet)for the OS (a) and SS (b). The prediction is the sum of the expected signal and background events. The shaded band includes both the statistical and systematic uncertainties.

Chapter 8

Sources of uncertainty

The analyses presented in this thesis consider a total of 146 individual variations corresponding to 30 sources of uncertainty. These sources of uncertainty are summarised in Table 8.1 and their impact on the measured value of the top-quark mass is discussed in Chapter 9. In this section the method of evaluating each systematic uncertainty is described. The effect of each uncertainty on the differential cross-section measurement is discussed in Chapter 10.

8.1 Luminosity

The uncertainty on the combined 2015+2016 integrated luminosity is 2.1% [158]. The luminosity and its uncertainty is measured using the LUCID-2 detector [75].

8.2 Data and MC statistics

The uncertainty on the size of the sample of data events is evaluated by performing the fit (Chapter 9) while keeping all nuisance parameters associated with systematic uncertainties constant. The uncertainty arising from the limited size of the MC samples used for the signal and background predictions includes the effect on the fit calibration and the uncertainty arising from the limited number of events in each sample.

Table 8.1 Summary of all the sources of uncertainty currently included in the analysis. Where appropriate, the number of independent components considered is indicated.

Source of uncertainty	Number of components
Detector systematics	
Electron energy scale and resolution	2
Electron efficiency	4
Electron charge mis-identification	1
Muon momentum scale and resolution	5
Muon reconstruction efficiency	2
Muon trigger, isolation, TTVA efficiency	6
JVT efficiency	1
JES	28
JER	1
$E_{\mathrm{T}}^{\mathrm{miss}}$ soft term	3
b-tagging efficiencies	27
Pileup modeling	1
Signal modelling	
NLO generator	2
PS and hadronisation	2
Parton shower α_S^{FSR}	1
ISR	2
Colour reconnection	1
Underlying event	1
b-quark fragmentation r_b	1
B, C production fractions	7
B, C branching ratios	5
PDFs	30
Background modelling	
$t\bar{t}$ dilepton	3
W+jets normalisation	3
Z+jets normalisation	2
Multijet normalisation	2
Single-top normalisation	1
SMT-fakes normalisation	1
SMT-fakes modelling	1
Other	
MC statistics	2
Luminosity	1

8.3 Leptons

The uncertainties associated with leptons arise from the trigger, reconstruction, identification and isolation, as well as the lepton momentum scale and resolution. Dedicated scale factors to correct for differences between data and MC simulation are used for reconstruction, identification and isolation efficiencies of electrons and muons in addition to the efficiency of the trigger used to record events.

The efficiency scale factors are derived using the tag-and-probe method using $Z \to \ell^+\ell^-$ ($\ell = e^-, \mu^-$) events in data and MC. The scale factors are applied on a per event basis to the MC samples to correct for differences. Each scale factor has an associated uncertainty that is also applied as a per event weight. The total uncertainty on the efficiency scale factors for high-p_{T} leptons is $< 0.5\%$ for muons across the entire p_{T} spectrum [159] and electrons that satisfy $p_{\mathrm{T}} > 30$ GeV. For low-p_{T} electrons the uncertainty exceeds 1% [160].

Uncertainties also originate from the correction factors that correct for differences in the lepton momentum scale and resolution between data and MC. These correction factors are measured using the reconstructed dilepton invariant mass in both $Z \to \ell^+\ell^-$ and $J/\psi \to \ell^+\ell^-$ decays. Additional measurements of E/p in $W \to e^-\nu$ events, where E is the electron energy measured in the calorimeter and p is the electron momentum measured in the ID. The uncertainty on the momentum scale is evaluated by performing the the measurement again with the momentum scale varied by ± 1 standard deviation. For the scale resolution the measurement is repeated with the lepton resolution smeared.

The systematic uncertainty associated with the electron charge misidentification is evaluated using the method outlined in [160]. The scale factors for correcting the differences in electron charge misidentification between data and MC are calculated using $Z \to e^- e^+$ events.

Due to the soft muons using the standard tight quality working point, the standard uncertainty prescriptions can be used [92]. Additional studies have been performed to verify the scale factors for isolated muons are also valid for muons inside jets.

8.4 Jets and missing transverse energy

The systematic uncertainties associated with the jet energy scale are evaluated by varying the jet energies according to the variations that were derived in the calibration process described in Section 4.2.4. For this analysis, a total of 26 variations are used to evaluate the jet energy scale uncertainties. A full description of their derivation can be found in [96, 97]. For 24 of the variations, the standard prescription is used; however, for two of the variations an analysis-specific procedure is used. These are detailed in Section 8.5 and Section 8.6.

The jet energy scale uncertainty is around 5.5% for jets with $p_{\mathrm{T}} = 25$ GeV. The uncertainty decreases with increasing p_{T}. For the range 100 GeV $< p_{\mathrm{T}} <$ 1.5 TeV, the uncertainty is below 1.5%. Although the observable used in the analysis, $m_{\ell\mu}$, is purely leptonic, the jet uncertainties contribute to the total uncertainty of the event selection using jets. The uncertainty on the efficiency for passing the JVT requirements is evaluated by varying the scale factors within their uncertainties [161].

The uncertainty associated with the jet energy resolution was measured at 8 TeV in Run 1 of the LHC [162]. Additional uncertainties are included for the extrapolation from Run 1 to Run 2 conditions. The uncertainty is propagated to the analysis by smearing the jet p_{T} in the MC.

The additional SMT-jet energy scale correction has an associated statistical and systematic uncertainty. The systematic uncertainty is propagated into the analysis in a correlated way. For each systematic variation the corresponding correction factor is applied.

8.5 Jet flavour composition uncertainty

Jets can originate from either a gluon or a quark and their respective kinematics and properties vary. These differences will affect how the jet propagates through the detector. The main difference is the response of the calorimeters. The response is defined as $\mathcal{R} = p_{\mathrm{T}}^{\mathrm{reco}}(\mathrm{jet})/p_{\mathrm{T}}^{\mathrm{truth}}(\mathrm{jet})$ and varies between light quarks and gluon jets in MC. The difference in response is due to gluon jets containing more particles and therefore those particles have, on average, lower p_{T}

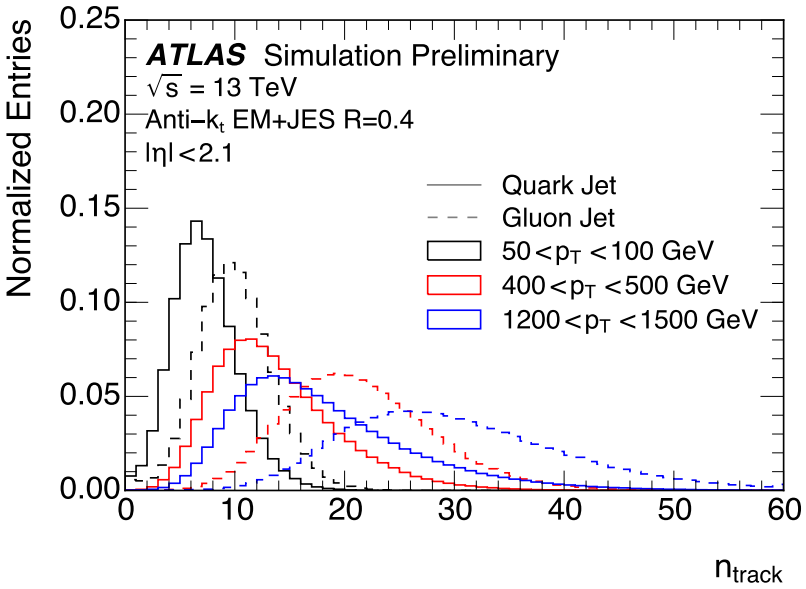

Figure 8.1 Distribution of the track multiplicity, n_{track}, for jets initiated from quark and gluons using the PYTHIA8 generator [166].

than jets originating from light quarks. The calorimeters perform better for higher p_{T} particles, which means the response will vary with p_{T}. The difference in particle multiplicity in the jet stems from the colour factor for gluons being $C_A = 3$ and for jets $C_F = 4/3$ [163, 164]. The ratio of the number of particles in gluon jets, N_g, to quark jets, N_q at leading order is given by

$$\frac{N_g}{N_q} = \frac{C_A}{C_F}. \tag{8.1}$$

A comparison of track multiplicity in a jet, n_{track}, between quark and gluon initiated jets can be seen in Figure 8.1. Due to the lower p_{T} of jets originating from gluons, the particles have a lower probability of penetrating further into the calorimeter and therefore suggests a lower response. The difference in calorimeter response between light quark and gluon jets can be up to 10%, depending on the jet p_{T} and calibration scheme [165].

To evaluate the systematic uncertainty associated with the flavour response, the variation $\Delta\mathcal{R}_{\mathcal{S}}$ for a given sample $\mathcal{S}$ is given by

$$\Delta\mathcal{R}_{\mathcal{S}} = \Delta f_g(\mathcal{R}_g - \mathcal{R}_q) + f_g\Delta\mathcal{R}_g, \tag{8.2}$$

where $\mathcal{R}_q$ and $\mathcal{R}_g$ are the responses to light quark and gluon jets, respectively, $f_g \pm \Delta f_g$ is the gluon fraction plus its uncertainty and $\Delta\mathcal{R}_g$ is the uncertainty on the gluon response, derived from the difference in response between MC generators [165].

The different response due to light quark and gluon initiated jets can impact analyses where the flavour composition for the sample is not known. By estimating the flavour composition of a given sample, the uncertainty can be reduced. In the default setup, $f_g = 0.5 \pm 0.5$ is used as a conservative estimate of the flavour composition.

8.5.1 Flavour composition estimation method

To reduce the uncertainty associated with the jet flavour composition, the flavour composition of the MC samples used in the analysis are measured. The process used is as follows:

- All jets that pass the detector level requirements are matched to jets at particle level with a requirement $\Delta R < 0.3$;
- The partonic flavour of each jet is defined by the closest ($\Delta R < 0.3$) and most energetic parton according to the truth record;
- The jet flavour composition is mapped in bins of p_{T} and η as f_g depends on these variables;
- f_g is calculated in each bin where $f_g = \frac{N^{\text{jet}}_{\text{gluon}}}{N^{\text{jet}}_{\text{gluon}} + N^{\text{jet}}_{\text{light-quark}}}$;
- Δf_g is then calculated by comparing f_g from three MC samples:
  - **MC generator** - the absolute difference in f_g between the nominal Powheg+Phythia8 and aMC@NLO+Pythia8 samples;
  - **Parton showering and hadronisation** - the absolute difference in f_g between the nominal Powheg+Phythia8 and Powheg+Herwig7 samples;
  - **ISR/FSR** - half of the absolute difference in f_g between the nominal Powheg+Phythia8 sample and the radiation high/low samples of Powheg+Pythia8.
- The final Δf_g comes from the three components added in quadrature.

8.5.2 Flavour composition in the event topology

The flavour composition is estimated in the four channels used in the analysis; e+jets and μ+jets for both 2015 and 2016 data runs. The selection used is the same as the nominal analysis selection. Plots of the gluon fraction in each of the channels are shown in Figure 8.2 . In order to make use of the full reduce the statistical uncertainty associated with the limited number of events in the MC simulation, the four channels are combined in to one. Figure 8.3 shows the comparison of the gluon fraction in each channel, split by η region. The larger gluon fraction at low p_{T} will be due to ISR radiation from gluons or pileup so they are not likely to be high p_{T}. The low number of events in the MC sample is apparent in the 2015 channels. However, the gluon fractions for each channel are comparable, showing no dependence on channel. This means that the combined fractions can be safely used.

The gluon fraction varies as a function of jet-p_{T} and jet-η and it is generally around $0.3 - 0.6$. The improvement in the uncertainty associated with the jet flavour composition comes from the reduction in the uncertainty on the gluon fraction. Instead of being 100%, as in the default case, the uncertainty is generally closer to 50% and often lower. In Figure 8.3, each η region shows the same shaped distribution where the gluon fraction is higher at lower jet-p_{T}. This is due to the lower p_{T} jets more often originating from pileup and therefore more likely to be gluon initiated jets.

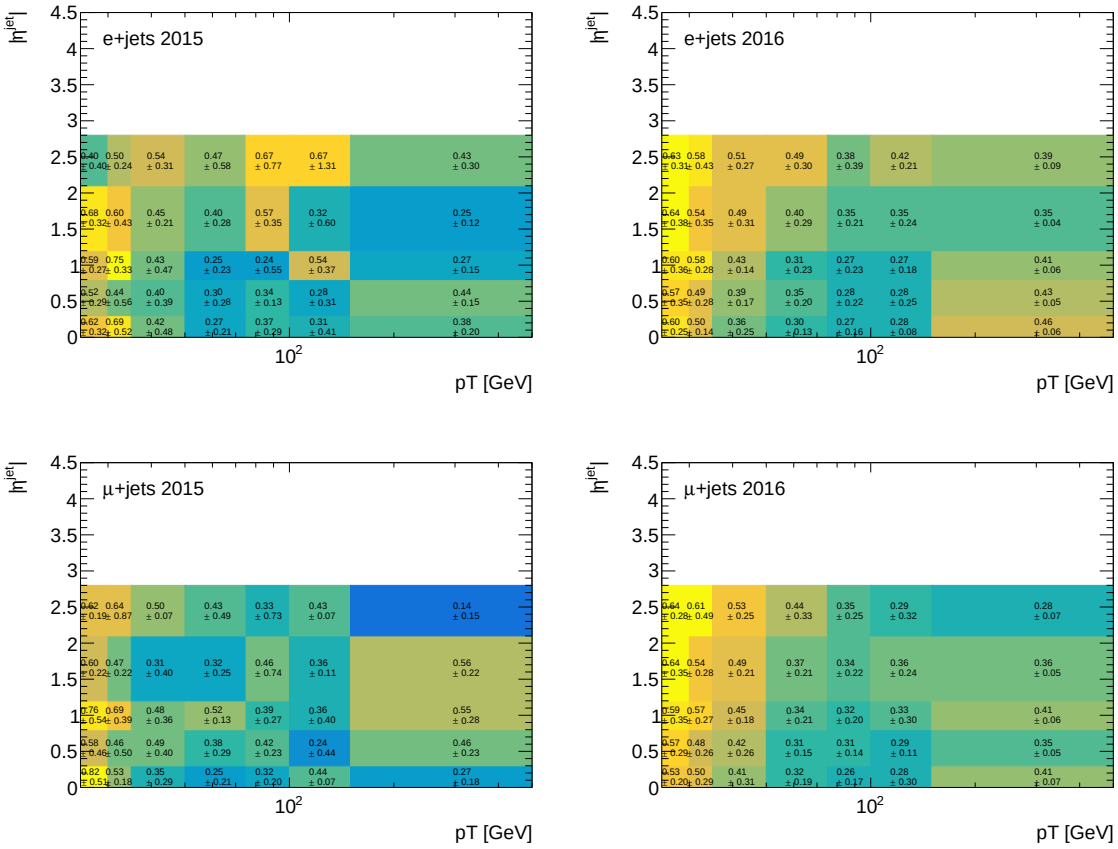

Figure 8.2 Plots of the gluon fraction as a function of jet-p_{T} and jet-η with its associated uncertainty in each of the four channels.

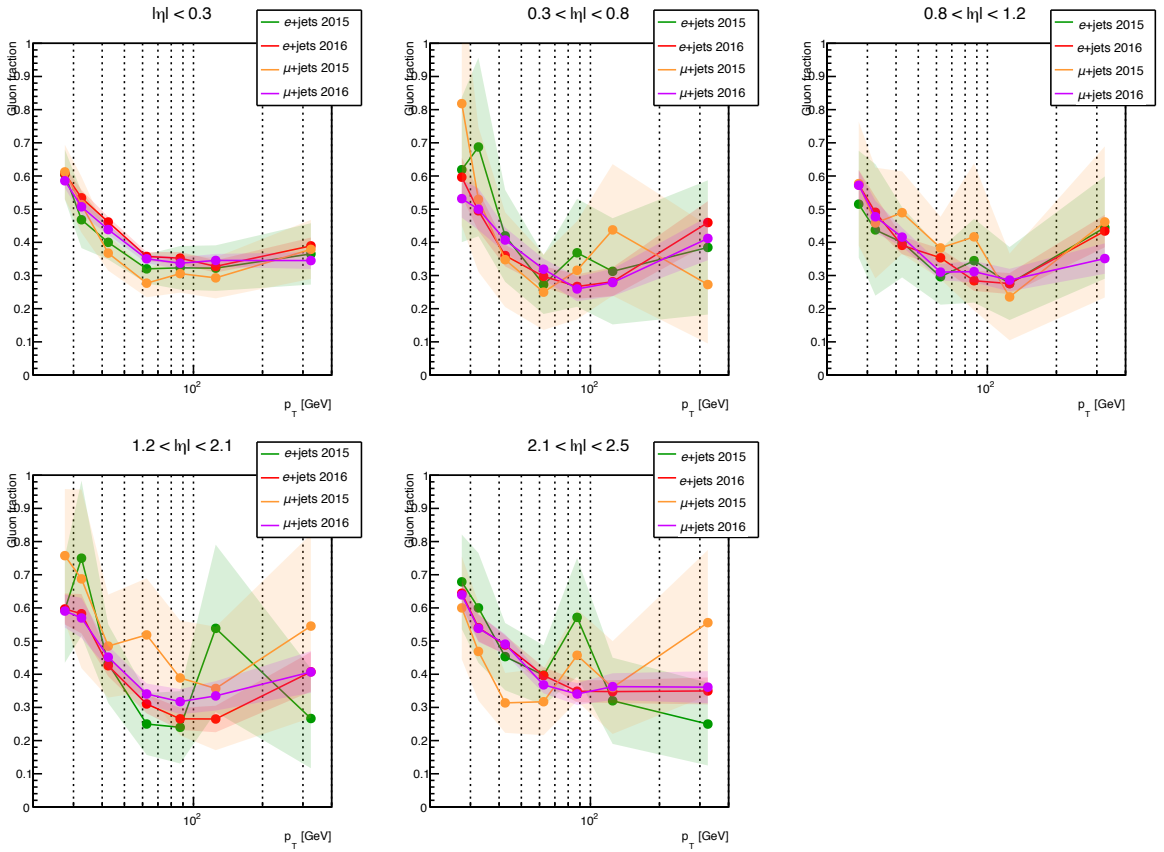

Figure 8.3 Plots of gluon fraction as a function of jet p_{T} in five η regions. Each colour represents a different channel and run year as described in the legend. Uncertainty bands include the statistical error on the gluon fraction.

8.6 Pileup ρ topology uncertainty

As discussed in Section 4.2.4, one of the key variables used in the pileup correction stage of the jet calibration is the pileup p_{T} density, ρ. The ρ for each event is a measure of the underlying pileup activity in the event that will contribute to the measured p_{T} of a given jet. The pileup density is estimated from the median of many k_t algorithm clustered jets with no minimum p_{T} threshold. Jets clustered with the k_t algorithm are used because the algorithm tends to cluster lower-p_{T} pileup jets. ρ is defined as

$$\rho = \mathrm{median}\left\{\frac{p_{\mathrm{T},i}^{\mathrm{jet}}}{A_i^{\mathrm{jet}}}\right\}, \tag{8.3}$$

where each k_t jet has a momentum $p_{\mathrm{T},i}^{\mathrm{jet}}$ and area A_i^{jet}. This can be understood as the energy density in the event coming from pileup events. In events with more pileup, it should be expected that ρ is also higher.

To correct a given anti-k_t jet's p_{T}, the ρ of an event is taken into account. To correct the jet-p_{T}, the following equation is used

$$p_{\mathrm{T}}^{\mathrm{corr}} = p_{\mathrm{T}}^{\mathrm{jet}} - \rho \times A^{\mathrm{jet}}, \tag{8.4}$$

where ρ indicates the pileup activity in the event and the area, A^{jet}, is a estimate of how susceptible a jet is to pileup interactions.

8.6.1 Uncertainty on ρ

To assess the uncertainty on ρ, the dependence of ρ on the mean number of interactions per bunch crossing, $\langle\mu\rangle$, is studied in three different event topologies: Z+jets, γ+jets and dijet. The uncertainty is derived from any bias between the event topologies. In principle the ρ for an event should be topology invariant. For each topology, both MC and data is used, with two different MC generators compared.

In each topology, ρ is plotted as a function of $\langle\mu\rangle$ and then a linear fit is performed on the profile of this distribution. To assess the difference between ρ in MC and data, across the three topologies, the difference in the slope and intercept of the fit are studied. The effect on the slope is given by

$$\Delta s = \left(\frac{\partial\rho}{\partial\langle\mu\rangle}_{\text{data}}^{\text{channel 1}} - \frac{\partial\rho}{\partial\langle\mu\rangle}_{\text{data}}^{\text{channel 2}}\right) - \left(\frac{\partial\rho}{\partial\langle\mu\rangle}_{\text{MC}}^{\text{channel 1}} - \frac{\partial\rho}{\partial\langle\mu\rangle}_{\text{MC}}^{\text{channel 2}}\right), \tag{8.5}$$

where channel 1 and 2 denote all possible pairings of the three topologies. The effect on the modelling of the intercept is given by

$$\Delta I = \left(\rho(\langle\mu\rangle^{\text{ref}})_{\text{data}}^{\text{channel 1}} - \rho(\langle\mu\rangle^{\text{ref}})_{\text{data}}^{\text{channel 2}}\right) - \left(\rho(\langle\mu\rangle^{\text{ref}})_{\text{MC}}^{\text{channel 1}} - \rho(\langle\mu\rangle^{\text{ref}})_{\text{MC}}^{\text{channel 2}}\right), \tag{8.6}$$

where $\langle\mu\rangle^{\text{ref}}$ is the mean value of $\langle\mu\rangle$ for the given year of data taking and $\rho(\langle\mu\rangle^{\text{ref}})$ is the value of ρ for $\langle\mu\rangle^{\text{ref}}$ as taken from the fit.

The uncertainty associated with the slope and intercept is derived using the average area of the jets (πR^2) and the mean jet energy calibration factor at $p_{\text{T}} = 25$ GeV averaged over each η bin, C^{JES}. This is used to propagate the max(Δs) and max(ΔI) to make a systematic shift of the calibrated jet p_{T}. The systematic shift due to the uncertainty of the slope fitted to the ρ dependence on $\langle\mu\rangle$ is given by

$$\Delta^{s}_{p_{\text{T}}} = \pm\text{max}(\Delta s) \times C^{\text{JES}} \times \pi R^2 \times (\langle\mu\rangle - \langle\mu\rangle^{\text{ref}}), \tag{8.7}$$

and the systematic shift due to the uncertainty on the value of ρ is given by

$$\Delta^{I}_{p_{\text{T}}} = \pm\text{max}(\Delta I) \times C^{\text{JES}} \times \pi R^2. \tag{8.8}$$

As discussed in Section 4.2.4, the jet pileup correction has a dependence of the reconstructed jet p_{T} on both $\langle\mu\rangle$ and the average number of primary vertices, $\langle N_{PV}\rangle$. Both dependencies have an associated systematic uncertainty, $\Delta^{\langle\mu\rangle}_{p_{\text{T}}}$ and $\Delta^{\langle N_{PV}\rangle}_{p_{\text{T}}}$. Both $\Delta^{s}_{p_{\text{T}}}$ and $\Delta^{\langle\mu\rangle}_{p_{\text{T}}}$ have a functional dependence on $\langle\mu\rangle$ and it is observed that $\Delta^{\langle\mu\rangle}_{p_{\text{T}}}$ is dominant in all cases so $\Delta^{s}_{p_{\text{T}}}$ is ignored.

8.6.2 Event selection

To estimate the uncertainty on ρ, events are selected for the three event topologies using the following event selection requirements.

Z+jets

- Passing the following triggers: electron channel - `HLT_2e17_lhmvloose_nod0`, muon channel - `HLT_2mu14`;
- $p_{\mathrm{T}}^{\text{leading-jet}} > 10$ GeV and $|\eta^{\text{jet}}| < 4.5$;
- Exactly 2 leptons with $p_{\mathrm{T}} > 20$ GeV and $|\eta| < 2.4$;
- The 2 leptons are required to have an invariant mass $66 < m_{\ell\ell} < 116$ GeV and must have opposite electric charge;
- $\Delta\phi(\text{jet}, Z) > 2.8$;
- Lepton isolation from jets $\Delta R > 0.35$.

The reference p_{T} for the Z+jets topology is defined as $p_{\mathrm{T}}^{\text{ref}} = p_{\mathrm{T}}^{\mathrm{Z}} \cdot |\cos\Delta\phi(\mathrm{Z}, \text{jet})|$.

γ+jets

- Passing the trigger `HLT_g140_loose`
- $p_{\mathrm{T}}^{\text{leading-jet}} > 10$ GeV and $|\eta^{\text{jet}}| < 4.5$
- At least one photon with $p_{\mathrm{T}}^{\gamma} > 150$ GeV - tight ID
- $\Delta\phi(\text{jet}, \gamma) > 2.8$
- Photon isolation from jets $\Delta R > 0.2$

Dijets

- Passing the unprescaled trigger: `HLT_j400`
- Two jets with $p_{\mathrm{T}} > 25$ GeV with the leading jet $p_{\mathrm{T}} > 450$ GeV and $|\eta^{\text{jet}}| < 4.5$

- At least one of the two leading jets within $|\eta^{\text{jet}}| < 0.8$
- $\Delta\phi(\text{probe-jet}, \text{reference-jet}) > 2.5$

where the reference jet is the jet in the well-calibrated reference region and the probe jet is the more forward jet. These definitions come from the event topologies defined for the jet calibration procedures [165].

8.6.3 Control plots

For the Z+jets topology, the data and MC prediction from the two generators is compared for several important variables. The control plots for the γ+jets and dijets can be found in Appendix A.

8.6.3.1 Z+jets

The comparisons between the data and MC predictions for the Z+jets topology can be seen in Figures 8.4 and 8.5. For most observables there is a good agreement between data and MC. However, the subleading jet-p_{T}, Figure 8.4d, shows a large discrepancy in the high jet-p_{T} region for the Powheg+Pythia sample. This discrepancy is to be expected. In Z+jets, the Powheg generator calculates up to NLO for Z+0-jets and LO for Z+1-jet. Therefore, the second jet in the event will be generated from the showering in Pythia which is only LO. This also explains the slight slope seen in the leading jet-p_{T}.

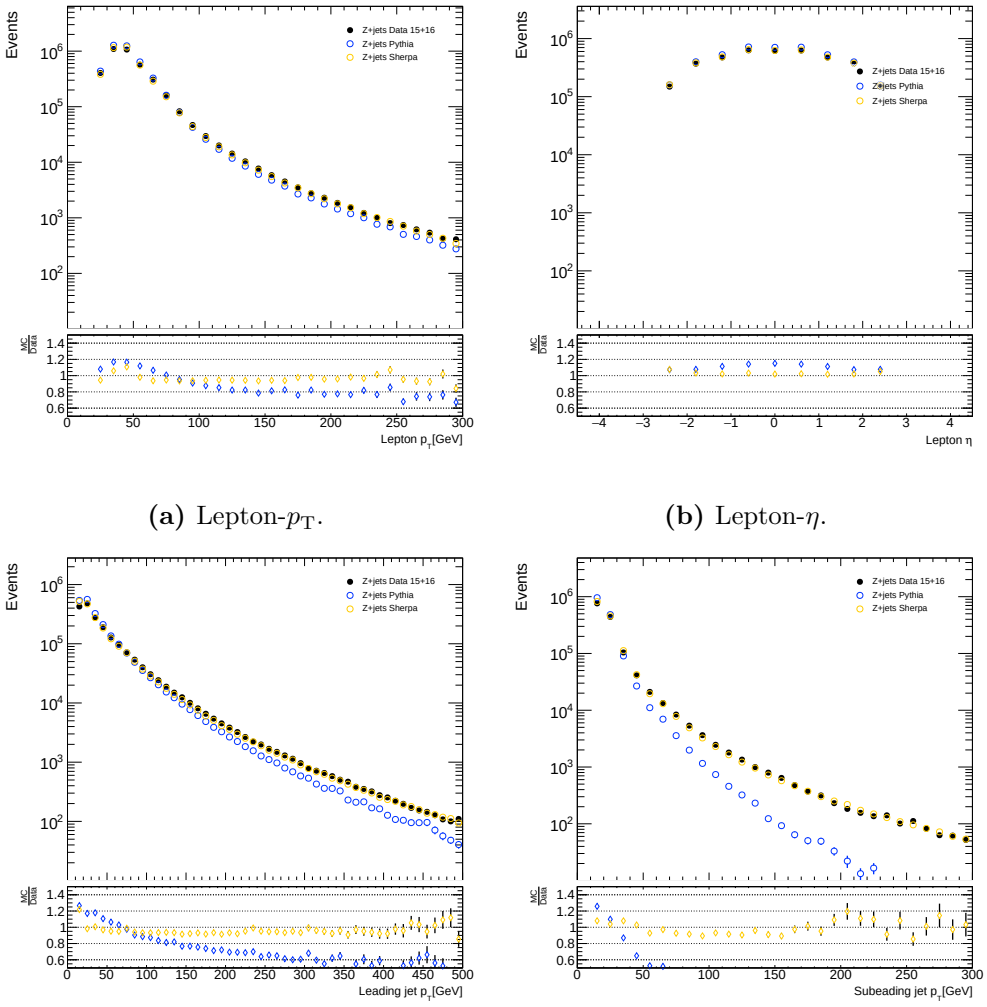

(a) Lepton-p_{T}.

(b) Lepton-η.

(c) Leading jet-p_{T}.

(d) Sub-leading jet-p_{T}.

Figure 8.4 A comparison of the data and two MC predictions for (a) lepton-p_{T}, (b) lepton-η, (c) leading jet-p_{T} and (d) subleading jet-p_{T} for the Z+jets topology.

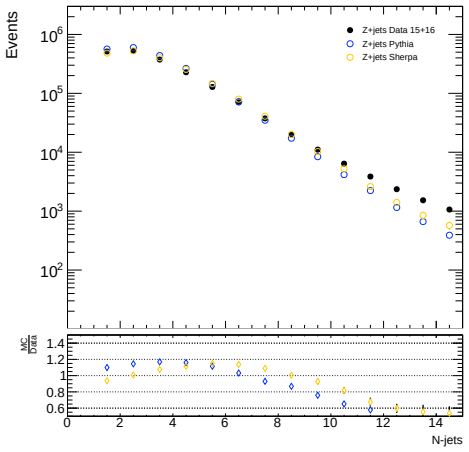

(a) Jet multiplicity in the event.

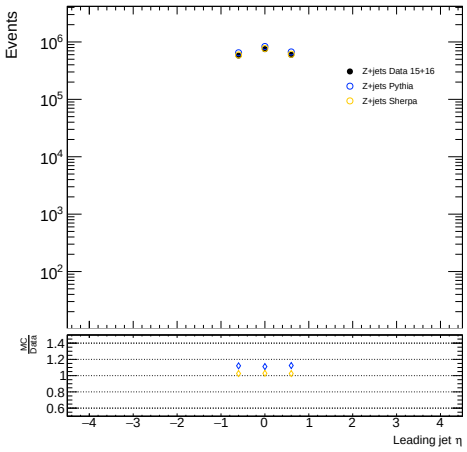

(b) Leading jet-η.

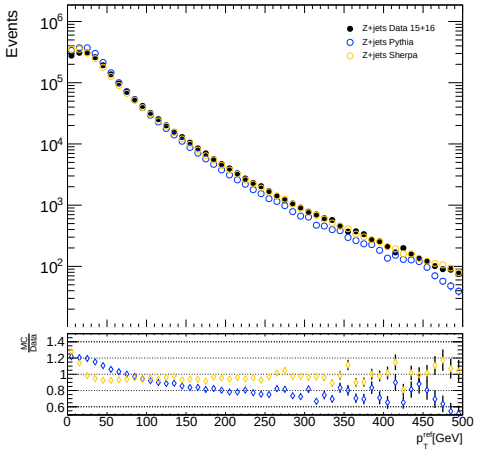

(c) $p_{\mathrm{T}}^{\mathrm{ref}}$.

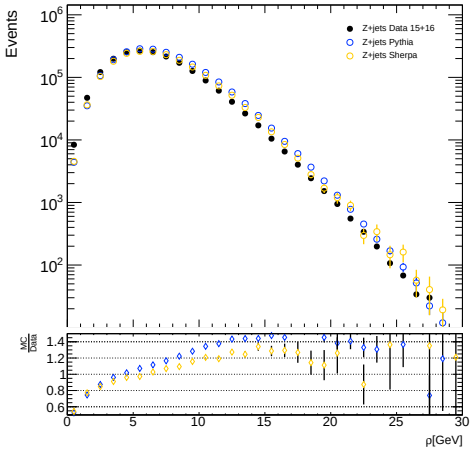

(d) ρ.

Figure 8.5 A comparison of the data and two MC predictions for (a) jet multiplicity, (b) leading jet-η, (c) reference object p_{T} and (d) ρ for the Z+jets topology.

8.6.4 ρ vs $\langle\mu\rangle$ fits

To extract the dependence of ρ on $\langle\mu\rangle$, the profile of ρ vs $\langle\mu\rangle$ is plotted and a performed. The fits for each event topology can be seen in Figures 8.6 to 8.8. The results of the fit for each parameter is shown in the figure legend.

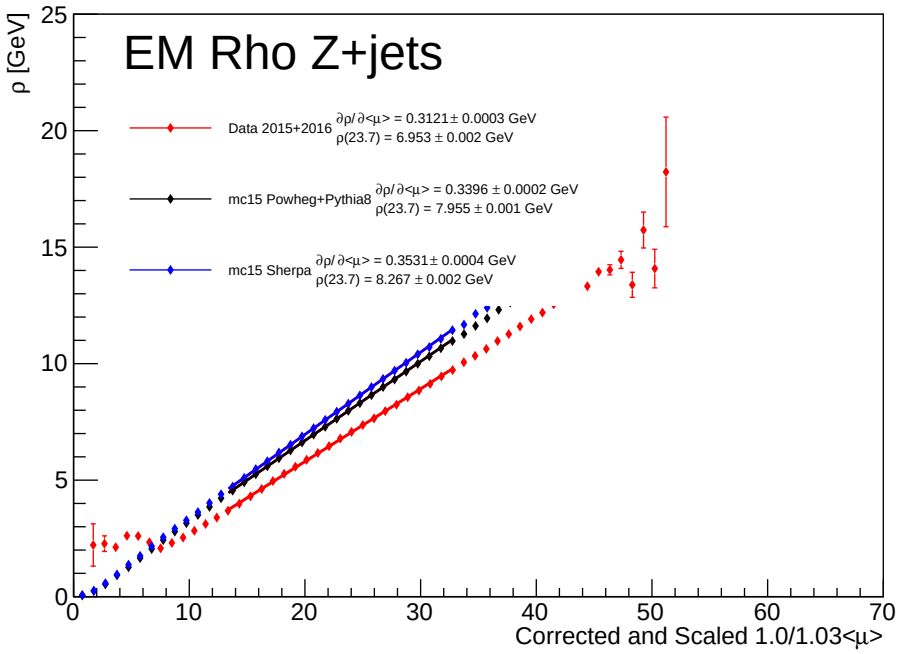

Figure 8.6 Linear fit of ρ vs $\langle\mu\rangle$ profile for the Z+jets topology.

8.6.5 ρ uncertainty result

The final uncertainty is calculated using the fits shown in Section 8.6.4 as input to the procedure outlined in Section 8.6.1. The final result is a 2D map of the fractional uncertainty binned in jet-p_{T} and jet-η. The final result can be seen in Figure 8.9. For a jet with $p_{\mathrm{T}} = 25$ GeV and $\eta = 0$ the fractional uncertainty is 1.76%. At low-p_{T}, the ρ pileup uncertainty dominates the jet energy uncertainty because the pileup contribution to the jet-p_{T} is a larger fraction of the overall jet-p_{T}.

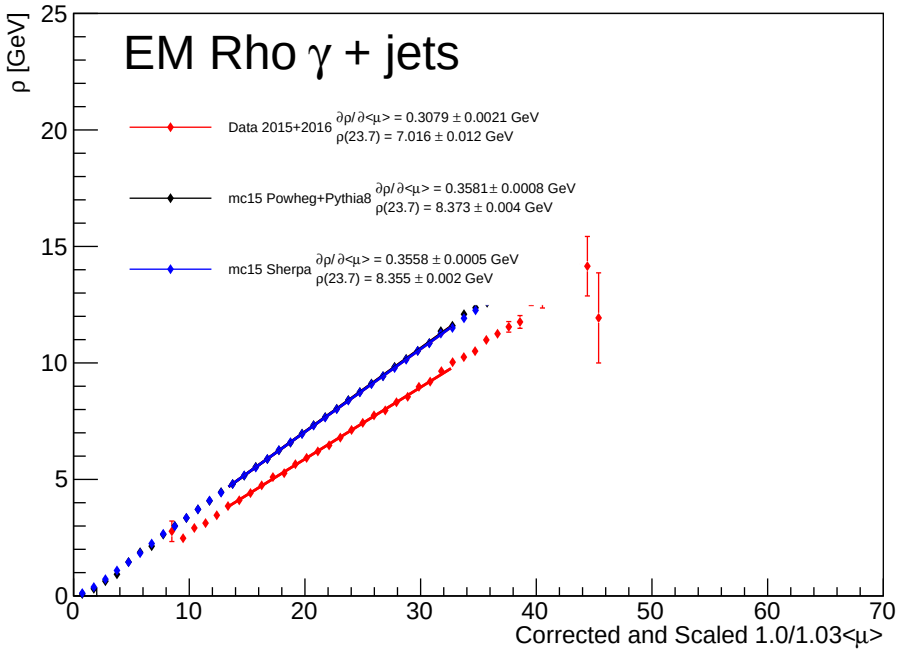

Figure 8.7 Linear fit of ρ vs $\langle\mu\rangle$ profile for the γ+jets topology.

8.7 Flavour tagging

In order to correct the b-tagging efficiencies in MC samples to match those in data, correction scale factors are derived. The scale factors are derived separately for jets originating from b, c and light quarks [167–169]. Jets originating from b and c quarks are derived as a function of p_{T} whereas the light jet efficiency is scaled by p_{T}- and η-dependent factors. The uncertainties on these scale factors are estimated by varying each source of uncertainty up and down by one standard deviation. The uncertainties are fed into an eigenvariation model (EV). The EV employs a reduction scheme such that only large variations are treated separately and smaller variations are combined. These uncertainties are taken as uncorrelated for b, c and light jets.

The tagging efficiencies have a dependence on the ratio of the hadron-p_{T} and jet-p_{T} and the minimum angle between the jet being tagged and the neighbouring jets. These dependencies are observed between different parton shower and hadronisation models. To account for the differences between the parton shower and hadronisation model used in the MC samples used

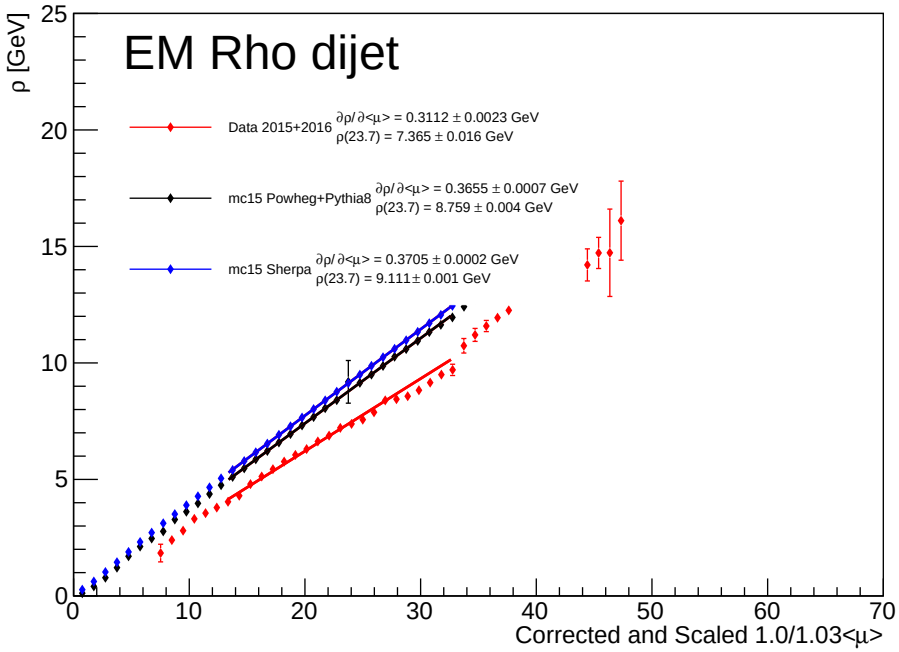

Figure 8.8 Linear fit of ρ vs $\langle\mu\rangle$ profile for the dijet topology.

to derive the tagging efficiencies and the models used in the samples in the analysis, MC-to-MC correction factors are also applied. The overall uncertainty from the flavour tagging ranges between 2–12% depending on the jet-p_{T} [98].

8.8 Pileup

The distribution of the average number of interactions per bunch crossing in MC are reweighted to match the observed conditions in data. The uncertainty is evaluated according to the uncertainty on the average number of interactions per bunch crossing [158]. Additional MC-to-MC scale factors for the lepton efficiencies are also applied to the pileup variation samples to remove the lepton efficiency dependence on pileup conditions.

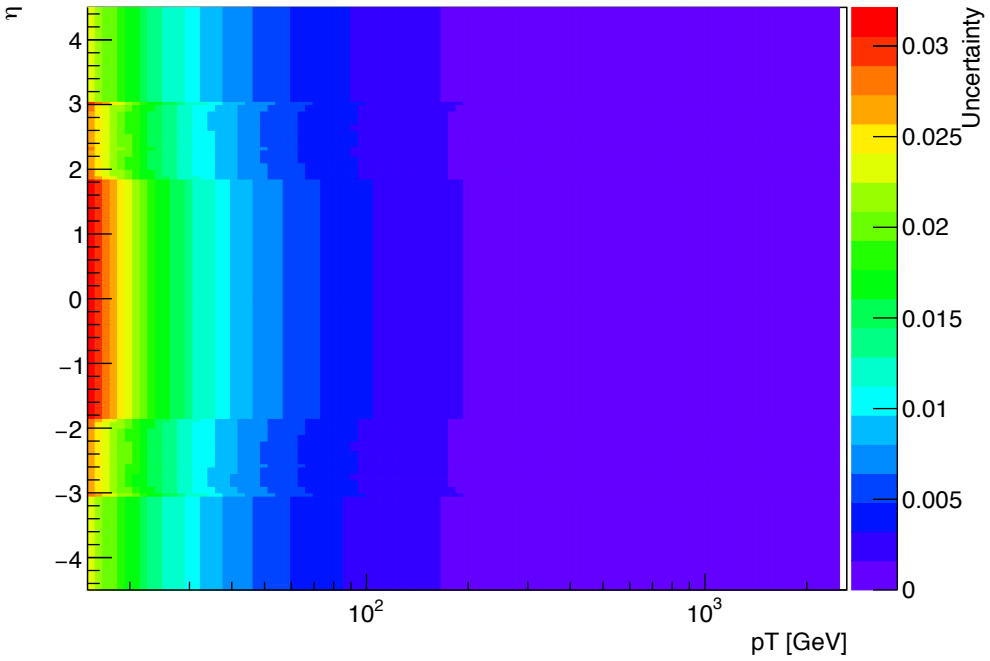

Figure 8.9 Fractional uncertainty map for ρ binned in jet-p_{T} and jet-η.

8.9 Signal modelling

Several sources of uncertainty associated with the modelling of the $t\bar{t}$ MC samples are considered. Uncertainties that modify the kinematics of the prompt lepton and the b-hadron from which the soft muon originates are key to the measurement. The uncertainty associated with the $t\bar{t}$ inclusive cross-section does not affect the analysis since no information is extracted from the number of events selected after background subtraction. The uncertainties associated with the simulation $t\bar{t}$ production and decay are split into five individual uncertainties: the uncertainty from the choice of MC event generator, the choice of parton shower and hadronisation model, the uncertainty on the fitted value of the b-quark fragmentation parameter r_b, the choice of parameters related to the initial-state QCD radiation and the choice of parton shower radiation parameters. Although there is likely double counting by including several different sources of uncertainty related to the same processes, the prescription was enforced during the ATLAS review process.

8.9.1 b and c hadron production fractions

The uncertainty associated with the b and c hadron production fractions is derived from the rescaling procedure outlined in Section 6.1.2.1. The scale factors, Table 6.1, which correct the MC simulation to the most recent measurements of the production factors, have an associated uncertainty which derives from the uncertainty from the measurements of the production fractions. These uncertainties are propagated throughout the analysis.

8.9.2 b and c hadron to μ branching ratios

Similarly to the production fractions, the uncertainties associated with the branching ratios of hadrons to μ are derived from the procedure outlined in Section 6.1.2.2. The scale factors, given in Table 6.2, that correct the MC simulation to the most recent measurements of the branching ratios, have an associated uncertainty that derives from the uncertainty on the measurements of the production fractions. These uncertainties are propagated throughout the analysis.

In addition, a further check is performed to verify the uncertainty associated with the inclusive $b \to \mu$ branching ratio is sufficient. In the $b \to c\mu$ transition, the type of D meson will affect the kinematics of the decay. A test is performed to check the exclusive branching ratio uncertainties for heavier D mesons is covered by the inclusive uncertainty. The decays studied are:

1. $B^0 \to D^- \mu\nu$
2. $B^0 \to D^*(2010)^- \mu\nu$
3. $B^+ \to \overline{D^0} \mu\nu$
4. $B^+ \to \overline{D^*}(2007)^0 \mu\nu$

as well as their charge conjugates. For each of these decays, the kinematics are checked in events selected using the following requirements:

- $p_{\mathrm{T}}^{\mathrm{jet}} > 25$ GeV
- $|\eta^{\mathrm{jet}}| < 2.5$

Table 8.2 Comparison of the BR ratios between the PDG values and from MC.

Decays	PDG (2014)	MC
$\frac{BR(B^0 \to D^- \mu\nu)}{BR(B^0 \to D^*(2010)^- \mu\nu)}$	0.44 ± 0.01	0.44 ± 0.01
$\frac{BR(B^+ \to \overline{D^0} \mu\nu)}{BR(B^+ \to \overline{D^*}(2007)^0 \mu\nu)}$	0.40 ± 0.01	0.40 ± 0.01

- $p_{\mathrm{T}}^{\mathrm{lep}} > 27$ GeV
- $N_{\mathrm{jet}} \geq 3$
- $N_{\text{b-jet}} \geq 1$

Plots comparing the kinematics of events from the neutral and charged b-hadron decays can be seen in Figure 8.10 and 8.11. For the heavier resonance decays there is a shift towards a harder $p_{\mathrm{T}}^{\text{smt-}\mu}$ distribution as expected. This, in turn, leads to a harder $m_{\ell\mu}$ spectrum for heavier resonance decays. The $p_{\mathrm{T}}^{\text{smt-jet}}$ remains almost unchanged.

Further checks are carried out to test that EvtGen correctly decays the b hadrons. The ratio of the PDG [7] branching ratios for each decay is taken and compared to the ratio found from the samples. Table 8.2 summarises the results, which are found to be consistent with those from the PDG.

To assess the effect of heavier resonance decays on the uncertainties, the effect of applying the exclusive decay uncertainties is assessed and compared to the inclusive decay uncertainty. In Table 8.3, the systematic between the inclusive decay, $B^0 \to D^*(2010)^- \mu\nu$ decay and $B^+ \to \overline{D^*}(2007)^0 \mu\nu$ is compared. The shift is calculated by weighting events up and down by the uncertainty associated with each decay in the optimised signal selection region and taking the mean of the $m_{\ell\mu}$ distribution. The inclusive shift is significantly larger than the shift of the individual exclusive decays and therefore using only the inclusive uncertainty in the final measurement is sufficient. Figure 8.12 shows the effect of the systematic shift for the exclusive decays.

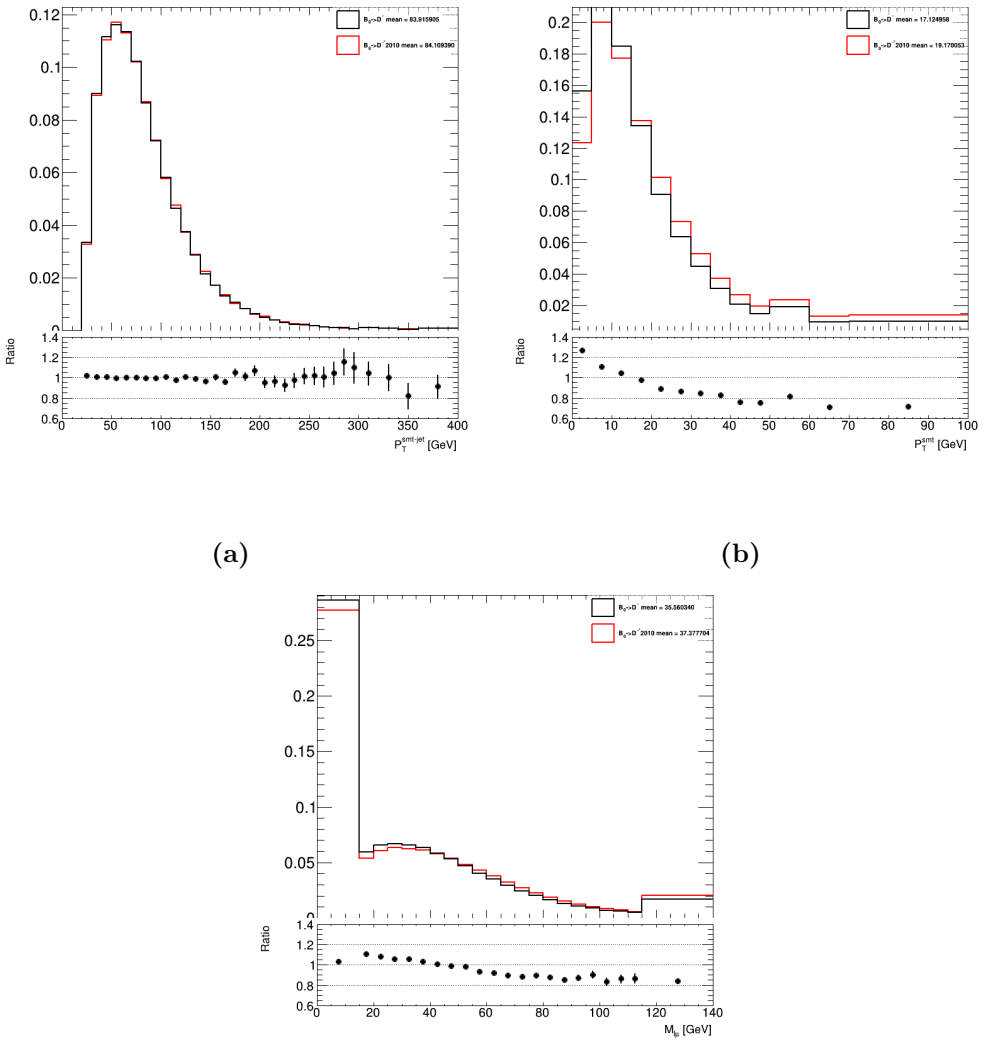

(a) **(b)**

(c)

Figure 8.10 Comparison between $B^0 \to D^- \mu\nu$ (black) and $B^0 \to D^*(2010)^- \mu\nu$ (red) for (a) $p_{\mathrm{T}}^{\text{smt-jet}}$, (b) $p_{\mathrm{T}}^{\text{smt-}\mu}$ and (c) $m_{\ell\mu}$.

Table 8.3 The shifts on the mean of the $m_{\ell\mu}$ distributions, arising from applying the individual decay uncertainties.

	Inclusive $b \to \mu$ (GeV)	Exclusive $B^0 \to D^*(2010)^- \mu\nu$ (GeV)	Exclusive $B^+ \to \overline{D^*}(2007)^0 \mu\nu$ (GeV)
Up	0.026	0.006	0.015
Down	-0.027	-0.006	-0.015

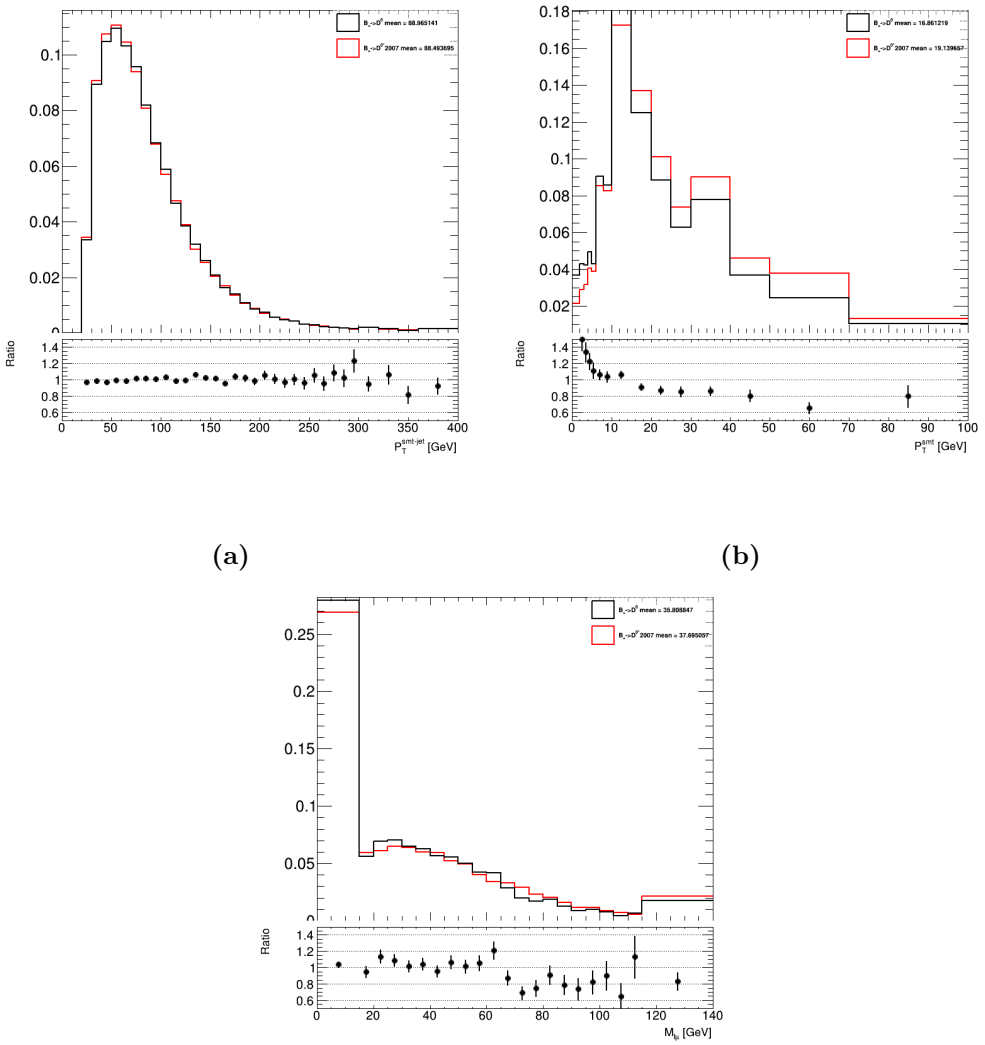

(a) **(b)**

(c)

Figure 8.11 These plots show the comparison between $B^+ \to \overline{D^0}\mu\nu$ (black) and $B^0 \to D^*(2010)^-\mu\nu$ (red) for (a) $p_{\mathrm{T}}^{\text{smt-jet}}$, (b) $p_{\mathrm{T}}^{\text{smt-}\mu}$ and (c) $m_{\ell\mu}$.

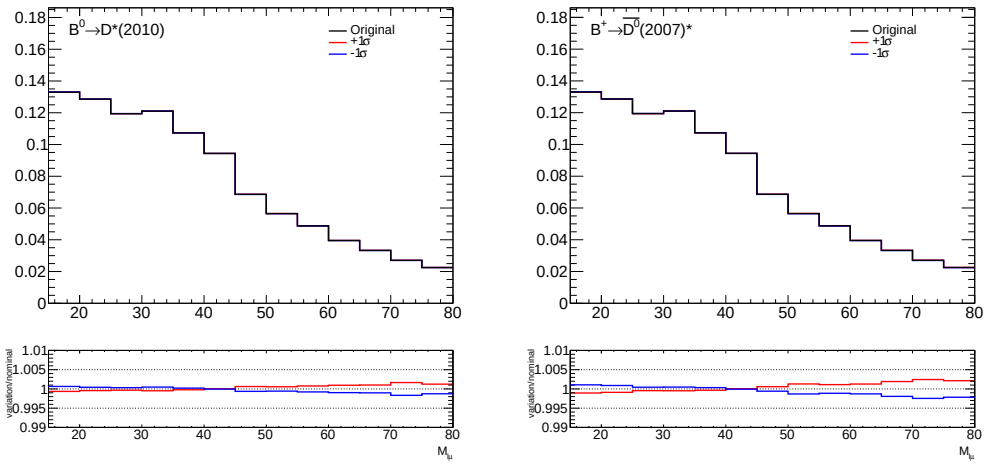

(a) **(b)**

Figure 8.12 (a) Comparison of the effect of the systematic uncertainty for $B^0 \to \overline{D^0}(2010)\mu\nu$ and (b) $B^+ \to \overline{D^*}(2007)^0\mu\nu$ exclusive decays.

8.9.3 MC event generator

The uncertainty associated with the choice of MC event generator, or NLO matching scheme, in the $t\bar{t}$ MC sample is assessed by comparing a sample generated with Powheg+Pythia8 with a sample generated with MadGraph_aMC@NLO+Pythia8 (shortened to aMC@NLO+Pythia8 in this section). The aMC@NLO matching requires specific Pythia8 settings in order to retain the NLO accuracy. These settings switch off the matrix-element corrections for both initial and final state radiation and the global-recoil settings are used for the final state radiation emissions. These settings are different to those used in the Pythia8 samples, which is used to shower the nominal Powheg sample. Therefore, comparing the nominal Powheg+Pythia8 with the aMC@NLO+Pythia8 sample would have an artificially large uncertainty, which is not due to the NLO emission but rather differences in the description of the final state radiation. Additional uncertainties are attributed to the final state radiation, therefore, to avoid double counting of uncertainties, a sample of aMC@NLO+Pythia8 is generated with the same Pythia8 settings as the aMC@NLO+Pythia8 sample. Additionally, the $t\bar{t}$ p_{T}

distribution is known to be modelled poorly in aMC@NLO+Pythia8; therefore the $t\bar{t}$ p_{T} distribution is reweighted to that of the Powheg+Pythia8.

8.9.4 Underlying event and colour reconnection

The underlying event and colour reconnection can affect the amount of radiation emitted from the b-quark and therefore impact the kinematics of the b-hadron. These effects can modify the shape of the $m_{\ell\mu}$ distribution.

To estimate the uncertainty arising from colour reconnection, two new samples are generated. In one sample, the colour reconnection strength in the Pythia8 default settings is set to the maximum value. This setting reconnects all hadrons. The other sample sets the colour reconnection strength to zero so no hadrons are reconnected. As a cross check to verify the effect of reconnection in the top decay products, a comparison with the "Early resonance decay" (ERD) model is performed. In the ERD model, the top quarks and W-bosons are allowed to decay before colour reconnection takes place. In this model the top quark decay products directly participate in colour reconnection. The impact on the measured value of the top quark mass is found to be negligible.

The variations for the underlying event are provided by eigentunes of the A14 Pythia8 tuning [113].

8.9.5 PDFs

The PDF set used in the nominal $t\bar{t}$ Powheg+Pythia8 sample is NNPDF3.0. The uncertainty is evaluated using the PDF4LHC15 error set [170] by reweighting the nominal Powheg+Pythia8 sample with 30 weights. The value for m_t is extracted for each weight and then the total systematic is taken as the sum in quadrature of the 30 variations.

8.9.6 Initial-state QCD radiation uncertainties

The uncertainty on the modelling of the initial-state QCD radiation is estimated with samples generated by varying the scales in Powheg+Pythia8. A sample with increased initial state radiation is generated with a normalisation and factorisation scale increased by a factor of 0.5, a doubled value of h_{damp} and a larger α_S^{ISR}. This sample corresponds to the Pythia8 A14 Var3cUp variation [171]. A sample with decreased initial state radiation is generated using renormalisation and factorisation scales increased by a factor of two and a lower α_S^{ISR} value. This sample corresponds to the Pythia8 A14 Var3cDw variation.

8.9.7 *b*-quark fragmentation parameter r_b uncertainty

As discussed in Section 6.1.1, the nominal $t\bar{t}$ signal sample uses a custom tuning, A14-r_b, derived from a fit to $Z \to b\bar{b}$ LEP data. The uncertainty from the fit of r_b is taken as the variance associated with a uniform distribution between the two extreme fitted values of r_b ($r_b = 1.024$ and $r_b = 1.096$). The result of the fit is $r_b = 1.05 \pm 0.021$. Two additional samples with $r_b = 1.029$ and $r_b = 1.071$ are used as the systematic variation. The effect of r_b variation on x_B can be seen in Figure 8.13 in addition to the final state radiation uncertainty.

8.9.8 Parton shower and hadronisation model uncertainties

To assess the systematic uncertainty associated with the parton shower and hadronisation model, a comparison between the nominal $t\bar{t}$ MC sample and an alternative model is used. The alternative model used is Powheg+Herwig7.1.3, which has an alternative shower algorithm, hadronisation model, underlying event and colour reconnection. The Herwig7.1.3 generator is chosen due to its improved shower description for heavy quark fragmentation and a new tune to e^+e^- data. Within the Herwig7.1.3 generator there are two shower algorithms to choose from: angular ordered shower or dipole shower. The angular ordered shower model agrees with x_B measurements from LEP better than the dipole shower model, therefore it is used for this analysis.

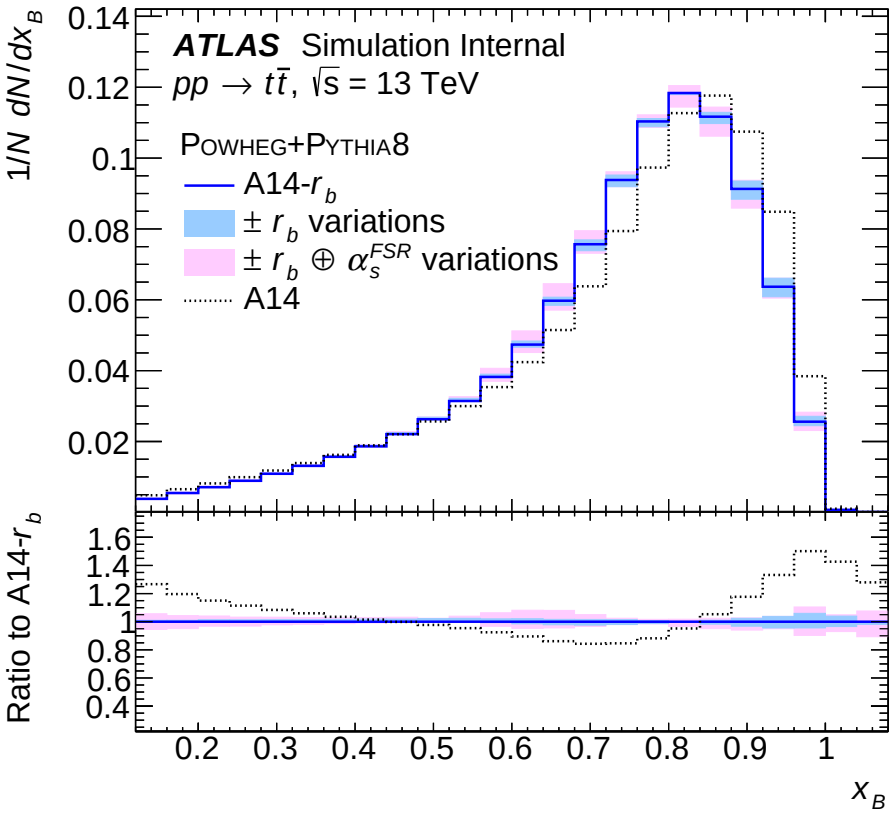

Figure 8.13 A comparison of the A14-r_b and A14 tunings of POWHEG+PYTHIA8 as a function of x_B. The uncertainty associated with r_b is shown in light blue and both r_b and FSR uncertainty is shown in pink.

8.9.9 Parton shower α_s^{FSR}

Commonly, the uncertainty on the final state radiation is evaluated with additional MC samples with the final state radiation renormalisation, $\mu_{\mathrm{R}}^{\mathrm{FSR}}$, and factorisation scales, $\mu_{\mathrm{F}}^{\mathrm{FSR}}$, varied up and down by an arbitrary factor of two. The upper range of variations varies in literature from 1.25 to $\sqrt{2}$ [134]. A newer technique based on producing event-by-event weights has recently become available [172]. Due to technical issues, the event reweighting method cannot be used in this analysis. It is, however, shown in [172] that a variation of a factor two for $\mu_{\mathrm{R}}^{\mathrm{FSR}}$ and $\mu_{\mathrm{F}}^{\mathrm{FSR}}$ using the event reweighting is approximately equivalent to a factor of an explicit $\sqrt{2}$ variation. Therefore, explicit factors of $\sqrt{2}$ and $1/\sqrt{2}$ are used for the up and down variations.

Variations of $\mu_{\mathrm{R}}^{\mathrm{FSR}}$ and $\mu_{\mathrm{F}}^{\mathrm{FSR}}$ also affect the fragmentation of the event. In order to remove the variation of fragmentation effects, the r_b for the final state radiation variation samples is refitted to LEP data using the same method outlined in Section 6.1.1. In a further step to remove any possibility of double counting uncertainties, the x_B distribution for the variation samples are reweighted to match the nominal $t\bar{t}$ sample.

8.10 Background modelling

8.10.1 $t\bar{t}$ dilepton

The modelling of the $t\bar{t}$ dilepton sample has three sources of systematic uncertainty. Similarly to the $t\bar{t}$ signal sample, the $t\bar{t}$ dilepton sample has an associated uncertainty from the modelling of initial state radiation, the choice of NLO matching and the modelling of the parton shower and hadronisation. These are estimated with a similar procedure as the $t\bar{t}$ signal. For the initial state radiation modelling, the uncertainty is derived from the same samples as the $t\bar{t}$ signal. The NLO matching uncertainty is derived from a comparison between the aMC@NLO+Pythia8 and the nominal $t\bar{t}$ sample. Finally, the parton shower and hadronisation model uncertainty is derived from the comparison between Powheg+Herwig7.0.4 and the nominal $t\bar{t}$ sample.

8.10.2 $t\bar{t}$ SMT-fake uncertainties

The uncertainty on the SMT-fake component originates from the SMT scale factor. The uncertainty on the scale factor is applied to all events where the soft muon is considered an SMT-fake. An additional uncertainty is applied to the SMT-fake component to cover the uncertainty on the modelling. The nominal $t\bar{t}$ sample is compared to an additional sample simulated with SHERPA.

8.10.3 Non-$t\bar{t}$ backgrounds

For the single top quark background, an uncertainty of $^{+5\%}_{-4\%}$ is applied to the total cross-section for single-top quark production [128–130]. An uncertainty associated with initial and final state radiation is also added and is evaluated in a similar manner to the method used for $t\bar{t}$ signal. Additional uncertainties were considered for NLO matching, parton shower and hadronisation and Wt, however, the effects are found to be negligible.

An uncertainty of 30% is applied to the Z+jets background. This uncertainty is applied independently for light and heavy flavour jet components of the Z+jets. This uncertainty is derived from simulation and verified in a data control region around the Z boson mass peak.

For the W+jets background, the uncertainty on the normalisation flavour fraction is derived from the data-driven method detailed in Section 6.2.1. The total uncertainty for the normalisation and flavour fraction is around 22% for $Wb(b)$ and Wcc components and approximately 45% for the Wc and 23% for W+light jets.

A 50% normalisation uncertainty is applied to the diboson background, which includes the uncertainty on the inclusive cross section and additional jet production [173].

Finally, a 30% systematic uncertainty is applied to the multijet background event yields derived from comparisons with data yields in control regions similar to the event selection but enriched in events from multijet background events.

Chapter 9

Mass extraction

After the event selection detailed in Chapter 5 has been applied, the distribution of the invariant mass of the prompt lepton and the soft muon, $m_{\ell\mu}$, is used to determine the mass of the top quark m_t. A *binned-template profile likelihood fit* is performed on the range $15 < m_{\ell\mu} < 80$ GeV. The reduced range is considered because the tail is more sensitive to $t\bar{t}$ modelling uncertainties and higher order corrections as well as the Z+jets background. The fit is performed on the two orthogonal samples, OS and SS, simultaneously and their sensitivity can be seen in Figure 9.1. This chapter first details the binned-template profile likelihood fit procedure and then discusses the fit verification and results.

9.1 Binned template profile-likelihood fit

9.1.1 Binned likelihood fit

A likelihood fit uses a likelihood function to assess the goodness of fit between a given model and a sample of data. In particle physics, the likelihood model for the number of events in a given bin of a distribution is given by a Poisson likelihood model. This Poisson likelihood model describes the probability of observing n data events in bin i, given some number of predicted signal, S and background B events. The number of signal events will vary depending on the model used for the prediction and this is normally included as a factor, μ, often referred to as

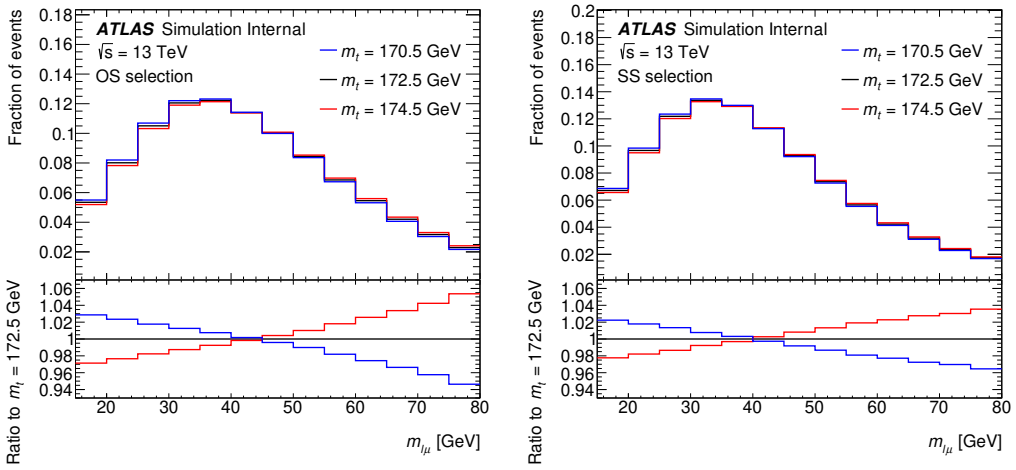

(a) **(b)**

Figure 9.1 Sensitivity of the $m_{\ell\mu}$ distribution to the input top-quark mass, estimated using simulated events for (a) OS and (b) SS samples.

the *signal strength*. This factor is referred to as the parameter of interest (POI). The likelihood is given by

$$L(n|\mu) = \prod_i \text{Pois}(n_i|\mu S_i + B_i). \tag{9.1}$$

The optimal value for the POI is then given by the maximum of the likelihood or, equivalently, the minimum of the negative log-likelihood and is denoted by $\hat{\mu}$. This is known as the maximum likelihood estimate (MLE) [174].

9.1.2 Binned profile likelihood fit

The predictions for the signal and background events have associated systematic uncertainties. These systematic uncertainties can be included in the fit as additional parameters referred to as *nuisance parameters*. Each systematic uncertainty is included as a Gaussian constrained nuisance parameter. The likelihood is modified as follows

$$L(n|\mu, \boldsymbol{\theta}) = \prod_i \text{Pois}(n_i|\mu S_i + B_i) \cdot \prod_s \text{Gaus}(a_s|\theta_s), \tag{9.2}$$

where a_s will normally come from some auxillary measurement such as the jet energy scale described in Section 4.2.4. The auxillary measurement will also have an associated uncertainty which is included in this term. The parameter θ_s refers to the nuisance parameter. Similar to the case without systematic uncertainties included, the MLEs are given by $\hat{\mu}$ and $\hat{\boldsymbol{\theta}}$.

The total uncertainty on the measurement can be estimated by using the *profile likelihood ratio*. This is given by

$$\lambda(\mu) = \frac{L(\mu, \hat{\hat{\boldsymbol{\theta}}}(\mu))}{L(\hat{\mu}, \hat{\boldsymbol{\theta}})}, \tag{9.3}$$

where $\hat{\hat{\boldsymbol{\theta}}}(\mu)$ is known as the conditional maximum likelihood estimate (CMLEs) [174]. This is the value of $\boldsymbol{\theta}$ that maximises the likelihood at a fixed μ. This term is often referred to as the *profiled value of* $\boldsymbol{\theta}$. Using $\lambda(\mu)$, a test statistic t_μ can be constructed in order to quantify the agreement of the data with a given value of μ,

$$t_\mu = -2 \ln \lambda(\mu). \tag{9.4}$$

The uncertainty on $\hat{\mu}$ can then be calculated from confidence intervals [174].

9.1.3 Binned template profile-likelihood fit

The binned profile likelihood fit works for estimating the value of some signal strength from a given prediction. However, in the case of the top mass, rather than comparing to one signal prediction with an associated signal strength, the top mass is extracted from fitting to multiple predictions. To achieve this, the problem formulation is changed: instead of predictions being in the form of $\mu S(\boldsymbol{\theta})$, they are a function of a *template* with the form $S(\mu, \boldsymbol{\theta})$.

To achieve this, a technique known as *signal morphing* is employed. A set of N templates, in the form of histograms $h_{i \in N}$, are generated at different values of m_t. The assumption is that any value of m_t can be generated from a linear combination of h_i. The signal prediction as a

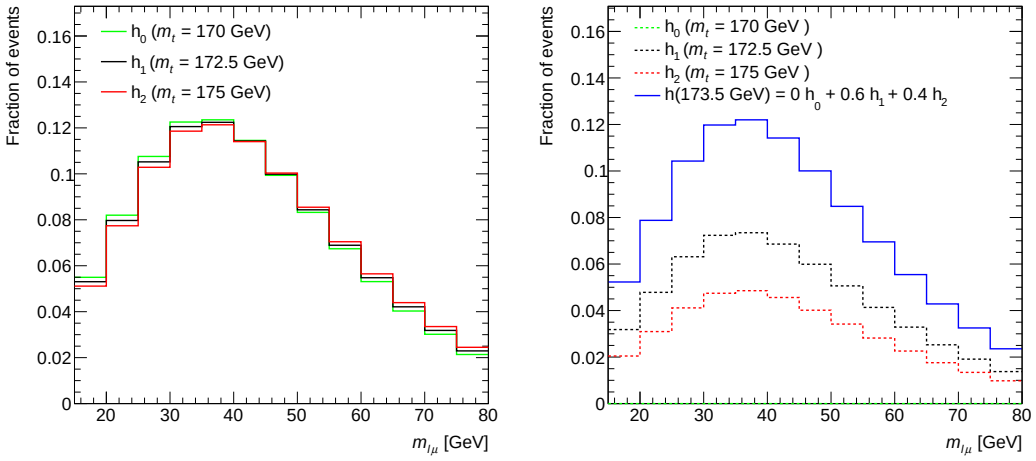

(a) **(b)**

Figure 9.2 Visualisation of the morphing technique.

function of m_t can be expressed as

$$h(m_t) = \sum_{i}^{N} w_i(m_t) h_i. \tag{9.5}$$

The weight, w_i is built using piece-wise linear interpolation and is described by

$$w_i = \begin{cases} 0 & \text{if } m_t < m_{t,i-1}, \\ 1 - m_{t,i} - m_t \frac{}{m_{t,i} - m_{t,i-1}} & \text{if } m_{t,i-1} < m_t < m_{t,i}. \\ 1 - m_t - m_{t,i} \frac{}{m_{t,i+1} - m_{t,i}} & \text{if } m_{t,i} < m_t < m_{t,i+1}. \\ 0 & \text{if } m_t > m_{t,i+1}. \end{cases}$$

An illustration of the method can be seen in Figure 9.2.

To improve the stability of the fit, a smoothing procedure is applied to the signal template. The bin contents of each prediction as a function of m_t is assumed to be linear. The bin content is fitted with a linear function and the bin contents for each m_t point are taken as the exact value of the fit. Implementing the smoothing procedure for the signal samples produces a more

parabolic negative log-likelihood distribution therefore, the asymptotic approximation can be used [175].

9.2 Fit setup

The fit is performed using the binned template profile-likelihood method outlined in the previous section. Both the OS and SS samples are fitted simultaneously, with three free parameters free in the fit: m_t which controls the shape of the $m_{\ell\mu}$ distribution for $t\bar{t}$ events and normalisation factors for the OS and SS regions, k_{tt}^{OS} and k_{tt}^{SS}. The normalisation factors fix the number of predicted events to the observed data and no m_t information is extracted.

As discussed in Chapter 8, there are a large number of systematic variations in this analysis. Since many of these systematics are considered a priori, a pruning procedure is applied to reduce the number of insignificant variations. The procedure removes from the fit systematic variations that do not affect the total prediction by more than 0.05% in a given bin. This cut-off value does not affect the overall uncertainty (< 0.03 GeV effect) significantly, however, it does reduce the complexity of the fit.

The fit method and event selection are optimised to minimise the total uncertainty on m_t while keeping the central value blinded.

9.2.1 Fit validation

Two validation tests are performed. The first is used to check the validity of the asymptotic approximation. To do so, toy experiments are generated and histograms are build where the bin content is derived by Poisson fluctuating the Asimov dataset. Here, the Asimov dataset is a dataset where the number of events in a given bin is exactly the expectation value [175]. The fit procedure is performed on these toy experiments and the resulting distribution of m_t is expected to follow Gaussian behaviour with a mean equal to the nominal top-quark mass ($m_t = 172.5$ GeV) and a standard deviation compatible with the statistical uncertainty of the fit to Asimov (see Section 9.3). Using 1000 toys the resultant distribution is Gaussian in shape

with a mean of 172.523 ± 0.015 GeV and a standard deviation of 0.460 ± 0.011 GeV. The mean is compatible with the nominal m_t value and the standard deviation is compatible with the statistical uncertainty of the fit to Asimov data (0.467 GeV).

The second test is used to check the closure of the fitting procedure. The fit is performed on histograms built in the same way as those constructed from the Asimov dataset. However, instead of the nominal expectation value in each bin, the alternative m_t expectation values are used. The fit is found to recover the correct value for m_t within errors in each case and therefore the fit is assumed to be linear and unbiased.

9.3 Fit to Asimov dataset

To assess the statistical and systematic uncertainty of the measurement, the fit is performed on the Asimov dataset with an input $m_t = 172.5$ GeV. The fitted value of m_t is exactly the input and the total uncertainty is

$$\pm 0.76 \text{ GeV} = \pm 0.40 \text{ (stat)} \pm 0.65 \text{ (syst)} \text{ GeV}.$$

The statistical uncertainty is obtained by repeating the fit while keeping constant all systematic uncertainty nuisance parameters. The systematic uncertainty is then obtained from the quadratic difference between the total and statistical uncertainties.

From the fit to the Asimov dataset there should be no pulls and only very small constraints. The pull is defined as

$$\text{pull} = \frac{(\hat{\theta} - \theta_0)}{\Delta\theta}, \tag{9.6}$$

where θ_0 is the value of the nuisance parameter from the auxillary measurement, $\hat{\theta}$ is the estimate of the nuisance parameter from the fit and $\Delta\theta$ is the uncertainty on the nuisance parameter. If the mean of the pull distribution is not 0, this would indicate the fit has altered the value of the nuisance parameter. Similarly, if the width of the distribution is less than 1,

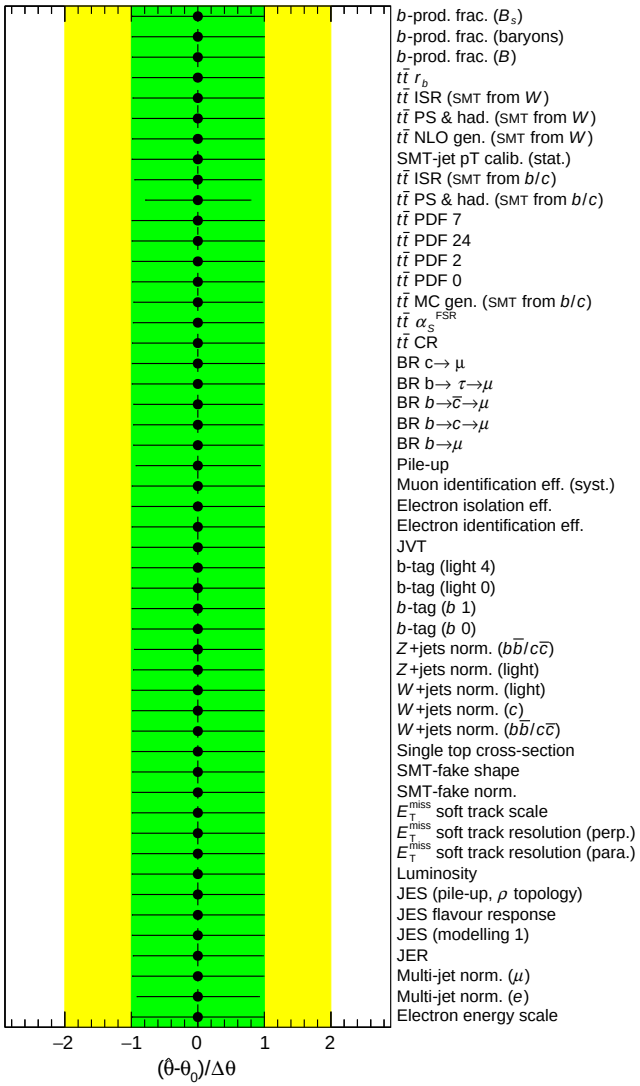

Figure 9.3 Distribution of the nuisance parameter pulls and constraints from the fit to the Asimov dataset.

the uncertainty on the nuisance parameter has been constrained. Figure 9.3 shows the pulls and constraints for the nuisance parameters in the fit to the Asimov dataset and it can be seen that the fit is behaving well with all pulls centred at 0. The ranking plot is shown in Figure 9.4. In the plot, the pulls and constraint information for each nuisance parameter is combined with their impact on the measurement. It can be that there is very little change in the value and uncertainty of the nuisance parameters, indicating the fit is behaving well.

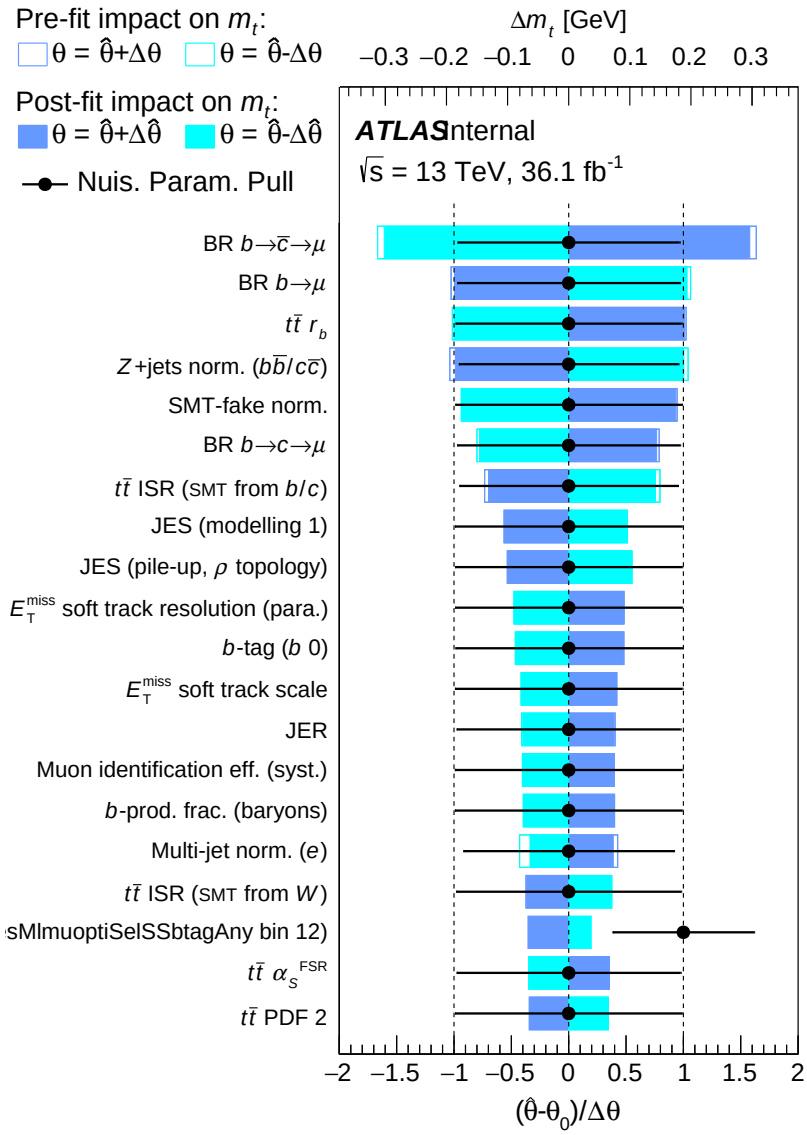

Figure 9.4 Ranking plot from the combined fit to the Asimov dataset.

9.4 Fit to data

Before the final unblinding of the result, cross checks are performed with the data, but with the fitted value of m_t kept blinded. The pulls of the nuisance parameters are checked as well as the post-fit control plots. Figure 9.5 shows the nuisance parameter pulls and constraints. All nuisance parameters have small or no pull and very few are constrained, indicating the fit is behaving well. Figures 9.6 to 9.12 show the post-fit comparisons between data and MC prediction. All control plots show good agreement between data and MC prediction within 2 standard deviations.

9.5 Result

The final result of the fit to the OS and SS samples in data is

$$m_t = 174.44 \pm 0.39(\text{stat}) \pm 0.64(\text{syst}) = 0.76(\text{stat+syst}) \text{ GeV}.$$

The goodness of fit is tested using the saturated model technique [176]. The resulting probability is 56%. The fitted values for the two normalisation factors are as follows

$$k_{tt}^{\text{OS}} = 1.030 \pm 0.009(\text{stat+syst})$$

$$k_{tt}^{\text{SS}} = 1.065 \pm 0.011(\text{stat+syst})$$

The normalisation factors are both close to unity, indicating the MC prediction is acceptable. The breakdown of the impact of the different groups of systematics can be seen in Table 9.1 and the corresponding ranking plot is shown in Figure 9.13. The addition of the systematic uncertainties to the fit reduces the total systematic uncertainty on the measurement by 2.6%.

Checks are also performed by fitting the OS and SS samples separately, resulting in the following values for the top-quark mass: $m_t(\text{OS}) = 174.63 \pm 0.86$ GeV and $m_t(\text{SS}) = 173.88 \pm 1.22$ GeV.

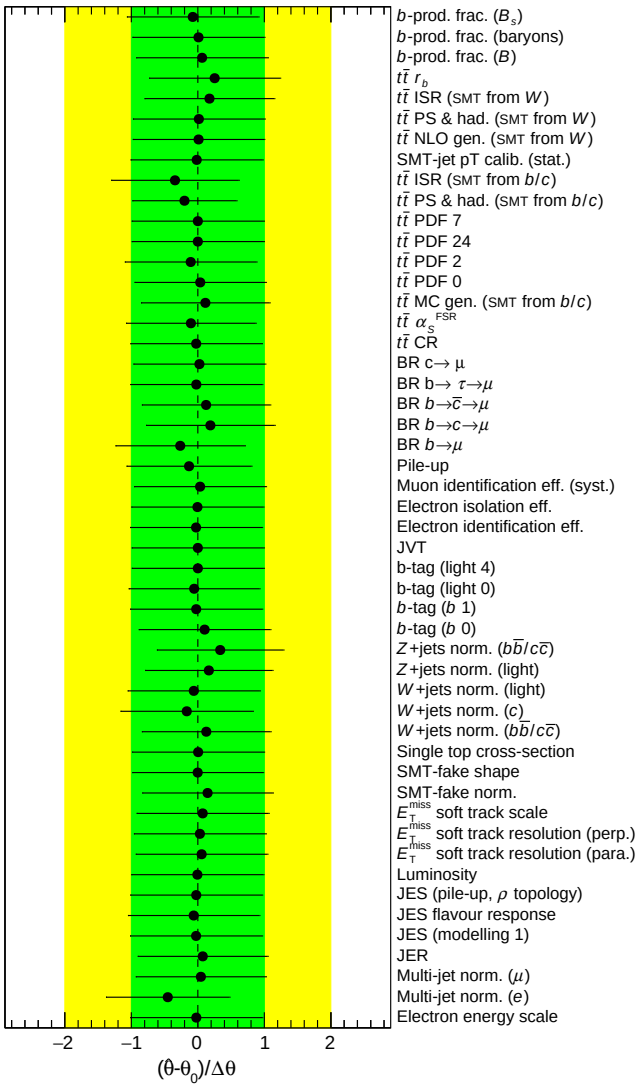

Figure 9.5 Distribution of the nuisance parameter pulls and constraints from data.

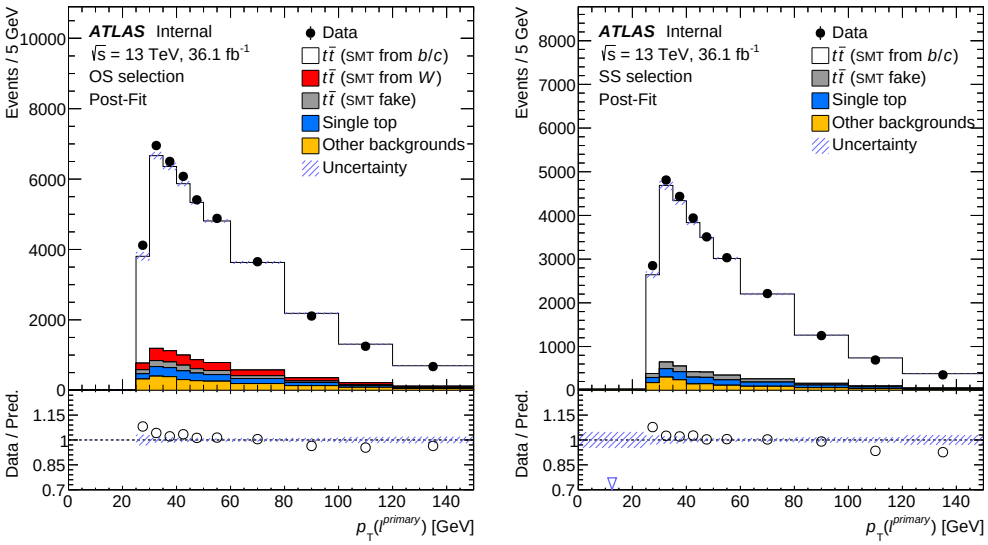

(a) $p_{\mathrm{T}}(\ell^{\mathrm{primary}})$ in the OS selection. **(b)** $p_{\mathrm{T}}(\ell^{\mathrm{primary}})$ in the SS selection.

Figure 9.6 Comparison of data and prediction for $p_{\mathrm{T}}(\ell^{\mathrm{primary}})$ for the OS (a) and SS (b). The prediction is the sum of the expected signal and background events. The uncertainty band includes the statistical and systematic uncertainies.

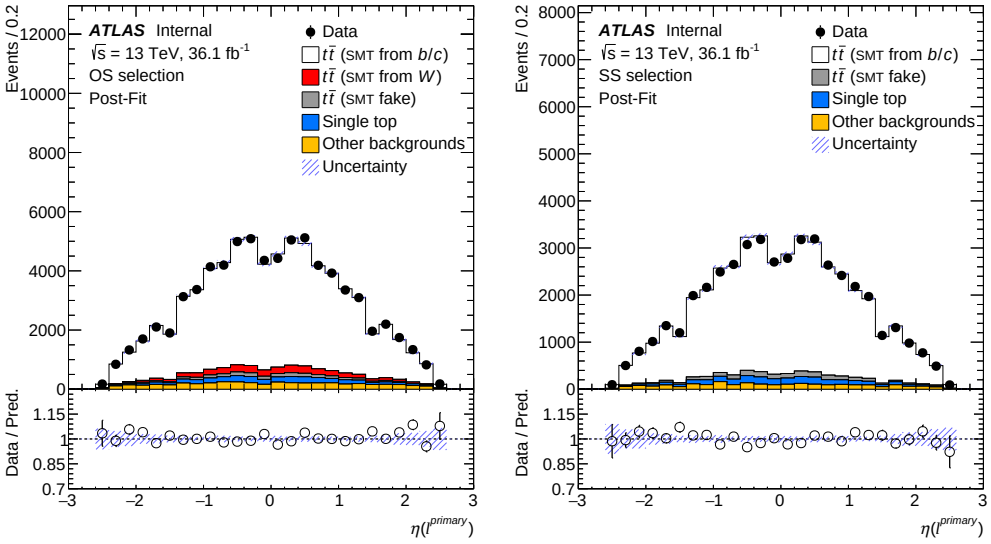

(a) $\eta(\ell^{\mathrm{primary}})$ in the OS selection. **(b)** $\eta(\ell^{\mathrm{primary}})$ in the SS selection.

Figure 9.7 Comparison of data and prediction for $\eta(\ell^{\mathrm{primary}})$ for the OS (a) and SS (b). The prediction is the sum of the expected signal and background events. The uncertainty band includes the statistical and systematic uncertainies.

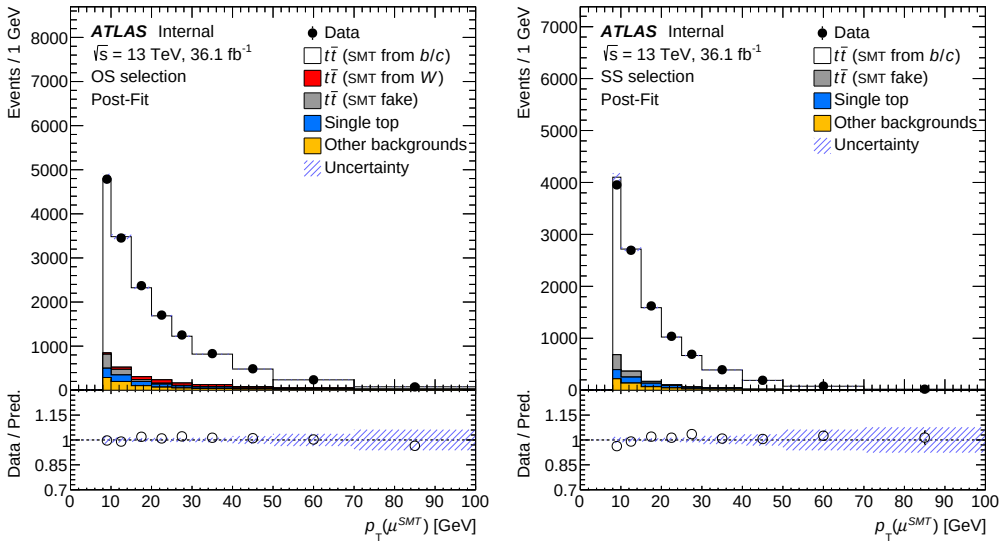

(a) $p_{\mathrm{T}}(\mu^{\mathrm{SMT}})$ in the OS selection. **(b)** $p_{\mathrm{T}}(\mu^{\mathrm{SMT}})$ in the SS selection.

Figure 9.8 Comparison of data and prediction for $p_{\mathrm{T}}(\mu^{\mathrm{SMT}})$ for the OS (a) and SS (b). The prediction is the sum of the expected signal and background events. The uncertainty band includes the statistical and systematic uncertainies.

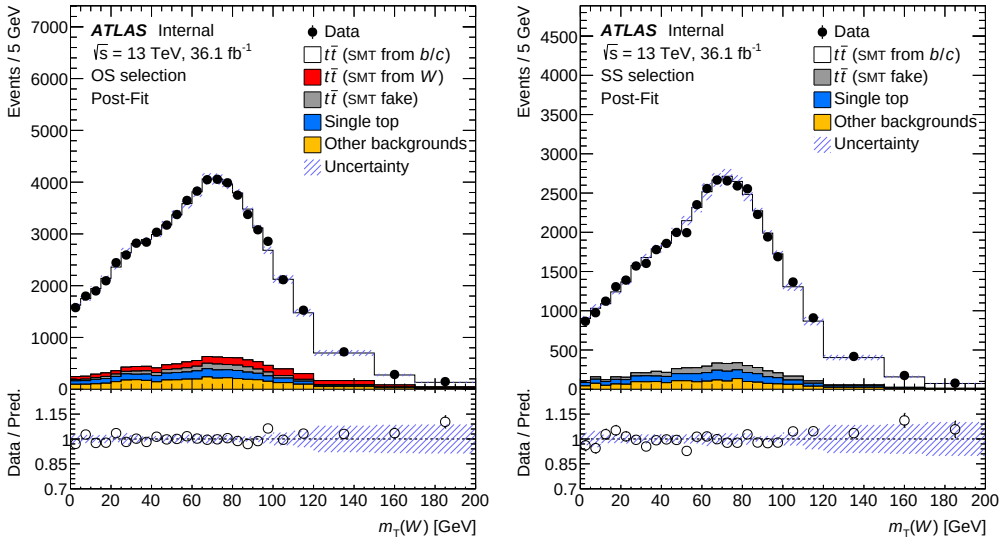

(a) $m_{\mathrm{T}}(W)$ in the OS selection. **(b)** $m_{\mathrm{T}}(W)$ in the SS selection.

Figure 9.9 Comparison of data and prediction for $m_{\mathrm{T}}(W)$ for the OS (a) and SS (b). The prediction is the sum of the expected signal and background events. The uncertainty band includes the statistical and systematic uncertainies.

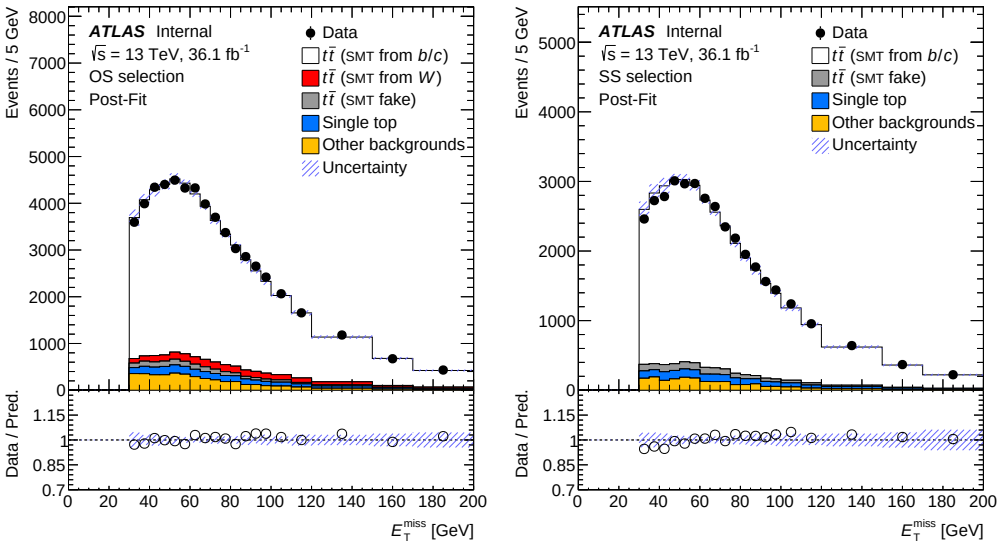

(a) $E_{\mathrm{T}}^{\mathrm{miss}}$ in the OS selection. **(b)** $E_{\mathrm{T}}^{\mathrm{miss}}$ in the SS selection.

Figure 9.10 Comparison of data and prediction for $E_{\mathrm{T}}^{\mathrm{miss}}$ for the OS (a) and SS (b). The prediction is the sum of the expected signal and background events. The uncertainty band includes the statistical and systematic uncertainies.

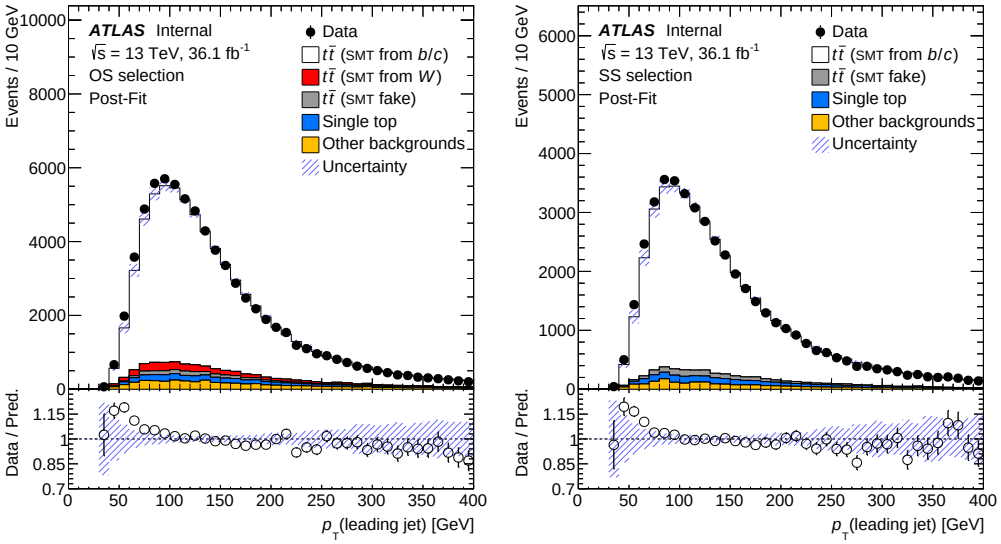

(a) p_{T}(leading jet) in the OS selection. **(b)** p_{T}(leading jet) in the SS selection.

Figure 9.11 Comparison of data and prediction for p_{T}(leading jet) for the OS (a) and SS (b). The prediction is the sum of the expected signal and background events. The uncertainty band includes the statistical and systematic uncertainies.

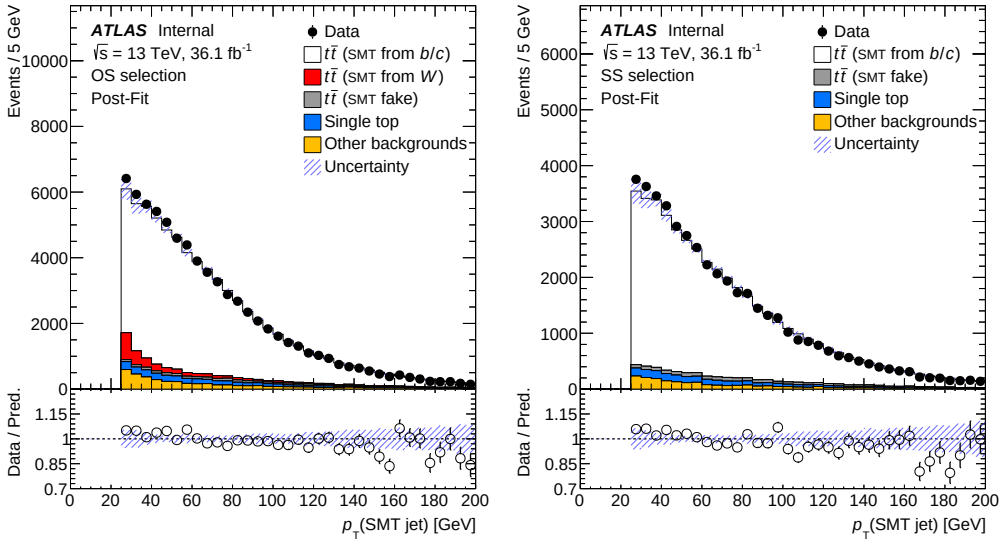

(a) p_{T}(SMT jet) in the OS selection. **(b)** p_{T}(SMT jet) in the SS selection.

Figure 9.12 Comparison of data and prediction for p_{T}(SMT jet)for the OS (a) and SS (b). The prediction is the sum of the expected signal and background events. The uncertainty band includes the statistical and systematic uncertainies.

The two values extracted agree within uncertainties. Further checks are performed by fitting the electron and muon channels, the different prompt lepton charges and different b-tagging and event selections separately. All tests produced compatible results.

A key issue that often appears in top-quark property measurements is the mismodelling of the top-quark p_{T} in current MC simulations. As can be seen in Figure 9.6, there is a disagreement between data and MC prediction for the primary lepton p_{T}, which stems from the mismodelling of the top-quark p_{T}. A test was performed in a fit for the top-quark mass using both the $m_{\ell\mu}$ distribution and the primary lepton p_{T} simultaneously to check if the mismodelling of the top-quark p_{T} spectrum affects the measurement. The test produced a top-quark mass that is compatible with that from the nominal analysis and which resulted in a similar χ^2 value.

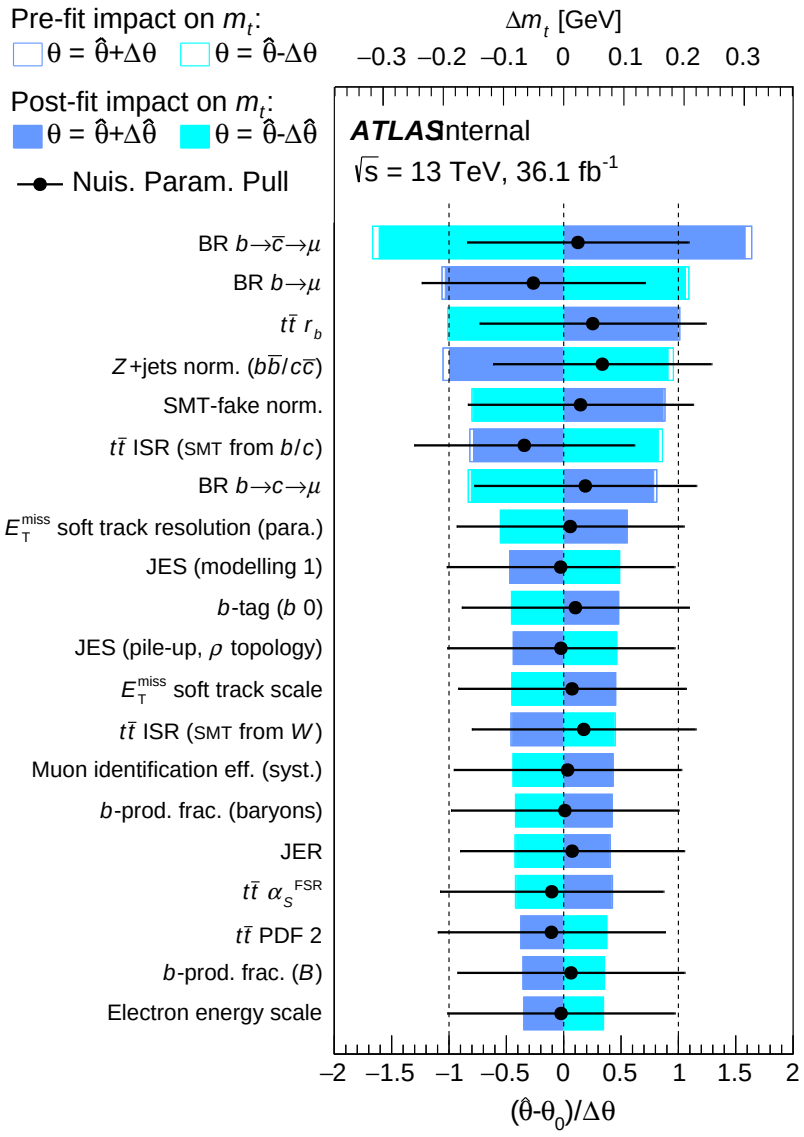

Figure 9.13 Ranking plot from the combined fit to data.

Table 9.1 Breakdown of the impact of the various sources of uncertainty on m_t, as obtained from the combined OS+SS binned template profile-likelihood fit to the real data.

Source of uncertainty	Impact on m_t [GeV]	Stat. precision [GeV]
Statistical and datasets		
Data statistics	0.39	
Signal and background model statistics	0.16	
Luminosity	< 0.01	± 0.01
Pile-up	0.04	± 0.03
Modelling of signal processes		
Monte Carlo event generator	0.04	± 0.06
b, c-hadron production fractions	0.11	± 0.01
b, c-hadron decay BRs	0.40	± 0.01
b-quark fragmentation r_b	0.19	± 0.06
Parton shower α_S^{FSR}	0.08	± 0.04
Parton shower and hadronisation model	0.07	± 0.07
Initial-state QCD radiation	0.18	± 0.08
Underlying event	< 0.01	± 0.03
Colour reconnection	< 0.01	± 0.02
Choice of PDFs	0.07	± 0.01
Modelling of background processes		
Soft muon fake	0.16	± 0.03
Multi-jet	0.06	± 0.02
Single top	0.01	± 0.01
W/Z+jets	0.17	± 0.01
Detector response		
Leptons	0.12	± 0.01
Jet energy scale	0.13	± 0.02
Soft muon jet p_{T} calibration	< 0.01	± 0.01
Jet energy resolution	0.08	± 0.05
Jet vertex tagger	< 0.01	± 0.01
b-tagging	0.10	± 0.01
Missing transverse momentum	0.15	± 0.01
Total systematic uncertainty	0.64	± 0.04
Total uncertainty	0.76	± 0.03

9.6 Conclusions

A measurement of the top-quark mass using a novel technique, utilising the partial reconstruction of the top-quark decay products has been presented. The resulting measurement is currently the most precise top-quark mass measurement from direct reconstruction of its decay products, by the ATLAS Collaboration. The result of $m_t = 174.44 \pm 0.39(\text{stat}) \pm 0.64(\text{syst}) = 0.76(\text{stat+syst})$ GeV is consistent with the current ATLAS combination of top-quark mass measurements within 2.2 standard deviations. The main uncertainties are from the b-quark decay and fragmentation, as well as the modelling of the top-quark pair production. As discussed in Section 6.1.1, the modelling of b-quark fragmentation in the simulation is not good. In order to improve this, the MC tuning should be improved using differential cross-section measurements that have sensitivity to the b-quark fragmentation. Currently, the MC generators used by the ATLAS Collaboration are tuned using only LEP data for the b-quark fragmentation. Including measurements from the LHC should help improve the MC tuning.

It is clear from this measurement that the soft muon has sensitivity to the b-quark fragmentation and therefore the kinematics of observables related to it are good candidates for differential cross-section measurements. The next chapter will detail differential cross-section measurements using observables related to the soft muon.

Chapter 10

Measurement of top-quark pair differential cross-sections

Using the same objects, event selection and systematic uncertainties as were used in the top-quark mass analysis presented in the previous chapters, the following chapter details the differential cross-section measurements.

10.1 Analysis outline

In the previous chapter, the top quark mass was measured using the invariant mass of a soft muon and a charged lepton from the leptonically decaying W boson produced in the decay of a $t\bar{t}$ pair. One of the dominant uncertainties in the measurement originates from the b-quark fragmentation. As discussed in Section 6.1.1, the modelling of the b-quark fragmentation in the standard tuning used for ATLAS MC samples does not describe the observed data for observables related to the soft muon well. To improve this modelling, a refit to LEP data is performed to update the tuning.

Currently, the standard ATLAS MC tunes, such as A14 [177] and Monash [134], only use LEP data for observables sensitive to b-fragmentation. To improve the MC predictions for

observables related to the decay products of b quarks, measuring observables in LHC data that are sensitive to b-fragmentation is required.

Using observables built from the soft muon kinematics used in the top-quark mass measurement, differential cross-sections are measured and compared with various signal predictions. These signal predictions have different fragmentation parameterisations or completely differing hadronisation models. The agreement between data and these models can give an indication of which MC generators perform best.

This is an exploratory study using the same 36.1 fb^{-1} of data as the top quark mass measurement and which will be used to identify new observables that could be used in a full Run 2 differential cross-section analysis. Non-optimal jet definitions at particle level mean the precision of this exploratory study will likely be lower than a full Run 2 study.

10.1.1 Observables

Observables are chosen for their dependence on the hadronisation and heavy quark fragmentation parameters of the MC predictions. The measured observables are:

- $m_{\ell\mu}$ - The invariant mass of the charged lepton originating from the leptonically decaying W-boson and the soft muon;
- $p_{\text{T}}(W\text{-lepton})$ - The transverse momentum of the charged lepton originating from leptonically decaying W-boson;
- $p_{\text{T}}(\mu\text{-soft})$ - The transverse momentum of the soft muon;
- $p_{\text{T}}^{\text{rel}}(\mu\text{-soft})$ - The transverse momentum of the soft muon transverse to the axis of the SMT jet, which is given by

$$p_{\text{T}}^{\text{rel}}(\mu\text{-soft}) = \frac{|\mathbf{p}(\mu\text{-soft}) \times \mathbf{p}(\text{SMT jet})|}{|\mathbf{p}(\text{SMT jet})|}; \tag{10.1}$$

- $p_{\mathrm{T}}^{\mathrm{z}}(\mu\text{-soft})$ - The transverse momentum of the soft muon longitudinally to the axis of the SMT jet, which is given by

$$p_{\mathrm{T}}^{\mathrm{z}}(\mu\text{-soft}) = \frac{\mathbf{p}(\mu\text{-soft}) \cdot \mathbf{p}(\text{SMT jet})}{|\mathbf{p}(\text{SMT jet})|^2}; \tag{10.2}$$

- $p_{\mathrm{T}}(\mu\text{-soft})/p_{\mathrm{T}}(\text{SMT jet})$ - The ratio of the transverse momentum of the soft muon and the transverse momentum of the SMT jet;

- $p_{\mathrm{T}}(\text{SMT jet})$ - The transverse momentum of the SMT jet.

From the studies performed in the top mass extraction analysis, $m_{\ell\mu}$ has a clear dependence on the heavy quark fragmentation due to the soft muon component. The $p_{\mathrm{T}}(W\text{-lepton})$ will be sensitive to various NLO generator models. Both $p_{\mathrm{T}}^{\mathrm{rel}}(\mu\text{-soft})$ and $p_{\mathrm{T}}^{\mathrm{z}}(\mu\text{-soft})$ have sensitivity to both the p_{T} and axis of the soft muon and the SMT jet. The ratio $p_{\mathrm{T}}(\mu\text{-soft})/p_{\mathrm{T}}(\text{SMT jet})$ acts as a proxy for x_B, discussed in Section 6.1.1. Although the B-hadron is not fully reconstructed, $p_{\mathrm{T}}(\mu\text{-soft})$ acts as a proxy and therefore the ratio with the SMT jet p_{T} will carry similar information as x_B. Although $p_{\mathrm{T}}(W\text{-lepton})$ does not have sensitivity to b-fragmentation, the measurement of the differential cross-section in a new fiducial region is useful. It has been shown in previously top-quark differential cross-section analyses [178] that there is a disagreement between data and MC in the $p_{\mathrm{T}}(W\text{-lepton})$ observable therefore, further measurements in different phase spaces are important.

10.2 Unfolding

In particle physics, the distributions of measured observables are subject to the effects of limited detector resolution, acceptance and efficiency effects. The distorted measured distributions will have random noise and bias effects when compared with the underlying true distribution. Often, it is useful to compare the measurements of an underlying physics process between experiments where the effects of detector distortion will vary. Similarly, comparing with a new theoretical prediction is much simpler without the need to simulate the detector response. In order to

estimate the underlying true distribution for a given measured distribution, a method known as *unfolding* is used.

The problem of unfolding can be summarised as estimating the probability distribution of some data where no parametric form is available. Unfolding falls into the category of *inverse problems* in mathematics and is also referred to as *deconvolution* or *unsmearing* [179].

This section outlines the formulation of the unfolding problem as well as an overview of the method used in this analysis.

10.2.1 Problem formulation

The aim of unfolding is to estimate some $f_{\text{truth}}(y)$ probability density function from an observed random variable x. In particle physics, the measured distributions will generally not be a continuous function but rather a binned histogram. For the true probability density function $f_{\text{truth}}(y)$, the probability of a measurement to be in bin j is given by

$$p_j = \int_{\text{bin } j} f_{\text{truth}}(y)\, dy. \tag{10.3}$$

If an experiment is performed with a total number of events m_{tot}, the expected number of events is given by the expectation value of the total number of events, $E[m_{\text{tot}}] = \mu_{\text{tot}}$. Therefore, the expected number of events in bin j is given by

$$\mu_j = \mu_{\text{tot}} p_j. \tag{10.4}$$

Using these expected values, the true histogram $\boldsymbol{\mu} = (\mu_1, \dots \mu_M)$ with M bins can be built.

In addition to the true histogram, the measured values of x are also binned into a histogram of N bins, $\mathbf{n} = (n_1, \dots, n_N)$. In a similar way to the process described in Chapter 9, the number of events in a given bin n_i can be modelled as an independent Poisson variable with an expectation value ν_i. The expected histogram of the observed data is then given by $\boldsymbol{\nu} = E[\mathbf{n}]$.

The expected number of observed events in a given bin is related to the true number of events in that bin. The relation depends on the effects of the detector response, efficiency, acceptance and the presence of background events. The expected number of observed events in bin i is given by

$$\nu_i = \sum_{j=1}^{M} R_{ij}\,\mu_j + \beta_i, \tag{10.5}$$

where β_i are the number of entries in bin i originating from background events and R_{ij} is the ijth element of the *response matrix*. Each element of the response matrix is defined by

$$R_{ij} = P(\text{observed in bin } i | \text{true value in bin } j), \tag{10.6}$$

and R an $N \times M$ matrix. The response matrix is built using a MC event generator to produce the true data. The true data is then passed through the detector reconstruction process to create the corresponding expected measured data. Equation 10.6 can be generalised to the histograms for each quantity

$$\boldsymbol{\nu} = R\boldsymbol{\mu} + \boldsymbol{\beta}. \tag{10.7}$$

The goal of unfolding is then to construct estimators $\hat{\boldsymbol{\mu}}$ for the true histograms, given some observed data $\mathbf{n}$.

The obvious solution, assuming $N = M$, is to invert Equation 10.7

$$\boldsymbol{\mu} = R^{-1}(\boldsymbol{\mu} - \boldsymbol{\beta}). \tag{10.8}$$

Another obvious choice is to use the observed data as an estimator for $\boldsymbol{\nu}$. It can be easily shown that $\hat{\boldsymbol{\nu}} = \mathbf{n}$ is also the maximum likelihood and least squares solution [179]. The estimator for $\boldsymbol{\mu}$ is then given by

$$\hat{\boldsymbol{\mu}} = R^{-1}(\mathbf{n} - \boldsymbol{\beta}). \tag{10.9}$$

The estimator built by simply inverting the response matrix, while unbiased, can have extremely large variances and strong correlations between neighbouring bins. This effect arises from the fact that the detector response will generally smear out any fine structure in the true distribution. In the case where $\boldsymbol{\nu}$ is unfolded with R^{-1}, the exact $\boldsymbol{\mu}$ distribution is returned. However, in a real measurement $\mathbf{n}$ is used as an estimator for $\boldsymbol{\nu}$. The measured data will have a fine structure from statistical fluctuations and so applying R^{-1} to the measured data will lead to large oscillations between neighbouring bins.

In order to combat these effects, a technique known as *regularisation* is employed. The general idea of regularisation is to introduce some measure of smoothness to the true histogram $\boldsymbol{\mu}$. One approach is to instead of minimising the negative log-likelihood, to minimise a *cost functional*

$$\Phi(\boldsymbol{\mu}) = -\alpha \log L(\boldsymbol{\mu}) + S(\boldsymbol{\mu}), \tag{10.10}$$

where α is some regularisation parameter and $S(\boldsymbol{\mu})$ is a regularisation function which penalises high variance in the distribution. The regularisation parameter is used to control the bias-variance trade-off. It can be shown that the maximum likelihood estimator for $\boldsymbol{\mu}$ has the minimum variance for an unbiased estimator. Therefore, by reducing the variable with regularisation, there must be an increase in bias. There are many different possible regularisation functions which can be used [180–182].

10.2.2 Unfolding methods

There exists a plethora of methods to perform regularised unfolding in a particle physics setting. Methods include using Tikhonov regularisation [183], single valued decomposition [184] and a Fully Bayesian Unfolding method [185]. Recently, the use of Gaussian Processes for unfolding has been developed [186]. There are also many literature reviews of the field available [187–189].

One of the more commonly used methods in particle physics, and specifically top quark physics, is an iterative technique based on *expectation maximisation*. In particle physics, this method is more commonly referred to as the D'Agostini method [190] or the Richardson-Lucy

algorithm [191–193]. Instead of using a regularisation function, this method takes an iterative approach.

First, a set of probabilities of an event being found in each bin are determined, $\mathbf{p} = (p_1, \ldots, p_M)$. For the first iteration, the probability can be taken as $p_i = 1/M$ for bins of equal size. The initial estimators for $\boldsymbol{\mu}$ are given by

$$\hat{\boldsymbol{\mu}}^{(0)} = n_{\text{tot}}\, \mathbf{p}^{(0)}. \tag{10.11}$$

Then, for each iteration, the estimator for the true number of events in a given bin i is defined by

$$\hat{\mu}_i^{(k+1)} = \sum_{j=1}^{N} \left(\frac{R_{ij} p_i^{(k)}}{\sum_l R_{jl} p_l^{(k)}} \right) n_j, \tag{10.12}$$

where n_j is the observed number of events with the background subtracted. In each iteration, the new prior probabilities are taken as the result of the previous iteration, $\mathbf{p}^{(k)} = \hat{\boldsymbol{\mu}}^{(k-1)}/\mu_{\text{tot}}$. The inverse of the response matrix can be thought of as the conditional probability that the true value is in bin i, given that it was found in bin j, $R_{ij}^{-1} = P(\text{true value in bin } i | \text{measured in bin } j)$. The method uses Bayes' theorem to rewrite this conditional probability in terms of the response matrix and the prior probabilities.

In this iterative method, the number of iterations is considered as the regularisation parameter. As the number of iterations increases, the resulting estimator tends towards the maximum likelihood estimator. This means that a larger number of iterations increases the variance but decreases the bias.

10.2.3 Unfolding in differential cross-section measurements

In differential cross-section measurements, unfolding is used in order to compare a given observable to different theoretical predictions. These unfolded measurements allow theorists to compare their models to existing measurements or for experimentalists to tune MC simulation parameters.

When unfolding, the measured data can be unfolded to different *levels* of truth. At these levels, the objects that make up the true prediction can vary. As discussed in Section 5.7, at *particle level*, observables are built from stable particles before their interaction with the detector. Another possibility is *parton level*, where observables are derived from the final state output of the matrix element calculation. In this analysis, particle level observables are used because at parton level, the soft muon will not be defined due to its origin in the hadronisation process.

In order to calculate the differential cross-section for an observable X, in bin j the following equation is used

$$\frac{\mathrm{d}\sigma}{\mathrm{d}X_j} = \frac{1}{\mathcal{L}} \frac{1}{\Delta X_j} \frac{1}{\varepsilon_j} \sum_i \left[\mathcal{M}_{ij}^{-1}\right]^{\mathsf{T}} f_i^{\mathrm{acc}} (n_i - \beta_i). \tag{10.13}$$

Here, the index $i = 1, \ldots, N$ runs over the measured bins and $j = 1, \ldots, M$ over the unfolded bins. For this analysis, the number of measured bins and unfolded bins are equal, $N = M$. The integrated luminosity is given by $\mathcal{L}$ and ΔX_j is the width of bin j. ε_j represents the efficiency of detection. The efficiency is defined as the ratio of the number of events passing both particle level and reconstructed level selection requirements and the number of events passing the particle level selection and is given by

$$\varepsilon_j = \frac{n_j^{\mathrm{reco} \wedge \mathrm{particle}}}{n_j^{\mathrm{particle}}}. \tag{10.14}$$

The efficiency correction is applied to correct for inefficiency of reconstruction. Similarly, the acceptance f_i^{acc} is defined as the ratio of the number of events passing both particle level and reconstructed level selection requirements with the number of events passing the reconstructed level selection and is given by

$$f_i^{\mathrm{acc}} = \frac{n_j^{\mathrm{reco} \wedge \mathrm{particle}}}{n_j^{\mathrm{reco}}}. \tag{10.15}$$

The acceptance factor corrects for event which are reconstructed but fall outside of the particle level fiducial cuts. The term $\mathcal{M}_{ij}^{-1}$ is known as the migration matrix and is related to the

response matrix via

$$R_{ij} = \frac{\varepsilon_j}{f_i^{\text{acc}}} \times \mathcal{M}_{ij}. \tag{10.16}$$

This term represents whichever regularised unfolding procedure is being used, which, in this case, is the D'Agostini method. Finally, n_i and β_i are the observed number of events and background events, respectively, in bin i.

The migration matrices, efficiency and acceptance factors derived from MC for each observable can be seen in Figures 10.1 to 10.7. For the leptonic observables the migration matrices are very diagonal, as expected. However, the matrices for the jet observables have a significant contribution from off-diagonal elements. This is not a physical phenomena or detector effect, but rather, it is due to the definition of a jet at particle level. The particle level jet definition in the software release used for this analysis includes the charged leptons and neutrinos in the jet clustering. At reconstructed level, however, neither are included. This manifests as particle level jets having harder p_{T} spectra and therefore the migration matrices are much less diagonal. While this is not a major problem, it is more optimal to have diagonal migration matrices for unfolding.

10.2.4 Regularisation optimisation

In the D'Agostini method for unfolding, the number of iterations, r, determines the regularisation. In order to determine the optimal regularisation, in a similar manner to the binning optimisation, a semi-automated procedure is used.

First, the reconstructed and particle level MC samples are split into two equal subsamples, referred to as *training* and *test* samples. The training samples are used to build the migration matrix, efficiency and acceptance factors. The test sample is then treated as pseudodata and is unfolded using the correction factors derived with the training sample. For each bin in a given observable, toy experiments are thrown by sampling from a Gaussian distribution defined with a mean given by the number of events in the given bin and variance given by the corresponding

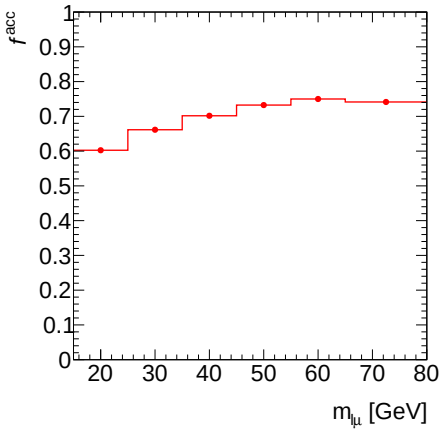

(a) Acceptance f^{acc}.

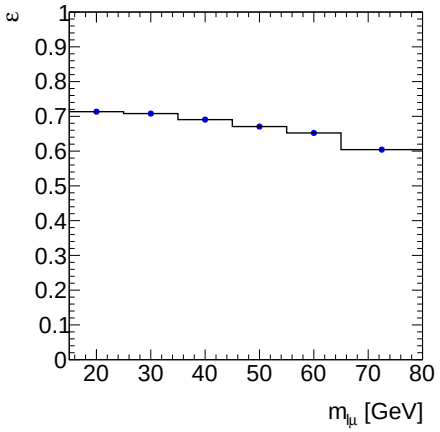

(b) Efficiency ε

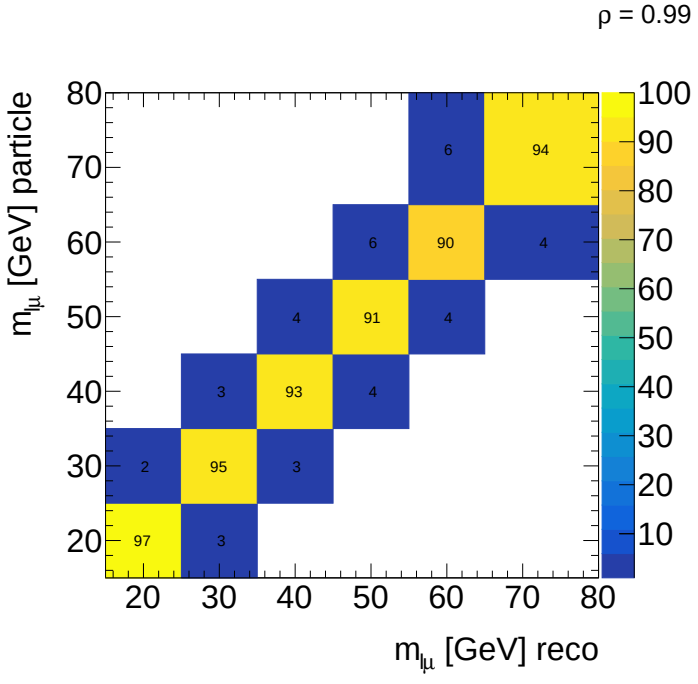

(c) Migration matrix

Figure 10.1 Correction factors for $m_{\ell\mu}$.

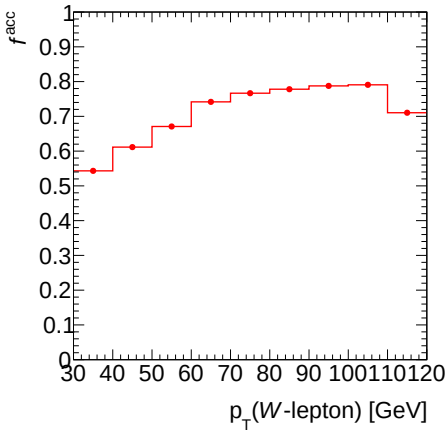

(a) Acceptance f^{acc}.

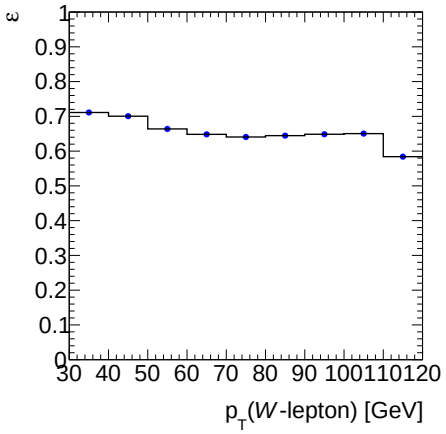

(b) Efficiency ε

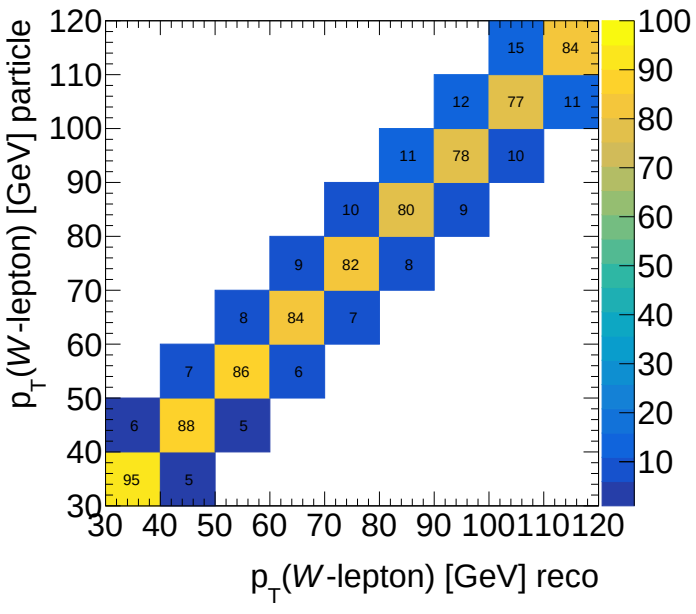

(c) Migration matrix

Figure 10.2 Correction factors for p_{T}(*W*-lepton).

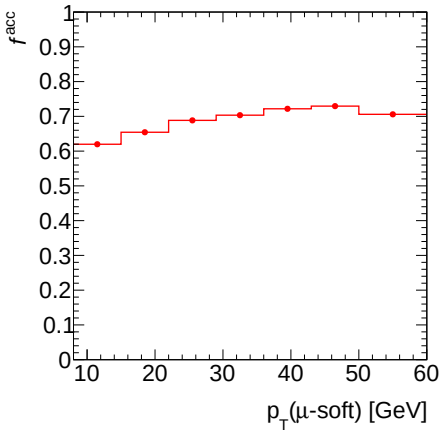

(a) Acceptance f^{acc}.

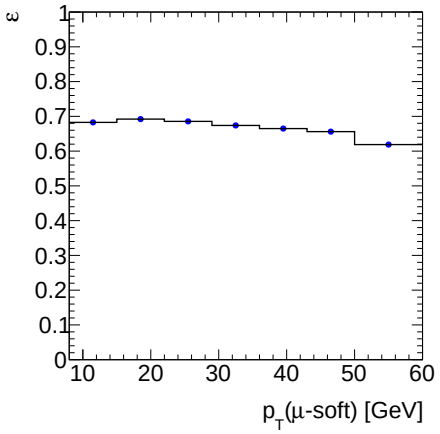

(b) Efficiency ε

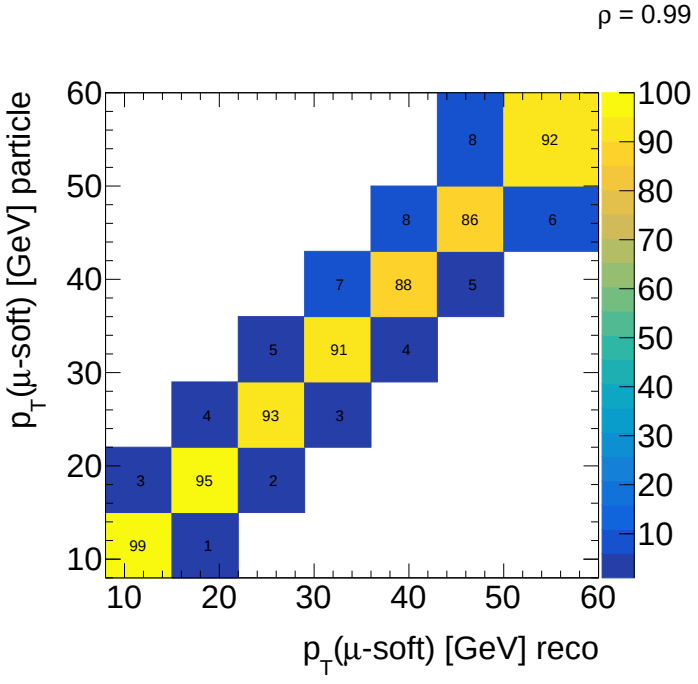

(c) Migration matrix

Figure 10.3 Correction factors for $p_{\text{T}}(\mu\text{-soft})$.

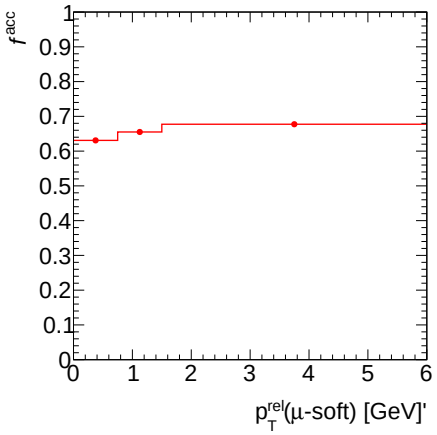

(a) Acceptance f^{acc}.

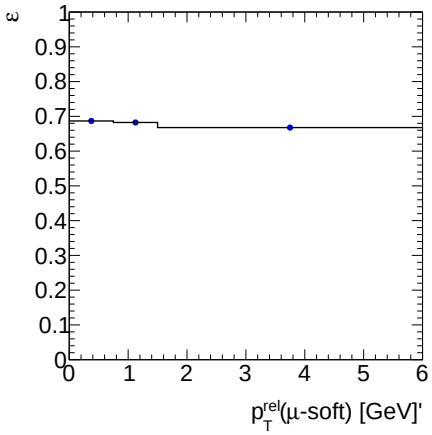

(b) Efficiency ε

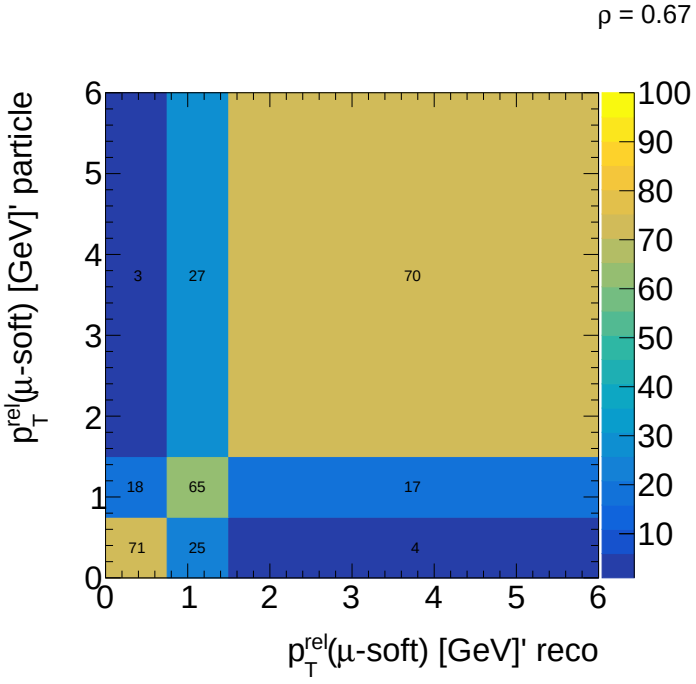

(c) Migration matrix

Figure 10.4 Correction factors for $p_{\text{T}}^{\text{rel}}(\mu\text{-soft})$.

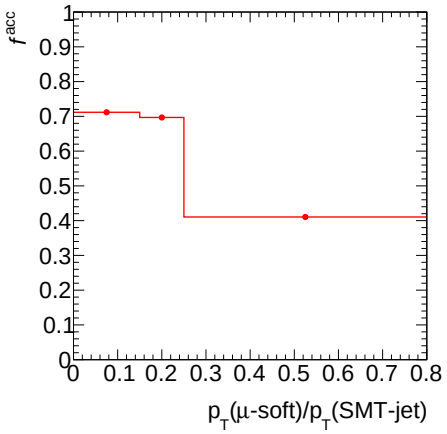

(a) Acceptance f^{acc}.

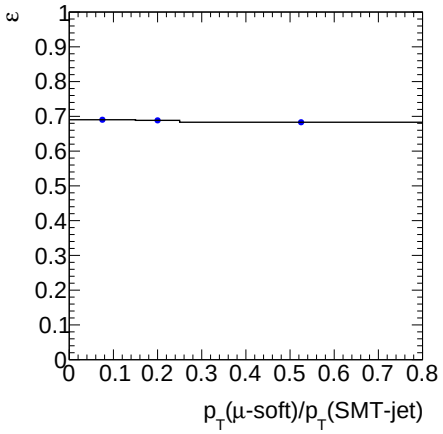

(b) Efficiency ε

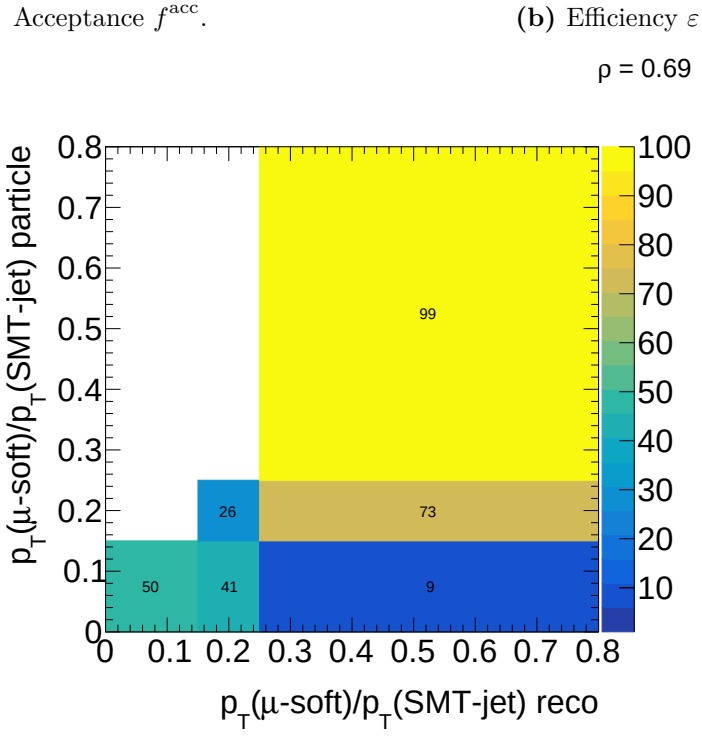

(c) Migration matrix

Figure 10.5 Correction factors for $p_{\text{T}}(\mu\text{-soft})/p_{\text{T}}(\text{SMT jet})$.

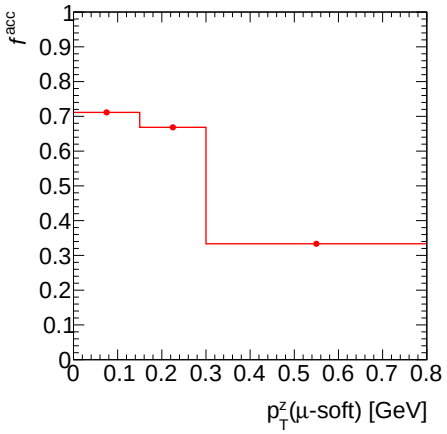

(a) Acceptance f^{acc}.

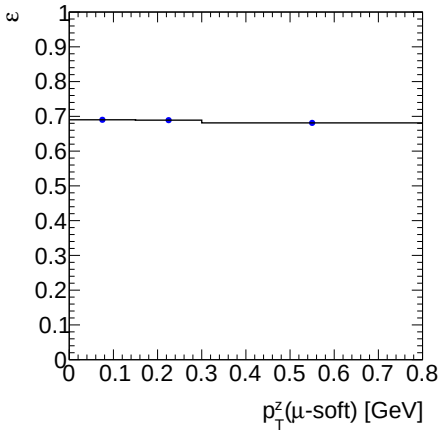

(b) Efficiency ε

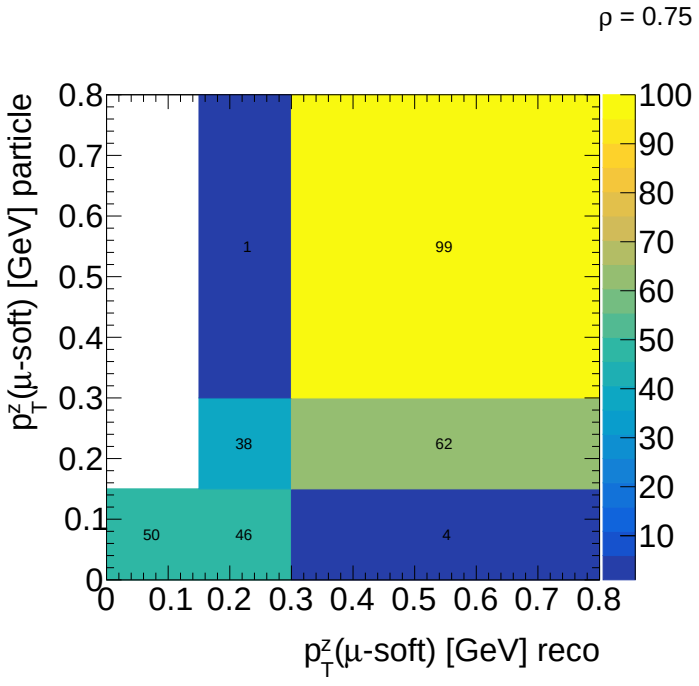

(c) Migration matrix

Figure 10.6 Correction factors for $p_{\text{T}}^{\text{z}}(\mu\text{-soft})$.

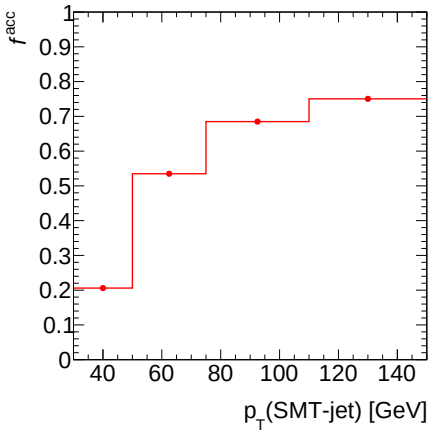

(a) Acceptance f^{acc}.

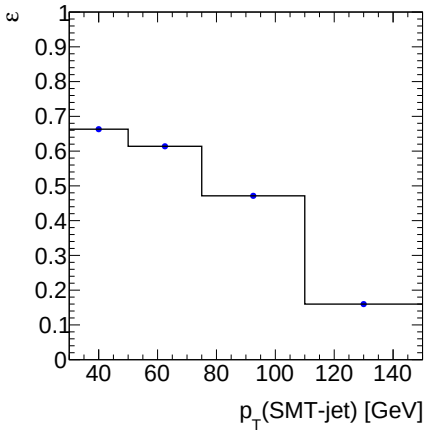

(b) Efficiency ε

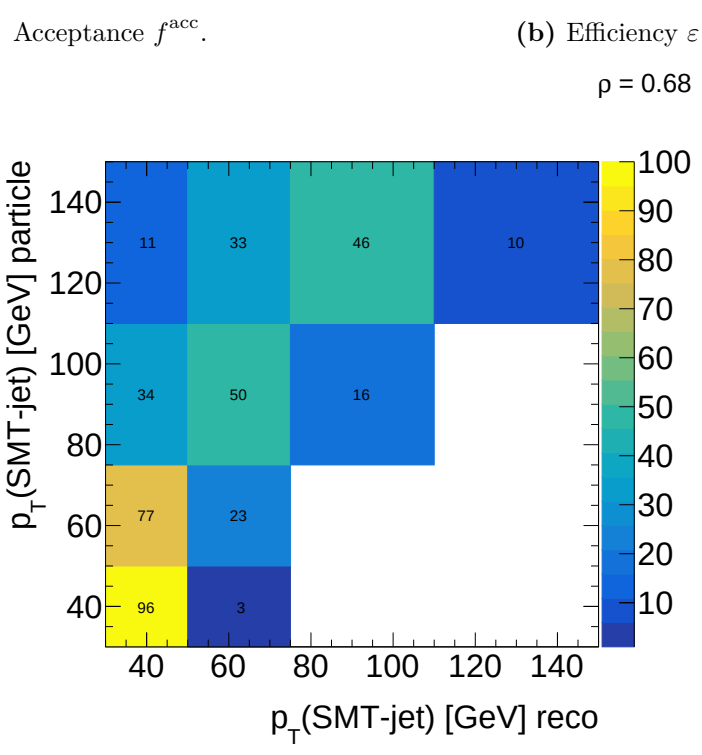

(c) Migration matrix

Figure 10.7 Correction factors for p_{T}(SMT jet).

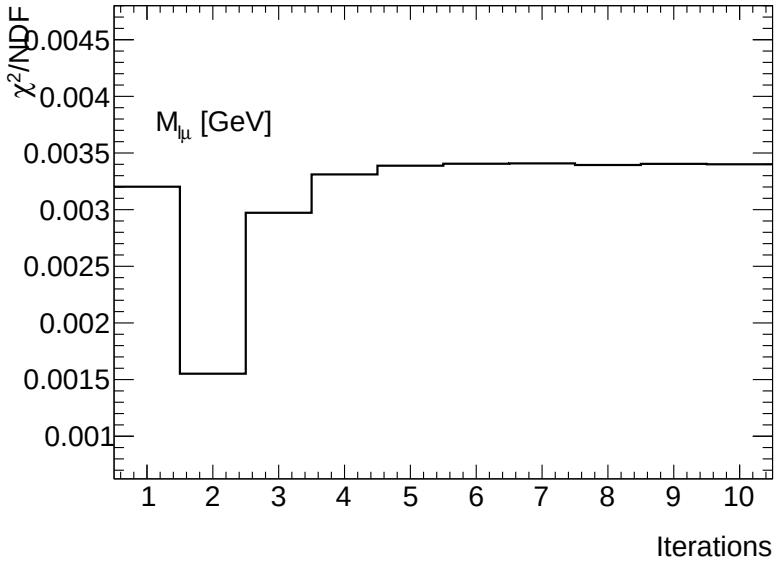

Figure 10.8 The χ^2/NDF as a function of the number of iterations used for the D'Agostini unfolding method for the $m_{\ell\mu}$ observable.

bin variance. Alternative samples are built using the toy experiments and each sample is unfolded using the correction factors derived from the training samples. For each alternative sample a χ^2 test statistic is calculated to assess the agreement between the unfolded alternative sample and the underlying truth. This procedure is repeated with values of $r = 1, \ldots, 10$ for each observable. The mean of the χ^2 test statistic for each value of r is calculated and the r corresponding to the lowest χ^2 is used as the initial regularisation parameter. An example of a plot of the χ^2 as a function of the number of iterations can be seen in Figure 10.8.

As discussed in the previous section, the number of iterations controls the regularisation of the unfolding. More iterations will tend to produce a result with lower bias, with the opposite being true with fewer iterations. Therefore, in order to pick the optimal regularisation parameter the unfolding validation tests must also be taken into account. Using the validation methods in Sections 10.2.5 and 10.2.6, the regularisation can be further optimised. The final result suggests $r = 2$ is the optimal parameter for all observables.

10.2.5 Closure test

In order to validate the unfolding procedure with the given migration matrices, efficiency and acceptance terms, *closure* and *stress* tests are performed. The closure test ensures that the unfolding procedure is performed correctly. There are two types of closure test: a *technical* closure test and *split* closure test.

The technical closure test is performed to check the unfolding code is working correctly. For this test, the reconstructed distribution is unfolded and compared with the particle level distribution. The same events that are used to derive the migration matrix and correction factors are used as input, therefore the expectation is the unfolded distribution is exactly the truth. This test serves predominantly as a sanity check.

The split closure test splits the reconstructed and particle level MC samples into two equal subsamples, as in the previous section. The unfolded pseudodata is compared to the test sample particle level distribution and a χ^2 test statistic is calculated. If the p-value is > 0.05 then the sample is considered to close. However, if this condition is not met, then the bin edges and widths are adjusted.

For all observables the samples were considered to close with the final binning configurations and the comparisons between unfolded pseudodata and the particle level test samples can be seen in Figures 10.9 and 10.10.

10.2.6 Stress tests

The other validation test is the stress test. The stress test assesses the unfolding procedures' ability to recover an acceptable estimate for the underlying truth distribution when the shape of the measured data is different from the truth distribution used to derive the correction factors. There are three stress tests used to validate the unfolding: a *data/MC discrepancy* stress test, a *linear* stress test and a *bump injection* stress test. In a similar manner to the closure test, the MC samples are split in half with one treated as a test sample and the other a training sample. The pseudodata and particle level test distribution are reweighted to alter the shape of the

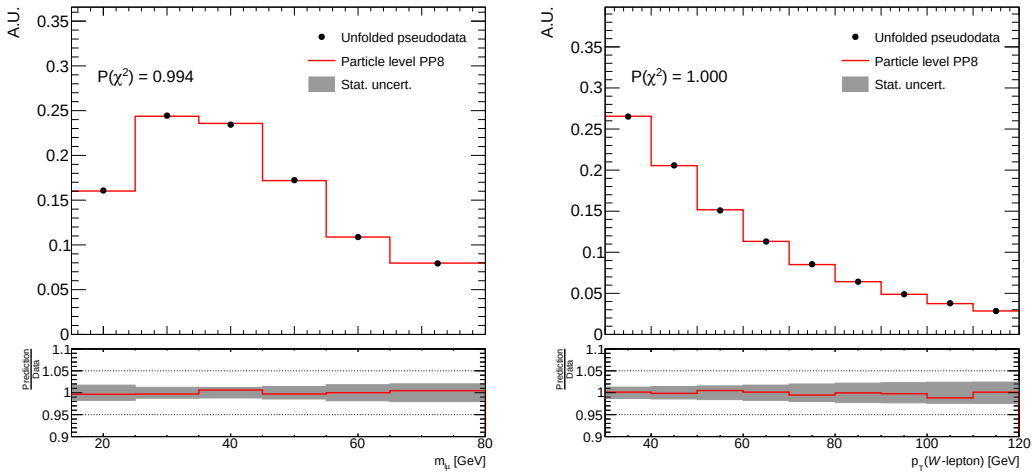

(a) $m_{\ell\mu}$

(b) $p_{\mathrm{T}}(W\text{-lepton})$

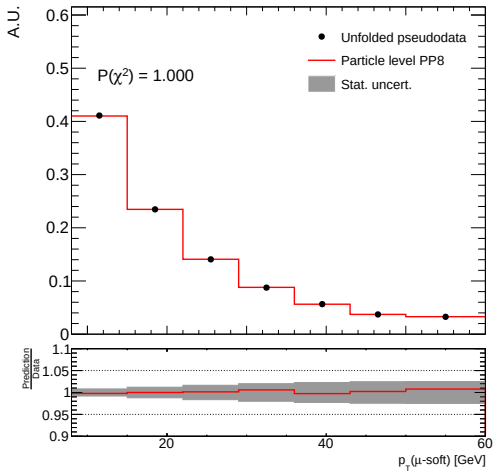

(c) $p_{\mathrm{T}}(\mu\text{-soft})$

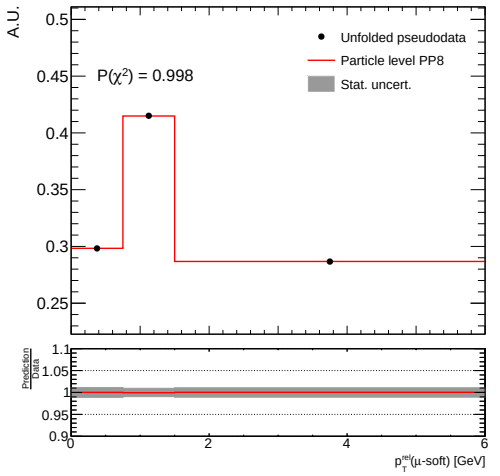

(d) $p_{\mathrm{T}}^{\mathrm{rel}}(\mu\text{-soft})$

Figure 10.9 The split closure tests for a selection of observables. The unfolded pseudodata is compared to the MC prediction from the training sample and the uncertainty bands include the statistical uncertainty on the unfolding.

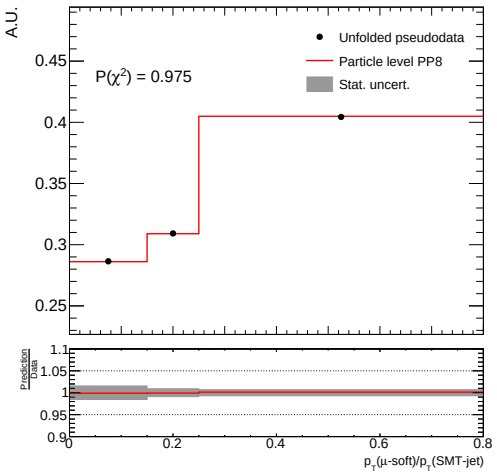

(a) $p_{\mathrm{T}}(\mu\text{-soft})/p_{\mathrm{T}}(\text{SMT jet})$

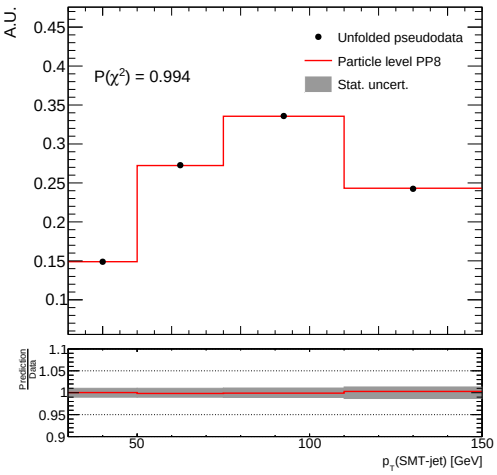

(b) $p_{\mathrm{T}}(\text{SMT jet})$

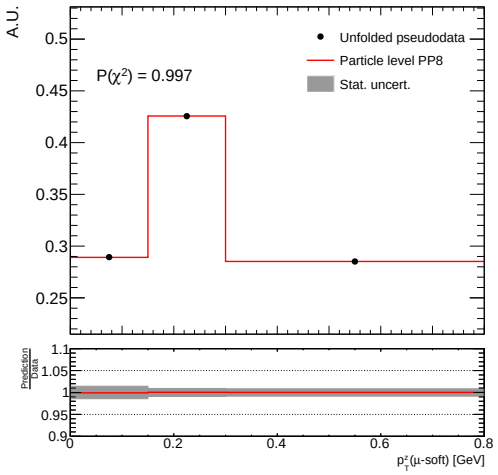

(c) $p_{\mathrm{T}}^{\mathrm{z}}(\mu\text{-soft})$

Figure 10.10 The split closure tests for a selection of observables. The unfolded pseudodata is compared to the MC prediction from the training sample and the uncertainty bands include the statistical uncertainty on the unfolding.

distribution with respect to the training sample, which is used to derive the correction factors. The stressed pseudodata is unfolded and compared to the test particle level distribution. The disagreement between the unfolded pseudodata and the particle level distribution indicates any bias in the unfolding procedure.

For the data/MC discrepancy stress test, the distributions are reweighted with a factor based on the discrepancy between data and MC predictions at reconstructed level. Each bin of the pseudodata distribution is reweighted with

$$f_i = \frac{n_i^{\text{data}}}{n_i^{\text{MC}}}, \tag{10.17}$$

where n_i are the number of events in a given bin for the data and MC distributions at reconstructed level.

In addition to the data/MC discrepancy stress test, a linear stress test is performed to more aggressively stress the unfolding procedure. In the linear stress test the distributions are reweighted to artificially inject a difference in the agreement between pseudodata and training sample. This difference will result in a linear slope in the ratio of the pseudodata and reconstructed level training sample. Each bin in the pseudodata and test sample is reweighted with

$$f_i = \left((1+k) - \left(\frac{2ki}{N} \right) \right), \tag{10.18}$$

where i is the bin number, N is the total number of bins and k is a factor that can be changed to increase or decrease the linear slope injected. The reweighting is performed with $k = -0.01, -0.02, -0.05, -0.1, 0.01, 0.02, 0.05, 0.1$. These factors correspond to a $2k \times 100\%$ linear slope in the agreement between pseudodata and reconstructed training sample. As the factor increases, the agreement between the unfolded stressed pseudodata and the particle level distribution is expected to get worse. For this test there is no level of agreement that must be achieved for the test to be "passed", but rather to find the limit at which the unfolding procedure is no longer producing reasonable estimators.

The results of the data/MC and linear stress tests are shown in Figures 10.11 to 10.14. The original prediction is also shown to illustrate the difference between the stressed and original predictions. The linear stress tests show good agreement for $|k| = 0.05$. However, for most observables, the unfolding procedure breaks down for $|k| = 0.1$. For all observables the data/MC test shows good agreement. The unfolding procedure is therefore considered robust with the given binning and regularisation parameter.

The bump injection test is used to check that the unfolding procedure does not smooth out any unexpected deviations in the measured data. These deviations could be caused by some unknown particle that manifests as a peak in a distribution. The bump injection stress test is only performed on the $m_{\ell\mu}$ observable because the other observables are unlikely to contain some resonant mass peak. Although the $m_{\ell\mu}$ distribution is also unlikely to contain a resonant mass peak, the test is performed for completeness. The pseudodata and MC simulation distributions are injected with a bump by reweighting each bin by a factor

$$f_i = 1 + k \exp\left(\frac{(m_i - m_0)^2}{2\sigma^2}\right) \tag{10.19}$$

where m_i is the mass in bin i, m_0 is the mass of the hypothetical resonance and σ is its width. An additional scale factor k is also included.

An example of the bump injection stress test can be seen in Figure 10.15. The underlying stressed prediction is found to be recovered by the unfolding procedure for an injected bump with parameters $|k| = 0.1$, $m_0 = 60$ GeVand $w = 7$ GeV.

10.3 Binning optimisation

For each given observable, the differential cross-section is measured in a binned histogram with specific bin widths and bin edges. The location of the edges and width of the bins are important parameters to optimise in a differential cross-section measurement. The bins need to be fine

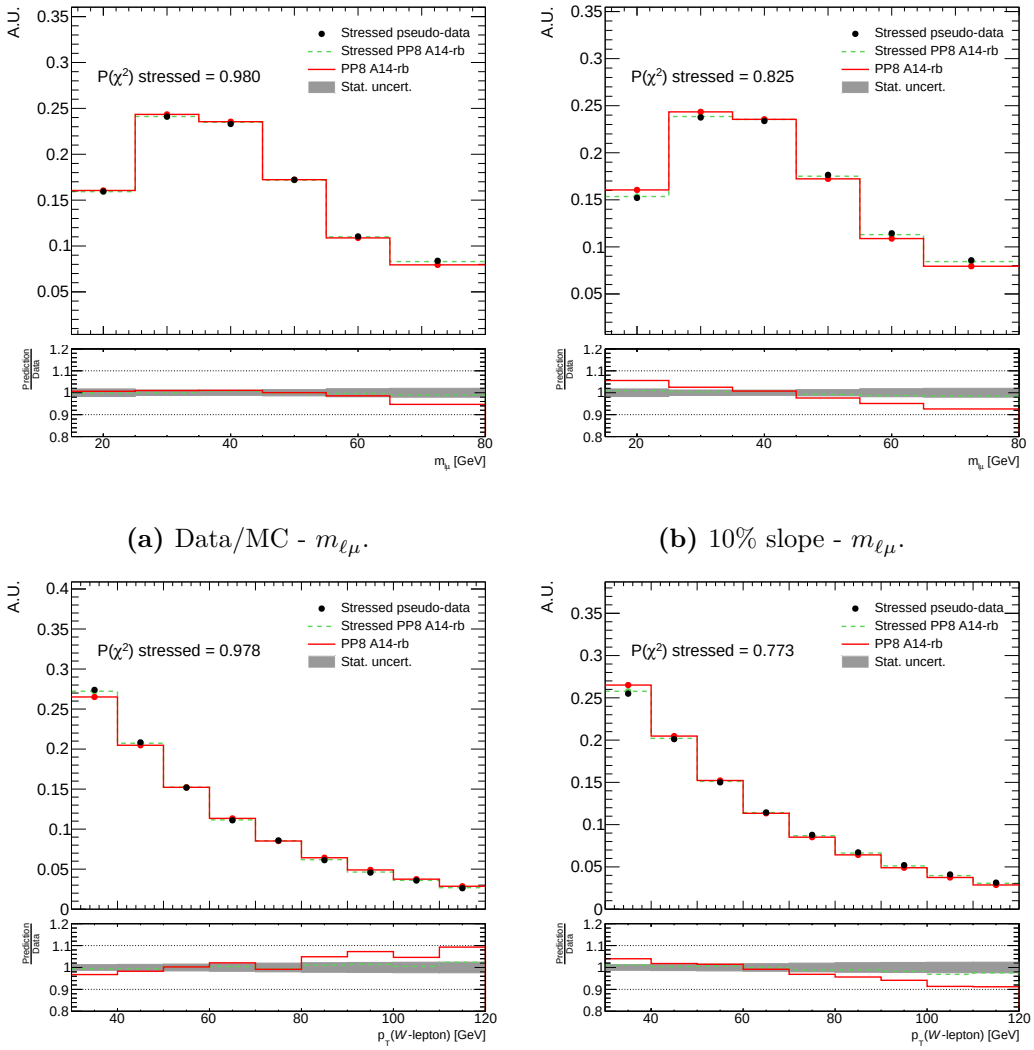

(a) Data/MC - $m_{\ell\mu}$.

(b) 10% slope - $m_{\ell\mu}$.

(c) Data/MC - $p_{\mathrm{T}}(W\text{-lepton})$.

(d) 10% slope - $p_{\mathrm{T}}(W\text{-lepton})$.

Figure 10.11 The data/MC (left) and linear (right) stress tests for $m_{\ell\mu}$ and $p_{\mathrm{T}}(W\text{-lepton})$. The stressed pseudodata is compared with the stressed test particle level sample and the uncertainty band includes the statistical uncertainty on the unfolding.

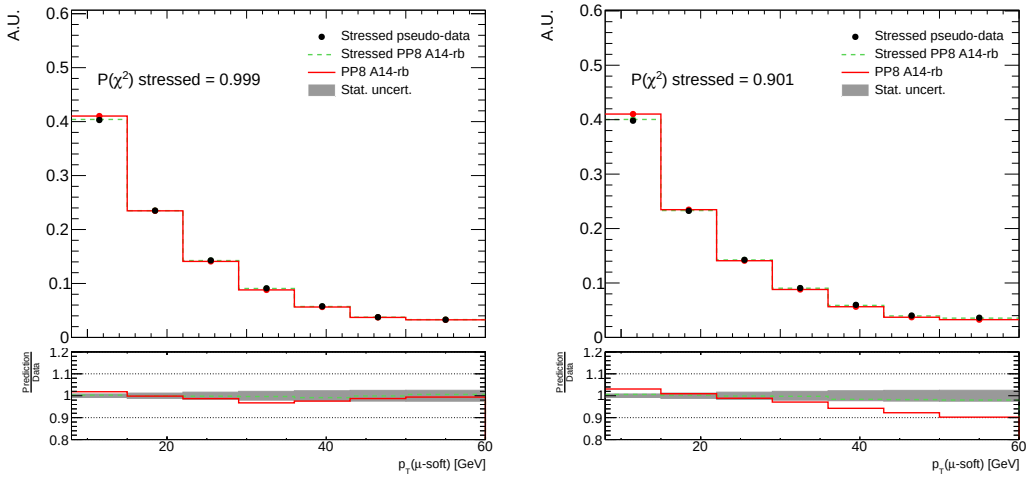

(a) Data/MC - $p_{\mathrm{T}}(\mu\text{-soft})$.

(b) 10% slope - $p_{\mathrm{T}}(\mu\text{-soft})$.

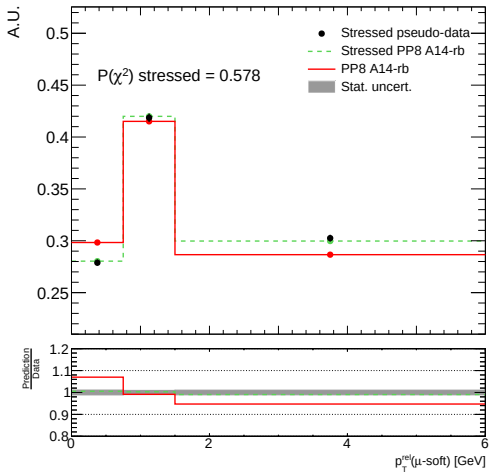

(c) Data/MC - $p_{\mathrm{T}}^{\mathrm{rel}}(\mu\text{-soft})$.

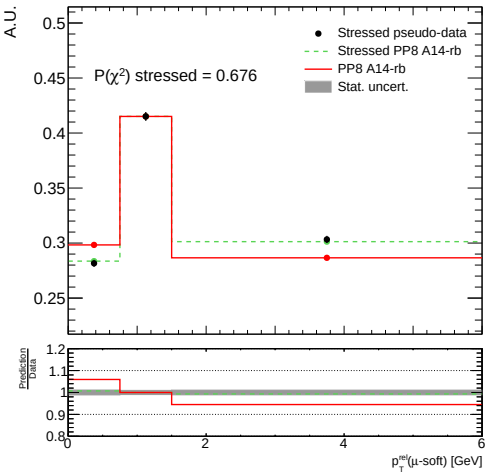

(d) 10% slope - $p_{\mathrm{T}}^{\mathrm{rel}}(\mu\text{-soft})$.

Figure 10.12 The data/MC (left) and linear (right) stress tests for $p_{\mathrm{T}}(\mu\text{-soft})$ and $p_{\mathrm{T}}^{\mathrm{rel}}(\mu\text{-soft})$. The stressed pseudodata is compared with the stressed test particle level sample and the uncertainty band includes the statistical uncertainty on the unfolding.

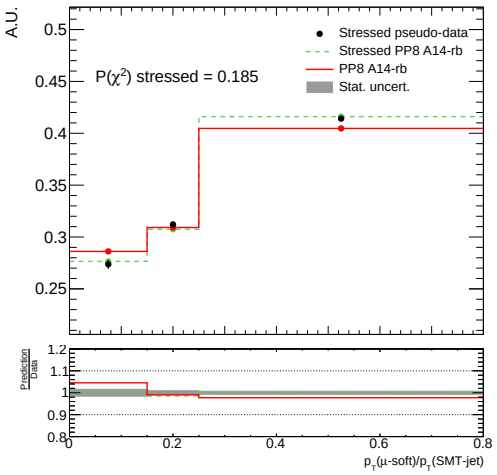

(a) Data/MC - $p_{\mathrm{T}}(\mu\text{-soft})/p_{\mathrm{T}}(\text{SMT jet})$.

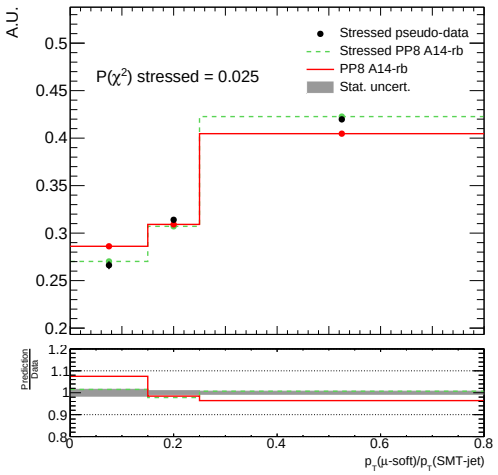

(b) 10% slope - $p_{\mathrm{T}}(\mu\text{-soft})/p_{\mathrm{T}}(\text{SMT jet})$.

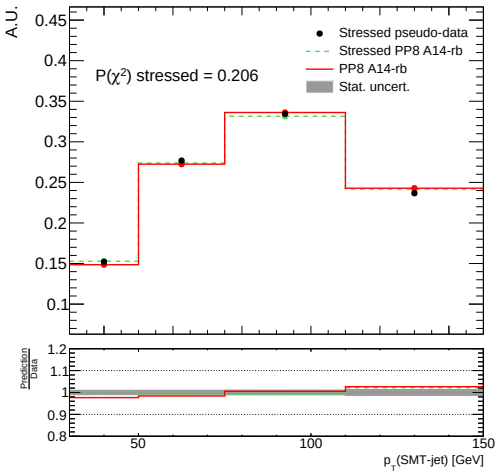

(c) Data/MC - $p_{\mathrm{T}}(\text{SMT jet})$.

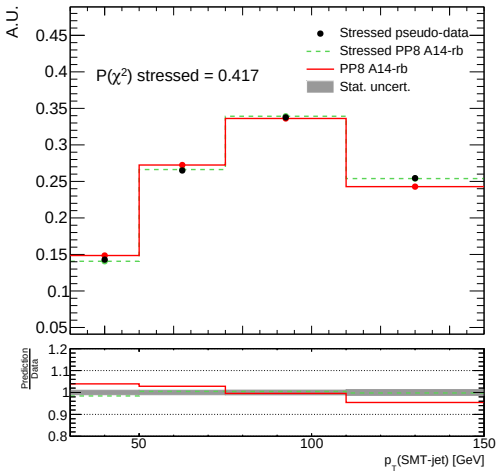

(d) 10% slope - $p_{\mathrm{T}}(\text{SMT jet})$.

Figure 10.13 The data/MC (left) and linear (right) stress tests for $p_{\mathrm{T}}(\mu\text{-soft})/p_{\mathrm{T}}(\text{SMT jet})$ and $p_{\mathrm{T}}(\text{SMT jet})$. The stressed pseudodata is compared with the stressed test particle level sample and the uncertainty band includes the statistical uncertainty on the unfolding.

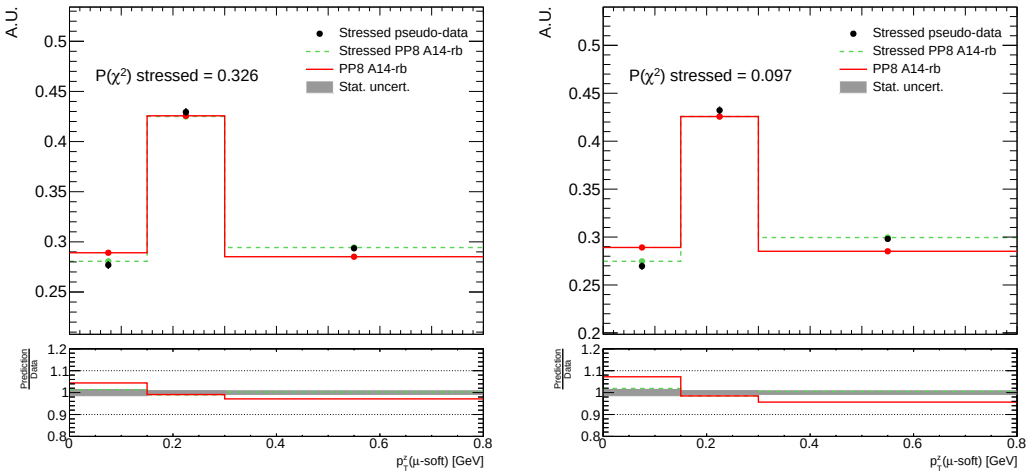

(a) Data/MC - $p_{\mathrm{T}}^{\mathrm{z}}(\mu\text{-soft})$. **(b)** 10% slope - $p_{\mathrm{T}}^{\mathrm{z}}(\mu\text{-soft})$.

Figure 10.14 The data/MC (left) and linear (right) stress tests for $p_{\mathrm{T}}^{\mathrm{z}}(\mu\text{-soft})$. The stressed pseudodata is compared with the stressed test particle level sample and the uncertainty band includes the statistical uncertainty on the unfolding.

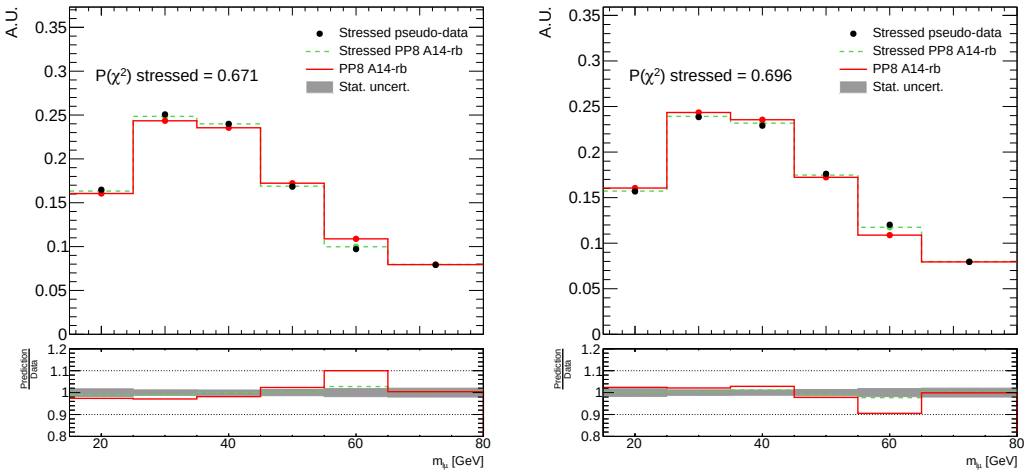

(a) $k = -0.1$, $m_0 = 60$ GeV and $w = 7$ GeV. **(b)** $k = 0.1$, $m_0 = 60$ GeV and $w = 7$ GeV.

Figure 10.15 The bump injection stress tests for $m_{\ell\mu}$. The stressed pseudodata is compared with the stressed test particle level sample and the uncertainty band includes the statistical uncertainty on the unfolding.

enough to extract information or differentiate between different predictions, however, if the bins are too fine then the statistical and systematic uncertainties may be too large. In order to optimise the binning, a semi-automated approach is used based on the resolution of the observables. Manual adjustments are then made based on the uncertainties and the unfolding procedure.

The first step involves an algorithm that uses the resolution of each observable. The absolute difference between the particle level and reconstructed level values for each observable is determined across 200 fine bins. The resolution is defined as the RMS standard deviation of this quantity. The algorithm begins from the left hand side and merges bins until two criteria are satisfied:

- The bin has a width greater than $\delta\times$ the resolution of the observable, where δ is manually chosen.
- The bin has a statistical error below $5\% \times N$ where N is the number of fine bins within the merged bin.

Once both criteria are met, the bin is merged and the algorithm moves onto the next leftmost bin. If the bin has a smaller bin width than the previous one, the two bins are merged. The δ parameter varies between 1.0 and 2.5 in steps of 0.1.

While the algorithm outlined bases the binning configurations on the resolution of the observables, this alone is not sufficient. The binning configuration has an effect on several aspects of the measurement. First, the bin-to-bin migrations in the migration matrix will have an effect on the stability of the unfolding. Ideally, migration matrices are as diagonal as possible to improve the stability of the unfolding. Migration matrices with large off-diagonal components can cause instability in the unfolding procedure, which can manifest as problems in the closure tests and stress tests, discussed in Sections 10.2.5 and 10.2.6 The binning configurations are therefore manually adjusted to maximise the diagonality of the migration matrices and agreement in closure and stress tests.

Finally, the statistical and systematic uncertainties will also depend on the binning configurations. Additional manual adjustments are made to the binning configurations after the data have been run through the entire analysis chain.

The final binning configurations chosen for each observable can be seen in Figures 10.16 and 10.17 where the reconstructed level distribution for each observable is shown. Note the final bin is not an overflow bin.

10.4 Systematic uncertainties

The systematic uncertainties in the differential cross-section measurement use exactly the same variations as in the top quark mass measurement. Each variation is unfolded using the corrections factors derived from the nominal MC predictions and then compared to the particle level prediction for the variation. For detector systematics the particle level prediction is the same as the nominal prediction, however, for the signal modelling uncertainties, the particle level prediction is a separate sample. For most systematic uncertainties an up and down variation exists and so the uncertainty can be asymmetric. However, for samples where there is only one variation the symmetric difference from the nominal is taken as the uncertainty.

The uncertainty associated with the limited MC statistics is estimated using toy experiments. Alternative samples are generated by sampling a Gaussian distribution with a mean of the given bin content and a width given by the bin contents' variance. These alternative samples are unfolded and the standard deviation of the distribution of each bin is taken as the statistical uncertainty on the MC sample.

As discussed in Section 8.9.3, in the top quark mass measurement, the uncertainty associated with the NLO matching scheme is estimated by comparing the aMC@NLO+Pythia8 sample with a Powheg+Pythia8 sample with the same Pythia8 settings as aMC@NLO+Pythia8. To estimate the uncertainty on the differential cross-section, the aMC@NLO+Pythia8 sample is unfolded with correction factors derived from the Powheg+Pythia8 sample with the

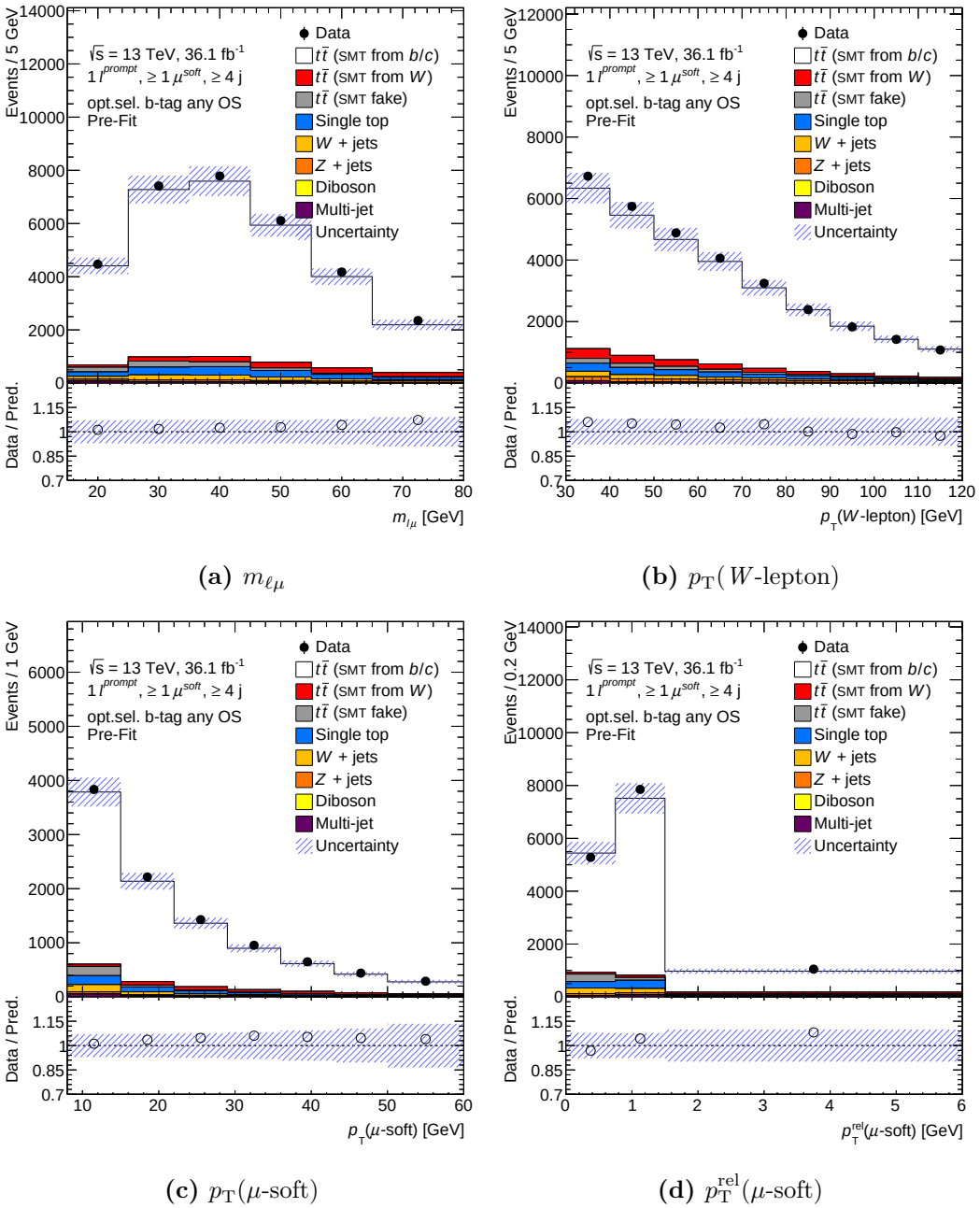

(a) $m_{\ell\mu}$ **(b)** $p_{\mathrm{T}}(W\text{-lepton})$

(c) $p_{\mathrm{T}}(\mu\text{-soft})$ **(d)** $p_{\mathrm{T}}^{\mathrm{rel}}(\mu\text{-soft})$

Figure 10.16 Comparison between data and MC predictions at reconstructed level for several observables. The uncertainty bands include both the systematic and statistical uncertainties.

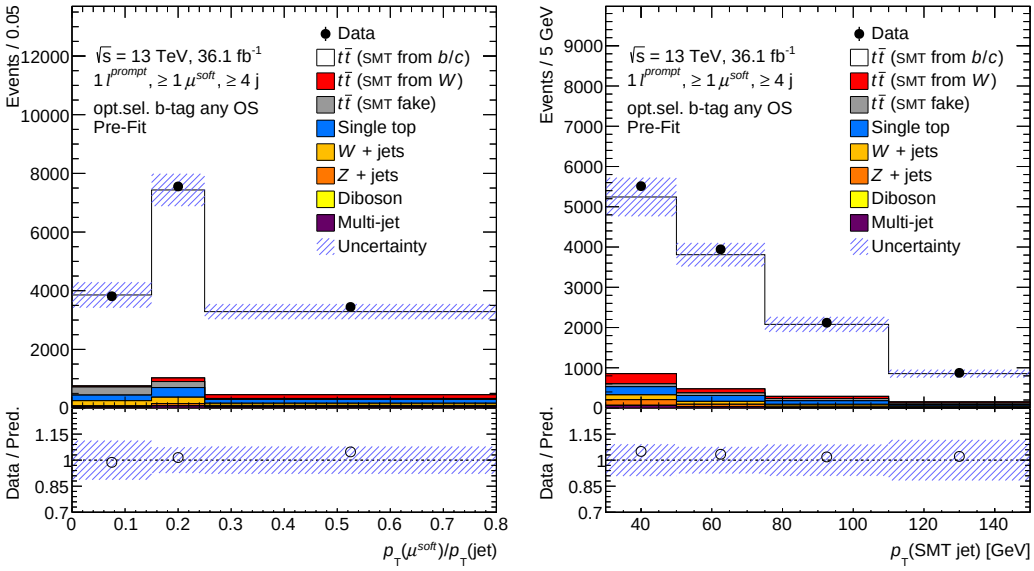

(a) $p_{\mathrm{T}}(\mu\text{-soft})/p_{\mathrm{T}}(\text{SMT jet})$ **(b)** $p_{\mathrm{T}}(\text{SMT jet})$

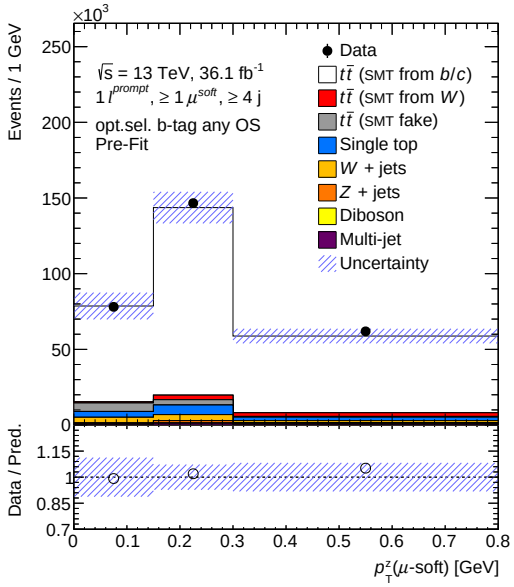

(c) $p_{\mathrm{T}}^{\mathrm{z}}(\mu\text{-soft})$

Figure 10.17 Comparison between data and MC predictions at reconstructed level for several observables. The uncertainty bands include both the systematic and statistical uncertainties.

Table 10.1 A breakdown of the systematics uncertainties in each bin for $m_{\ell\mu}$. The uncertainties are given in %.

Bins [GeV]	15–25	25–35	35–45	45–55	55–65	65–80
$m_{\ell\mu}$ [GeV]	$1.6 \cdot 10^{-2}$	$2.4 \cdot 10^{-2}$	$2.3 \cdot 10^{-2}$	$1.7 \cdot 10^{-2}$	$1.1 \cdot 10^{-2}$	$5.6 \cdot 10^{-3}$
Total Uncertainty [%]	$^{+1.7}_{-1.5}$	$^{+1.4}_{-1.4}$	$^{+1.2}_{-1.2}$	$^{+1.5}_{-1.7}$	$^{+1.7}_{-1.5}$	$^{+4.6}_{-4.7}$
Statistics [%]	±1.0	±0.8	±0.8	±1.0	±1.2	±1.4
Systematics [%]	$^{+1.2}_{-1.0}$	$^{+1.1}_{-1.1}$	$^{+0.8}_{-0.9}$	$^{+1.1}_{-1.4}$	$^{+1.1}_{-0.8}$	$^{+4.4}_{-4.4}$
Background	$^{+0.4}_{-0.4}$	±0.2	-	±0.2	±0.3	$^{+0.7}_{-0.7}$
Flavour tagging	±0.1	-	-	-	±0.1	±0.2
Underlying event and colour reconnection	$^{+0.7}_{-0.1}$	$^{+0.3}_{-0.5}$	$^{-}_{-0.1}$	$^{+0.1}_{-0.7}$	$^{+0.5}_{-0.2}$	$^{+0.7}_{-}$
Parton shower α_s^{FSR}	-	-	-	$^{-}_{-0.5}$	$^{+0.2}_{-}$	$^{+0.3}_{-}$
MC event generator	±0.4	±0.4	±0.3	±0.7	±0.4	±0.6
Parton shower and hadronisation model	±0.3	±0.4	±0.1	±0.3	±0.1	±0.7
Initial-state QCD radiation	$^{-}_{-0.2}$	$^{+0.2}_{-}$	$^{+0.1}_{-}$	$^{-}_{-0.2}$	$^{+0.4}_{-0.3}$	$^{-}_{-0.2}$
Jet energy scale	±0.4	$^{+0.4}_{-0.4}$	$^{+0.5}_{-0.5}$	±0.3	$^{+0.3}_{-0.3}$	$^{+2.5}_{-2.5}$
Leptons and E_T^{miss} Soft Jets	$^{+0.6}_{-0.7}$	$^{+0.6}_{-0.6}$	$^{+0.6}_{-0.6}$	$^{+0.7}_{-0.6}$	$^{+0.4}_{-0.4}$	$^{+3.3}_{-3.4}$
Luminosity	-	-	-	-	-	±0.1
PDF	-	-	-	-	±0.1	±0.2
Pile-up	-	-	-	-	-	-
b-quark fragmentation r_b	$^{+0.3}_{-}$	$^{+0.3}_{-0.2}$	$^{-}_{-0.3}$	$^{-}_{-0.2}$	$^{+0.5}_{-}$	$^{+0.5}_{-0.4}$
b, c production fractions and decay BRs	±0.3	±0.2	-	±0.2	$^{+0.3}_{-0.3}$	$^{+0.4}_{-0.4}$

different Pythia8 settings rather than the nominal sample. The uncertainty is then calculated in the same way as the other single sided uncertainties.

The systematic uncertainties for each observable are shown in Tables 10.1 to 10.7. In most bins of most observables the systematic uncertainty is larger than the statistical. Overall, detector systematics are relatively small when compared with signal modelling systematics. The only large detector systematic that has a major effect is related to the leptons and $E_{\mathrm{T}}^{\mathrm{miss}}$. In higher p_{T} bins for most observables, this uncertainty is dominant. For the majority of bins however, both the parton shower and hadronisation and generator uncertainties are dominant.

Table 10.2 A breakdown of the systematics uncertainties in each bin for $p_{\mathrm{T}}(W\text{-lepton})$. The uncertainties are given in %.

Bins [GeV]	30–40	40–50	50–60	60–70	70–80	80–90	90–100	100–110	110–120
$p_T(W\text{-lepton})$ [GeV]	$2.7 \cdot 10^{-2}$	$2.1 \cdot 10^{-2}$	$1.5 \cdot 10^{-2}$	$1.1 \cdot 10^{-2}$	$8.5 \cdot 10^{-3}$	$6.1 \cdot 10^{-3}$	$4.6 \cdot 10^{-3}$	$3.6 \cdot 10^{-3}$	$2.6 \cdot 10^{-3}$
Total Uncertainty [%]	$^{+1.5}_{-1.3}$	$^{+1.3}_{-1.3}$	$^{+1.6}_{-1.6}$	$^{+1.8}_{-1.8}$	$^{+1.9}_{-2.3}$	$^{+2.2}_{-2.7}$	$^{+3.0}_{-3.0}$	$^{+3.5}_{-3.0}$	$^{+4.8}_{-4.6}$
Statistics [%]	±0.8	±1.0	±1.1	±1.3	±1.4	±1.6	±1.9	±2.2	±2.7
Systematics [%]	$^{+1.2}_{-1.0}$	$^{+0.8}_{-0.8}$	$^{+1.0}_{-1.0}$	$^{+1.1}_{-1.1}$	$^{+1.1}_{-1.8}$	$^{+1.3}_{-2.1}$	$^{+2.3}_{-2.3}$	$^{+2.7}_{-2.0}$	$^{+3.9}_{-3.6}$
Background	±0.2	-	-	±0.1	±0.2	±0.2	±0.2	±0.2	±0.3
Flavour tagging	-	-	-	-	-	-	±0.1	$^{+0.1}_{-0.1}$	±0.2
Underlying event and colour reconnection	$^{+0.6}_{-0.5}$	$^{+0.1}_{-}$	$^{+0.3}_{-0.4}$	$^{+0.6}_{-0.3}$	$^{-}_{-1.2}$	$^{-}_{-1.3}$	$^{+0.4}_{-0.3}$	$^{+1.9}_{-}$	$^{+1.2}_{-0.8}$
Parton shower α_s^{FSR}	-	$^{-}_{-0.2}$	-	$^{-}_{-0.3}$	$^{+0.2}_{-0.2}$	$^{-}_{-0.5}$	$^{+0.6}_{-}$	$^{+0.3}_{-0.5}$	$^{-}_{-0.5}$
MC event generator	±0.5	±0.5	±0.7	±0.8	±0.6	±0.5	±1.2	±0.8	±2.3
Parton shower and hadronisation model	±0.3	±0.1	±0.5	±0.5	-	-	±0.6	±0.6	±0.4
Initial-state QCD radiation	$^{+0.4}_{-0.1}$	-	-	$^{+0.3}_{-0.2}$	-	$^{-}_{-0.5}$	$^{+0.2}_{-0.6}$	$^{-}_{-0.6}$	$^{+1.1}_{-0.3}$
Jet energy scale	$^{+0.2}_{-0.2}$	$^{+0.4}_{-0.4}$	$^{+0.3}_{-0.3}$	$^{+0.2}_{-0.2}$	$^{+0.6}_{-0.6}$	$^{+0.6}_{-0.7}$	$^{+0.8}_{-0.8}$	$^{+0.4}_{-0.4}$	$^{+1.7}_{-1.8}$
Leptons and E_T^{miss} Soft Jets	$^{+0.6}_{-0.6}$	$^{+0.4}_{-0.4}$	$^{+0.4}_{-0.3}$	±0.2	$^{+0.8}_{-0.8}$	$^{+0.9}_{-1.0}$	$^{+1.3}_{-1.4}$	$^{+1.1}_{-1.1}$	$^{+1.5}_{-1.5}$
Luminosity	-	-	-	-	-	-	-	-	-
PDF	±0.4	±0.3	±0.1	-	±0.3	±0.5	±0.7	±1.0	±1.3
Pile-up	-	±0.1	-	-	-	-	-	-	-
b-quark fragmentation r_b	$^{+0.3}_{-}$	-	$^{+0.2}_{-}$	$^{-}_{-0.3}$	$^{-}_{-0.6}$	$^{-}_{-0.7}$	$^{+0.5}_{-0.2}$	$^{+0.5}_{-}$	$^{+0.7}_{-}$
b, c production fractions and decay BRs	±0.1	-	-	-	-	±0.1	$^{+0.1}_{-0.1}$	±0.2	±0.2

Table 10.3 A breakdown of the systematics uncertainties in each bin for $p_{\mathrm{T}}(\mu\text{-soft})$. The uncertainties are given in %.

Bins [GeV]	8–15	15–22	22–29	29–36	36–43	43–50	50–60
$p_T(W\text{-lepton})$ [GeV]	$5.8 \cdot 10^{-2}$	$3.4 \cdot 10^{-2}$	$2.0 \cdot 10^{-2}$	$1.3 \cdot 10^{-2}$	$8.2 \cdot 10^{-3}$	$5.3 \cdot 10^{-3}$	$3.3 \cdot 10^{-3}$
Total Uncertainty [%]	$^{+2.1}_{-2.0}$	$^{+1.8}_{-2.0}$	$^{+1.5}_{-1.5}$	$^{+2.6}_{-2.5}$	$^{+4.5}_{-4.7}$	$^{+6.6}_{-6.7}$	$^{+11.7}_{-11.9}$
Statistics [%]	±0.5	±0.8	±1.0	±1.4	±1.7	±2.1	±2.4
Systematics [%]	$^{+2.0}_{-1.9}$	$^{+1.5}_{-1.8}$	$^{+1.0}_{-1.0}$	$^{+2.1}_{-2.1}$	$^{+4.1}_{-4.3}$	$^{+6.2}_{-6.3}$	$^{+11.4}_{-11.6}$
Background	$^{+0.5}_{-0.5}$	$^{+0.2}_{-0.2}$	±0.3	$^{+0.4}_{-0.4}$	$^{+0.6}_{-0.6}$	±0.9	$^{+1.4}_{-1.4}$
Flavour tagging	$^{+0.2}_{-0.2}$	-	-	$^{+0.3}_{-0.2}$	$^{+0.5}_{-0.5}$	$^{+0.7}_{-0.7}$	$^{+0.9}_{-0.9}$
Underlying event and colour reconnection	$^{+0.3}_{-}$	$^{-}_{-0.8}$	$^{+0.4}_{-0.2}$	$^{+0.4}_{-0.1}$	$^{+0.5}_{-}$	$^{+0.2}_{-0.3}$	$^{+0.9}_{-}$
Parton shower α_s^{FSR}	$^{+0.2}_{-}$	$^{-}_{-0.3}$	-	$^{+0.3}_{-0.1}$	$^{-}_{-0.6}$	$^{+0.5}_{-0.3}$	$^{+0.3}_{-}$
MC event generator	±1.1	±0.6	±0.5	±1.6	±2.4	±3.1	±5.0
Parton shower and hadronisation model	±0.7	±0.6	±0.5	±0.4	±0.8	±0.4	±0.2
Initial-state QCD radiation	$^{+0.2}_{-}$	$^{-}_{-0.3}$	-	-	$^{+0.1}_{-0.9}$	$^{+0.5}_{-0.6}$	$^{+1.3}_{-0.3}$
Jet energy scale	$^{+0.8}_{-0.8}$	$^{+0.9}_{-0.9}$	±0.3	$^{+0.7}_{-0.7}$	$^{+1.9}_{-1.9}$	$^{+3.1}_{-3.2}$	$^{+6.4}_{-6.6}$
Leptons and E_T^{miss} Soft Jets	$^{+0.9}_{-0.9}$	$^{+0.9}_{-0.8}$	±0.2	$^{+0.8}_{-0.8}$	$^{+2.3}_{-2.4}$	$^{+4.0}_{-4.1}$	$^{+7.7}_{-8.0}$
Luminosity	-	-	-	-	-	-	$^{+0.2}_{-0.2}$
PDF	±0.3	-	±0.1	±0.3	±0.5	±0.7	±1.0
Pile-up	-	-	-	±0.1	±0.1	-	$^{+0.3}_{-0.3}$
b-quark fragmentation r_b	$^{+0.4}_{-}$	$^{-}_{-0.5}$	$^{+0.2}_{-0.2}$	$^{+0.3}_{-}$	$^{-}_{-0.7}$	$^{+1.1}_{-0.2}$	$^{+0.9}_{-}$
b, c production fractions and decay BRs	$^{+0.4}_{-0.4}$	-	±0.3	$^{+0.4}_{-0.4}$	$^{+0.5}_{-0.5}$	$^{+0.6}_{-0.6}$	$^{+0.6}_{-0.6}$

Table 10.4 A breakdown of the systematics uncertainties in each bin for $p_{\mathrm{T}}^{\mathrm{rel}}(\mu\text{-soft})$. The uncertainties are given in %.

Bins [GeV]	0–0.75	0.75–1.50	1.50–6
$p_T^{\mathrm{rel}}(\mu\text{-soft})$ [GeV]	$3.7 \cdot 10^{-1}$	$5.6 \cdot 10^{-1}$	$6.8 \cdot 10^{-2}$
Total Uncertainty [%]	$^{+2.4}_{-2.4}$	$^{+1.3}_{-1.2}$	$^{+3.5}_{-3.7}$
Statistics [%]	± 0.6	± 0.3	± 0.6
Systematics [%]	$^{+2.3}_{-2.2}$	$^{+1.2}_{-1.1}$	$^{+3.5}_{-3.6}$
Background	$^{+0.6}_{-0.6}$	$^{+0.2}_{-0.2}$	± 0.6
Flavour tagging	$^{+0.3}_{-0.3}$	± 0.1	± 0.1
Underlying event and colour reconnection	$^{+0.5}_{-}$	-	$^{-}_{-0.5}$
Parton shower α_s^{FSR}	$^{+0.1}_{-0.1}$	-	$^{-}_{-0.2}$
MC event generator	± 0.3	± 0.2	± 0.5
Parton shower and hadronisation model	± 1.2	-	± 1.3
Initial-state QCD radiation	-	$^{+0.2}_{-}$	$^{-}_{-0.3}$
Jet energy scale	$^{+0.8}_{-0.8}$	$^{+0.5}_{-0.5}$	$^{+1.5}_{-1.6}$
Leptons and E_T^{miss} Soft Jets	$^{+1.2}_{-1.2}$	$^{+1.0}_{-0.9}$	$^{+2.6}_{-2.7}$
Luminosity	-	-	± 0.1
PDF	-	-	-
Pile-up	± 0.4	± 0.1	± 0.7
b-quark fragmentation r_b	-	$^{+0.2}_{-}$	-
b, c production fractions and decay BRs	$^{+0.8}_{-0.8}$	± 0.2	$^{+0.6}_{-0.6}$

Table 10.5 A breakdown of the systematics uncertainties in each bin for $p_{\mathrm{T}}(\mu\text{-soft})/p_{\mathrm{T}}(\text{SMT jet})$. The uncertainties are given in %.

Bins	0–0.15	0.15–0.25	0.25–0.80
$p_T(\mu\text{-soft})/p_T(\text{SMT jet})$	$1.8 \cdot 10^0$	$3.1 \cdot 10^0$	$7.5 \cdot 10^{-1}$
Total Uncertainty [%]	$^{+6.9}_{-7.0}$	$^{+2.1}_{-2.2}$	$^{+4.1}_{-4.1}$
Statistics [%]	± 0.7	± 0.2	± 0.4
Systematics [%]	$^{+6.9}_{-6.9}$	$^{+2.0}_{-2.1}$	$^{+4.1}_{-4.1}$
Background	$^{+0.8}_{-0.8}$	$^{+0.3}_{-0.2}$	$^{+0.3}_{-0.3}$
Flavour tagging	± 0.2	± 0.1	± 0.1
Underlying event and colour reconnection	$^{-}_{-0.2}$	$^{+0.4}_{-0.4}$	$^{+0.5}_{-0.3}$
Parton shower α_s^{FSR}	-	$^{-}_{-0.4}$	$^{+0.2}_{-0.1}$
MC event generator	± 3.8	± 0.9	± 2.0
Parton shower and hadronisation model	± 2.4	± 1.0	± 2.5
Initial-state QCD radiation	$^{+0.2}_{-}$	$^{+0.1}_{-0.5}$	$^{+0.2}_{-0.2}$
Jet energy scale	$^{+2.4}_{-2.4}$	± 0.7	± 1.2
Leptons and E_T^{miss} Soft Jets	$^{+4.5}_{-4.5}$	$^{+1.3}_{-1.3}$	$^{+2.2}_{-2.2}$
Luminosity	-	-	-
PDF	± 0.4	± 0.2	± 0.2
Pile-up	± 0.2	-	± 0.1
b-quark fragmentation r_b	$^{+0.2}_{-0.2}$	$^{-}_{-0.1}$	$^{+0.2}_{-0.2}$
b, c production fractions and decay BRs	$^{+0.6}_{-0.6}$	$^{+0.1}_{-0.1}$	$^{+0.3}_{-0.3}$

Table 10.6 A breakdown of the systematics uncertainties in each bin for p_{T}(SMT jet). The uncertainties are given in %.

Bins [GeV]	30–50	50–75	75–110	110–150
$p_T^{SMT-jet}$ [GeV]	$7.6 \cdot 10^{-3}$	$1.1 \cdot 10^{-2}$	$9.6 \cdot 10^{-3}$	$5.9 \cdot 10^{-3}$
Total Uncertainty [%]	$^{+5.0}_{-5.0}$	$^{+3.2}_{-3.2}$	$^{+0.9}_{-1.2}$	$^{+5.7}_{-5.7}$
Statistics [%]	± 0.7	± 0.4	± 0.3	± 0.6
Systematics [%]	$^{+5.0}_{-5.0}$	$^{+3.2}_{-3.1}$	$^{+0.8}_{-1.1}$	$^{+5.7}_{-5.6}$
Background	± 0.3	± 0.2	$^{+0.1}_{-0.1}$	± 0.2
Flavour tagging	$^{+0.5}_{-0.6}$	± 0.2	$^{+0.3}_{-0.3}$	± 0.3
Underlying event and colour reconnection	$^{+0.9}_{-0.6}$	$^{+0.3}_{-}$	$^{-}_{-0.5}$	$^{+0.4}_{-0.3}$
Parton shower α_s^{FSR}	$^{+0.2}_{-0.1}$	$^{+0.2}_{-}$	$^{-}_{-0.2}$	$^{+0.5}_{-0.1}$
MC event generator	± 1.6	± 1.3	± 0.1	± 2.3
Parton shower and hadronisation model	± 2.7	± 0.4	± 0.4	± 0.6
Initial-state QCD radiation	$^{+0.5}_{-0.4}$	-	$^{-}_{-0.6}$	$^{+0.4}_{-}$
Jet energy scale	$^{+1.5}_{-1.5}$	$^{+1.2}_{-1.2}$	$^{+0.2}_{-0.2}$	$^{+2.2}_{-2.2}$
Leptons and E_T^{miss} Soft Jets	$^{+3.3}_{-3.4}$	$^{+2.5}_{-2.5}$	$^{+0.6}_{-0.5}$	$^{+4.5}_{-4.5}$
Luminosity	-	-	-	-
PDF	± 0.4	± 0.3	-	± 0.7
Pile-up	± 0.2	-	-	± 0.1
b-quark fragmentation r_b	-	$^{+0.2}_{-}$	$^{-}_{-0.3}$	$^{+0.4}_{-}$
b, c production fractions and decay BRs	± 0.2	± 0.1	-	± 0.2

Table 10.7 A breakdown of the systematics uncertainties in each bin for $p_{\mathrm{T}}^{\mathrm{z}}(\mu\text{-soft})$. The uncertainties are given in %.

Bins [GeV]	0–0.15	0.15–0.30	0.30–0.80
$p_T^{\mathrm{z}}(\mu\text{-soft})$ [GeV]	$1.8 \cdot 10^0$	$2.9 \cdot 10^0$	$5.9 \cdot 10^{-1}$
Total Uncertainty [%]	$^{+7.1}_{-7.2}$	$^{+2.0}_{-2.1}$	$^{+5.9}_{-5.8}$
Statistics [%]	± 0.7	± 0.2	± 0.5
Systematics [%]	$^{+7.1}_{-7.1}$	$^{+1.9}_{-2.0}$	$^{+5.9}_{-5.8}$
Background	$^{+0.8}_{-0.8}$	± 0.3	$^{+0.4}_{-0.4}$
Flavour tagging	± 0.2	± 0.1	± 0.1
Underlying event and colour reconnection	$^{+0.1}_{-0.3}$	$^{+0.2}_{-0.4}$	$^{+0.9}_{-0.4}$
Parton shower α_s^{FSR}	-	$^{-}_{-0.4}$	$^{+0.4}_{-0.2}$
MC event generator	± 3.9	± 0.8	± 2.8
Parton shower and hadronisation model	± 2.6	± 0.8	± 3.9
Initial-state QCD radiation	$^{+0.3}_{-}$	$^{-}_{-0.3}$	$^{+0.2}_{-0.3}$
Jet energy scale	$^{+2.5}_{-2.5}$	$^{+0.7}_{-0.7}$	$^{+1.6}_{-1.6}$
Leptons and E_T^{miss} Soft Jets	$^{+4.5}_{-4.6}$	$^{+1.3}_{-1.3}$	$^{+2.7}_{-2.6}$
Luminosity	-	-	-
PDF	± 0.4	± 0.2	± 0.1
Pile-up	± 0.2	-	± 0.1
b-quark fragmentation r_b	$^{+0.2}_{-0.1}$	$^{-}_{-0.2}$	$^{+0.4}_{-0.2}$
b, c production fractions and decay BRs	$^{+0.7}_{-0.6}$	± 0.1	$^{+0.4}_{-0.5}$

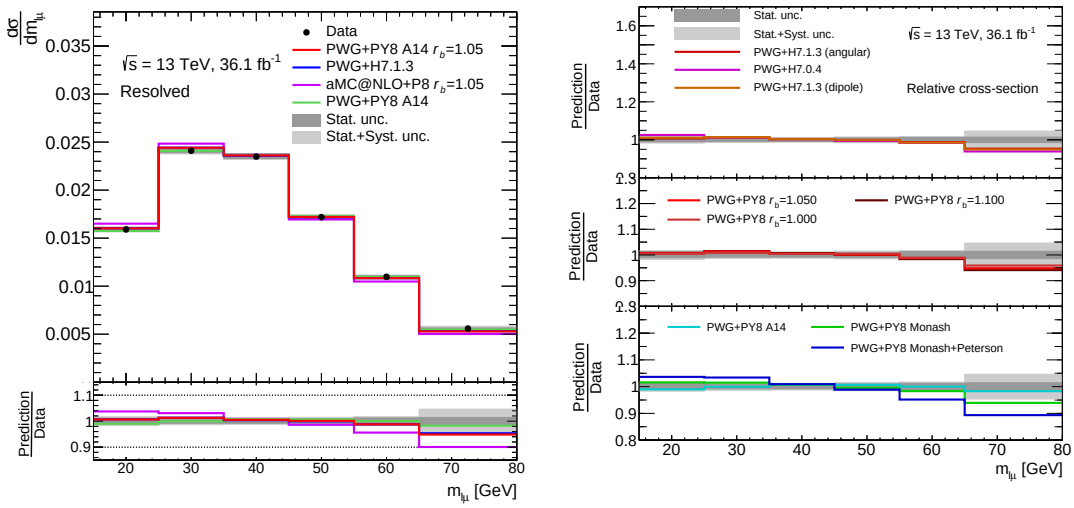

(a) **(b)**

Figure 10.18 Comparison between the measured normalised differential cross-section and various signal predictions for $m_{\ell\mu}$. (a) shows several standard signal predictions and (b) compares signal predictions with various hadronisation parameters.

10.5 Results

The unfolded normalised differential cross-section results are shown in this section. In Figures 10.18a, 10.19a, 10.20a, 10.21a, 10.22a, 10.23a, and 10.24a, the differential cross-section for each observable is shown with some standard MC predictions overlaid. The statistical and systematic uncertainties are shown in each plot. Figures 10.18b, 10.19b, 10.20b, 10.21b, 10.22b, 10.23b, and 10.24b show the ratio of various predictions with different hadronisation and fragmentation parameters and the normalised differential cross-sections. Full details of the signal predictions used can be found in Section 5.2.

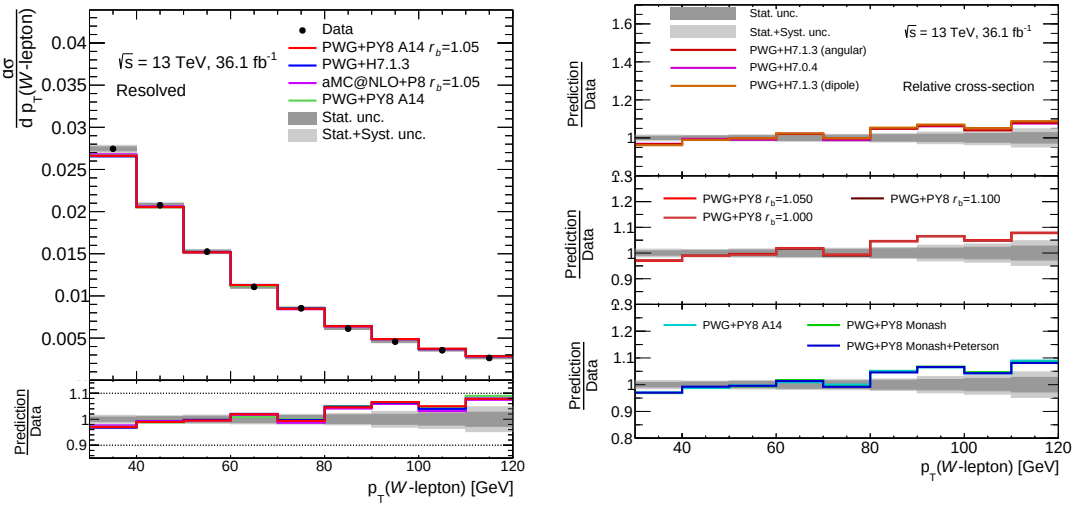

(a) **(b)**

Figure 10.19 Comparison between the measured normalised differential cross-section and various signal predictions for $p_{\mathrm{T}}(W\text{-lepton})$. (a) shows several standard signal predictions and (b) compares signal predictions with various hadronisation parameters.

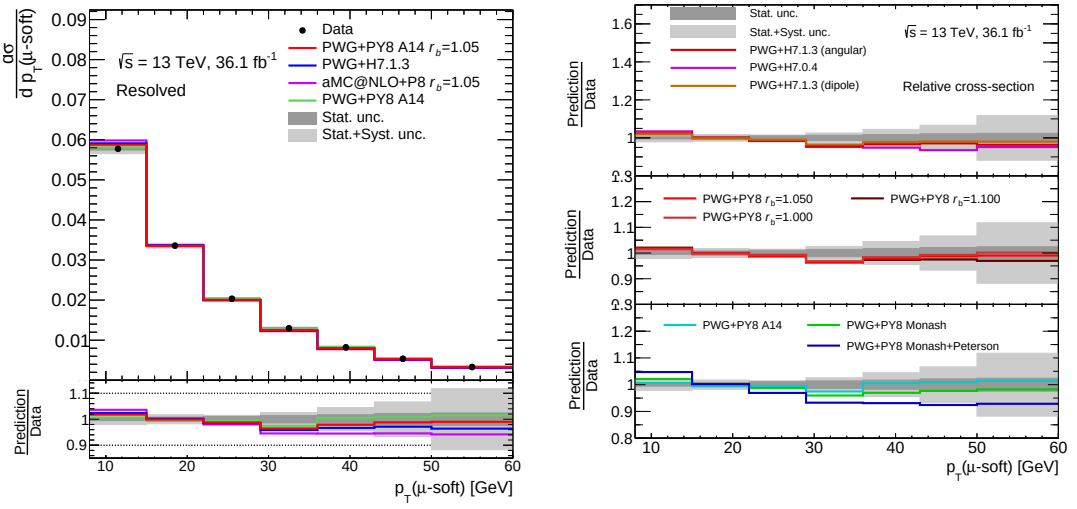

(a) **(b)**

Figure 10.20 Comparison between the measured normalised differential cross-section and various signal predictions for $p_{\mathrm{T}}(\mu\text{-soft})$. (a) shows several standard signal predictions and (b) compares signal predictions with various hadronisation parameters.

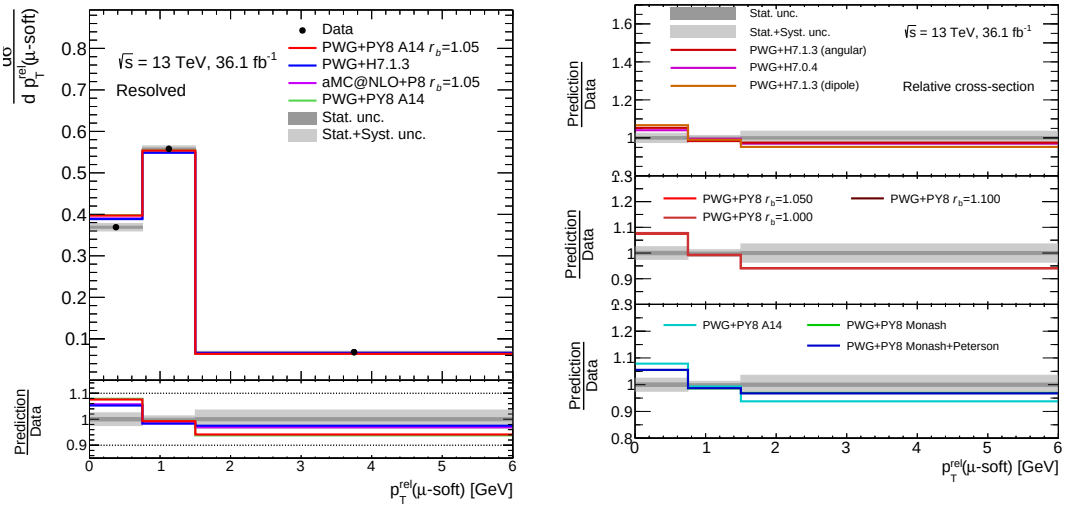

(a) **(b)**

Figure 10.21 Comparison between the measured normalised differential cross-section and various signal predictions for $p_{\mathrm{T}}^{\mathrm{rel}}(\mu\text{-soft})$. (a) shows several standard signal predictions and (b) compares signal predictions with various hadronisation parameters.

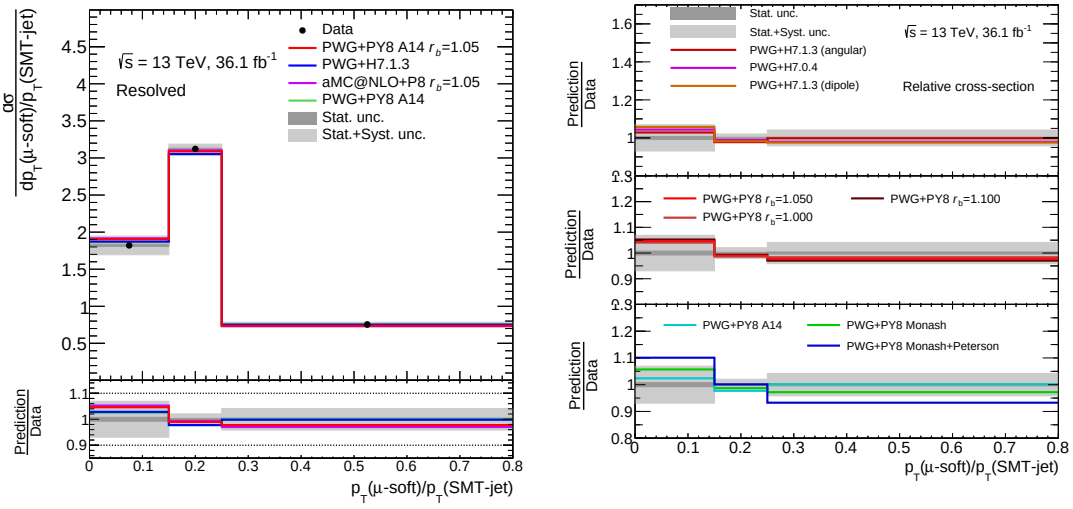

(a) **(b)**

Figure 10.22 Comparison between the measured normalised differential cross-section and various signal predictions for $p_{\mathrm{T}}(\mu\text{-soft})/p_{\mathrm{T}}(\text{SMT jet})$. (a) shows several standard signal predictions and (b) compares signal predictions with various hadronisation parameters.

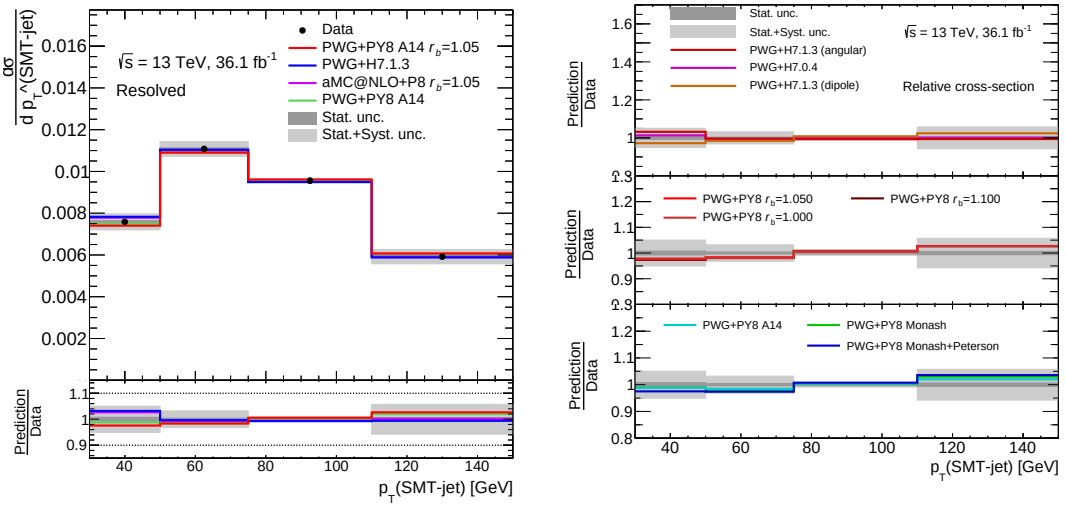

(a) **(b)**

Figure 10.23 Comparison between the measured normalised differential cross-section and various signal predictions for p_{T}(SMT jet). (a) shows several standard signal predictions and (b) compares signal predictions with various hadronisation parameters.

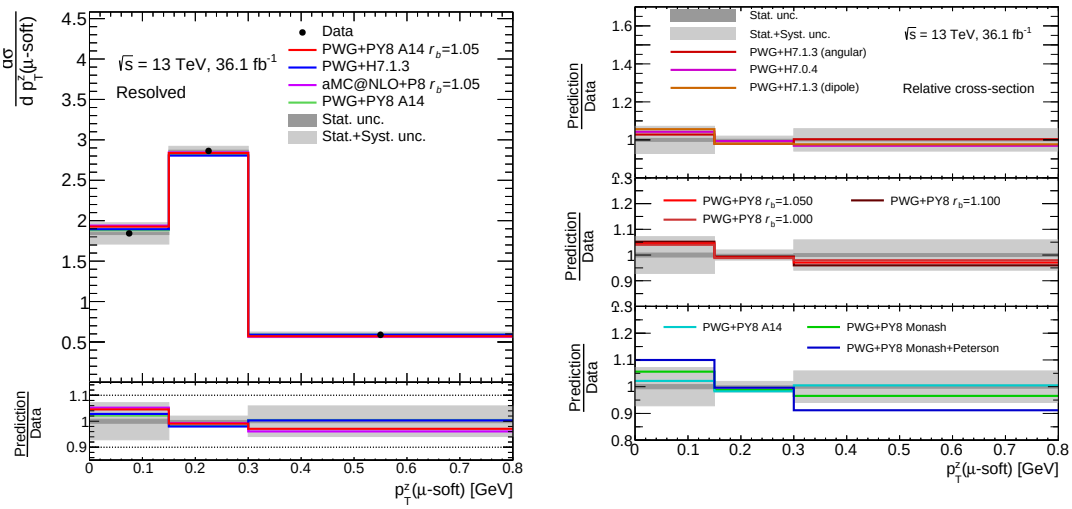

(a) **(b)**

Figure 10.24 Comparison between the measured normalised differential cross-section and various signal predictions for $p_{\mathrm{T}}^{\mathrm{z}}(\mu\text{-soft})$. (a) shows several standard signal predictions and (b) compares signal predictions with various hadronisation parameters.

10.5.1 Comparison with predictions

In order to quantify the level of agreement between a given prediction and a differential cross-section, a χ^2 test statistic is calculated. The χ^2 is calculated using

$$\chi^2 = U^{\mathsf{T}} C^{-1} U, \tag{10.20}$$

where U are vectors of the difference between the data and prediction and C is the full covariance matrix.

The final covariance matrix is constructed using two different methods. The first uses toy experiments to calculate the covariance from the statistical uncertainty and the detector systematics. Alternative distributions are produced by applying bin-by-bin Poisson weights to the data. The Poisson weight for a given bin uses an expectation value set to the number of events in the bin. Each bin is then scaled by the corresponding systematic uncertainty variation. The alternative distribution is then unfolded using the nominal procedure and differential cross-sections are measured. The results of these toy experiments are used to calculate the covariance. The covariance is calculated using 10000 toys.

The second method is used to calculate the signal modelling uncertainties. This method sums seven separate covariance matrices corresponding to the parton shower and hadronisation model, choice of NLO matching scheme, initial and final state radiation, r_b fragmentation parameter, colour reconnection and underlying event uncertainties. The matrices are calculated by multiplying the measured cross-section in each bin by the systematic variation. The bin-to-bin correlation is set to unity for each systematic.

Using the χ^2 and the number of degrees of freedom, the p-value for each prediction is calculated. If the p-value is greater than 0.05, the prediction and data are said to agree. Table 10.8 shows the χ^2/NDF and p-value for each prediction and each observable.

Table 10.8 Comparison of the relative differential cross-sections and several different predictions. For each prediction he χ^2 test statistic and p-value is calculated. p-values highlighted in red indicate the prediction hypothesis is rejected for the given observable.

Model	$m_{\ell\mu}$		p_{T}(SMT jet)		$p_{\mathrm{T}}(\mu\text{-soft})/p_{\mathrm{T}}$(SMT jet)		$p_{\mathrm{T}}^{\mathrm{rel}}(\mu\text{-soft})$		$p_{\mathrm{T}}(\mu\text{-soft})$		$p_{\mathrm{T}}^{\mathrm{z}}(\mu\text{-soft})$		$p_{\mathrm{T}}(W\text{-lepton})$	
	χ^2/NDF	p-value	χ^2/NDF	p-value	χ^2/NDF	p-value	χ^2/NDF	p-value	χ^2/NDF	p-value	χ^2/NDF	p-value	χ^2/NDF	p-value
PWG+H7.0.4	4.3/5	0.50	1.2/3	0.76	0.9/2	0.65	1.3/2	0.52	12.3/6	0.06	0.6/2	0.76	19.5/8	**0.01**
PWG+H7.1.3 (angular)	1.8/5	0.87	4.8/3	0.19	1.8/2	0.41	8.5/2	**0.01**	8.1/6	0.23	1.7/2	0.43	18.0/8	**0.02**
PWG+H7.1.3 (dipole)	2.5/5	0.78	2.2/3	0.53	1.9/2	0.38	4.5/2	0.10	5.5/6	0.48	2.5/2	0.29	23.4/8	**<0.01**
PWG+PY8 A14	1.1/5	0.96	0.7/3	0.87	1.7/2	0.42	3.6/2	0.16	3.0/6	0.81	1.2/2	0.55	15.8/8	**0.05**
PWG+PY8 A14 $r_b = 1.000$	1.1/5	0.95	1.6/3	0.67	1.1/2	0.59	4.5/2	0.11	4.2/6	0.65	1.0/2	0.61	17.2/8	**0.03**
PWG+PY8 A14 $r_b = 1.029$	1.1/5	0.95	1.4/3	0.71	0.9/2	0.65	4.7/2	0.09	4.5/6	0.61	0.8/2	0.66	17.4/8	**0.03**
PWG+PY8 A14 $r_b = 1.05$	1.7/5	0.88	1.3/3	0.73	0.9/2	0.65	3.8/2	0.15	5.9/6	0.44	0.9/2	0.65	17.8/8	**0.02**
PWG+PY8 A14 $r_b = 1.071$	2.5/5	0.78	1.9/3	0.58	0.9/2	0.62	3.4/2	0.19	5.5/6	0.48	0.9/2	0.65	16.6/8	**0.03**
PWG+PY8 A14 $r_b = 1.100$	2.7/5	0.74	2.2/3	0.53	0.7/2	0.71	3.8/2	0.15	6.2/6	0.40	0.7/2	0.71	17.1/8	**0.03**
PWG+PY8 A14 FSR Hi	1.4/5	0.93	0.8/3	0.85	1.9/2	0.40	4.8/2	0.09	1.8/6	0.94	1.5/2	0.48	18.7/8	**0.02**
PWG+PY8 A14 FSR Lo	0.6/5	0.99	1.0/3	0.81	1.5/2	0.48	6.7/2	**0.04**	3.4/6	0.76	1.3/2	0.53	18.5/8	**0.02**
PWG+PY8 FSR Hi $r_b = 1.0356$	2.2/5	0.83	2.0/3	0.58	0.8/2	0.67	3.8/2	0.15	5.9/6	0.44	0.8/2	0.67	17.5/8	**0.03**
PWG+PY8 FSR Lo $r_b = 1.0802$	1.4/5	0.92	1.0/3	0.80	0.9/2	0.63	3.8/2	0.15	5.0/6	0.54	0.9/2	0.65	16.6/8	**0.03**
PWG+PY8 ISR Hi	0.1/5	1.00	1.4/3	0.69	2.8/2	0.24	10.9/2	**<0.01**	2.0/6	0.92	2.6/2	0.27	19.9/8	**0.01**
PWG+PY8 ISR Hi $r_b = 1.05$	1.3/5	0.94	3.1/3	0.38	1.2/2	0.54	6.6/2	**0.04**	4.9/6	0.55	1.5/2	0.48	21.5/8	**<0.01**
PWG+PY8 ISR Lo	1.9/5	0.86	0.9/3	0.83	1.6/2	0.44	3.9/2	0.14	1.9/6	0.93	1.1/2	0.59	15.2/8	0.06
PWG+PY8 ISR Lo $r_b = 1.05$	1.7/5	0.89	1.1/3	0.78	0.6/2	0.76	2.9/2	0.24	5.2/6	0.52	0.5/2	0.79	15.3/8	0.05
PWG+PY8 Monash	3.6/5	0.61	1.8/3	0.62	1.3/2	0.51	6.5/2	**0.04**	7.2/6	0.31	1.4/2	0.48	18.7/8	**0.02**
PWG+PY8 Monash+Peterson	22.7/5	**<0.01**	2.2/3	0.54	1.1/2	0.57	6.0/2	0.05	25.0/6	**<0.01**	1.6/2	0.44	16.4/8	**0.04**
aMC@NLO+PY8	10.0/5	0.07	8.4/3	**0.04**	1.0/2	0.59	8.0/2	**0.02**	9.8/6	0.13	0.4/2	0.83	15.2/8	0.06
aMC@NLO+PY8 $r_b = 1.05$	22.5/5	**<0.01**	4.1/3	0.25	0.2/2	0.89	5.5/2	0.07	17.9/6	**<0.01**	0.2/2	0.88	7.3/8	0.50

10.6 Discussion

Overall, most predictions have a reasonable agreement with data in the majority of observables. The $p_{\mathrm{T}}(W\text{-lepton})$ distribution, however, shows disagreement between data and most predictions. The disagreement is a known problem and has been seen in previous analyses [194]. The POWHEG+PYTHIA8 generator is known to predict a harder top-quark-p_{T} spectrum than observed in data. In Ref. [194], it is noted that reweighting the nominal POWHEG+PYTHIA8 sample to match NNLO QCD predictions for the top-quark-p_{T} spectrum. Unfortunately, such a sample was not available for this analysis.

Although the $p_{\mathrm{T}}(W\text{-lepton})$ distribution highlights the issue with MC simulation of the top-quark-p_{T} spectrum, the aim of this analysis was to investigate the MC simulation of hadronisation and fragmentation. Firstly, it can be seen that the observables that should be sensitive to the b-quark fragmentation show no discrimination between the r_b variation samples. As discussed in Section 6.1.1, r_b controls the position of the peak in the x_B distribution. This will change the fraction of energy that is transferred from the b-quark to the b-hadron. Although changes in this energy transfer greatly affected the top-quark mass extraction, the differences in the differential cross-section are not large enough to reject any of the r_b signal predictions.

While changing just a single parameter in the b-quark fragmentation parameterisation shows little discrimination, the change of b-quark fragmentation parameterisation does. The Monash+Peterson prediction uses the Monash tuning and the Peterson [195] b-quark fragmentation parameterisation. The Monash+Peterson prediction is disfavored by both the $m_{\ell\mu}$ and $p_{\mathrm{T}}(\mu\text{-soft})$ distributions. The Monash prediction, however, is only disfavored by the $m_{\ell\mu}$ distribution, suggesting that the Peterson parameterisation is worse than the Lund-Bowler parameterisation, which is used in all other PYTHIA samples. Furthermore, it is interesting to note that the HERWIG samples, which use a non-parametric description of the b-quark fragmentation, are also not disfavoured. The only exception is the $p_{\mathrm{T}}^{\mathrm{rel}}(\mu\text{-soft})$ distribution.

The modelling of the $p_{\mathrm{T}}^{\mathrm{rel}}(\mu\text{-soft})$ observable is very sensitive to the hadronisation and fragmentation. It shows the worst agreement overall, out of the observables sensitive to hadronisation and fragmentation. Poor modelling of this observable can be seen for several predictions. The

poor modelling of this observable is one reason why it is not used in the SMT, even though it is a useful discriminant for selecting soft muons.

Overall, the observables investigated do not show disagreement for many predictions. It is important to note, however, the binning for many of these observables could be much finer with increased statistics and a particle level jet definition that more closely matches the reconstructed level one. Observables such as $p_{\mathrm{T}}^{\mathrm{rel}}(\mu\text{-soft})$ and $p_{\mathrm{T}}^{\mathrm{z}}(\mu\text{-soft})$ would benefit from more than three bins and would likely show more discriminating power between models. Furthermore, measurements of these observables using the full Run 2 dataset will be useful for MC tuning. Currently, no differential cross-section measurements of observables that are sensitive to b-quark fragmentation at the LHC exist, so their extraction and inclusion in MC tuning procedures would be valuable.

Chapter 11

Conclusions

In this thesis, measurements of the top-quark mass and of the differential $t\bar{t}$ cross-sections have been presented. The top-quark mass measurement utilises a novel technique based on the partial reconstruction of the top-quark mass using a fully-leptonic observable. The invariant mass of the lepton from the decay of the W-boson and a muon from the semileptonic decay of a b-hadron is constructed and a profile likelihood fit is performed. The extracted top-quark mass of $m_t = 174.44 \pm 0.39\,(\text{stat}) \pm 0.64\,(\text{syst}) = 0.76\,(\text{stat+syst})$ GeV is consistent with the current ATLAS combination of top-quark mass measurements within 2.2 standard deviations. This measurement is currently the most precise top-quark mass measurement using direct reconstruction of the top-quark decay products.

One of the main uncertainties of the analysis is that associated with the b-quark fragmentation. This uncertainty is large, in part, because of poor modelling of the b-quark fragmentation in ATLAS MC simulation. In order to improve the MC simulation, measurements of differential cross-sections in ATLAS data that are sensitive to b-quark fragmentation should be used as input to the MC tuning process. The first measurement of top-quark differential cross-sections that are sensitive to b-quark fragmentation in ATLAS is presented. The differential cross-sections as a function of seven observables are compared to various signal predictions and a χ^2 test statistic is calculated. With the partial Run 2 dataset, the power of these observables to discriminate between different signal predictions is limited because of statistics and a sub-optimal particle level jet definition.

The measurement of the top-quark mass is systematically dominated and therefore would not benefit much by performing the analysis with the full Run 2 dataset. The main area of improvement for the analysis is the modelling of the b-quark fragmentation, which the differential cross-section measurement should help with.

Aside from a full Run 2 measurement of the differential cross-section of observables sensitive to b-quark fragmentation, a measurement of the top-quark mass at particle level may also be interesting. As discussed in Section 2.2.3, the measurement of the top-quark mass and the interpretation of the mass is a complex topic. In the top-quark mass measurement presented in this analysis, the measured mass is considered to be the MC mass, m_t^{MC}. Measurement of the top-quark pole mass, m_t^{pole}, is normally performed by extracting it from differential cross-sections for top-quark pair production and comparing to fixed order calculations. In principle, a similar measurement could be performed using the differential cross-section measurement of $m_{\ell\mu}$. However, due to the soft muon originating from a non-perturbative process (hadronisation), a fixed order calculation is not possible.

Discussions with a Alexander Mitov [196] suggested that it could be possible to calculate a pseudo-fixed order calculation for this process and therefore a more theoretically sound top-quark mass measurement could be performed. This work would require input from theorists to calculate the differential cross-sections but the top-quark mass extraction would be straightforward to implement.

References

[1] ATLAS Collaboration, *Measurement of the top quark mass using a leptonic invariant mass in pp collisions at $\sqrt{s}$ = 13 TeV with the ATLAS detector.* ATLAS-CONF-2019-046, Oct, 2019. http://cds.cern.ch/record/2693954.

[2] D. Hanneke, S. Fogwell, and G. Gabrielse, *New Measurement of the Electron Magnetic Moment and the Fine Structure Constant.* Physical Review Letters **100**(12) (Mar, 2008) . http://dx.doi.org/10.1103/PhysRevLett.100.120801.

[3] M. E. Peskin and D. V. Schroeder, *An Introduction to Quantum Field Theory.* Westview Press, 1995.

[4] M. Thomson, *Modern Particle Physics.* Cambridge University Press, 2013.

[5] D. Griffiths, *Introduction to Elementary Particles.* Wiley, 2008.

[6] B. R. Martin and G. Shaw, *Particle Physics.* John Wiley and Sons, 1995.

[7] M. Tanabashi *et al.* (Particle Data Group), *Review of Particle Physics.* Physical Review D **98**(030001) (2018) .

[8] E. Noether, *Invariante Variationsprobleme.* Nachrichten von der Gesellschaft der Wissenschaften zu Göttingen, Mathematisch-Physikalische Klasse (1918) pp. 235–257. https://eudml.org/doc/59024.

[9] S. L. Glashow, *The renormalizability of vector meson interactions.* Nuclear Physics **10** (1959) pp. 107–117.

[10] A. Salam and J. C. Ward, *Weak and electromagnetic interactions.* Il Nuovo Cimento **11**(4) (1959) pp. 568–577.

[11] S. Weinberg, *A Model of Leptons.* Physical Review Letters **19**(21) (1967) pp. 1264–1266.

[12] M. Kobayashi and T. Maskawa, *CP-Violation in the Renormalizable Theory of Weak Interaction.* Progress of Theoretical Physics **49**(2) (1973) pp. 652–657.

[13] N. Cabibbo, *Unitary Symmetry and Leptonic Decays.* Physical Review Letters **10**(12) (1963) pp. 531–533.

[14] G. Prosperi, M. Raciti, and C. Simolo, *On the running coupling constant in QCD*. Progress in Particle and Nuclear Physics **58**(2) (Apr, 2007) p. 387–438. http://dx.doi.org/10.1016/j.ppnp.2006.09.001.

[15] P. W. Higgs, *Broken Symmetries and the Masses of Gauge Bosons*. Physical Review Letters **13**(16) (1964) pp. 508–509.

[16] P. W. Higgs, *Broken symmetries, massless particles and gauge fields*. Physics Letters **12**(2) (1964) pp. 132–133.

[17] F. Englert and R. Brout, *Broken Symmetry and the Mass of Gauge Vector Mesons*. Physical Review Letters **13**(9) (1964) pp. 321–323.

[18] G. S. Guralnik, C. R. Hagen, and T. W. B. Kibble, *Global Conservation Laws and Massless Particles*. Physical Review Letters **13**(20) (1964) pp. 585–587.

[19] ATLAS Collaboration, *Observation of a new particle in the search for the Standard Model Higgs boson with the ATLAS detector at the LHC*. Physics Letters B **716**(1) (2012) pp. 1–29.

[20] CMS Collaboration, *Observation of a new boson at a mass of 125 GeV with the CMS experiment at the LHC*. Physics Letters B **716**(1) (Sep, 2012) p. 30–61. http://dx.doi.org/10.1016/j.physletb.2012.08.021.

[21] R. D. Klauber, *The Seesaw Mechanism*. http://www.quantumfieldtheory.info/TheSeesawMechanism.htm (accessed on 2/02/2020).

[22] Perl, M. L. et al., *Evidence for Anomalous Lepton Production in $e^+ - e^-$ Annihilation*. Physics Review Letters **35** (Dec, 1975) pp. 1489–1492. https://link.aps.org/doi/10.1103/PhysRevLett.35.1489.

[23] Herb, S. W. et al., *Observation of a Dimuon Resonance at 9.5 GeV in 400-GeV Proton-Nucleus Collisions*. Physical Review Letters **39** (Aug, 1977) pp. 252–255.

[24] CDF Collaboration, *Observation of Top Quark Production in pp Collisions with the Collider Detector at Fermilab*. Physical Review Letters **74**(14) (1995) pp. 2626–2631.

[25] D0 Collaboration, *Observation of the Top Quark*. Physical Review Letters **74**(14) (1995) pp. 2632–2637.

[26] ATLAS Collaboration, *Measurement of the top quark mass in the $t\bar{t} \to$ dilepton channel from $\sqrt{s}$ =8 TeV ATLAS data*. Physics Letters B **761** (2016) pp. 350 – 371.

[27] Particle Data Group, *Bottom Quark*. http://pdg.lbl.gov/2019/listings/rpp2019-list-b-quark.pdf (accessed on

16/12/2019).

[28] Particle Data Group, *Top Quark*. http://pdg.lbl.gov/2019/reviews/rpp2018-rev-top-quark.pdf (accessed on 16/12/2019).

[29] A. D. Martin, W. J. Stirling, R. S. Thorne, and G. Watt, *Parton distributions for the LHC*. The European Physical Journal C **63**(2) (Jul, 2009) pp. 189—- 285. http://dx.doi.org/10.1140/epjc/s10052-009-1072-5.

[30] J. Erler and M. Schott, *Electroweak precision tests of the Standard Model after the discovery of the Higgs boson*. Progress in Particle and Nuclear Physics **106** (May, 2019) p. 68–119. http://dx.doi.org/10.1016/j.ppnp.2019.02.007.

[31] A. H. Hoang, *The Top Mass: Interpretation and Theoretical Uncertainties*, 2014.

[32] M. Beneke, P. Marquard, P. Nason, and M. Steinhauser, *On the ultimate uncertainty of the top quark pole mass*. Physics Letters B **775** (2017) pp. 63 – 70. http://www.sciencedirect.com/science/article/pii/S0370269317308663.

[33] P. Nason, *The Top Quark Mass at the LHC*, 2018.

[34] P. Marquard, A. V. Smirnov, V. A. Smirnov, and M. Steinhauser, *Quark Mass Relations to Four-Loop Order in Perturbative QCD*. Physical Review Letters **114**(14) (Apr, 2015) . http://dx.doi.org/10.1103/PhysRevLett.114.142002.

[35] G. Degrassi, S. Di Vita, J. Elias-Miró, J. R. Espinosa, G. F. Giudice, G. Isidori, and A. Strumia, *Higgs mass and vacuum stability in the Standard Model at NNLO*. Journal of High Energy Physics **2012**(8) (Aug, 2012) . http://dx.doi.org/10.1007/JHEP08(2012)098.

[36] CMS Collaboration, *Measurement of the top quark mass with lepton+jets final states using pp collisions at* $\sqrt{s} = 13$ *TeV*. The European Physical Journal C **78**(11) (Nov, 2018) . http://dx.doi.org/10.1140/epjc/s10052-018-6332-9.

[37] ATLAS Collaboration, *Top Quark Mass Summary Plots*. ATL-PHYS-PUB-2019-036, Sep, 2019. http://cds.cern.ch/record/2690526.

[38] CMS Collaboration, *Measurement of* $\mathrm{t\bar{t}}$ *normalised multi-differential cross sections in pp collisions at* $\sqrt{s} = 13$ *TeV, and simultaneous determination of the strong coupling strength, top quark pole mass, and parton distribution functions*, 2019.

[39] ATLAS Collaboration, *Measurement of the top quark mass in the* $t\bar{t} \to$ *lepton+jets channel from* $\sqrt{s} = 8$ *TeV ATLAS data and combination with previous results*. Eur. Phys. J. C **79** (2019) p. 290, arXiv:1810.01772 [hep-ex].

[40] ATLAS Collaboration, *Measurement of the top quark mass in the $t\bar{t} \to$ dilepton channel from $\sqrt{s} = 8$ TeV ATLAS data*. Phys. Lett. B **761** (2016) p. 350, arXiv:1606.02179 [hep-ex].

[41] ATLAS Collaboration, *Measurement of lepton differential distributions and the top quark mass in $t\bar{t}$ production in pp collisions at $\sqrt{s} = 8$ TeV with the ATLAS detector*. Eur. Phys. J. C **77** (2017) p. 804, arXiv:1709.09407 [hep-ex].

[42] CDF Collaboration, *Measurement of the Top Quark Mass Using the Invariant Mass of Lepton Pairs in Soft Muon b-tagged Events*. Phys. Rev. D **80** (2009) p. 051104, arXiv:0906.5371 [hep-ex].

[43] CMS Collaboration, *Measurement of the mass of the top quark in decays with a J/ψ meson in pp collisions at 8 TeV*. JHEP **12** (2016) p. 123, arXiv:1608.03560 [hep-ex].

[44] L. Evans and P. Bryant, *LHC Machine*. Journal of Instrumentation **3**(S08001) (2008) .

[45] UA1 Collaboration, *Experimental observation of isolated large transverse energy electrons with associated missing energy at s=540 GeV*. Physics Letters B **122** (1983) pp. 103–116.

[46] UA2 Collaboration, *Observation of single isolated electrons of high transverse momentum in events with missing transverse energy at the CERN pp collider*. Physics Letters B **122**(5) (1983) pp. 476–485.

[47] UA1 Collaboration, *Experimental Observation of Lepton Pairs of Invariant Mass Around 95-GeV/c^2 at the CERN SPS Collider*. Physics Letters B **126** (1983) pp. 398–410.

[48] UA2 Collaboration, *Evidence for Z0 —> e+ e- at the CERN anti-p p Collider*. Physics Letters B **129** (1983) pp. 130–140.

[49] NA62 Collaboration, *NA62: Technical Design Document*. NA62-10-07, 2010. https://cds.cern.ch/record/1404985.

[50] S. P. et al., *Monitoring and Modelling of the LHC Emittance and Luminosity Evolution in 2018*. Journal of Physics: Conference Series **1350** (Nov, 2019) p. 012011.

[51] R. Steerenberg, *LHC Report: The LHC is full!* https://home.cern/news/news/accelerators/lhc-report-lhc-full (accessed on 02/03/20).

[52] CERN, *The CERN Accelerator Complex*. https://cds.cern.ch/record/2636343 (accessed on 13/07/2019).

[53] ATLAS Experiment, CERN, *Computer generated image of the whole ATLAS detector*. https://cds.cern.ch/record/1095924 (accessed on 20/11/2019).

[54] ATLAS Collaboration, *ATLAS inner detector: Technical Design Report.* CERN-LHCC-97-016, ATLAS-TDR-4, 1997. https://cdsweb.cern.ch/record/331063.

[55] ATLAS Experiment, CERN, *Computer generated image of the ATLAS inner detector.* https://cds.cern.ch/record/1095926 (accessed on 20/11/2019).

[56] ATLAS Collaboration, *ATLAS Insertable B-Layer Technical Design Report.* CERN-LHCC-2010-013, ATLAS-TDR-19, 2010. https://cdsweb.cern.ch/record/1291633.

[57] ATLAS Collaboration, *Track Reconstruction Performance of the ATLAS Inner Detector at* $\sqrt{s} = 13$ *TeV.* ATL-PHYS-PUB-2015-018, Jul, 2015. http://cds.cern.ch/record/2037683.

[58] ATLAS Collaboration, *ATLAS liquid-argon calorimeter: Technical Design Report.* CERN-LHCC-96-041, ATLAS-TDR-2, 1996. https://cdsweb.cern.ch/record/331061.

[59] ATLAS Collaboration, *The ATLAS Experiment at the CERN Large Hadron Collider.* Journal of Instrumentation **3**(S08003) (2008) .

[60] ATLAS Collaboration, *ATLAS tile calorimeter: Technical Design Report.* CERN-LHCC-96-042, ATLAS-TDR-3, 1996. https://cdsweb.cern.ch/record/331062.

[61] M. Aharrouche *et al.*, *Energy linearity and resolution of the ATLAS electromagnetic barrel calorimeter in an electron test-beam.* Nuclear Instruments and Methods in Physics Research A **568** (2006) pp. 601–623.

[62] ATLAS Collaboration, *Results from a new combined test of an electromagnetic liquid argon calorimeter with a hadronic scintillating-tile calorimeter.* Nuclear Instruments and Methods in Physics Research A **449** (2000) pp. 462–477.

[63] ATLAS Collaboration, *ATLAS muon spectrometer: Technical Design Report.* CERN-LHCC-97-022, ATLAS-TDR-10, 1997. https://cdsweb.cern.ch/record/331068.

[64] ATLAS Collaboration, *Monitored drift tubes in ATLAS.* ATL-M-PN-129, 1996. https://cds.cern.ch/record/319197.

[65] T. Argyropoulos, *Cathode strip chambers in ATLAS : Installation, commissioning and in situ performance* in 2008 IEEE Nuclear Science Symposium Conference Record, 2008.

[66] ATLAS Experiment, CERN, *Computer generated image of the ATLAS Muons subsystem.* https://cds.cern.ch/record/1095929 (accessed on 20/11/2019).

[67] ATLAS Collaboration, *ATLAS central solenoid: Technical Design Report.* CERN-LHCC-97-021, ATLAS-TDR-9, 1997. https://cdsweb.cern.ch/record/331067.

[68] ATLAS Collaboration, *ATLAS barrel toroid: Technical Design Report.* CERN-LHCC-97-019, ATLAS-TDR-7, 1997. https://cdsweb.cern.ch/record/331065.

[69] ATLAS Collaboration, *ATLAS end-cap toroids: Technical Design Report.* CERN-LHCC-97-020, ATLAS-TDR-8, 1997. https://cdsweb.cern.ch/record/331066.

[70] ATLAS Collaboration, *ATLAS level-1 trigger: Technical Design Report.* CERN-LHCC-98-014, ATLAS-TDR-12, 1998. https://cdsweb.cern.ch/record/381429.

[71] ATLAS Collaboration, *ATLAS high-level trigger, data-acquisition and controls: Technical Design Report.* CERN-LHCC-2003-022, ATLAS-TDR-16, 2003. https://cdsweb.cern.ch/record/616089.

[72] ATLAS Collaboration, *Overview of TDAQ system.* https://twiki.cern.ch/twiki/bin/view/AtlasPublic/ApprovedPlotsDAQ (accessed on 18/3/20).

[73] G. Crone *et al.*, *The ATLAS ReadOut System – Performance with first data and perspective for the future.* Nuclear Instruments and Methods in Physics Research A **623** (2010) pp. 534–536.

[74] LHC Experiments Committee, CERN, *LHC computing Grid: Technical Design Report.* CERN-LHCC-2005-024, LCG-TDR-001, 2004. https://cds.cern.ch/record/840543.

[75] G. Avoni *et al.*, *The new LUCID-2 detector for luminosity measurement and monitoring in ATLAS.* JINST **13**(07) (2018) p. P07017.

[76] ATLAS Collaboration, P. Jenni, M. Nessi, and M. Nordberg, *Zero Degree Calorimeters for ATLAS.* CERN-LHCC-2007-001. LHCC-I-016, Jan, 2007. https://cds.cern.ch/record/1009649.

[77] P. Jenni, M. Nordberg, M. Nessi, and K. Jon-And, *ATLAS Forward Detectors for Measurement of Elastic Scattering and Luminosity.* Technical Design Report ATLAS. CERN, Geneva, 2008. https://cds.cern.ch/record/1095847.

[78] R. K. Ellis, W. J. Stirling, and B. R. Webber, *QCD and collider physics*. Camb. Monogr. Part. Phys. Nucl. Phys. Cosmol. **8** (1996) pp. 1–435.

[79] B. Andersson, G. Gustafson, G. Ingelman, and T. Sjöstrand, *Parton fragmentation and string dynamics*. Physics Reports **97**(2) (1983) pp. 31 – 145. http://www.sciencedirect.com/science/article/pii/0370157383900807.

[80] G. Marchesini and B. R. Webber, *Simulation of QCD Jets Including Soft Gluon Interference*. Nucl. Phys. **B238** (1984) pp. 1–29.

[81] T. Sjöstrand, S. Mrenna, and P. Skands, *PYTHIA 6.4 physics and manual*. Journal of High Energy Physics **2006**(026) (2006) .

[82] S. Bähr *et al.*, *Herwig++ physics and manual*. The European Physical Journal C **58** (2008) pp. 639–707.

[83] SLAC, *Monte Carlo Simulations*. https://theory.slac.stanford.edu/our-research/simulations (accessed on 10/3/20).

[84] S. Agostinelli *et al.*, *Geant4 – a simulation toolkit*. Nuclear Instruments and Methods in Physics Research A **506** (2003) pp. 250–303.

[85] J. Allison *et al.*, *Geant4 Developments and Applications*. IEEE Transactions on Nuclear Science **53** (2006) pp. 270–278.

[86] J. Allison *et al.*, *Recent developments in Geant4*. Nuclear Instruments and Methods in Physics Research A **835** (2016) pp. 186–225.

[87] E. Richter-Was, D. Froidvaux, and L. Poggioli, *ATLFAST 2.0 a fast simulation package for ATLAS*. ATL-PHYS-98-131, 1998. https://cds.cern.ch/record/683751.

[88] R. Frühwirth, *Application of Kalman filtering to track and vertex fitting*. Nuclear Instruments and Methods in Physics Research A **262** (1987) pp. 444–450.

[89] W. Waltenberger, R. Frühwirth, and P. Vanlaer, *Adaptive vertex fitting*. Journal of Physics G: Nuclear and Particle Physics **34**(12) (2007) .

[90] ATLAS Collaboration, *Electron reconstruction and identification in the ATLAS experiment using the 2015 and 2016 LHC proton–proton collision data at* $\sqrt{s} = 13$ *TeV*. The European Physical Journal C **79**(8) (Aug, 2019) .

[91] J. Illingworth and J. Kittler, *A survey of the Hough transform*. Computer Vision, Graphics, and Image Processing **44** (1988) pp. 87–116.

[92] ATLAS Collaboration, *Muon reconstruction performance of the ATLAS detector in proton–proton collision data at $\sqrt{s}$ =13 TeV*. The European Physical Journal C **76**(292) (2016) .

[93] J. E. Huth *et al.*, *Toward a standardization of jet definitions* in 1990 DPF Summer Study on High-energy Physics: Research Directions for the Decade (Snowmass 90) Snowmass, Colorado, June 25-July 13, 1990, 1990, pp. 0134–136. http://lss.fnal.gov/cgi-bin/find_paper.pl?conf-90-249.

[94] M. Cacciari, G. P. Salam, and G. Soyez, *The anti-k_t jet clustering algorithm*. Journal of High Energy Physics **2008**(063) (2008) .

[95] ATLAS Collaboration, *Topological cell clustering in the ATLAS calorimeters and its performance in LHC Run 1*. The European Physical Journal C **77**(490) (2017) .

[96] ATLAS Collaboration, *Jet energy scale measurements and their systematic uncertainties in proton-proton collisions at $\sqrt{s} = 13\,TeV$ with the ATLAS detector*. Physical Review D **96**(7) (Oct, 2017) . http://dx.doi.org/10.1103/PhysRevD.96.072002.

[97] ATLAS Collaboration, *Monte Carlo Calibration and Combination of In-situ Measurements of Jet Energy Scale, Jet Energy Resolution and Jet Mass in ATLAS*. ATLAS-CONF-2015-037, 2015. https://cds.cern.ch/record/2044941.

[98] ATLAS Collaboration, *Measurements of b-jet tagging efficiency with the ATLAS detector using $t\bar{t}$ events at $\sqrt{s} = 13$ TeV*. Journal of High Energy Physics **2018**(8) (Aug, 2018) . http://dx.doi.org/10.1007/JHEP08(2018)089.

[99] ATLAS Collaboration, *Expected performance of the ATLAS b-tagging algorithms in Run-2*. https://cds.cern.ch/record/2037697.

[100] ATLAS Collaboration, *Performance of missing transverse momentum reconstruction with the ATLAS detector using proton–proton collisions at $\sqrt{s} = 13$ TeV*. The European Physical Journal C **78**(11) (Nov, 2018) .

[101] A.D. Martin et al., *Parton distributions for the LHC*. Eur. Phys. J. C **63** (2009) p. 189, arXiv:0901.0002 [hep-ph].

[102] A.D Martin et al., *Uncertainties on α_S in global PDF analyses and implications for predicted hadronic cross sections*. Eur. Phys. J. C **64** (2009) p. 653, arXiv:0905.3531 [hep-ph].

[103] ATLAS Collaboration, *ATLAS tunes of PYTHIA6 and PYTHIA8 for MC11*. ATL-PHYS-PUB-2011-009 (2011) . https://cds.cern.ch/record/1363300.

[104] D. J. Lange, *The EvtGen particle decay simulation package*. Nucl. Instrum. Meth. A **462** (2001) pp. 152–155.

[105] T. Gleisberg *et al.*, *Event generation with SHERPA 1.1*. Journal of High Energy Physics **2009**(007) (2009) .

[106] S. Frixione, P. Nason, and G. Ridolfi, *A Positive-weight next-to-leading-order Monte Carlo for heavy flavour hadroproduction*. JHEP **09** (2007) p. 126, arXiv:0707.3088.

[107] P. Nason, *A new method for combining NLO QCD with shower Monte Carlo algorithms*. Journal of High Energy Physics **2004**(040) (2004) .

[108] S. Frixione, P. Nason, and O. C, *Matching NLO QCD computations with parton shower simulations: the POWHEG method*. Journal of High Energy Physics **2007**(070) (2007) .

[109] S. Alioli *et al.*, *A general framework for implementing NLO calculations in shower Monte Carlo programs: the POWHEG BOX*. Journal of High Energy Physics **2010**(43) (2010) .

[110] NNPDF, R. D. Ball *et al.*, *Parton distributions for the LHC Run II*. JHEP **04** (2015) p. 040, arXiv:1410.8849 [hep-ph].

[111] S. Frixione, E. Laenen, P. Motylinski, and B. R. Webber, *Angular correlations of lepton pairs from vector boson and top quark decays in Monte Carlo simulations*. JHEP **04** (2007) p. 081, arXiv:hep-ph/0702198.

[112] T. Sjöstrand, S. Ask, J. R. Christiansen, R. Corke, N. Desai, P. Ilten, S. Mrenna, S. Prestel, C. O. Rasmussen, and P. Z. Skands, *An Introduction to PYTHIA 8.2*. Comput. Phys. Commun. **191** (2015) p. 159, arXiv:1410.3012 [hep-ph].

[113] ATLAS Collaboration, *ATLAS Run 1 Pythia8 tunes*. https://cdsweb.cern.ch/record/1966419. ATL-PHYS-PUB-2014-021.

[114] M. Czakon and A. Mitov, *Top++: A program for the calculation of the top-pair cross-section at hadron colliders*. Comput. Phys. Commun. **185** (2014) p. 2930, arXiv:1112.5675 [hep-ph].

[115] M. Cacciari, M. Czakon, M. Mangano, A. Mitov, and P. Nason, *Top-pair production at hadron colliders with next-to-next-to-leading logarithmic soft-gluon resummation*. Phys. Lett. B **710** (2012) p. 612, arXiv:1111.5869 [hep-ph].

[116] P. Bärnreuther, M. Czakon, and A. Mitov, *Percent Level Precision Physics at the Tevatron: First Genuine NNLO QCD Corrections to $q\bar{q} \to t\bar{t}$*. Phys. Rev. Lett. **109** (2012) p. 132001, arXiv:1204.5201 [hep-ph].

[117] M. Czakon and A. Mitov, *NNLO corrections to top-pair production at hadron colliders: the all-fermionic scattering channels*. JHEP **12** (2012) p. 54, arXiv:1207.0236

[hep-ph].

[118] M. Czakon and A. Mitov, *NNLO corrections to top-pair production at hadron colliders: the quark-gluon reaction*. JHEP **01** (2013) p. 80, arXiv:1210.6832 [hep-ph].

[119] M. Czakon, P. Fiedler, and A. Mitov, *Total Top-Quark Pair-Production Cross Section at Hadron Colliders Through* $\mathcal{O}(\alpha_S^4)$. Phys. Rev. Lett. **110** (2013) p. 252004, arXiv:1303.6254 [hep-ph].

[120] T. Gleisberg and S. Höche, *Comix, a new matrix element generator*. JHEP **12** (2008) p. 039, arXiv:0808.3674 [hep-ph].

[121] S. Schumann and F. Krauss, *A Parton shower algorithm based on Catani-Seymour dipole factorisation*. JHEP **03** (2008) p. 038, arXiv:0709.1027 [hep-ph].

[122] S. Höche, F. Krauss, M. Schönherr, and F. Siegert, *QCD matrix elements + parton showers: The NLO case*. JHEP **04** (2013) p. 027, arXiv:1207.5030 [hep-ph].

[123] ATLAS Collaboration, *Measurements of differential cross sections of top quark pair production in association with jets in pp collisions at* $\sqrt{s} = 13$ *TeV using the ATLAS detector*. JHEP **10** (2018) p. 159, arXiv:1802.06572 [hep-ex].

[124] S. Frixione, E. Laenen, P. Motylinski, B. R. Webber, and C. D. White, *Single-top hadroproduction in association with a W boson*. JHEP **07** (2008) p. 029, arXiv:0805.3067 [hep-ph].

[125] P. Artoisenet, R. Frederix, O. Mattelaer, and R. Rietkerk, *Automatic spin-entangled decays of heavy resonances in Monte Carlo simulations*. JHEP **03** (2013) p. 015, arXiv:1212.3460 [hep-ph].

[126] T. Sjöstrand, S. Mrenna and P. Skands,, *PYTHIA 6.4 Physics and Manual*. JHEP **05** (2006) p. 036, arXiv:hep-ph/0603175 [hep-ph].

[127] P. Z. Skands, *Tuning Monte Carlo Generators: The Perugia Tunes*. Phys. Rev. D **82** (2010) p. 074018, arXiv:1005.3457.

[128] N. Kidonakis, *Two-loop soft anomalous dimensions for single top quark associated production with a W- or H-*. Phys. Rev. D **82** (2010) p. 054018, arXiv:1005.4451 [hep-ph].

[129] N. Kidonakis, *NNLL resummation for s-channel single top quark production*. Phys. Rev. D **81** (2010) p. 054028, arXiv:1001.5034 [hep-ph].

[130] N. Kidonakis, *Next-to-next-to-leading-order collinear and soft gluon corrections for t-channel single top quark production*. Phys. Rev. D **83** (2011) p. 091503, arXiv:1103.2792 [hep-ph].

[131] ATLAS Collaboration, "Estimation of non-prompt and fake lepton backgrounds in final states with top quarks produced in proton-proton collisions at $\sqrt{s} = 8$ TeV with the ATLAS detector." ATLAS-CONF-2014-058, 2014. https://cds.cern.ch/record/1951336.

[132] B. Andersson, G. Gustafson, G. Ingelman, and T. Sjostrand, *Parton Fragmentation and String Dynamics*. Phys. Rept. **97**(31) (1983) p. 145.

[133] M. Bowler, *e+ e- Production of Heavy Quarks in the String Model*. Z. Phys. C **11**(31) (1981) p. 169.

[134] P. Skands, S. Carrazza, and J. Rojo, *Tuning Pythia 8.1: the Monash 2013 tune*. European Physical Journal C **74** (2014) p. 3024, arXiv:1404.5630v1.

[135] ALEPH Collaboration, *Study of the fragmentation of b quarks into B mesons at the Z peak*. Phys. Lett. B **512** (2001) p. 30, arXiv:hep-ex/0106051.

[136] OPAL Collaboration, *Inclusive analysis of the b quark fragmentation function in Z decays at LEP*. Eur. Phys. J. C **29** (2003) p. 463, arXiv:hep-ex/0210031 [hep-ex].

[137] SLD Collaboration, *Precise Measurement of the b-Quark Fragmentation Function in Z^0 Boson Decays*. Phys. Rev. Lett. **84** (2000) p. 4300.

[138] DELPHI Collaboration, *A measurement of the branching fractions of the b-quark into charged and neutral b-hadrons*. Phys. Lett. B **576** (2003) pp. 29–42, arXiv:0311005.

[139] A. Buckley, H. Hoeth, H. Lacker, H. Schulz, and J. E. Von Seggern, *Systematic event generator tuning for the LHC*. Eur. Phys. J. C **65** (2010) pp. 331–357, arXiv:0907.2973 [hep-ph].

[140] A. Buckley, J. Butterworth, L. Lonnblad, D. Grellscheid, H. Hoeth, J. Monk, H. Schulz, and F. Siegert, *Rivet user manual*. Comput. Phys. Commun. **184** (2013) pp. 2803–2819, arXiv:1003.0694 [hep-ph].

[141] Heavy Flavour Averaging Group (HFAG), *Averages of b-hadron, c-hadron, and τ-lepton properties as of summer 2014*. (2014) , arXiv:1412.7515 [hep-ex].

[142] CDF Collaboration, . Phys. Rev. D **77** (2008) p. 072003, arXiv:0801.4375.

[143] CDF Collaboration, *Measurement of Ratios of Fragmentation Fractions for Bottom Hadrons in p-pbar Collisions at $\sqrt{s}$=1.96 TeV*. Phys. Rev. Lett. **84** (2000) pp. 1663–1668, arXiv:9909011.

[144] CDF Collaboration, *Measurement of b quark fragmentation fractions in the production of strange and light B mesons in $p\bar{p}$ collisions at $\sqrt{s} = 1.8$TeV*. Phys. Rev. D **60** (1999) p. 092005.

[145] CDF Collaboration, *First measurement of the ratio of branching fractions* $\mathcal{B}(\Lambda_b^0 \to \Lambda_c^+ \mu^- \overline{\nu}_\mu)/\mathcal{B}(\Lambda_b^0 \to \Lambda_c^+ \pi^-)$. Phys. Rev. D **79** (2009) p. 032001, arXiv:0810.3213.

[146] LHCb Collaboration, *Measurement of b hadron production fractions in 7 TeV pp collisions*. Phys. Rev. D **85** (2012) p. 032008, arXiv:1111.2357.

[147] LHCb Collaboration, *Determination of* f_s/f_d *for 7 TeV pp Collisions and Measurement of the* $B^0 \to D^- K^+$ *Branching Fraction*. Phys. Rev. Lett. **107** (2011) p. 211801, arXiv:1106.4435.

[148] LHCb Collaboration, *Measurement of the fragmentation fraction ratio* f_s/f_d *and its dependence on B meson kinematics*. JHEP **04** (2013) p. 001, arXiv:1301.5286.

[149] ATLAS Collaboration, *Determination of the Ratio of b-Quark Fragmentation Fractions* f_s/f_d *in pp Collisions at* $\sqrt{s} = 7$ TeV *with the ATLAS Detector*. Phys. Rev. Letter **115** (2015) p. 262001, arXiv:1507.08925 [hep-ex].

[150] E. Lohrmann, "A Summary of Charm Hadron Production Fractions," 2011. arXiv:1112.3757 [hep-ex].

[151] DELPHI Collaboration, *A study of B0B0 mixing using semileptonic decays of B hadrons produced from Z0*. Phys. Lett. B **301** (1993) pp. 145–154.

[152] L3 Collaboration, *Measurements of Z0* $\to$ *bb decays and the semileptonic branching ratio BR* $(b \to \ell + X)$. Phys. Lett. B **261** (1991) pp. 177–187.

[153] L3 Collaboration, *Measurement of the branching ratios* $b \to e\nu X$, $\mu\nu X$, $\tau\nu X$ *and* νX. Z. Phys. C **71** (1996) pp. 379–390.

[154] OPAL Collaboration, *Measurements of inclusive semileptonic branching fractions of b hadrons in Z decays*. Eur. Phys. J. C **13** (2000) pp. 225–240, arXiv:9906041.

[155] LEP Electroweak Working Group and the SLD Heavy Flavour and Electroweak Groups, "Final input parameters for the LEP/SLD heavy flavour analyses." LEPHF 2001-01, 2001. https://www.cern.ch/LEPEWWG/heavy/.

[156] J. Blanco, V. Boisvert, L. Cerrito, N. Cooper-Smith, J. D. Morris, M. Rose, G. Salamanna, G. Snidero, and M. Vanadia, *Calibration of the* χ^2_{match}*-based Soft Muon Tagger algorithm*. ATL-COM-PHYS-2012-008, Jan, 2012. https://cds.cern.ch/record/1411939. updates to be expected.

[157] ATLAS Collaboration, *Measurements of charge and CP asymmetries in b-hadron decays using top-quark events collected by the ATLAS detector in pp collisions at* $\sqrt{s} = 8$ *TeV*. Journal of High Energy Physics **2017**(2) (Feb, 2017) .

http://dx.doi.org/10.1007/JHEP02(2017)071.

[158] ATLAS Collaboration, "Luminosity determination in pp collisions at $\sqrt{s} = 13$ TeV using the ATLAS detector at the LHC." Atlas-conf-2019-021, 2019. https://cds.cern.ch/record/2677054.

[159] ATLAS Collaboration, *Muon reconstruction performance of the ATLAS detector in proton–proton collision data at* $\sqrt{s} = 13$ *TeV*. Eur. Phys. J. C **76** (2016) p. 292, arXiv:1603.05598 [hep-ex].

[160] ATLAS Collaboration, *Electron reconstruction and identification in the ATLAS experiment using the 2015 and 2016 LHC proton–proton collision data at* $\sqrt{s} = 13$ *TeV*. Eur. Phys. J. **79** (2019) p. 639, arXiv:1902.04655 [hep-ex].

[161] ATLAS Collaboration, *Performance of pile-up mitigation techniques for jets in pp collisions at* $\sqrt{s} = 8$ *TeV using the ATLAS detector*. Eur. Phys. J. C **76** (2016) p. 581, arXiv:1510.03823 [hep-ex].

[162] ATLAS Collaboration, *Data-driven determination of the energy scale and resolution of jets reconstructed in the ATLAS calorimeters using dijet and multijet events at* $\sqrt{s} = 8$ *TeV*. ATLAS-CONF-2015-017, 2015. https://cds.cern.ch/record/2008678.

[163] J. Gallicchio and M. D. Schwartz, *Quark and Gluon Tagging at the LHC*. Phys. Rev. Lett. **107** (Oct, 2011) p. 172001. https://link.aps.org/doi/10.1103/PhysRevLett.107.172001.

[164] ATLAS Collaboration, *Light-quark and gluon jet discrimination in pp collisions at* $\sqrt{s} = 7$ *TeV with the ATLAS detector*. The European Physical Journal C **74**(8) (Aug, 2014) p. 3023. https://doi.org/10.1140/epjc/s10052-014-3023-z.

[165] ATLAS Collaboration, *Jet energy measurement and its systematic uncertainty in proton–proton collisions at* $\sqrt{s} = 7$ *TeV with the ATLAS detector*. The European Physical Journal C **75**(1) (Jan, 2015) p. 17. https://doi.org/10.1140/epjc/s10052-014-3190-y.

[166] ATLAS Collaboration, *Quark versus Gluon Jet Tagging Using Charged Particle Multiplicity with the ATLAS Detector*. ATL-PHYS-PUB-2017-009, May, 2017. http://cds.cern.ch/record/2263679.

[167] ATLAS Collaboration, *Measurements of b-jet tagging efficiency with the ATLAS detector using* $t\bar{t}$ *events at* $\sqrt{s} = 13$ *TeV*. JHEP **08** (2018) p. 089, arXiv:1805.01845 [hep-ex].

[168] ATLAS Collaboration, "Measurement of b-tagging efficiency of c-jets in $t\bar{t}$ events using a likelihood approach with the ATLAS detector." ATLAS-CONF-2018-001, 2018. https://cds.cern.ch/record/2306649.

[169] ATLAS Collaboration, "Calibration of light-flavour b-jet mistagging rates using ATLAS proton–proton collision data at $\sqrt{s} = 13$ TeV." ATLAS-CONF-2018-006, 2018. https://cds.cern.ch/record/2314418.

[170] J. Butterworth, S. Carrazza, A. Cooper-Sarkar, A. D. Roeck, J. Feltesse, S. Forte, J. Gao, S. Glazov, J. Huston, Z. Kassabov, R. McNulty, A. Morsch, P. Nadolsky, V. Radescu, J. Rojo, and R. Thorne, *PDF4LHC recommendations for LHC Run II*. Journal of Physics G: Nuclear and Particle Physics **43**(023001) (2016) .

[171] ATLAS Collaboration, "Simulation of top-quark production for the ATLAS experiment at $\sqrt{s} = 13$ TeV." ATL-PHYS-PUB-2016-004, 2016. https://cds.cern.ch/record/2120417.

[172] S. Mrenna and P. Skands, *Automated parton-shower variations in Pythia 8*. Phys. Rev. D **94** (2016) p. 074005, arXiv:1605.08352 [hep-ph].

[173] ATLAS Collaboration, "Multi-boson simulation for 13 TeV ATLAS analyses." ATL-PHYS-PUB-2016-002, 2016. https://cds.cern.ch/record/2119986.

[174] K. Cranmer, *Practical Statistics for the LHC*. arXiv:1503.07622.

[175] G. Cowan, K. Cranmer, E. Gross, and O. Vitells, *Asymptotic formulae for likelihood-based tests of new physics*. The European Physical Journal C **71**(2) (Feb, 2011) . http://dx.doi.org/10.1140/epjc/s10052-011-1554-0.

[176] R. D. Cousins, "Generalization of Chisquare Goodness-of-Fit Test for Binned Data Using Saturated Models, with Application to Histograms," 2013. https://www.semanticscholar.org/paper/Generalization-of-Chisquare-Goodness-ofFit-Test-for-Cousins/f816576fdb04547e4db2f72656136060849b3ecf.

[177] ATLAS Collaboration, *ATLAS Run 1 Pythia8 tunes*. ATL-PHYS-PUB-2014-021, 2014. https://cds.cern.ch/record/1966419.

[178] ATLAS Collaboration, *Measurements of top-quark pair differential cross-sections in the lepton+jets channel in pp collisions at $\sqrt{s} = 13$ TeV using the ATLAS detector*. Journal of High Energy Physics **2017**(191) (2017) .

[179] G. D. Cowan, *Statistical Data Analysis*. Oxford University Press, 1998.

[180] A. Tikhonov, *On the solution of ill-posed problems and the method of regularization*. Mat. Sb. **151**(3) (1963) pp. 501–504.

[181] D. L. Phillips, *A Technique for the Numerical Solution of Certain Integral Equations of the First Kind*. J. ACM **9**(1) (Jan, 1962) pp. 84–97.

[182] M. Schmelling, *The method of reduced cross-entropy: A general approach to unfold probability distributions*. Nucl. Inst. Methods Phys. Res. A **340**(2) (1994) pp. 400–412.

[183] S. Schmitt, *TUnfold, an algorithm for correcting migration effects in high energy physics*. Journal of Instrumentation **7**(10) (Oct, 2012) p. T10003–T10003. http://dx.doi.org/10.1088/1748-0221/7/10/T10003.

[184] A. Höcker and V. Kartvelishvili, *SVD approach to data unfolding*. Nuclear Instruments and Methods in Physics Research Section A: Accelerators, Spectrometers, Detectors and Associated Equipment **372**(3) (Apr, 1996) p. 469–481. http://dx.doi.org/10.1016/0168-9002(95)01478-0.

[185] G. Choudalakis, *Fully Bayesian Unfolding*, 2012.

[186] A. J. Bozson, G. D. Cowan, and F. Spanò, *Unfolding with Gaussian Processes*. arXiv:1811.01242. http://arxiv.org/abs/1811.01242.

[187] G. Cowan, *A survey of unfolding methods for particle physics* in Proc. Conference on Advanced Statistical Techniques in Particle Physics, Durham, England, Mar., 2002, pp. 248–257. http://www.ippp.dur.ac.uk/old/Workshops/02/statistics/proceedings/cowan.pdf.

[188] V. Blobel, *Unfolding Methods in Particle Physics* in Proc. PHYSTAT 2011 Workshop on Statistical Issues Related to Discovery Claims in Search Experiments and Unfolding, 2011, pp. 240–251. CERN, Geneva, Switzerland.

[189] F. Spanò, *Unfolding in particle physics: a window on solving inverse problems*. EPJ Web Conf. **55** (2013) p. 03002.

[190] G. D'Agostini, *A multidimensional unfolding method based on Bayes' theorem*. Nucl. Inst. Methods Phys. Res. A **362** (1995) pp. 487–498.

[191] L. B. Lucy, *An iterative technique for the rectification of observed distributions*. Astron. J. **79** (1974) pp. 745–754.

[192] W. H. Richardson, *Bayesian-Based Iterative Method of Image Restoration*. J. Opt. Soc. Am. **62**(1) (Jan, 1972) pp. 55–59. http://www.osapublishing.org/abstract.cfm?URI=josa-62-1-55.

[193] G. Zech, *Iterative unfolding with the Richardson-Lucy algorithm*. Nucl. Inst. Methods Phys. Res. A **716** (2013) pp. 1–9, arXiv:1210.5177.

[194] ATLAS Collaboration, *Measurement of the $t\bar{t}$ production cross-section and lepton differential distributions in e dilepton events from pp collisions at $\sqrt{s} = 13$ TeV with the ATLAS detector*, 2019.

[195] C. Peterson, D. Schlatter, I. Schmitt, and P. M. Zerwas, *Scaling violations in inclusive e^+e^- annihilation spectra*. Phys. Rev. D **27** (Jan, 1983) pp. 105–111. https://link.aps.org/doi/10.1103/PhysRevD.27.105.

[196] A. Mitov. Personal communication.

Appendix A

ρ topology control plots

γ+jets

The comparisons between the data and MC predictions for the γ+jets topology can be seen in Figures A.1 and A.2. In these comparisons, the data and MC predictions are normalised to unity, as some MC samples are missing. Again the agreement is good across all observables. The uncertainties on the ratio plot are incorrect, however, the ratio value itself is. These plots cannot be reproduced with the correct uncertainties due to an irretrievable loss of data.

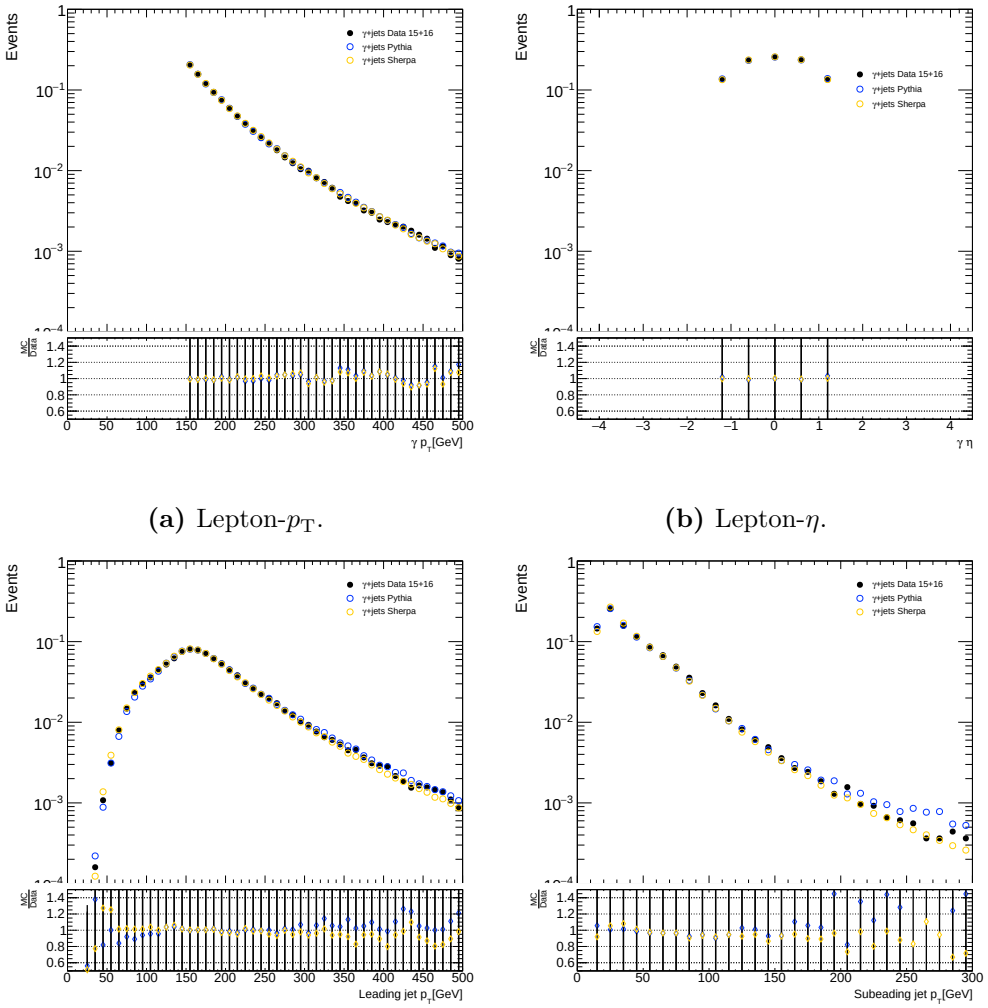

(a) Lepton-p_{T}. **(b)** Lepton-η.

(c) Leading jet-p_{T}. **(d)** Sub-leading jet-p_{T}.

Figure A.1 A comparison of the data and two MC predictions for (a) γ-p_{T}, (b) γ-η, (c) leading jet-p_{T} and (d) subleading jet-p_{T} for the γ+jets topology.

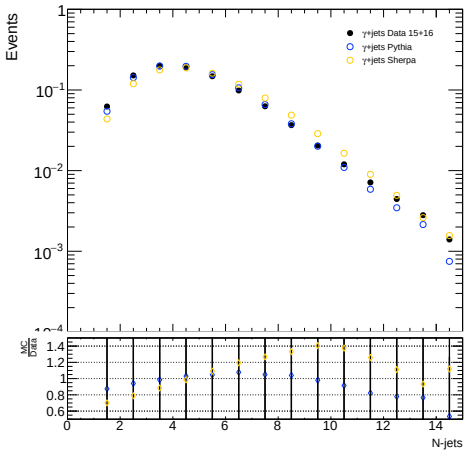

(a) Jet multiplicity in the event.

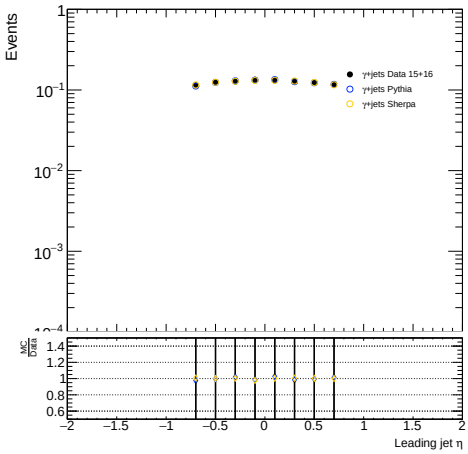

(b) Leading jet-η.

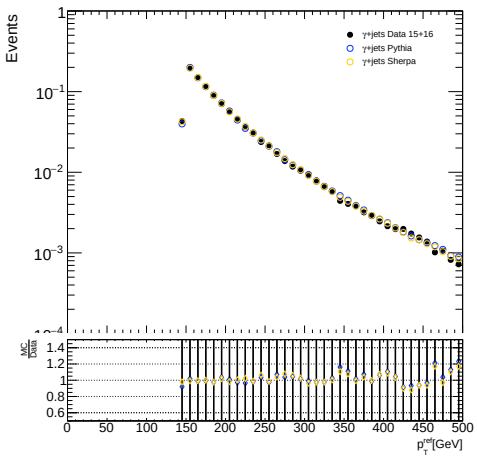

(c) $p_{\mathrm{T}}^{\mathrm{ref}}$.

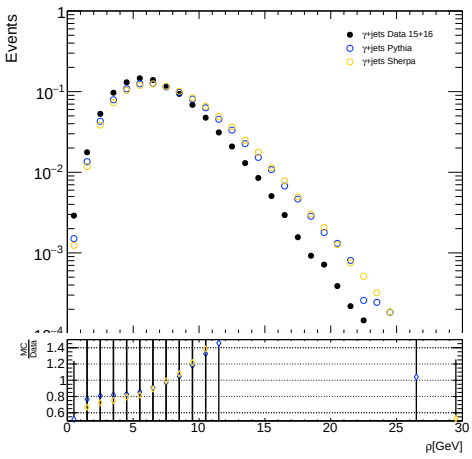

(d) ρ.

Figure A.2 A comparison of the data and two MC predictions for (a) jet multiplicity, (b) leading jet-η, (c) reference object p_{T} and (d) ρ for the γ+jets topology.

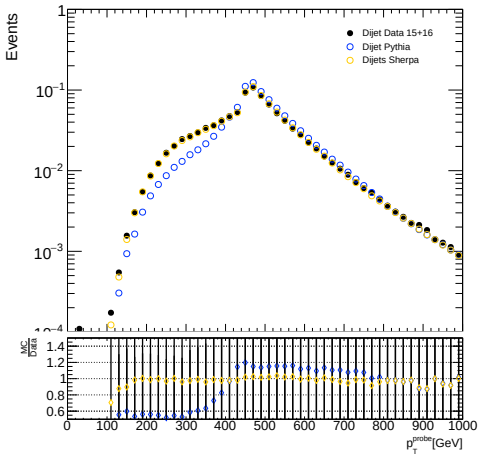

(a) Lepton-p_{T}.

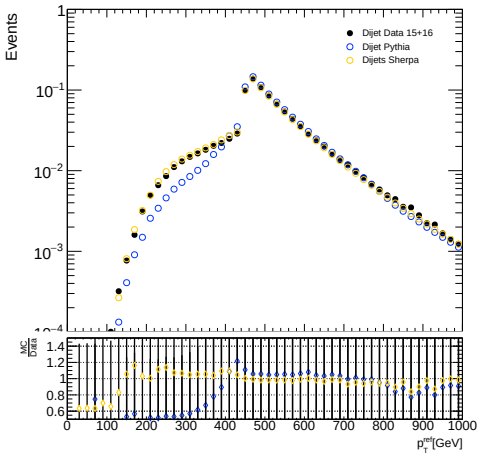

(b) Lepton-η.

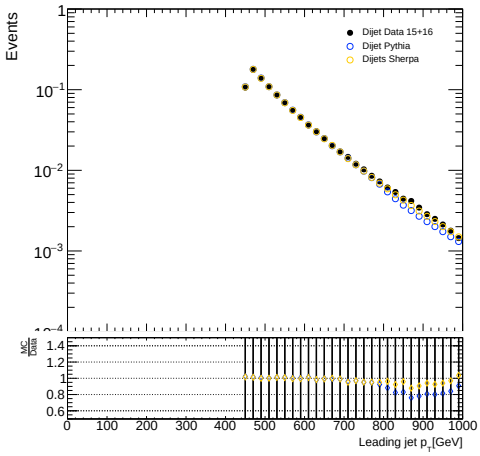

(c) Leading jet-p_{T}.

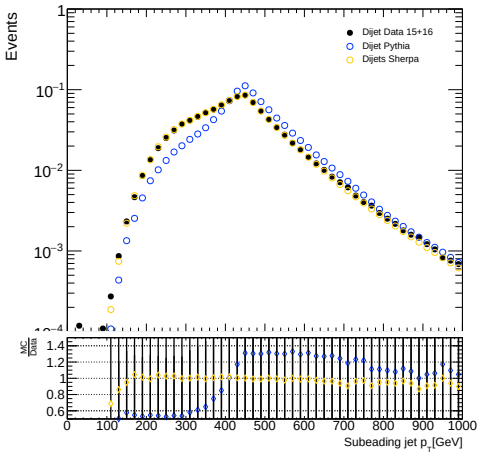

(d) Sub-leading jet-p_{T}.

Figure A.3 A comparison of the data and two MC predictions for (a) probe jet-p_{T}, (b) reference jet-p_{T}, (c) leading jet-p_{T} and (d) subleading jet-p_{T} for the dijet topology.

Dijets

The comparisons between the data and MC predictions for the dijets topology can be seen in Figures A.3 and A.4. Similarly for the dijet, the data and MC prediction samples are normalised to unity. There is good agreement across all observables. The uncertainties on the ratio plot are incorrect however, the ratio value itself is. These plots cannot be reproduced with the correct uncertainties due to an irretrievable loss of data.

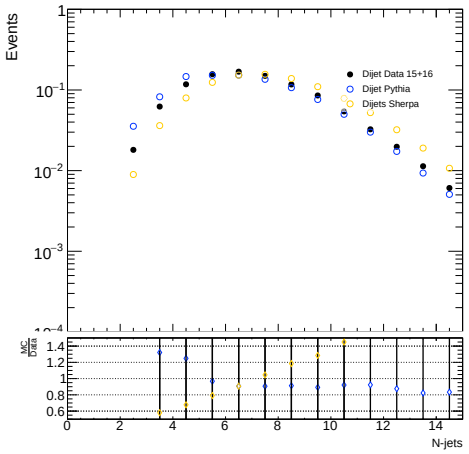

(a) Jet multiplicity in the event.

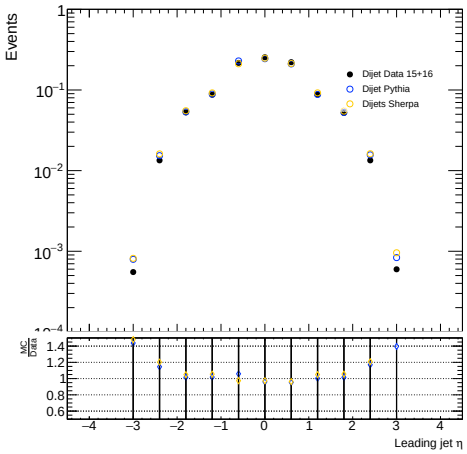

(b) Leading jet-η.

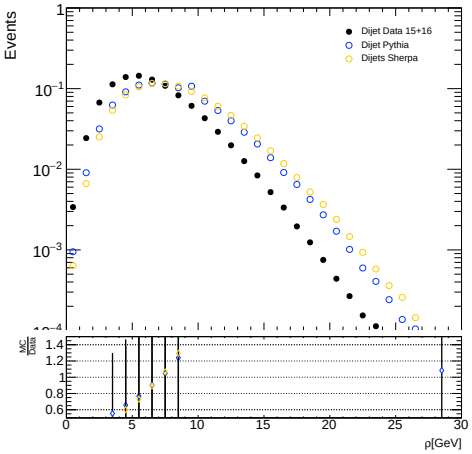

(c) ρ.

Figure A.4 A comparison of the data and two MC predictions for (a) jet multiplicity, (b) leading jet-η, (c) raverage interactions per event and (d) ρ for the dijet topology.